LATE QUATERNARY PALEOCEANOGRAPHIC HISTORY OF THE PACIFIC SECTOR OF THE SOUTHERN OCEAN BASED ON DIATOM EVIDENCE

Dissertation zur Erlangung des akademischen Grades
eines Doktors der Naturwissenschaften

Dr. rer. nat.

am Fachbereich 5 (Geowissenschaften) der
Universität Bremen

vorgelegt von
Verena Katharina Benz

Bremerhaven, Januar 2016

Gutachter: **Prof. Dr. Ralf Tiedemann**

Alfred-Wegener-Institut Helmholtz-Zentrum für Polar- und Meeresforschung, Bremerhaven

Universität Bremen FB5 Geowissenschaften, Bremen

PD Dr. Karin Zonneveld

MARUM – Zentrum für Marine Umweltwissenschaften, Bremen

Universität Bremen FB5 Geowissenschaften, Bremen

Eidesstattliche Erklärung

Hiermit erkläre ich an Eides statt, dass ich die vorliegende Arbeit ohne unzulässige Hilfe Dritter und unter Verwendung keiner als der von mir angegebenen Quellen und Hilfsmittel angefertigt habe. Die aus fremden Quellen wörtlich oder inhaltlich übernommenen Informationen sind als solche kenntlich gemacht.

Bremerhaven, 19.01.2016

Verena Benz

„DO, OR DO NOT, THERE IS NO TRY"

YODA

Abstract

The last transition from a full glacial to a full interglacial state is of special importance to investigate processes that control the Earth's climate evolution. Out of phase interhemispheric climate variability over the last deglaciation has been associated with orbital induced insolation changes as well as with the "bipolar seesaw", hence related to changes in the strength of the Atlantic Meridional Overturning Circulation (AMOC). The Southern Ocean (SO) as only water territory connecting the Pacific, Atlantic and Indian Ocean, plays a crucial role as southern limb of the AMOC in propagating signals within its basins and into the different world oceans. The Antarctic Circumpolar Current (ACC), steered by the strong Southern Westerly Winds (SWW), redistributes heat, salt and nutrients via wind-driven upwelling and thus has the high potential of regulating atmospheric CO_2 concentration via the biological pump as well as surface and deep-water ventilation. Sea surface temperature and sea-ice extent are important surface water parameters related to the oceanic frontal and current systems as well as to water mass formation via brine release and bioproductivity changes.

Despite numerous marine studies from the Pacific sector of the SO, the (sub)antarctic realm is still underrepresented in paleoceanographic research. This thesis examines the environmental changes of the last 30,000 years (30 kyr) in the Pacific sector of the SO using diatom-based transfer function estimates of summer sea surface temperature (SSST) and winter sea-ice (WSI) concentrations reconstructed from 17 selected sediment cores. Including available sea surface temperatures and sea-ice records from the Pacific sector the thesis objectives are primarily a basin and circum-Antarctic wide comprehension of last glacial, deglacial and Holocene climate variability with respect to forcing mechanisms, lead-lag conditions and ice-ocean-atmosphere-ocean feedbacks.

The first manuscript deals with the reconstruction of temperature and sea-ice signals during the Last Glacial Maximum (LGM; 19-23 kyr before present, BP) in the Pacific sector of the SO using new diatom data from a total of 17 cores. Consistent with estimates from previous studies, the Pacific sector shows a distinct basin-wide cooling with a temperature decrease of ≥ 4 K in the present Subantarctic Zone. Most prominent is an E-W gradient concerning the cold-water expansion and the maximum extent of winter sea ice (WSI) that results from strong topographic forcing also steering the frontal system. Hence, the frontal system was characterized by colder SSSTs Atmospheric forcing mechanisms such as the SWW and the El Niño Southern Oscillation (ENSO) are proposed to amplify the E-W

gradient and to have a high regional impact in the Pacific sector. Regarding the average latitudinal expansion of the cold-water realm and the WSI extent in the different SO sectors, a coherent and uniform circum-Antarctic picture of the LGM time slice arises.

The second manuscript carefully examines the deglacial history of the Pacific sector of the SO, based in the same set of sediment cores. A major outcome is a decoupling of the eastern Pacific sector to its western counterpart and the other SO sectors, which has not been shown before. An early deglacial warming around 22 kyr BP observed in the eastern sector is in close agreement with a warming in the adjacent West Antarctic Ice Sheet (WAIS), and is most likely related to the rising Southern Hemisphere insolation. Hence, the synchronous CO_2 rise recorded in East and West Antarctica might have been triggered by the shutdown of the AMOC, rapid sea-ice retreat due to intense warming and strong upwelling due to strengthened SWW. Over the course of the deglaciation, the Pacific records show the common "Antarctic timing" consisting of increasing temperatures until the Antarctic Holocene Optimum (AHO; ~12-9 kyr BP) only interrupted by the Antarctic Cold Reversal (ACR; ~14.5-12.5 kyr BP). A sole contribution of the WAIS to meltwater pulse 1 A (14,400 yr BP) can not be ascertained as less cooling occurred during the ACR than expected by model simulations.

The Holocene climate in the SO is of special importance in deciphering small-scale changes induced by atmospheric forcings, which allos to infer possible present climate changes. The sediment cores, presented in the third manuscript, are relatively high resolved for SO sediments (8-34 cm/kyr) and were retrieved in the western Pacific's Antarctic Zone. The SSST and WSI estimates show a Mid-Holocene cooling which corroborates results from model simulations of freshwater shedding from the rapid WAIS retreat. This sea surface cooling, most likely originating in the Pacific sector is propagated via the "cold water route" into the other SO sectors. The variability of warm and cold periods during the Mid- and Late Holocene reveals a strong dependence to regional influencing factors such as the close vicinity to the sea ice edge as well as to the atmospheric shift of a SWW-to a ENSO-goverend climate state.

In summary, this thesis provides for the first time SSST and winter sea-ice estimates in the Pacific sector of the SO on a wide spatial range and for time slices whose paleoceanographic history is crucial for the understanding of global climate change. The investigated environmental parameters point to the sensitivity of this SO sector, concerning the drainage of the WAIS and the impact of atmospheric changes, that has the high potential of triggering climate change.

Kurzfassung

Der Übergang von vollen Glazial- zu vollen Interglazialbedingungen ist von besonderer Bedeutung für die Untersuchung von Prozessen, welche die Entwicklung des Erdklimas kontrollieren. Die phasenverschobenen Klimaschwankungen der beiden Hemisphären während der letzten Deglaziation werden mit Veränderungen der Sonneneinstrahlung in Verbindung gebracht, die von Orbitalparametern gesteuert werden, sowie mit der "bipolaren Wippe" und darausfolgenden Änderungen in der Stärke der "Atlantischen Meridionalen Umwälz-Zirkulation" (AMOC). Der Südozean (SO), welcher als einziges Wassergebiet den Pazifischen, Atlantischen und Indischen Ozean verbindet, spielt eine entscheidende Rolle als südliche Komponente der AMOC, da er Signale innerhalb seiner Becken, sowie in den verschiedenen Weltozeanen, verbreitet. Der Antarktische Zirkumpolarstrom, der um die Antarktis zirkuliert und durch die starke südliche Westwinddrift (SWW) angetrieben wird, verteilt Wärme, Salz und Nährstoffe durch Tiefenwasserauftrieb um. Hierdurch besitzt er das große Potenzial, durch die "biologische Pumpe" sowie durch Oberflächen- und Tiefenwasserdurchlüftung, den CO_2-Gehalt der Atmosphäre zu regulieren. Meeresoberflächentemperatur und Meereisausdehnung sind wichtige Oberflächenparameter, die sowohl mit den ozeanischen Fronten- und Strömungssystemen assoziiert sind, als auch, durch Salzfreisetzung und Veränderungne der Bioproduktivität, mit Wassermassenbildung.

Trotz zahlreicher Studien aus dem pazifischen Sektor des SO ist der (sub)antarktische Bereich immer noch hinsichlich paläozeanographischer Untersuchungen unterrepräsentiert. Diese Dissertation rekonstruiert Oberflächentemperaturen des Sommers (SSST) und Meereiskonzentrationen des Winters (WSI), mit Hilfe von Diatomeen-basierten Transferfunktionen. Im Vergleich mit verfügbaren Oberflächentemperaturen und Meereisaufzeichnungen des pazifischen Sektors werden Änderungen in den Umweltbedingungn der letzten 30.000 Jahre untersucht. Hauptziele dieser Dissertation sind vor allem das becken- und zirkumantarktischweite Verständnis der Klimavariabilitat des letzten Glazials, Deglazials und des Holozäns, mit Fokus auf Steuerungsmechanismen, vor- bzw. nachlaufender Bedingungen und Eis-Ozean-Atmosphären-Rückkopplungen.

Das erste Manuskript beschäftigt sich, unter Benutzung neuer Diatomeendaten von insgesamt 17 Sedimentkernen, mit der Rekonstruktion von Temperatur- und Meereissignalen während des letzten Glazialen Maximums (LGM; 19.000 – 23.000 Jahre vor heute). Übereinstimmend mit Ergebnissen aus vorhergegangenen Untersuchungen zeigt der

pazifische Sektor eine ausgeprägte beckenweite Abkühlung, mit Temperaturabnahmen von ≥4 K in der Subantarktischen Zone. Besonders markant ist ein Ost-West Gradient hinsichtlich der Kaltwasserausbreitung und der maximalen Meereisausbreitung im Winter, der durch starke topographische Restriktion, welche auch das Frontensystem steuert, hervorgerufen wird. Daraus resultierend war das Frontensystem durch kältere SSST charakterisiert. Es wird angenommen, dass die atmosphärische Beeinflussung, etwa durch die SWW und die El Niño Südoszillation (ENSO), den Ost-West Gradienten verstärkt hat und eine starke regionale Bedeutung im pazifischen Sektor inne hatte. In Bezug auf die durchschnittliche Ausdehnung der Kaltwasserbereichs und der WSI Ausdehnung der einzelnen Südozeanbecken, entsteht ein einheitliches und gleichförmiges zirkumantarktisches Bild der LGM-Zeitscheibe .

Das zweite Manuskript untersucht die deglaziale Geschichte des pazifischen Sektors basierend auf derselben Sedimentkernauswahl. Eines der wichtigsten Ergebnisse ist die deglaziale Entkopplung des östlichen pazifischen Sektors zum westlichen Pendant und der anderen Sektoren des Südozeans, die bisher nicht bekannt war. Ein frühes deglaziales Erwärmen um 22.000 Jahre vor heute, das im östlichen Sektor beobachtet werden kann, steht in enger Beziehung zu der Erwärmung des angrenzenden Westantarktischen Eisschildes (WAIS), und ist höchstwahrscheinlich an die ansteigende Insolation in der Südhemisphäre gekoppelt. Folglich könnte der gleichzeitige CO_2-Anstieg, der sowohl aus der Ost- wie auch Westantarktis bekannt ist, vom Stillstand der AMOC sowie dem raschen Meereisrückgang, aufgrund von intensiver Erwärmung und starkem Tiefenwasserauftrieb, ausgelöst worden sein. Im Verlauf der Deglaziation zeigen die pazifischen Aufzeichnungen einen typischen „Antarktischen Zeitablauf", welcher bis zum Antarktischen Holozänen Optimum (AHO; ~12.000-9.000 Jahre vor heute) aus ansteigenden Temperaturen besteht, die nur durch den Antarktischen Kälteumschwung (ACR; ~14.500-12.500 Jahre vor heute) unterbrochen wurden. Eine alleinige Beteiligung des WAIS zum Schmelzwasserpuls 1A (14.400 Jahre vor heute) kann nicht bestätigt werden, da eine geringere Abkühlung während des ACR stattfand als von Modellierungen erwartet wurde.

Von besonderer Wichtigkeit ist das holozäne Klima des Südozeans, um kleinmaßstäbliche Veränderungen zu entschlüsseln, welche durch atmosphärischen Einfluss gesteuert werden. Damit können mögliche aktuelle Klimaänderungen abgeleitet werden. Die im dritten Manuskript untersuchten Sedimentkerne zeigen eine relativ hohe Auflösung (8-34 cm/1000 Jahre) und stammen aus dem antarktischen Bereich des westlichen Pazifiks. Die SSST und WSI Berechnungen zeigen eine Abkühlung während des mittleren Holozäns, welche Ergebnisse aus Modellierungen eines Frischwassereintrags des rasch zurückweichenden

WAIS bestätigen. Diese Abkühlung des Oberflächenwassers, die sehr wahrscheinlich im pazifischen Sektor ihren Ursprung hat, wird über die Kaltwasserroute in die übrigen Sektoren des Südozeans verbreitet. Die Schwankungen zwischen warmen und kalten Abschnitten während des Mittleren und Späten Holozäns zeigen eine starke Abhängigkeit von regional beeinflussenden Faktoren, wie etwa der Nähe zur Meereisgrenze und zum atmosphärischen Wechsel zwischen SWW und ENSO gesteuertem Klimazustand.

Insgesamt zeigt diese Dissertation zum erstem Mal SSST und WSI Berechnungen im pazifischen Südozean auf weiter räumlicher Ausdehnung und für Zeitscheiben, deren paläozeanographische Vergangenheit essentiell für das Verständnis des globalen Klimawandels ist. Die untersuchten Umweltparameter weisen auf eine Sensitivität dieses Südozeansektors, hinsichtlich der Entwässerung des WAIS und des Einflusses atmosphärischer Änderungen hin, welche auf das hohe Potential des pazifischen Sektors hindeutet, Klimaveränderungen auszulösen.

Acknowledgements

Foremost I want to thank my supervisors Rainer Gersonde and Ralf Tiedemann for the possibility to do my PhD on this highly interesting topic, their support and the chance to be part of a wonderful expedition. Special thanks go particularly to Rainer for his longlasting encourage, many constructive comments and discussions and interminable motivation throughout the last years to finally fullfill this project. Many thanks go further to Frank Lamy for his constant help during my years at the AWI. I am also much obliged to Karin Zonneveld for kindly rewieving my thesis.

This work could not have been done without the ongoing support of Oliver Esper, who shared his diatom and Southern Ocean knowledge whenever possible and needed. Thank you very much for your endurance with my constant worrying and asking. Thanks also to Silke Steph who introduced me to the isotope and foraminifer world. I am particularly thankful to Ute Bockfor her support and happy times in the lab – could have stayed there forever! Marianne Warnkross and Lisa Schönborn are gratefully acknowledged for support and help with the delicate issue of foram picking and isotope analysis.

Special thanks goes to the POLMAR coordinates Claudia Hanfland and Claudia Sprengel for giving me the opportunity to attend various scientific and soft skill courses, including one of the most inspiring sailing trip of my life. POLMAR is such a great platform for intra-AWI exchange of PhD students and further education besides science. The PhD Days 2012 eventually lead me to the Dokteam together with Mirja, Doro, Tobi, Nelly and Steffi. I am very thankful for the year together and the energy I gained from our work.

Very special thanks go to my fellow PhD students and Post Docs for both discussing scientific stuff, complaining about work, life and everything: Edith, Andrea, Sarah, Nadine, Franzi, Thomas, Johannes, Tanja, Henriette, Marie, Inès, Johann, Marc, Hartmut und Lars. I am thankful fo all the senseless debates, chatting, coffee/ beer meetings, destructive and hilarious evenings as well as feeling home when I needed a sleepover.

My deepest gratitude goes to my family for their unquestionable moral support and unfailing faith in me. Fortunately flatrates were invented!

Finally, I am endlessly thankful to Artur. Without your endurance, encouragement and endless humor this thesis would never have been completed. Thanks for always making me smile again

Contents

Chapter 1 – Introduction

1.1 General introduction and motivation

The Earth's climate is strongly influenced by the interaction of ocean and atmosphere via heat, gas and moisture exchange and associated feedbacks. Thus, knowledge of the behavior of the oceans interior processes and their changes on millennial time scales is crucial for the understanding of transitions between warm and cold climate end members. The understanding of feedback processes causing and associated with global climate transitions is crucial regarding the prediction of future changes with respect to the recent anthropogenic influence (IPCC, 2014). During the Late Quaternary the Earth´s climate was characterized by glacial/interglacial cycles that have been associated with insolation changes triggered by variations of the Earth´s orbital parameter and changes in the atmospheric CO_2 content (e.g. Hays et al., 1976; Huybers and Denton, 2008). However, the Northern and Southern Hemispheres show a decoupling of millennial scale climate variability over the last ~30,000 years (Blunier et al., 1998; EPICA Community Members, 2006). The asynchronous climate evolution is characterized by a lead-lag situation of abrupt cold periods in the Northern Hemisphere and corresponding warm events in the Southern Hemisphere known as the "bipolar seesaw" (e.g. Broecker, 1998) that is commonly related to the strength of the Atlantic Meridional Overturning Circulation (AMOC) redistributing heat between the two hemispheres (e.g. McManus et al., 2004). The Southern Ocean represents the lower cell of the AMOC and the only connection of the three largest global oceans, thus acts as important exchange area of water masses (Fig. 1.1; Lumpkin und Speer, 2007; Talley 2013). Hence, it is a key area for the propagation of climate change among all ocean basins.

The last glacial/interglacial climate transition has frequently been investigated in the Southern Hemisphere (e.g. CLlMAP, 1976, 1981; Gersonde et al., 2003a; Kilian and Lamy, 2012; Bostock et al., 2013 and references therein), but only limited information of climate evolution since the last glacial is available from the Pacific, even though this area represents the largest portion of the Southern Ocean. The Pacific sector is majorly important for deep and intermediate water mass formation (e.g. Orsi et al., 1995) and the exchange of water masses with the Atlantic sector via the "cold-water route" in the Drake Passage (Rintoul, 1991). Furthermore, the largely marine-based West Antarctic Ice Sheet (WAIS) that drains particularly into the Pacific sector, is strongly considered to disintegrate rapidly under rising global water temperatures and to contribute up to 3.20 m to the global sea level rise (Bamber, et al. 2009).
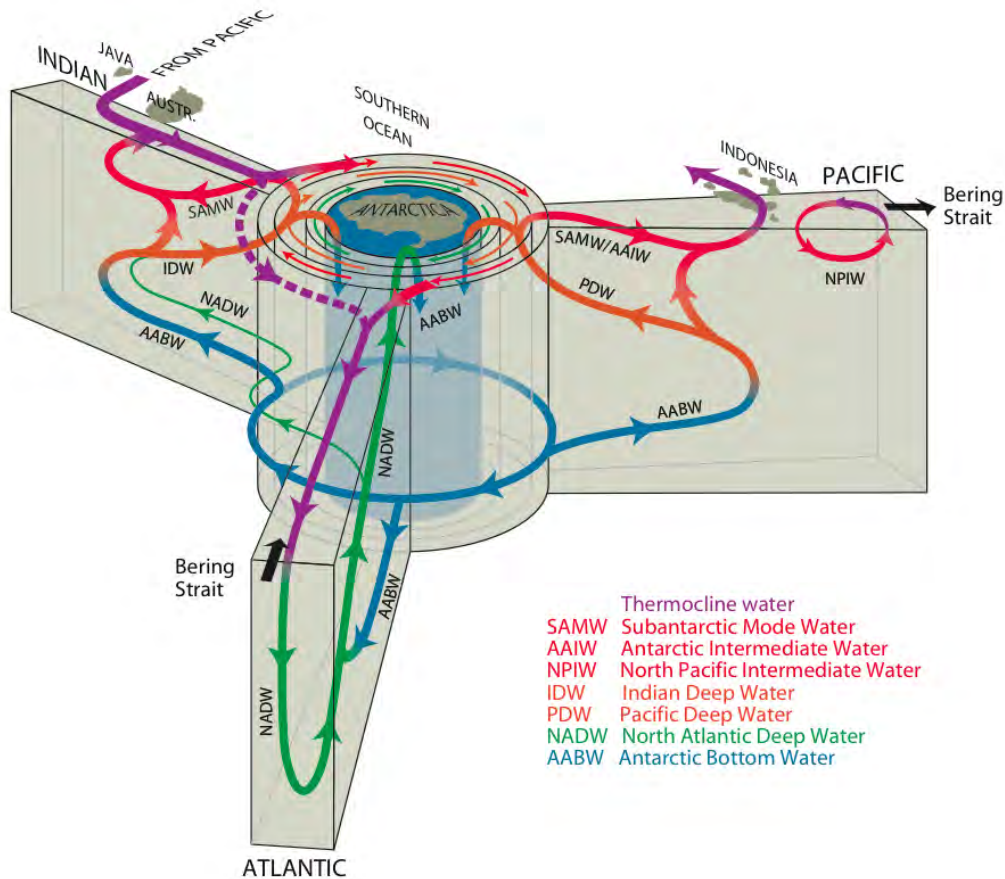
Figure 1.1: Schematic illustration of the modern global ocean meridional overturning circulation from a Southern Ocean perspective (after Talley, 2013).

Sea surface temperature (SST) cooling in the Pacific sector via meltwater intrusion from Antarctic ice shelves (Bintanja et al., 2015), particularly connected to WAIS retreat during the deglacial and the Holocene (Larter et al., 2014), has not been observed yet. Additional atmospheric forcing mechanisms such as the Southern Annular Mode (SAM) and the El Niño Southern Oscillation (ENSO) also exhibit high impacts on southern Pacific SST and sea-ice distribution. The dependency of the recent increase in sea-ice extent of the Ross Sea area on a positive SAM index (Turner et al., 2009; Thompson et al., 2011) might also be assumable for the Last Glacial Maximum (LGM). Furthermore, representing a High Nutrient-Low Chlorophyll (HNLC) area, higher dust-borne iron input during the LGM (Lamy et al., 2014) probably turned the Pacific's seasonal Sea Ice Zone into a carbon sink, lowering the atmospheric CO_2 content (Abelmann et al., 2015). The investigation of impact and response of the above mentioned atmospheric and oceanographic influences in the Pacific sector since the last glacial are of major importance with respect to recent climate change. Thus, it was the essential goal of the **BIPO**lar Climate **MAC**hinery project (ANT-XXVI/2-BIPOMAC), the first R/V Polarstern cruise across the South Pacific, to decipher the role of the Pacific sector

of the Southern Ocean in triggering, amplifying and propagating climate signals related to ocean-ice-atmosphere processes (Gersonde, 2011). In this thesis, diatom-based SSTs and sea-ice concentrations derived from sediment cores recovered during ANT-XVIII/5a and ANT-XXVI/2-BIPOMAC are used to provide insights into the glacial to interglacial development of the Pacific sector. As diatoms are belonging to the photosynthesizing phytoplankton, restricted to the euphotic zone, and represent the major contributor to the primary productivity as well as to the biogenic sedimentation in the opal-belt of the Southern Ocean, they are ideal candidates for the reconstructions of surface parameters through time.

The following subchapters highlight important oceanographic and environmental conditions of the Southern Ocean (*Chapter 1.2.1)* and the Pacific sector in particular (*Chapter 1.2.2*). An overview of relevant paleoceanographic research related to the emphasis of this thesis is provided (*Chapter 1.2.3*) as well as basic information on diatoms and the particular advantage of their application as paleoceanographic proxy (*Chapter 1.3). Chapter 1.4* and *Chapter 1.5* outline the objectives that will be approached by this thesis and specify the authors contribution to the subsequent manuscripts. In *Chapter 2* the studied sediment material and the applied proxies are introduced. Further methods used to gain basic core parameters for age determination are described as well as a short introduction into the applied multiproxy approach for the establishment of age models is given. *Chapters 3*, *4* and *5* represent the manuscripts with the main results of this thesis and are either under review or in preparation for submission. The main objectives of *Chapter 3* is the paleoceanographic reconstruction of the Last Glacial Maximum in the Pacific sector of the Southern Ocean, followed by the study of the Pacific's deglacial history (*Chapter 4*) and by regional observations of the Holocene in the western Pacific sector (*Chapter 5). Chapter 6* provides a conclusion compiling the major outcomes of the previously discussed time slices and future perspectives.

1.2   The Southern Ocean

1.2.1   Modern oceanographic and environmental conditions

Today, the Southern Ocean (latitudes south of ca. 50°S) represents the Earth's largest continuous current system, connecting the Atlantic, Pacific and Indian Oceans. Subsequently it acts as an important exchange area for gas, heat, and nutrient transport between the different water masses and ocean basins (Fig. 1.1; Rintoul et al., 2001).
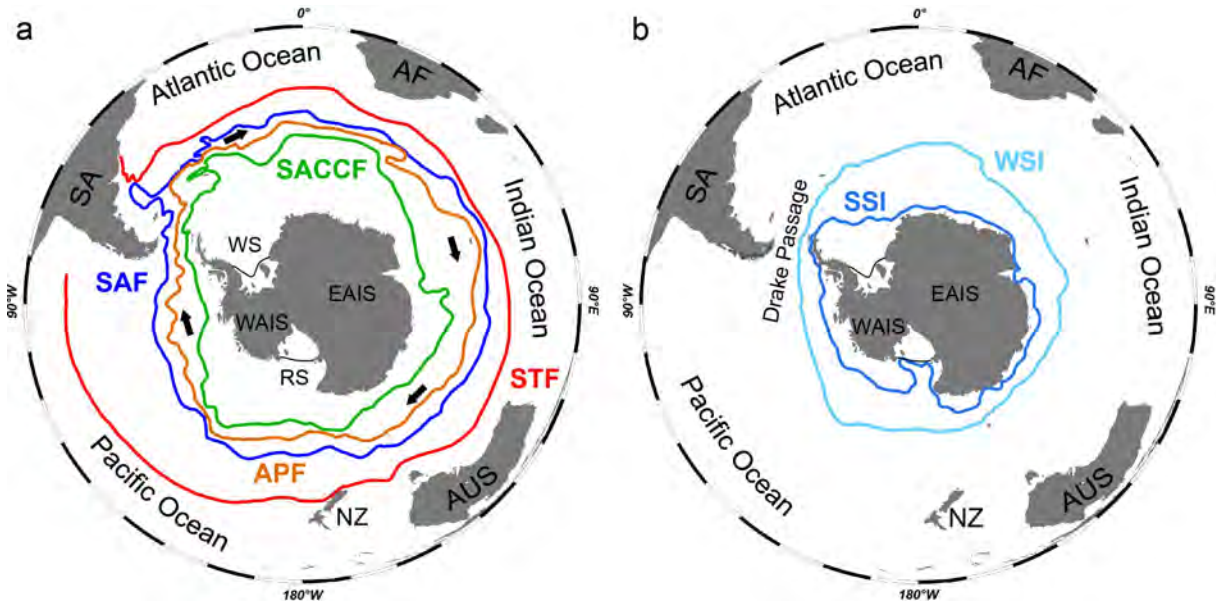
Figure 1.2: Map of the Southern Ocean sectors with **(a)** the northern (SAF) and southern (SACCF) boundary of the Antarctic Circumpolar Current (ACC), arrows indicate the eastward current direction of the ACC; and **(b)** the maximum winter and summer sea-ice (WSI/SSI) extent during September and February, respectively. ACC: Antarctic Circumpolar Current; AF: Africa; AUS: Australia; SA: South America; APF: Antarctic Polar Front; EAIS: East Antarctic Ice Sheet; NZ: New Zealand; RS: Ross Sea; SAF: Subantarctic Front, SACCF: southern ACC Front; STF: Subtropical Front; WAIS: West Antarctic Ice Sheet; WS: Weddell Sea. Oceanic fronts according to Orsi et al., (1995); Sea-ice extent after Reynolds et al. (2002, 2007).

The Southern Ocean circulation is dominated by the Antarctic Circumpolar Current (ACC) that maintains the exchange of heat and water masses within the Atlantic, Pacific and Indian sectors and is mainly driven by strong eastward blowing Southern Westerly Winds (SWW) (Fig. 1.2). The ACC represents the largest ocean current with a mean volume transport of ~130 Sverdrup through the Drake passage (1Sv = $10^6 m^3 s^{-1}$; Whitworth et al., 1982; Olbers et al., 2004) and is defined by deep reaching circum-polar fronts, mainly the Subantarctic Front (SAF), the Antarctic Polar Front (APF) and the Southern ACC Front (SACCF) (Fig.1.2 a; Orsi et al., 1995; Sokolov and Rintoul, 2009). The SAF and SACCF are traditionally specified as northern and southern ACC boundaries. The latter front further resembles roughly the average winter sea-ice expansion in the Southern Ocean (Fig.1.2 a, b; Reynolds et al., 2002, 2007). Additionally to the ACC fronts, the Subtropical Front (STF)

separates the cold and fresh subantarctic water from the warm and salty subtropical water, representing the only discontinuous front (Fig. 1.2 a; Orsi et al., 1995). The different fronts are generally defined by pronounced gradients of temperature, density and salinity, for instance the APF is associated with ~4°C SST (e.g. Orsi et al., 1995; Belkin and Gordon, 1996; Dong et al., 2006). Modern SSTs in the ACC region range between 0 and 8°C during summer and -1.5 and 6°C during winter (Olbers et al., 1992; Locarnini et al., 2010).

The currents within the ACC are of major importance for the recirculation of deep and bottom water masses to the surface maintaining the southern part of the global meridional overturning circulation (Fig. 1.1). The deepest water mass in the Southern Ocean, the Antarctic Bottom Water (AABW), is formed at the shelf regions of predominantly the Weddell and Ross Seas where water is cooled below the freezing point in shelf ice cavities and gets enriched with salt via brine rejection during ice formation. The newly formed cold, high saline, and dense water mass mixes with ambient Circumpolar Deep Water (CDW) and sinks down along the shelf break driving deep convection (Orsi et al., 1999). CDW is the most important water mass within the ACC regarding its volume and results from mixing of North Atlantic Deep Water (NADW) with Indian and Pacific deep waters (e.g. Orsi et al., 1995). Upwelling of nutrient-rich CDW around Antarctica is facilitated by so-called Ekman transport, which is caused by vertical northward water movement to the primarily eastward blowing SWW (Speer et al., 2000; Marshall and Speer, 2012). This upwelled water is transported northward and is eventually downwelled at the APF, forming Antarctic Intermediate Water (AAIW). Similarly, at the SAF downwelling of Subantarctic Mode Water (SAMW) occurs, overlaying the AAIW (McCartney, 1977; Orsi et al., 1995).

A major role in the entire Southern Ocean plays the seasonally largely varying extent of sea ice that impacts sea surface temperature, bioproductivity and export as well as ocean-atmosphere gas exchange (Figs. 1.2b, 1.3; e.g. Thomas and Dieckmann (Eds.), 2010 and references therein). Generally, for the growth of sea ice, SSTs below the freezing point of -1.8°C for seawater are necessary (Petrich and Eicken, 2010). The threshold for the presence of sea ice and, thus the maximum sea-ice edge is defined as 15% sea-ice concentration (Fig. 1.2b; Zwally et al., 2002) whereas the average sea-ice edge, representing consolidated sea ice, is at 40% sea-ice concentration (Gloersen et al., 1992). Based on this definition, sea ice reaches its maximum extent in September during the Southern Hemisphere (SH) winter (July-September), covering an area of ca. 19×10^6 km^2. The extent decreases significantly during February (austral summer) to approximately 3.5×10^6 km^2 (Comiso, 2010). The five-fold difference between summer and winter sea-ice cover has a huge impact on water column

stratification and primary productivity. Besides the earlier described formation of AABW under the shelf ice, the seasonal formation of sea ice contributes to a lesser extent to the bottom water formation via brine release. The rejection of salt during the freezing process forms saline and dense water masses causing vertical convection and preventing stratification (Fig. 1.3; Comiso, 2010). In contrast, during spring and summer, sea-ice retreat results in fresh meltwater lenses that favor upper water column stratification (Fig. 1.3; Comiso, 2010). Additionally, the release of dust-borne iron into the stratified surface water during sea-ice melt fuels prominent diatom blooms (Fig. 1.3; Arrigo and Thomas, 2004). With increasing sea-ice concentration the phytoplankton abundance decreases significantly. Thus, in areas covered by perennial sea ice, primary productivity reaches its minimum due to light and nutrient limitation. Extensive sea-ice cover can further act as an amplifier of global climate: by covering large ocean areas, the exchange between ocean and atmosphere is reduced and CO_2 can be stored in the deep ocean. Additionally, the high surface albedo of sea ice and the sustained snow cover on the sea ice support a cooler atmosphere during winter.
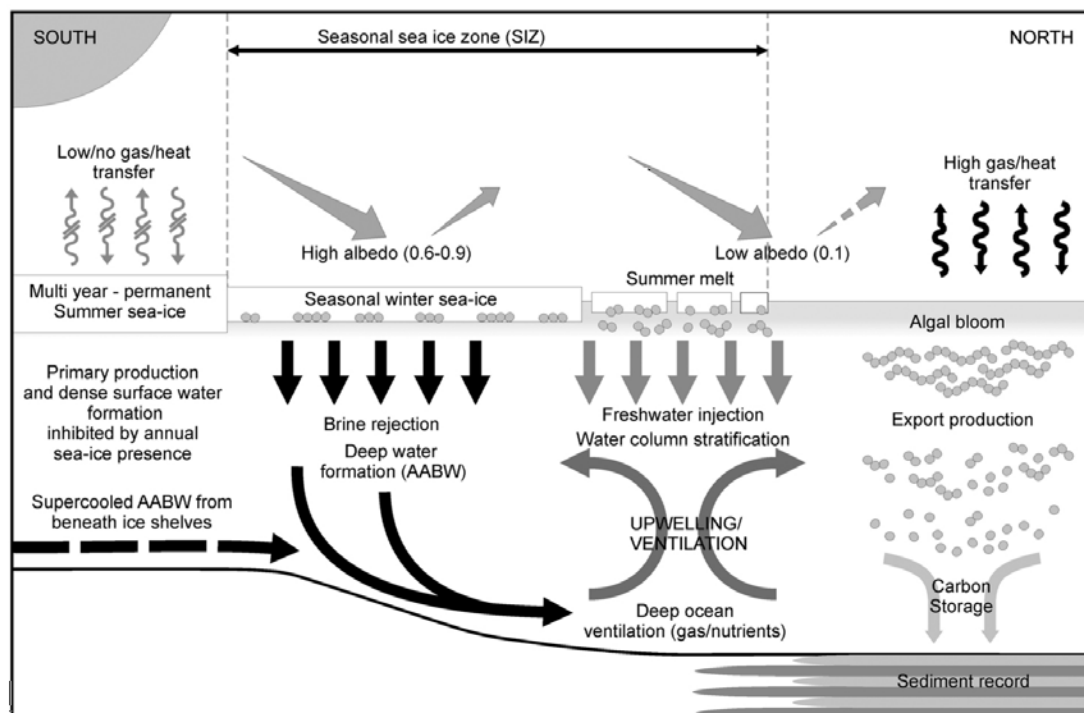
Figure 1.3: Schematic representation of sea-ice influence on oceanography, environment and climate (after Collins et al., 2012).

Although the Southern Ocean surface waters are repleted with nutrients such as nitrate, phosphate and silicate, relatively low productivity is observed, characterizing the Southern Ocean as largest HNLC regime (Arrigo et al., 1998, 2003). The low phytoplankton abundance is explained by the limiting factor of micronutrients, primarily the deficiency of

iron (Martin et al, 1990). Prominent phytoplankton blooms are thus restricted to regions with higher iron supply via windblown dust or fluvial discharge (Sullivan et al., 1993). An important mechanism called the "biological carbon pump" is closely aligned to the HNLC regime (Smetacek et al., 2004). Iron-fertilizing experiments showed that episodic iron supply resulted in extensive phytoplankton blooms dominated by weakly silicified diatoms, whose export to the seafloor sequesters CO_2 in the ocean's interior turning the Southern Ocean into an important carbon sink (Smetacek et al., 2004). In contrast, when iron is limited diatom species with heavily silicified shells prevail, causing higher accumulation of biogenic opal at the seafloor, and driving the silicon pump (Smetacek et al., 2004). The latter mechanism dominates in the modern ACC surface waters leading to the production of approximately one third of the global biogenic silica in the Southern Ocean (Tréguer and De La Rocha, 2013). Biogenic silica burial occurs south of ca. 60°S in the so-called "opal belt" that spans around the entire Antarctic continent between the APF and the SACCF (Fig. 1.4; Lisitzin, 1985; Geibert et al., 2005; Diekmann, 2007). North of the opal-dominated regime the carbonate amount in sediments increases, slowly replacing siliceous phytoplankton as primary sediment contributors. South of the WSI edge, export and preservation of opal is significantly reduced due to less productivity and considerable dissolution in the water column (Esper and Gersonde, 2014a). Here, the sediments contain higher terrigenous input from the Antarctic continent (Fig. 1.4; Lisitzin, 1962; Diekmann, 2007).
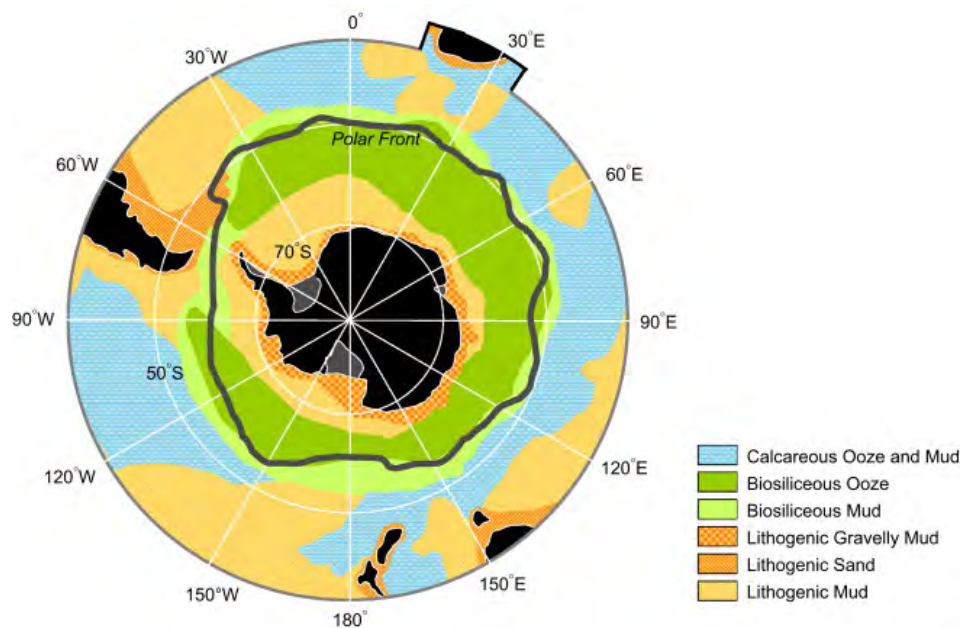
Fig. 1.4: Lithology of modern sediments in the Southern Ocean (after Diekmann, 2007).

1.2.2   The Pacific sector of the Southern Ocean

The basic processes such as modern oceanic circulation, bioproductivity and sea-ice-ocean interactions described in *Chapter 1.2.1* apply to the Pacific sector in the same manner as for the entire Southern Ocean (Fig. 1.5). However, certain conditions described below are unique in this Southern Ocean sector and influence the ACC-dominated circulation, the SST and sea-ice distribution pattern, and teleconnections with lower latitudes.
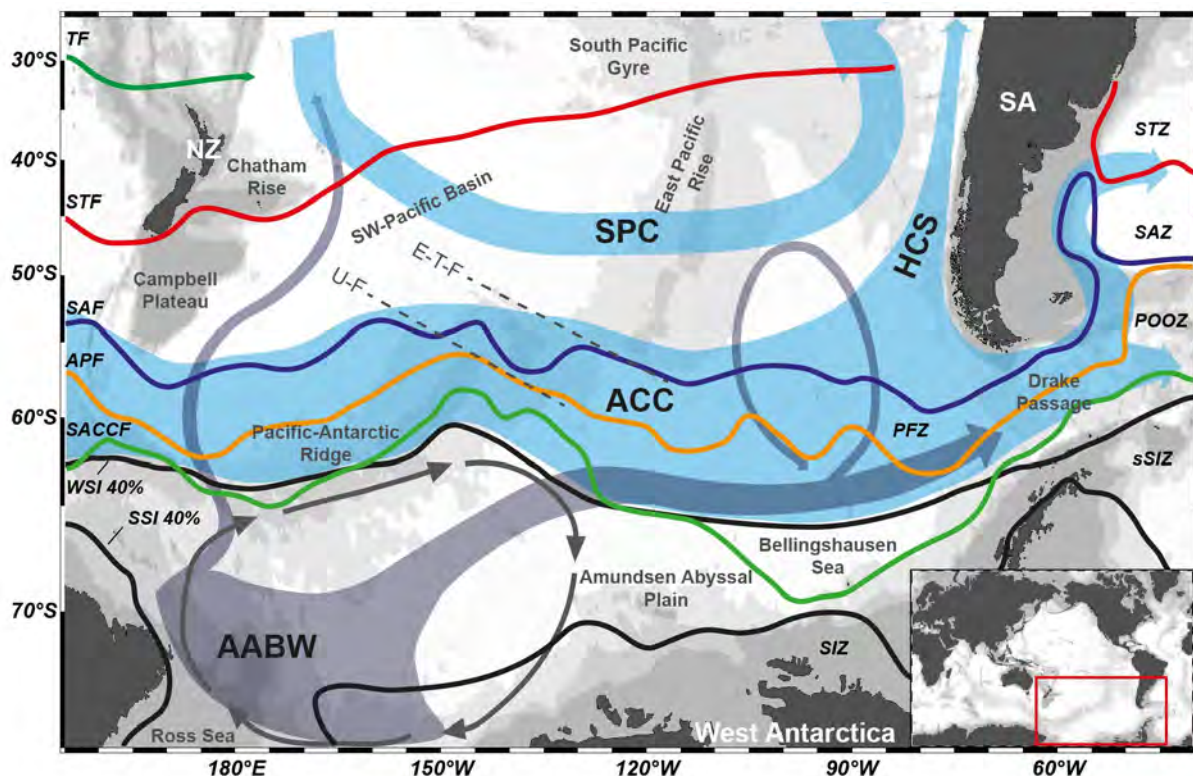
Figure 1.5: Frontal system of the Pacific Southern Ocean with a schematic view of the main currents. ACC: Antarctic Circumpolar Current; HCS: Humboldt Current System; SPC: South Pacific Current; WSI 40%/SSI 40%: modern winter/summer sea-ice edge with 40% sea-ice concentration (Reynolds et al., 2002, 2007); oceanic fronts according to Orsi et al. (1995) and Crundwell et al. (2008); TF: Tasman Front and associated current; STF: Subtropical Front; SAF: Subantarctic Front; APF: Antarctic Polar Front; SACCF: Southern Antarctic Circumpolar Current Front; STZ: Subtropical Zone; SAZ: Subantarctic Zone; PFZ. Polar Front Zone; POOZ: Permanent Open Ocean Zone; SIZ: Sea Ice Zone; sSIZ: seasonal Sea Ice Zone; U-F: Udintsev Fracture Zone System; E-T-F: Eltanin Tharp Fracture Zone System; NZ: New Zealand; SA: South America.

North of 50°S the Pacific Ocean is dominated by the anticyclonic South Pacific Gyre, that transports water from the tropical and subtropical Pacific and along the Tasman Front into subtropical and subantarctic regions via its southern limb the South Pacific Current (Fig. 1.5; Crundwell et al., 2008). In the eastern SAZ northern ACC water is deflected northward along the South American Coast exporting cold surface water via the Humboldt Current System (HCS) into the equatorial Pacific. However, the larger portion of the ACC is constricted eastward to its narrowest extent in the Drake Passage supplying the Atlantic sector by the so-called "cold-water route" with relatively cold and fresh surface water (Fig. 1.5;

Rintoul, 1991). Another important oceanographic feature is the cyclonic Ross Gyre caused by interactions between easterly and westerly winds as well as the Antarctic continental shelf, forming a cyclonic wind-stress field on the oceans surface (Gouretski, 1999). It favors the extent of sea ice and a greater northward expansion of the cold-water realm in the western Pacific sector. The AABW formed at the Ross Sea shelf spreads eastward within the ACC into the Atlantic sector and to a smaller extend into the Southwest Pacific Basin (Fig. 1.5).

The frontal system of the ACC as described in *Chapter 1.2.1* can be further classified into different zones that are from north to south the Subtropical Zone (STZ) and the Subantarctic Zone (SAZ), north of the STF and SAF. The APF is the southern boundary of the Polar Front Zone (PFZ) and the northern limit of the Permanent Open Ocean Zone (POOZ) that extends to the WSI edge (Fig. 1.5). The sea-ice influenced area is divided into the permanently sea-ice covered Sea Ice Zone (SIZ) and the seasonal SIZ (sSIZ). Oceanographic fronts and zones of the ACC are generally strongly influenced by the prominent bottom topography (Sokolov and Rintoul, 2009), represented in the Pacific sector especially by the Pacific-Antarctic Ridge and the East Pacific Rise (Fig. 1.5). The topographic steering of the ACC and the associated fronts leads to a gradient between the eastern and western Pacific sectors, regarding the latitudinal position of the frontal system and the sea-ice edges. In the western sector the three major ACC fronts, SAF, APF and SACCF are closely aligned north of the Pacific-Antarctic Ridge following its extent until the Udintsev and Eltanin-Tharp Fracture Zone systems (Fig. 1.5, Udintsev (Ed.), 2003). These fracture zones act as the only pathways for deep reaching fronts and currents between the Pacific-Antarctic Ridge and the East Pacific Rise. Further to the east, the frontal system passes the Amundsen Abyssal Plain that lacks distinct bottom topography, until reaching the Atlantic sector via the Drake Passage. Resulting from the topographic forcing, the fronts in the western sector remain relatively stable with narrow zones, that get even more contracted while crossing the fracture zones, whereas in the eastern sector the Amundsen Abyssal Plain favors higher seasonal and interannual variability (Sokolov and Rintoul 2009). Similar to the northward expansion of the cold-water realm in the western Pacific sector, the average winter sea-ice (WSI) extent (40% sea-ice concentration; Gloersen et al., 1992), reaching to approximately 60°S, is strongly influenced by the Ross Gyre and is further favored by southerly katabatic winds from the Antarctic Continent (Harangozo, 2004). Furthermore, the average WSI edge mirrors the trend of the Pacific-Antarctic Ridge and of the SACCF, both influenced by topographic forcing. In the eastern sector the WSI edge bends southward to ca. 65°S due to the lack of distinct bottom topography and a less pronounced northward cold-water realm

(Fig. 1.5; Reynolds et al., 2002, 2007). The average summer sea-ice (SSI) edge closely follows the coastline of Antarctica showing its farthest extent to ca. 65°S in the westernmost Pacific and around the Antarctic Peninsula in the Drake Passage (Fig. 1.5; Reynolds et al., 2002, 2007).

The east-west gradient in the Pacific sector is also related to the two main atmospheric climate modes of the Southern Hemisphere, SAM and ENSO (e.g. Lefebvre et al., 2004; Yuan, 2004; Sallée et al., 2008; Turner et al., 2009). A positive (negative) SAM index is related to lower (higher) sea level pressures at high latitudes and higher (lower) sea level pressures at low latitudes. A positive SAM mode is associated with increasing sea-ice extent in the Ross and Amundsen Sea sectors and less sea-ice extent in the Bellingshausen and the Weddell Seas (Lefebvre et al., 2004). Such dipole between the eastern Pacific and western Atlantic sector also forms in response to ENSO events, expressed by warmer temperatures and less sea ice in the Amundsen sector during years with warm El Niño events and colder conditions with more sea ice during cool La Niña events (Yuan, 2004). Additionally, the occurrence of a positive SAM together with La Niña events leads to an amplification of both mechanisms and thus a stronger response of the Antarctic dipole (Stammerjohn et al., 2008).

Of special importance in the Pacific sector is its role as major catchment area of the WAIS drainage. Housing the drainage of the Ross, Amundsen and Bellingshausen Seas that account for the majority of the total WAIS drainage (Ó Cofaigh et al., 2005; Mosola and Anderson, 2006; Smith et al., 2011), makes the Pacific sector an exceptional area to study impacts of meltwater intrusion caused by significant ice sheet retreat. As marine-based ice sheet, the WAIS reacts very sensitive to oceanographic and atmospheric changes (Joughin and Alley, 2011). Disintegration of the WAIS under a warming climate will not only cause global sea level rise (e.g. Bamber et al., 2009) but may also favors SST decrease and sea-ice formation in the adjacent areas due to the release of cold and fresh meltwater (e.g. Bintanja et al., 2015).

1.2.3   Relevant paleoceanographic research related to this thesis

Estimates of SST and sea-ice concentration are ideal parameters to monitor relatively rapid climate changes and their circum-Antarctic propagation. Marine microfossil studies in the Southern Ocean focusing on the estimation of SSTs and sea-ice concentration or duration were mainly conducted on sediment material retrieved from the Atlantic sector or restricted to continental margins (e.g. Pahnke et al., 2003; Bianchi and Gersonde, 2004; Gersonde et al.,

2003a, 2005; Pahnke and Sachs, 2006; Divine et al., 2010; Caniupán et al., 2011; Collins et al., 2012; Ho et al., 2012; Kilian and Lamy, 2012). Remote areas such as the (sub)polar Pacific are yet relatively underrepresented regarding open ocean records that would allow for comprehensive basin-wide reconstructions of last glacial, deglacial and Holocene environmental conditions as well as enabling circum-Antarctic comparison.

Primal estimates of SSTs in the Pacific sector were accomplished by Luz (1977) and Moore (1980), calculating winter SSTs derived from foraminiferal assemblages that were subsequently used for the first global LGM reconstructions (CLIMAP, 1976, 1981). Those reconstructions resulted in widespread, yet unevenly distributed cooling of up to 4 K in the Pacific sector and a latitudinal shift of the winter sea-ice (WSI) edge by approximately 5° northward based on sediment facies changes (CLIMAP, 1981). The CLIMAP reconstructions were later contradicted by diatom-derived summer SST (SSST) and winter sea-ice (WSI) estimates of Gersonde et al. (2005), proposing less cooling and a minor WSI extent in the Pacific sector. However, those results displayed overall low spatial coverage and low chronological control. Additional studies from the Pacific sector focusing on the LGM time slice were derived from lower latitudes, covering predominantly the STZ and the eastern equatorial Pacific (Barrows and Juggins, 2005; Kucera et al., 2005b) and showing prominent LGM cooling of up to 8 K during the LGM off New Zealand and 3K off Peru. Similar glacial values were found in single core studies accomplished at the Campbell Plateau and the Chatham Rise off New Zealand, as well as along the Chilean coast (Kim et al., 2002; Sikes et al., 2002; Pahnke et al., 2003; Pahnke and Sachs, 2006; Romero et al., 2006; Kaiser et al., 2008; Kaiser and Lamy, 2010; Caniupán et al., 2011; Ho et al., 2012). In the latter region, major cooling was suggested to result from the advection of cold subantarctic water, contradicting the low glacial cooling assumed by Gersonde et al. (2005). Thus, the Pacific sector may also have experienced stronger cooling comparable to those in the Atlantic sector (e.g. Gersonde et al., 2003a). However, subantarctic and antarctic SSST and sea-ice reconstructions are comparatively rare, comprising only two cores from the westernmost Pacific sector (~140°W) (Crosta et al., 2004; Ferry et al., 2015a, b) and two cores from the central Pacific (~120°W) (Mashiotta et al., 1999; Tapia et al., 2015), that point to a similar cooling and WSI expansion initially proposed by Gersonde et al. (2005). Besides proxy-based reconstructions, there are numerous coupled climate model simulations aiming at determining the sea-ice expansion during the LGM (e.g. Ballarotta et al., 2013; Goosse, et al, 2013; Zhang et al., 2013). Those model-based sea-ice reconstructions in the Pacific sector show a large variability regarding the maximum extent, and validation of these estimates is pending.

Most of the investigated cores from the Pacific's continental margins represent long-term records comprising besides the LGM also Termination I and the Holocene (e.g. Mashiotta et al., 1999; Pahnke and Sachs, 2006; Ferry et al., 2015b; Kaiser and Lamy, 2010). The general SST trend in the Pacific recorded at these core sites closely follows the "Antarctic timing" known from East Antarctic ice cores (EPICA Community Members, 2004; Jouzel et al., 2007) with the start of deglacial warming after ca. 19,000 years before present (yr BP). However, recent studies from the WAIS showed significant shelf ice retreat before the end of the LGM around 22 kyr BP (1000yr = 1 kyr) (e.g. Klages et al., 2014) and deglacial warming already beginning between 22 and 20 kyr BP (WAIS Divide Project Members, 2013). As retreat and melting of the WAIS can strongly influence the Pacific sector (see *Chapter 1.2.2*) such pattern might also be found in SST and sea-ice reconstruction from the adjacent ocean. However, none of the mentioned studies yet focused on a possible early warming. If a similar early deglacial evolution emerges from records in the Antarctic Pacific, this would imply a decoupling of the deglacial onset from the synchronous CO_2 rise recorded in Antarctic ice cores (Marcott et al., 2014). A similar out of phase relationship between antarctic and subantarctic records might as well occur over the entire deglaciation.

Although the Holocene period is of great importance to study climate variability regarding the recent warming, the recovery of sediment records from the open Pacific Ocean resolving this time slice is rather rare (Crosta et al., 2004; Ferry et al., 2015b). Exceptional sediment cores come from the antarctic shelf regions in the western Ross Sea and off Adélie Land (Cunningham et al., 1999; Denis et al., 2006; Crosta et al., 2008). Of special interest is an Early to Mid-Holocene cooling (10-8 kyr) that might be induced by a freshwater intrusion of the retreating WAIS (Mathiot et al., 2013). According to the feedback mechanisms between ocean and ice sheet, such cooling should be recorded within reach of the ACC. As the available records from lower and higher latitudes show to some extent contrasting results between cold and warm periods, regional factors may play a significant role, e.g. a close vicinity to the WSI edge or to the Antarctic continent as well as the influence of warmer northern water masses.

Overall, it has not yet been revealed whether similar impacts of the SWW, the ENSO and the SAM on sea ice and SSTs in the Pacific's Antarctic Zone occurred during the LGM, the deglacial and the Holocene as observed today (Yuan, 2004; Thompson et al., 2011).

1.3   **Diatoms as paleoclimate archive**

For temperature proxies from sediments with low or absent biogenic carbonate content but distinctly higher biogenic opal burial like the ones underlying the Southern Ocean, diatoms are one of the most promising species. Generally, diatoms are microscopic unicellular algae that occur in all aquatic environments representing a highly divers phytoplankton group with up to 100.000 species (Round et al., 1990). They consist of an extracellular skeleton, the silicified cell wall called frustule. This frustule is separated into two valves (Epivalve and Hypovalve) and the girdle (Cingulum) that eventually can get fossilized in sediments. The variability of structural features and the symmetry of the valves are the basic principles for diatom taxonomy. Diatoms with axial symmetry are called pennate diatoms, further subdivided into two groups with or without a raphe, whereas diatom species with radial symmetry are called centric diatoms. Characteristic patterns and arrangements of processes and perforations (Areolae) on the valvar plane are additional criteria for the identification on species or species group level.

As phototrophic organisms, diatoms are highly dependent on favorable growth conditions regarding sufficient nutrients and a certain amount of light. Thus, most diatom species dwell in the upper 50m of the water column (euphotic zone) and represent environmental conditions such as SST, nutrient, sea-ice concentration and water column stratification. Detailed phytoplankton studies from Southern Ocean surface waters found a close relationship between diatom assemblages and predominantly SST and sea-ice presence (e.g. Kozlova, 1966, Hargraves, 1968; Burckle et al., 1987). Related to these environmental parameters, roughly three species assemblages can be distinguished: the Antarctic, Subantarctic and the warm-temperate water diatom species. The Antarctic species comprise cold-water and sea-ice related species living in SSTs of -1.9 to 1.5°C, whereas the Subantarctic assemblage is dominated by open ocean species with SSTs reaching up to 5°C. Diatom species of the warm-temperate zone are typical for the PFZ and SAZ associated with SSTs over 5°C. The boundaries between the zones are yet transitional to a certain degree (Kozlova, 1966; Burckle et al., 1987). Similarly to surface water assemblages, the diatom distribution pattern in surface sediments of the Southern Ocean exhibits a zonal structure, dominated by cold-water and sea-ice related diatom species in the Southern Antarctic Zone close to the Antarctic continent, temperate species assemblages in the Northern Antarctic Zone around 60°S and warm diatom species in the SAZ (Fig. 1.6; Esper and Gersonde, 2014b and references therein).

Generally diatom growth in the Southern Ocean is exceptionally high during the spring-summer period under iron-replete conditions (see *Chapter 1.2.1*), forming massive blooms and resulting in the predominance of diatoms in the phytoplankton community. But even though diatoms contribute about 50-75% to the global primary productivity (Nelson et al., 1995; Tréguer et al., 1995; Tréguer and De la Rocha, 2013) only ~3% of the net biogenic opal production is exported to the sea floor as major dissolution occurs in the water column and subsequently in the sedimentary sequence (Lisitzin, 1985; Nelson et al., 1995). However, the biogenic opal content of up 72% in Southern Ocean sediments (Fig. 1.3; Lisitzin, 1985; Dieckmann, 2007), allows for the development of environmental reconstructions on the basis of the biogeographical distribution of diatom species. From the 1970s on first attempts were made using the relationship between the distribution patterns of diatom species and oceanographic parameters such as SST and sea ice in the Southern Ocean as models for the past (e.g. Burckle, 1972; DeFelice, 1979; Burckle, 1984a). One of the first numerical methods was the transfer function technique developed by Imbrie and Kipp (1971) transferring SST via factor analysis and regression of factor loadings to a preserved microfossil assemblage at the same location. A further attempt for a different transfer function approach was made by Hutson (1980) with the Modern Analog Technique (MAT) that searches for the best analogs between the assemblages of a surface sediment and a down-core sample. Since then various transfer functions based on diatom assemblages have been successfully used for paleoenvironmental reconstructions of SSTs and sea-ice concentration (e.g. Zielinski et al., 1998; Bianchi and Gersonde, 2004; Crosta et al., 1998a, b, 2004; Gersonde et al., 2005; Esper and Gersonde, 2014a, b; Ferry et al., 2015a, b).

1.4   Aims of the thesis

Using diatom transfer function-derived SSTs and sea-ice concentrations, this thesis provides for the first time reconstructions of the late Quaternary climate variability in the Pacific sector of the Southern Ocean on a wide spatial coverage (*Chapters 3-5*). The new SST and sea-ice estimates are used to cover the gap in paleoceanographic reconstructions concerning temperature and sea-ice patterns from Pacific and circum-Antarctic reconstructions of the LGM (*Chapter 3*). The following transition between the last glacial/interglacial, Termination I, was investigated to decipher a possible Southern Ocean interbasin asynchrony at the onset of the deglaciation, the impact of Pacific warming on the development of the "cold water route" and ocean/atmosphere exchange, as well as feedback mechanisms with the WAIS (*Chapter 4*). For the Holocene period, representing the present interglacial, SSTs and sea-ice concentration of high-resolved cores were analyzed for the detailed investigation of millennial-scale changes in the western Pacific sector. The results were interpreted within the context of a Mid-Holocene cooling associated with rapid WAIS retreat and the shift of a SWW- to ENSO-governed atmospheric circulation (*Chapter 5*).

Combined with previously published temperature and sea-ice records based on various proxy results from the Pacific, Atlantic and Indian sectors of the Southern Ocean this thesis addresses the following questions:

Question 1: ***Do SST and sea-ice distribution in the Pacific sector of the Southern Ocean corroborate the previously suggested minor cooling during the LGM compared to the Atlantic and Indian sector or do they contribute to a uniform circum-Antarctic SST and sea-ice pattern?***
(see *Chapter 3*)

Question 2: ***Are commonly applied coupled climate models able to reproduce proxy-based sea-ice extent during the LGM in the Southern Ocean?***
(see *Chapter 3*)

Question 3: ***How does topographic and atmospheric forcing influence the temperature and sea-ice expansion during the LGM and the deglacial and to what extent does it add to the configuration of the ACC, its frontal system and the cold-water route?***
(see *Chapter 3* and *4*)

Question 4: ***How significant is the impact of Southern Ocean waters on heat and nutrient conditions in the eastern Pacific mid- and low latitudes during the LGM?***

(see *Chapter 3*)

Question 5: ***What is the timing of the deglacial onset in the Subantarctic and Antarctic Pacific regarding SST increase and sea-ice retreat and of the paleoceanographic changes during Termination I?***

(see *Chapter 4*)

Question 6: ***To what extent might the deglacial warming in the Pacific sector have been decoupled from the other Southern Ocean basins and from the synchronous deglacial atmospheric CO_2 rise observed in Antarctic ice cores?***

(see *Chapter 4*)

Question 7: ***How large is the potential of SST and sea-ice reconstruction from the Pacific sector to decipher the contributions of the West Antarctic Ice Sheet to meltwater pulse 1 A and less prominent sea-level changes in the Holocene?***

(see *Chapter 4* and *5*)

Question 8: ***Do Holocene SST and sea-ice estimates support the simulated Early to Mid-Holocene cooling, suggested to be induced by meltwater shedding from the WAIS?***

(see *Chapter 5*)

Question 9: ***Do temperature and sea-ice estimates from high-resolution cores from the western Pacific sector mirror Holocene temperature trends associated with the Hypsithermal and Neoglacial and what are possible drivers of the sequence?***

(see *Chapter 5*)

1.5   Author's contribution

Manuscript 1 (*Chapter 3*)

I performed the sample treatment, diatom slide preparation and counting of the majority of cores (see *Table 2.1*) as well as the transfer function calculation described in this chapter. Oliver Esper provided diatom analyses for cores PS58/270-5, PS58/271-1, PS58/274-1, PS75/054-1 and PS75/072-4. For stable isotope measurements of cores PS75/072-4, PS75/073-2 and PS75/085-1 and AMS^{14}C measurements (*see Chapter 3.3.5, Table 3.3*) I picked major parts of the samples and was responsible for the instruction and evaluation of samples picked by students. I established all presented age models including and refining previously published ^{14}C ages and age models (*see Chapter 3.3.5*). I conducted major parts of the XRF measurements of studied cores that were used for the inter-core correlation.

I wrote the entire draft of the manuscript. Oliver Esper, Rainer Gersonde, Frank Lamy and Ralf Tiedemann contributed to the interpretation of the data and the fine-tuning of the age models. All co-authors reviewed the draft version and contributed to the discussion.

Manuscript 2 and 3 (*Chapter 4, 5*)

I performed the sample treatment, diatom slide preparation and counting as well as the transfer function calculation described in these chapters (see *Table 2.1*) for all cores except PS58/270-5, PS58/271-1, PS58/274-1, PS75/054-1 and PS75/072-4 that were provided by Oliver Esper. I performed the Principal Component Analysis (PCA) presented in *Chapter 4*. The core descriptions used for the facies changes over Termination I were done by myself for cores PS75/064-1, PS75/082-1, PS75/085-1, PS75/091-3, PS75/093-1, PS75/096-4 and PS75/097-4.

 I wrote the entire draft of the manuscripts. All co-authors contributed to the data interpretation and discussion. Oliver Esper and Rainer Gersonde reviewed the draft versions.

Chapter 2 – Material and Methods

2.1   Sediment material

The estimation of sea surface temperatures and sea-ice concentrations focuses on 17 sediment cores retrieved in the Pacific sector of the Southern Ocean, covering the area between 100° and 180°W and south of 50°S (Fig. 2.1; Tab. 2.1). The cores are located in all oceanographic zones with the majority of core sites located between the SAF and the winter sea-ice edge, covering the zone of strongest opal burial in the Southern Ocean. The intervals chosen for investigation focus on the last 30 kyr covering the last glacial to Holocene climate variability. In this time slice, the northernmost cores in the SAZ consist mainly of diatom- and foraminifera-bearing nannofossil ooze. Further to the South in the vicinity of the SAF, the content changes from foraminifera-bearing nannofossil-diatom-ooze to nannofossil-bearing diatom ooze. In the PFZ, between SAF and APF, the predominant facies is diatom ooze (Lisitzin, 1985; Gersonde, 2011).
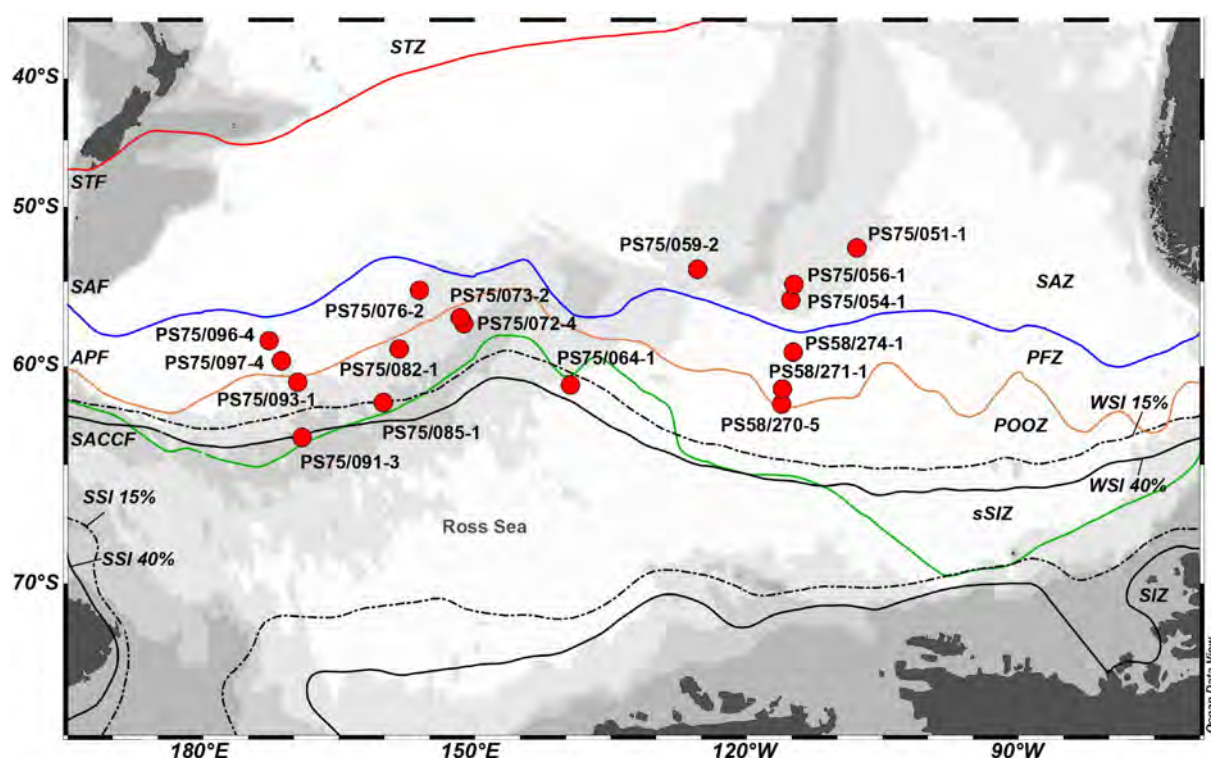
Figure 2.1: Locations of cores analyzed in this study (red circles, see also Tab. 2.1). WSI 15%/SSI 15%: modern winter/summer sea-ice edge with 15% sea-ice concentration, WSI 40%/SSI 40%: modern winter/summer sea-ice edge with 40% sea-ice concentration (Reynolds et al., 2002, 2007); oceanic fronts according to Orsi et al. (1995); STF: Subtropical Front, SAF: Subantarctic Front, APF: Antarctic Polar Front, SACCF: Southern Antarctic Circumpolar Current Front; STZ: Subtropical Zone SAZ: Subantarctic Zone, PFZ: Polar Front Zone, POOZ: Permanent Open Ocean Zone, sSIZ: seasonal Sea Ice Zone, SIZ: Sea Ice Zone.

Tale 2.1. Studied cores in the Pacific sector of the Southern Ocean

Core	Latitude	Longitude	Water depth (m)	Coring device[a]	Oceanographic Zone[b]	Recovery [cm]	Studied section [cm]	Cruise
PS58/270-5	62°01.68'S	116°07.38'W	4981	PC	POOZ	2295	2 – 2282 (OE)[c]	ANT XVIII/5a
PS58/271-1	61°14.58'S	116°02.82'W	5214	PC	PFZ	2442	6 – 2440 (OE)[c]	ANT XVIII/5a
PS58/274-1	59°12.42'S	114°53.28'W	5136	PC	PFZ	2328	TC 3 – 33, 1 – 2315 (OE)[c]	ANT XVIII/5a
PS75/051-1	52°48.73'S	107°48.33'W	3949	PC	SAZ	1873	0–50	ANT XXVI/2
PS75/054-1	56°09.11'S	115°07.98'W	4113	PC	SAZ	2238	TC 2 – 82, 1 – 302 (OE)[c]	ANT XXVI/2
PS75/056-1	55°09.74'S	114°47.31'W	3581	GC	SAZ	1021	3.75–213.75	ANT XXVI/2
PS75/059-2	54°12.90'S	125°25.53'W	3613	PC	SAZ	1398	0.5–90.5	ANT XXVI/2
PS75/064-1	61°00.74'S	139°27.85'W	4600	TC/PC	SSIZ	1543	TC 5–25, 2–306	ANT XXVI/2
PS75/072-4	57°33.51'S	151°13.17'W	3099	GC	POOZ	961	1.5 – 761.5 (OE)[c]	ANT XXVI/2
PS75/073-2	57°12.26'S	151°36.65'W	3234	KC	POOZ	368	2.5–362	ANT XXVI/2
PS75/076-2	55°31.71'S	156°08.39'W	3742	PC	PFZ	2095	1–55	ANT XXVI/2
PS75/082-1	59°02.48'S	158°51.82'W	4000	TC/PC	POOZ	1088	TC 5–85, 5–200	ANT XXVI/2
PS75/085-1	61°56.38'S	160°07.10'W	3734	PC	SSIZ	1974	10–600	ANT XXVI/2
PS75/091-3	63°41.66'S	169°04.47'W	2940	TC/PC	SSIZ	1344	TC 5–25, 1–240	ANT XXVI/2
PS75/093-1	60°52.33'S	169°32.89'W	3762	TC/PC	POOZ	1284	TC 5–90, 5–140	ANT XXVI/2
PS75/096-4	58°32.86'S	172°42.06'W	5057	TC/PC	PFZ	2279	TC 1–65, 1–80	ANT XXVI/2
PS75/097-4	59°42.02'S	171°21.44'W	4672	TC/PC	PFZ	1746	TC 1–65, 1–95	ANT XXVI/2

[a] Coring devices: TC Trigger Corer; PC Piston Corer; GC Gravity Corer; KC Kasten Corer
[b] Oceanographic zones: SAZ Subantarctic Zone; PFZ Polar Front Zone; POOZ Permanent Open Ocean Zone; SSIZ Seasonal Sea Ice Zone
[c] Diatom counting performed by Oliver Esper (OE)

2.2   Methods

2.2.1   Diatom slide preparation and microscopic evaluation

All cores were generally sampled at 5 cm intervals throughout the studied sections. The exception is core PS75/085-1 that was mostly sampled in 10 cm intervals, except for the interval from 505-560 cm sampled in 5 cm steps.

The cleaning of the sediment material and the preparation of permanent mounts for quantitative counting of diatoms for light microscopy was carried out according to the standard method established at the Alfred Wegener Institute Helmholtz Centre for Polar and Marine Research (AWI) (Gersonde and Zielinski, 2000). Freeze-dried subsamples of 0.5 g were boiled in a 400 ml beaker with ca. 15 ml of 35% hydrogen peroxide together with ca. 15 ml concentrated hydrochloric acid to dissolve carbonate and organic matter as well as to enhance the reaction and evaporate the peroxide. Purified water was added up to 400 ml, when the reaction was completed. After a settling time of approximately 24 hours, the water was gently removed using a water jet pump. This washing process was repeated a least 10 times to remove the acid and a portion of the clay fraction. The remaining acid-cleaned

sediment was transferred to 50 ml Nalgene bottles and diluted to exact 50 ml for storage and to guarantee quantitative preparation. For preservation 2 or 3 drops of formaldehyde were added.

For permanent mounts three ethanol-cleaned and grease-free cover glasses (Ø 18 mm) were placed in a petri dish of 48 mm in diameter. Then the petri dish was filled with purified water, containing a specific concentration of gelatine (0.094 g/l) to provide a better adhesion of suspended frustules on the cover glasses during the mounting process. From the homogenized suspension of the cleaned sediment in the Nalgene bottles a certain amount was pipetted from the center of the bottle and distributed evenly in the petri dish. The amount taken from the suspended sediment was determined depending on the concentration of diatoms frustules. After a settling time of two hours, a strip of absorptive paper was added so remove the water from the petri dish. The dry cover glasses where checked for a sufficient and even distribution of diatom frustules. Then two cover glasses were heated to 120°C on a heating plate and two drops of Meltmount ($n_D^{25} = 1.662$) were added. After two hours of evaporation time for the solvent toluene in the Meltmount, these cover glasses were fixed on a microscope slide. The third cover glass acted as backup for potential problems during the mounting process.

The counting of diatom slides was accomplished at a x1000 magnification with a Zeiss Axioplan 2 microscope. To achieve quantitative results for absolute calculation of valves per gram sediment, full traverses across the center of the slide with at least 400 counted specimens were investigated. Counting of diatom valves followed the method of Schrader and Gersonde (1978), and Zielinski (1993) (Fig. 2.1). Valves were counted as one unit for:

A. Centric diatoms with or without pseudonodulus (e.g. *Thalassiosira*, *Actinocyclus*), when more than half of the valve is present;

B. Spores of *Chaetoceros* sp., when one complete or more than half of the valve was present;

C. Centric diatoms with apical elevations (horns) (e.g. *Eucampia*), when more than half of the valve with apical elevation was present;

D. Araphid pennate diatoms (e.g. *Thalassionema*, *Thallasiothrix*), in case of the presence of two apical ends;

E. Pennate diatoms with canal raphe (e.g. *Fragilariopsis*), in cases when more than half of the valve was present, or central parts representing more than half of the valve;

F. Pennate mono- or biraphid diatoms (e g. *Navicula*), when more than half of the valve was present, or the central part with the central nodule;

G. *Rhizosolenia* sp., in case the process was present.
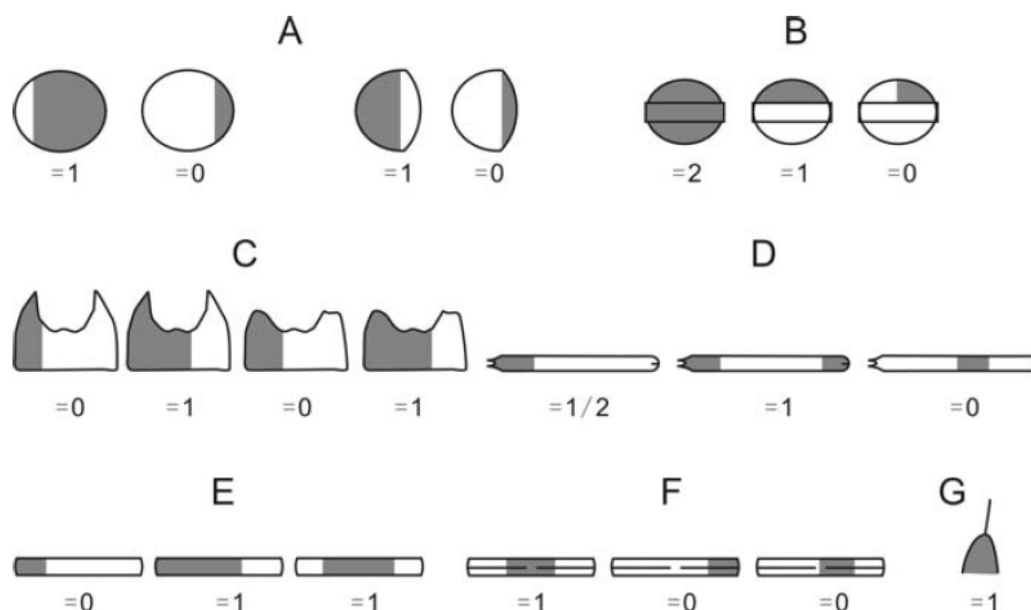
Figure 2.2: Schematic illustration of counting convention (after Zielinski, 1993)

Identification of the diatom species or species groups followed the taxonomy of Hasle and Syvertsen (1996), Zielinski and Gersonde (1997), and Armand and Zielinski (2001). Following Zielinski and Gersonde (1997), and Zielinski et al. (1998) some diatom taxa were combined to groups due to similar ecological behavior and/or gradual transition of different varieties (for details see *Chapter 3.3.3.*)

The preservation level of the diatom samples were noted during the counting process as it provides additional information for the robustness of the relative diatom counts, because selective dissolution may bias the diatom assemblage. Dissolution of preferentially weakly silicified diatom species (e.g. *Fragilariopsis curta*, *Fragilariopsis cylindrus*), that are important for the reconstruction of cold temperatures and sea-ice distribution, can lead to comparably too warm SSSTs and sea-ice concentrations. Three stages of preservation were distinguished following the definition proposed by Zielinski (1993) and Esper et al. (2010):

Good: diatom assemblage consists of an evenly mixture of heavily and weakly silicified species without enlargement of areolae or dissolution of the valve margin.

Moderate: heavy and weakly silicified diatom species are present, with areolae enlargement and valve margin dissolution as well as fragmentation of the weakly silicified species.

Poor: predominantly heavy silicified species are present, with strong dissolution of valve margins and areolae enlargement, distinct valve fragmentation due to dissolution.

2.2.2   Summer Sea Surface Temperature (SSST) reconstruction

The reconstruction of sea surface temperature (SST) via transfer function (TF) has been widely applied using different microfossil groups (e.g. Barrows and Juggins, 2005; Gersonde et al., 2005, de Vernal et al., 2005, Cortese et al., 2007). In general, TFs are based on the assumption that environmental conditions in the surface water, such as SST, salinity or productivity, are recorded in phyto- and zooplankton assemblages preserved in the sediment record. The modern relationship between the environmental variables and the composition of those assemblages provides a reference data set that can be applied to down-core assemblages resulting in the estimation of physical variables for past surface water conditions (e.g. Birks, 2003; Kucera et al., 2005b).

Due to the close correlation of SSSTs with diatom assemblages in the water column (as described in *Chapter 1.3)* as well as with the diatom distribution patters in the sediment (e.g. Zielinski and Gersonde, 1997; Armand et al., 2005, Crosta et al., 2005, Romero et al., 2005; Esper et al., 2010, Esper and Gersonde 2014b), the estimation of paleo-SST via a TF approach is most valuable for Southern Ocean sediments. However, there are limitations that need to be considered when interpreting the reconstructed temperature signal. One limitation is the bias of the diatom assemblage by selective dissolution of weakly silicified species that are predominantly indicators for cold temperatures. Consequently, samples from glacials influenced by sea ice and resulting enhanced dissolution of diatom species, display a dominance of robust species and thus reconstructions may be biased to warmer SSSTs than presumably present during cold time periods. Another limitation is the no-analog situation caused by exceeding abundance of single diatom taxa (e.g. *Eucampia antarctica* during glacials) in down-core samples compared to reference samples (Zielinski et al. 1998; Esper and Gersonde, 2014 a, b).

Different TF methods are available for the reconstruction of SSST. They include the Imbrie and Kipp Method (IKM, Imbrie and Kipp, 1971), the Modern Analog Technique (MAT, Hutson, 1980), the Weighted Average (WA; Birks et al., 1990) and the Weighted Averaging Partial Least Squares (WAPLS; ter Braak and Juggins, 1993). These methods were successfully applied for diatom-based reconstructions (e.g. Crosta et al., 1998b; 2004; Zielinski et al., 1998; Birks and Koç, 2002; Gersonde et al., 2005). The recently new

designed temperature TF for the Southern Ocean by Esper and Gersonde (2014b) improves the calculation of SSSTs due to its wide spatial coverage embedding two third of the Southern Ocean (Fig. 2.3). Esper and Gersonde (2014b) tested the above-mentioned TF methods to establish the most applicable method for the reconstruction of SSST and WSI paleoestimations in the Pacific and Atlantic sectors of the Southern Ocean. The accomplished reference dataset for all four methods included 336 reference samples from the Atlantic, Pacific and Indian sector of the Southern Ocean, with corresponding modern SSSTs derived from the Hydrographic Atlas of the Southern Ocean (HASO; Olbers et al., 1992). The HASO contains in situ SSST measurements (January-March) from <1900-1990, probably least influenced by the recent warming compared to other oceanographic databases like the World Ocean Atlas 2009 (Locarnini et al., 2010). Moreover, as previous diatom-based temperature reconstructions from the Atlantic sector used the HASO as reference temperature, the compatibility between those studies and the new reconstructions can be improved.

The accuracy of the TFs is displayed by the root mean square error of prediction (RMSEP) and the determination coefficient (R^2), where lower RMSEP and higher R^2 exhibit better accuracy. Moreover, the IKM method provides an additional quality criterion with the communality that displays the direct compatibility of a sample to the reference dataset. Lowest RMSEP of 0.782 °C was achieved by WAPLS, followed by the MAT TF with a RMSEP of 0.812°C and the WA method with lowest RMSEP of 0.974°C (Esper and Gersonde, 2014b). The IKM TF performed best with 29 diatom taxa and three factors resulting in a RMSEP of 0.833°C (Fig. 2.3). Furthermore, two subsets for the Pacific (107 samples) and Atlantic (151 samples) Southern Ocean calculated with IKM reached comparably good RMSEP with 0.68°C and 0.71°C, respectively (Esper and Gersonde, 2014b). Despite the generally better calibration of the IKM subsets, the supraregional TF IKM-D336/29/3q led to the best down-core performances due to the larger data set resulting in higher communalities and less to no no-analog conditions. The MAT method overall showed lower signal variability especially during glacial periods, thus express the least appropriate method to reconstruct SSST (Esper and Gersonde, 2014). Although the methods IKM, WA and WAPLS are similarly successful, the IKM TF is preferred in this study to ensure a better comparability to previous diatom-based SSST reconstructions in other Southern Ocean sectors (e.g. Gersonde et al., 2005). Hereby, the circum-Antarctic comparison of temperature evolution within several studies achieves a better quality.
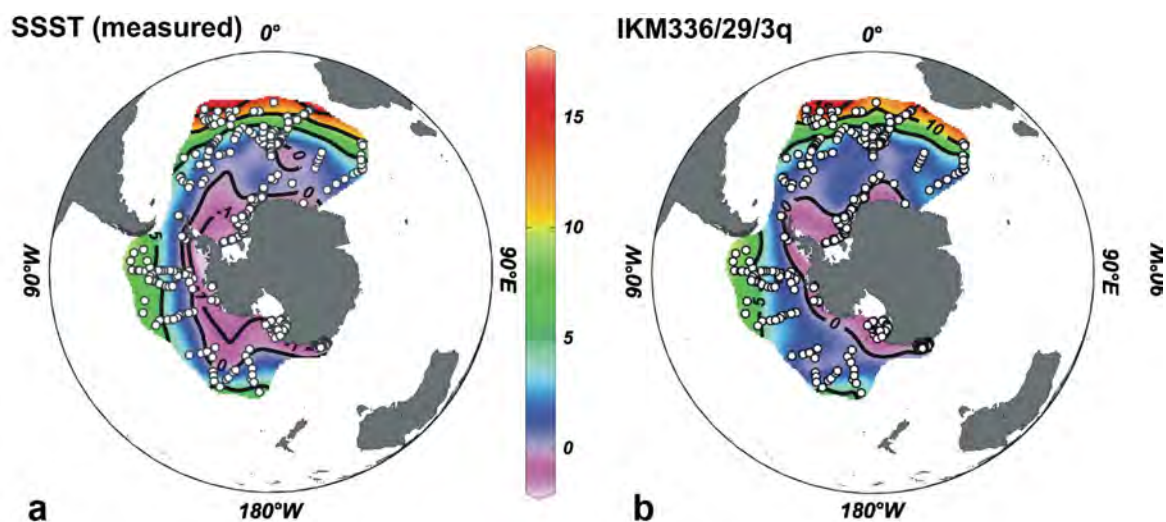
Figure 2.3: Comparison between measured summer sea surface temperature (SSST; from Olbers et al., 1992) and transfer function SSST estimates from the applied Imbrie and Kipp Method (IKM-D336-29-3q; after Esper and Gersonde, 2014b).

The TF IKM-D336/29/3q was applied to all cores in this study using logarithm-transformed diatom relative abundances to down-weight the dominance of single taxa like *Fragilariopsis kerguelensis*. The following equation was used:

$$L = LG \ (relative \ abundance \ x \ 1000+1) \hspace{2cm} (1)$$

The calculations were achieved with the software packages PaleoToolBox and WinTransfer (http://www.pangaea.de/Software/PaleoToolBox) (Sieger et al., 1999).

2.2.3 Sea-ice reconstruction

For the estimation of the sea-ice extent in the Southern Ocean, the most common reconstruction method is based on the relative abundance of cold water and sea-ice indicating diatom species like *F. curta* and *F. cylindrus* for winter sea ice (WSI) and *F. obliquecostata* for and summer sea ice (SSI), respectively (Gersonde and Zielinski, 2000). Additionally to the strong relation of specific diatom species to winter sea-ice concentration (Fig. 2.4), distinct drops in the sedimentation rates and the biogenic opal accumulation are indicators for the presence of extensive sea-ice cover (Gersonde and Zielinski, 2000; Esper and Gersonde, 2014a). Crosta et al. (1998a, b) reconstructed antarctic sea-ice extent via the annual length of sea-ice cover expressed as the number of month applying MAT to diatom assemblages. However, as the diatom sea-ice signal rather shows the presence/absence of sea ice than duration of sea-ice cover at a specific core site (Gersonde and Zielinski, 2000) such

reconstructions have to be treated with caution. As for temperature reconstructions, the sea-ice estimation is as well hampered by the dissolution of less silicified diatom taxa. Thus, especially the glacial sea-ice extent may be underestimated in regions where extensive sea-ice cover precluded diatom productivity, less opal burial and additionally enhanced dissolution
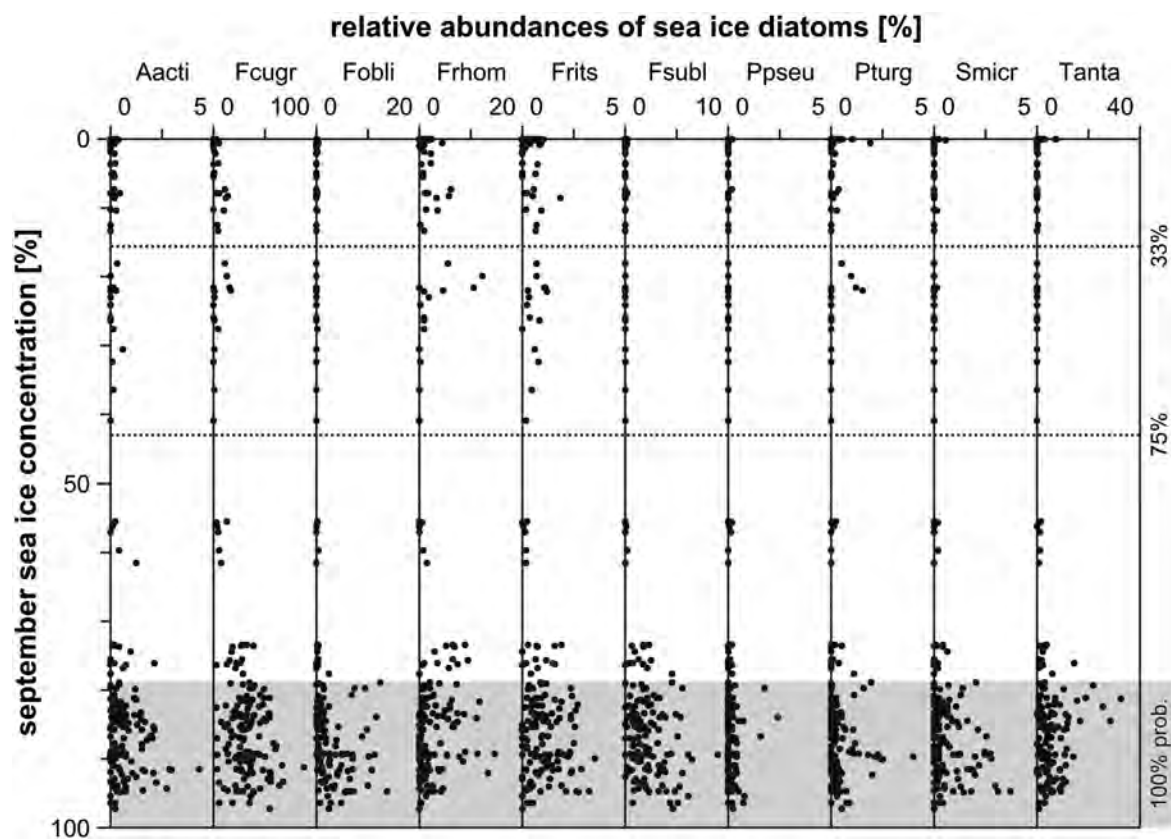
Figure 2.4: Relative abundance of selected diatom taxa/taxa groups in relation to winter sea-ice (September) concentration and probability (WSI; after Reynolds et al., 2002, 2007); Aacti: *Actinocyclus actinochilus*, Fcugr: *Fragliariopsis curta* group, Fobli: *F. obliquecostata*, Frhom: *F. rhombica*, Frits: *F. ritscheri*, Fsubl: *F. sublinearis*, Ppseu: *Porosira pseudodenticulata*, Pturg: *Pseudonitzschia turgiduloides*, Smicr: *Stellarima microtrias*, Tanta: *Thalassiosira antarctica* (after Esper and Gersonde, 2014b).

The new reference data set for diatom-based TF recently established by Esper and Gersonde (2014a) for the estimation of sea-ice concentration and probability in the Southern Ocean greatly enhances the ability to reconstruct antarctic sea ice. The environmental reference dataset is represented by high-resolution satellite data and in situ measurements from the NOAA Optimum Interpolation Sea Surface Temperature V2 collected between 1981 and 2010 (Reynolds, et al., 2002, 2007). For the maximum summer (February) and winter (September) extent, the monthly mean sea-ice concentration and probability was averaged over the entire available time span of >30 yr (Esper and Gersonde, 2014a). Out of the four

tested TF methods (IKM, MAT, WAPLS and WA) the TF estimates using MAT with a 274-sample/28 taxa reference set with 4 analogs (MAT-D274/28/4an) resulted in the lowest RMSEP of 5.52% for WSI and 8.93% for SSI concentration (Fig. 2.5). The 28 diatom species used for the sea-ice estimations are described in *Chapter 3.3.3*, *Table 3.2*. The WA and WAPLS method as well as the IKM technique, applied on a subset with 172 samples, performed less well with a RMSEP ranging from 7-11% for WSI concentration. The down-core application of the IKM and MAT techniques display lower signal variability for IKM for both seasons, especially pronounced during glacials (Esper and Gersonde, 2014a). An advantage of MAT is the use of a larger data set covering broader environmental condition. Furthermore, the unimodal distribution of sea ice in contrast to the linear behavior of temperature is better reflected by the search for best analogs rather than a palaeoenvironmental equation as it is produced by IKM.

The new designed TF MAT-D274/28/4an was applied to logarithm-transformed diatom counting (see *Chapter 2.2.2*, *equation 1*) of each individual core in this study using the software R (R Core team, 2012) with the additional packages Vegan (Oksanen et al., 2012) and Analogue (Simpson and Oksanen, 2012).
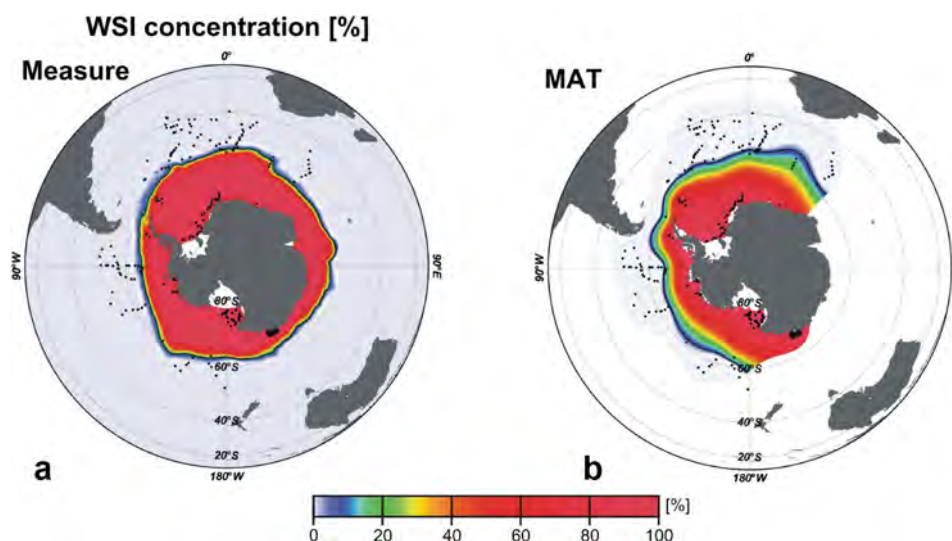
Figure 2.5: Comparison between measured mean winter sea-ice (WSI) concentration (from Reynolds et al., 2002, 2007) and transfer function WSI estimates from the applied Modern Analog Technique (MAT-D274-28-4an; after Esper and Gersonde, 2014a).

2.2.4   Oxygen isotope (δ^{18}O) measurements

Specimens of the planktic foraminifera *Neogloboquadrina pachyderma* sinistral were picked from the 125-250 μm fraction of freeze-dried and sieved sediment samples taken from cores PS75/072-4, PS75/73-2 and PS75/085-1. In general, approximately 100 μg (ca. 20-40 specimens) of foraminiferal carbonate was retrieved to achieve reliable results. Isotope

measurements were performed at the AWI (Bremerhaven) using a Thermo Finnigan MAT 253 directly coupled to an automated carbonate preparation device (Kiel 4) and calibrated via NIST-19 to the PDB scale. The precision of oxygen isotope measurements based on long term analyses of an internal standard (Solnhofen limestone) was better than 0.08‰. All values are reported in δ-notation vs. VPDB.

2.2.5   X-ray fluorescence (XRF) core logging

All cores were measured at a 1 cm resolution using an AVAATECH profiling X-ray Fluorescence (XRF) core scanner at the AWI (Bremerhaven) to determine the relative elemental composition of the sediment (counts per second). For this non-destructive measurement archive halves of split core segments were covered with a 4 μm thin SPEXSamplePrep Ultralene foil against contamination. In total, three measurement runs with different voltages (10kV, 30kV, 50kV) were performed at 1 mA and different counting times of 10, 15 and 30 seconds, respectively. The resulting data were corrected for section boundaries and core gaps to receive a continuously depth scaled record of each core. Presented elements in this study include iron (F), calcium (Ca), and the silicon /titanium ratio (Si/Ti) from the 10 kV measurements. These elements were used to establish precise age models for the presented cores via inter-core correlation and/or tuning to ice core records (see *Chapter 2.3)*. As such the different elements serve for the detection of glacial (Fe) and interglacial (Ca) periods as well as information on relative changes of biogenic opal (Si/Ti) related to cold and warm climates.

2.2.6   Magnetic susceptibility

To generate first rough age models immediately after core retrieval, measurements of physical properties using a GEOTEK Multi-Sensor Core Logger (MSCL) were established onboard R/V *Polarstern*. Due to the relatively high water content in diatom rich sediment cores, the XRF results from some cores were less useful for the detection of glacial/interglacial intervals. To provide a sufficient correlation of such cores the MSCL measurements were used. With this method the logging of unsplit core sections results in the magnetic susceptibility of the sediment cores. The magnetic susceptibility was measured using a Bartington M.S.2 susceptibility meter with a loop sensor. The specific magnetic susceptibility of the sediment modifies the sensors oscillator frequency via passing the loop sensor. Afterwards the variations are converted into magnetic susceptibility values (SI). The

core sections were measured at 1 cm steps with a count time of 10 seconds per step. The software Geotek MSCL 6.2 and Geotek Utilities 6.1 were used for measurements and dataprocessing (Gersonde, 2011). Furthermore, the physical properties were corrected for section boundaries.

2.2.7   Radiocarbon measurements

Radiocarbon measurements on foraminifera were used for the establishment of age models with highest possible accuracy. Therefore, 61 samples from selected core depths (*Chapter 3.3.5, Table 3.3*) were chosen for accelerated mass spectrometry ^{14}C age (AMS ^{14}C age) measurements. For this purpose monospecific samples of the two planktic foraminifera species *Globigerina bulloides* and *Neogloboquadrina pachyderma* sinistral where picked from the 125-250 μm fraction in six cores. Approximately 1000-1500 specimens were selected for conventional radiocarbon measurements at the National Ocean Science AMS facility (NOSAMS, 2.5 AMS) of the Woods Hole Oceanographic Institute (WHOI), USA. Additionally, samples from two cores (PS75/072-4, PS75/073-2) were measured at the Laboratory for Ion Beam Physics at the Eidgenössische Technische Hochschule (ETH) in Zürich, Switzerland, with the Mini radioCarbon Dating System (MICADAS, 0.2 MV AMS). As sediments from polar regions often lack sufficient amounts of carbonate, the MICADAS is of special interest as samples with >1000 μg $CaCO_3$ can be performed with comparatively precise results as conventional AMS ^{14}C measurements.

Raw ^{14}C ages were finally converted into calibrated calendar ages using the MARINE13 calibration curve (Reimer et al., 2013) with the software Calib 7.0 (Stuiver and Reimer, 1993, Stuiver et al., 2005). For detailed information on the selected sample depths and the used reservoir age correction please refer to *Chapter 3.3.5*.

2.3   Age constraints

Within the frame of this thesis the chronologies for all studied cores described in Table 1 were generated including slight modifications of the previously published age models of cores PS75/056-1, PS75/059-2, PS75/076-2 and PS75/093-1 (Lamy et al., 2014) and PS58/271-1 (Jacot des Combes et al., 2008). The age models are based on a multiproxy approach, combining AMS^{14}C measurements together and oxygen isotope stratigraphy together with inter-core correlation as well as correlation to antarctic ice cores via XRF

element counts/ratios as well as diatom abundance stratigraphy (*Chapter 3.3.5*). The resulting age determination assigned to Marine Isotope Stages according to Lisiecki and Raymo (2005) is pictured in Figure 2.6.

The establishment of age models in the Southern Ocean is rather challenging, as most sediment cores from the Antarctic Zone south of ca. 55°S contain only low or even absent biogenic carbonate content. Hence, age models based entirely on oxygen isotope ($\delta^{18}O$) stratigraphy and/or AMS^{14}C measurements of foraminiferal carbonate are hardly possible to generate. The alternative of dating the humic acid fraction in bulk sediment samples bears as well problems concerning the alteration of the samples and resulting errors of the retrieved age. Furthermore, in the Pacific sector of the Southern Ocean a problem arises from the poor knowledge of paleo-^{14}C reservoir ages for the open ocean. Most studies of reservoir ages in this part of the Southern Ocean derive from the surrounding continent margins (e.g. Sikes et al., 2000; Siani et al., 2013) and are subject to different oceanographic processes than the open ocean. However, it seems evident that during the deglacial and probably also the glacial upwelling of ^{14}C-depleted water masses led to significantly higher surface water reservoir ages than during the Holocene (Burke and Robinson, 2012; Siani et al., 2013; Skinner et al., 2010; 2015). As such, constant reservoir ages in the studied time slice of 30 kyr seem rather unlikely and higher reservoir ages have to be considered for the last (de)glacial. Holocene reservoir ages were applied according to Bard (1988).

Besides radiocarbon datings and $\delta^{18}O$-measurements, the XRF elemental analysis serves as alternative to establish consistent age models. Assuming a direct dependency between the increased deposit of iron-rich dust during glacial periods in the ocean basins and antarctic ice cores (e.g. Lamy et al., 2014) the Fe counts of each XRF core analysis can be correlated to the Fe and dust records from the EPICA Dome C ice core (EDC, Lambert et al., 2008; Martínez-Garcia et al., 2009). Similarly, the Ca counts as well as the Si/Ti ratio mirrors warmer periods with enhanced opal and carbonate burial, thus can be correlated together with the TF-derived SSST to the EDC temperature change (Jouzel et al., 2007) and the WAIS Divide ice core $\delta^{18}O$ record (WDC, WAIS Divide Project members, 2013).

To achieve highest possible accuracy for age models of all studied cores, the establishment of radiocarbon- and/or $\delta^{18}O$-dated records was primarily carried out. For further information on the selected sample depths for radiocarbon dating, reservoir ages and calibrated calendar ages please refer to *Chapter 3.3.5* (*Table 3.3*).

Subsequently, core sections with insufficient carbonate content and beyond the limits of radiocarbon dating were tuned to the EDC ice core. After such establishment of several reference cores the age models of the remaining cores without any carbonate based dating method, were generated via inter-core-correlation. Again the mentioned XRF counts and ratios (Fe, Ca, Si/Ti) were used together with the relative abundances of the diatom species *F. kerguelensis*, *E. antarctica* and *Chaetoceros* spp. to correlate cores from similar environmental areas and/or with a similar time resolution. Detailed information of correlation pointers used and the used parameter are described in the *Supplementary Information* of *Chapter 3 (Table S3.1)*.
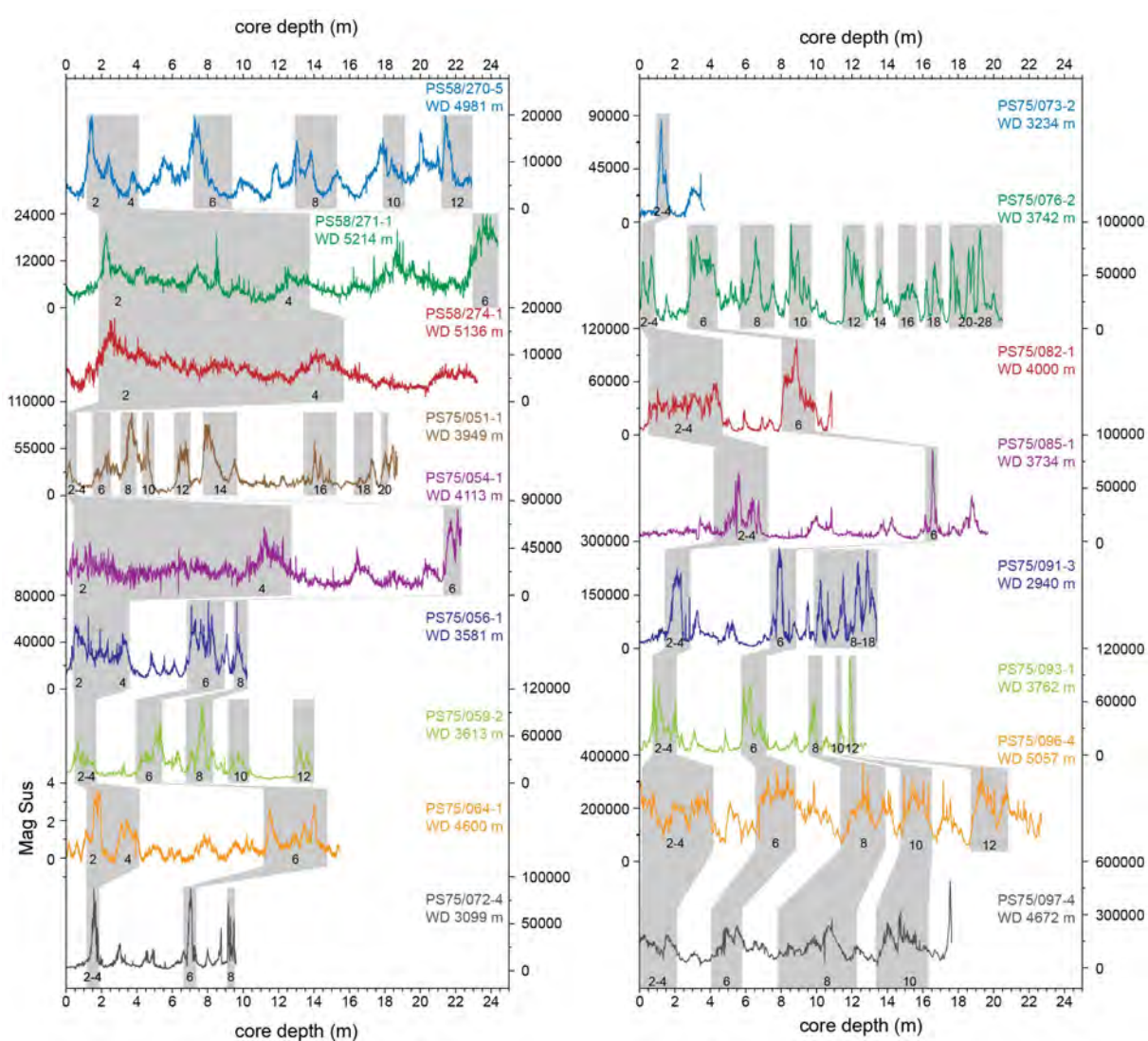
Figure 2.6: Classification of sediment intervals in different Marine Isotope Stages (MIS) according to Lisiecki and Raymo (2005). The y-axes displays the XRF iron counts (per second), except for PS75/064-1, where the magnetic susceptibility (SI) is pictured.

Chapter 3 – Last Glacial Maximum sea surface temperature and sea-ice extent in the Pacific sector of the Southern Ocean

Verena Benz*[a,b], Oliver Esper [a,b], Rainer Gersonde [a,b], Frank Lamy [a,b], Ralf Tiedemann [a,b]

[a]Alfred-Wegener-Institut Helmholtz-Zentrum für Polar- und Meeresforschung, Am Alten Hafen 26, 27568 Bremerhaven, Germany
[b]MARUM - Zentrum für Marine Umweltwissenschaften der Universität Bremen, Leobener Str. 28359 Bremen, Germany

Abstract

Sea surface temperatures and sea-ice extent are the most critical variables to evaluate the Southern Ocean paleoceanographic evolution in relation to the development of the global carbon cycle, atmospheric CO_2 variability and ocean-atmosphere circulation. In contrast to the Atlantic and the Indian sectors, the Pacific sector of the Southern Ocean has been insufficiently investigated so far. To cover this gap of information we present diatom-based estimates of summer sea surface temperature (SSST) and winter sea-ice concentration (WSI) from 17 sites in the polar South Pacific to study the Last Glacial Maximum (LGM) at the EPILOG time slice (19,000 – 23,000 cal. years BP). Applied statistical methods are the Imbrie and Kipp Method (IKM) and the Modern Analog Technique (MAT) to estimate temperature and sea-ice concentration, respectively. Our data display a distinct LGM east-west differentiation in SSST and WSI with steeper latitudinal temperature gradients and a winter sea-ice edge located consistently north of the Pacific-Antarctic Ridge in the Ross sea sector. In the eastern sector of our study area, which is governed by the Amundsen Abyssal Plain, the estimates yield weaker latitudinal SSST gradients together with a variable extended winter sea-ice field. In this sector, sea-ice extent may have reached sporadically the area of the present Subantarctic Front at its maximum LGM expansion. This pattern points to topographic forcing as major controller of the frontal system location and sea-ice extent in the western Pacific sector whereas atmospheric conditions like the Southern Annular Mode and the ENSO affected the oceanographic conditions in the eastern Pacific sector. Although it is difficult to depict the location and the physical nature of frontal systems separating the

glacial Southern Ocean water masses into different zones, we found a distinct temperature gradient in latitudes straddled by the modern Southern Subtropical Front. Considering that the glacial temperatures north of this zone are similar to the modern, we suggest that this represents the Glacial Southern Subtropical Front (GSSTF), which delimits the zone of strongest glacial SSST cooling (>4 K) to its North. The southern boundary of the zone of maximum cooling is close to the glacial 4°C isotherm. This isotherm, which is in the range of SSST at the modern Antarctic Polar Front (APF), represents a circum-Antarctic feature and marks the northern edge of the glacial Antarctic Circumpolar Current (ACC). We also assume that a glacial front was established at the northern average winter sea-ice edge, comparable with the modern Southern Antarctic Circumpolar Current Front (SACCF). During the glacial, this front would be located in the area of the modern APF. The northward deflection of colder than modern surface waters along the South American continent leads to a significant cooling of the glacial Humboldt Current surface waters (4-8 K), which affects the temperature regimes as far north as into tropical latitudes. The glacial reduction of ACC temperatures may also result in the significant cooling in the Atlantic and Indian Southern Ocean, thus may enhance thermal differentiation of the Southern Ocean and Antarctic continental cooling. Comparison with temperature and sea-ice simulations for the last glacial based on numerical simulations show that the majority of modern models overestimate summer and winter sea-ice cover and that there exists few models that reproduce our temperature data rather well.

3.1   Introduction

Physical and biological processes in the Southern Ocean play key roles in driving and amplifying global climate development. The Southern Ocean connects the Atlantic, Indian and Pacific Ocean basins, representing a critical "junction box" for global water mass exchange and redistribution. Atmosphere-ice-ocean interactions control the ventilation of deep- and bottom-waters as well as the export of intermediate water masses to mid and low latitudes (Ferrari et al., 2014). The interplay of stratification of water masses, formation and extent of sea ice, wind-driven upwelling and "biological pumping" impact atmosphere-ocean CO_2 exchange rates. The Southern Ocean represents a "High Nutrient-Low Chlorophyll" (HNLC) area where biological productivity and related carbon sequestration can be enhanced during climate conditions characterized by increased deposition of micro-nutrients (e.g. Fe) transported by wind or ice leading to atmospheric CO_2 drawdown and global cooling

(Sigman et al., 2010). Such conditions can best be studied in the Last Glacial Maximum (LGM), which represents a well accessible and datable Quaternary cold climate end-member, characterized by strongly expanded continental ice sheets (Clark et al., 2009), a maximum sea-level lowstand (-135 m, Yokoyama et al., 2000; Lambeck et al., 2014), and strongest annual mean sea surface cooling, reaching up to -10°C in the mid-latitude North Atlantic (MARGO Project Members, 2009). It depicts a global climate state fundamentally different from today and allows improving our understanding and prediction of physical and biological processes that steer water mass structure and formation as well as primary production and air-sea-gas exchange (Abelmann et al., 2015).

Sea surface temperatures (SST) and sea-ice cover are most important variables to reconstruct regional climate during the LGM. Sea surface temperatures present a parameter for the assignment of oceanic fronts and related temperature gradients (Orsi et al., 1995) as well as for the configuration and distribution of ocean current systems connected to the oceans surface. Closely linked to SSTs is the freezing and melting of sea ice, processes that are crucial for the formation of deep and bottom water masses via brine rejection (e.g. Antarctic Bottom Water) and the physical structure of the water column (Brandon et al., 2010). Furthermore, sea ice impacts the polar energy budge by ice-albedo feedback mechanisms and restrains the air-sea-gas exchange (Stephens and Keeling, 2000). Sea ice also affects primary productivity (Arrigo et al., 2008). During glacials, sea ice governs seasonal variability in surface-water structure and related ocean-atmosphere exchange rates, nutrient advection into surface waters and acts as storage platform for dust-born iron, turning the glacial Sea Ice Zone into a carbon sink (Abelmann et al., 2006, 2015).

Temperature and sea-ice estimates for the Southern Ocean LGM were presented for the first time by Hays et al. (1976) from a series of core sites located in the Atlantic and the western Indian sectors. Summer and winter SST estimates were calculated with a radiolarian-based transfer function (standard error 1.5°C for summer, 1.4°C for winter SST) using the Imbrie and Kipp Method (IKM) (Imbrie and Kipp, 1971). The extent of the LGM sea-ice field was estimated by mapping the lithological boundary between diatom-rich and diatom-poor sediments. In the broad absence of records allowing for the establishment of oxygen isotope stratigraphy, the LGM level, set at 18,000 years, was based on the abundance pattern of the radiolarian *Cycladophora davisiana*. As part of the first attempt to construct a global picture of the climate conditions during the LGM, project members of CLIMAP (1976, 1981) extended this to a circum-Antarctic view, including additional cores from the Pacific and Indian sectors. After various attempts to reconstruct last glacial sea ice considering

lithological boundaries (Cooke and Hays, 1982; Burckle et al., 1982; Burckle, 1983), Crosta et al. (1998a, b) were the first to present a circum-Antarctic sea-ice reconstruction using a transfer function (TF), the Modern Analog Technique (MAT) developed by Hutson (1980). The majority of the obtained sea-ice occurrence estimates (month/year) were derived from diatom assemblages in the CLIMAP (1976, 1981) Southern Ocean sample set, considering the original CLIMAP stratigraphic determination of the LGM. Gersonde et al. (2003a) reconstructed the LGM summer sea surface temperature (SSST) pattern in the Atlantic and eastern Indian sectors between the southern Subtropical and the seasonally sea-ice covered Antarctic Zone combining IKM and MAT estimates derived from three microfossil groups. Diatom sea-ice indicator species were used to estimate the extent of winter and summer sea ice, following the approach of Gersonde and Zielinski (2000). Gersonde et al. (2003a) developed well-constraint age models for the studied cores to relate the SSST and sea-ice results to a LGM time slice set between 23,000 – 19,000 calendar years before present (cal. yr BP) as proposed by the EPILOG working group (Mix et al. 2001). These data, combined with reevaluated LGM-data from Crosta et al. (1998a, b) and from additional core sites were used to map SSST and sea ice on a circum-Antarctic scale and at the EPILOG time slice (Gersonde et al. 2005) as part of the MARGO initiative for the reconstruction of the glacial surface ocean. For the first time, the paleoceanographic and stratigraphic data were quality controlled and ranked according to their accuracy level. Quality control resulted in highest levels for the Atlantic and western Indian sectors, while results from the Pacific sector displayed low quality levels and relatively low spatial cover (Gersonde et al., 2005; Bostock et al., 2013). As such, with the exception of near-continent areas (e.g. Sikes et al., 2002; Neil et al., 2004; Pahnke and Sachs, 2006; Lüer et al., 2009; Caniupán et al., 2011; Ho et al., 2012), the largest sector of the Southern Ocean remained little explored.

To cover this gap in information we studied LGM sections from 17 sediment cores recovered between 100°W and 180°E in the Pacific Southern Ocean (Gersonde, 2011). Using diatom-based transfer-function techniques (Esper and Gersonde, 2014a, b) and improved dating, we document SST and sea-ice conditions at the EPILOG LGM (E-LGM) time slice (23,000-19,000 cal. yr BP) at highest possible quality level. Our time slice includes the LGM sea level lowstand of ~134 m at 21,000 cal. yr BP (Lambeck et al., 2014). Our study presents a further step towards a high-quality circum-Antarctic documentation of the Southern Ocean surface conditions during the latest cold-climate end member, the LGM. We examine in detail the pattern of SST and sea-ice distribution in comparison with other Southern Ocean sectors to evaluate potential basin-basin differentiations and thus test the suggestion of

Gersonde et al. (2005) that LGM-cooling displays a non-uniform distribution in the Southern Ocean. We also analyze the impact of bottom topography and atmospheric circulation on LGM sea-ice distribution and SST pattern. This will help to better understand the configuration of the Antarctic Circumpolar Current (ACC) and related frontal systems in the last glacial Pacific sector and the adjacent sectors of the Southern Ocean. Our data are critical for the evaluation of the so-called "cold-water route" (Rintoul, 1991) that regulated Pacific-Atlantic heat and nutrient exchange and of the impact of Southern Ocean waters on heat, salt, moisture and nutrient conditions in eastern Pacific mid- and low latitudes during colder-than present conditions (e.g. Feldberg and Mix, 2002; Kucera et al., 2005b; Morey et al., 2005). As such, our new data provide critical data required to further validate and improve LGM climate scenarios and models (e.g. CLIMAP, 1976, 1981; Rojas et al., 2009; Ballarotta et al., 2013; Zhang et al, 2013), and their reliability.

3.2   Regional Setting

Our study area is located in the Pacific sector of the Southern Ocean between 180°E and 100°W (Fig. 3.1a). The studied cores document the glacial conditions between ca. 50°S and 65°S, thus between the modern southern Subantarctic Zone (SAZ) and the northern seasonal Sea Ice Zone (SIZ) in vicinity to the Southern Antarctic Circumpolar Front (SACCF) (Orsi et al., 1995; Reynolds et al., 2002; 2007). This zone is in the core of the Pacific section of the Antarctic Circumpolar Current (ACC), bounded to its north by the Subantarctic Front (SAF) (Orsi et al., 1995). In this area, modern summer and winter surface water temperatures range between ca. 0 to 8°C and -1.5 to 6°C, respectively (Olbers et al., 1992; Locarnini et al., 2010) (Fig. 3.1b, c). Surface sediment composition varies from primarily calcareous nannofossil ooze with varying diatom and foraminifera amounts in the SAZ to nannofossil-diatom oozes with only minor foraminifera content in the vicinity of the SAF (Gersonde 2011). Diatom ooze with opal content of 50-80% (Lisitzin, 1985; Geibert et al., 2005; Bradtmiller et al., 2009) is deposited in the Polar Front Zone (PFZ) and the Permanent Open Ocean Zone (POOZ), a zone between the Antarctic Polar Front (APF) and the average winter sea-ice edge (defined herein as ca. 40% sea-ice concentration), the latter being closely linked to the SACCF (Fig. 3.1a). The zone of enhanced biogenic opal deposition, the so-called Antarctic opal belt (Nelson et al., 2002; Geibert et al., 2005), is characterized by intensive Ekman upwelling of nutrient-repleted deep waters south of the maximum westerly winds (Speer et al., 2000; Orsi and Whitworth, 2005). The westerlies-

driven Ekman pumping also results in enhanced CO_2-outgassing in this zone (Lovenduski et al., 2007). Further south of the opal belt, in the area seasonally covered by sea ice the biogenic opal content in surface sediments drops to values <20% (Lisitzin, 1985; Geibert et al., 2005).
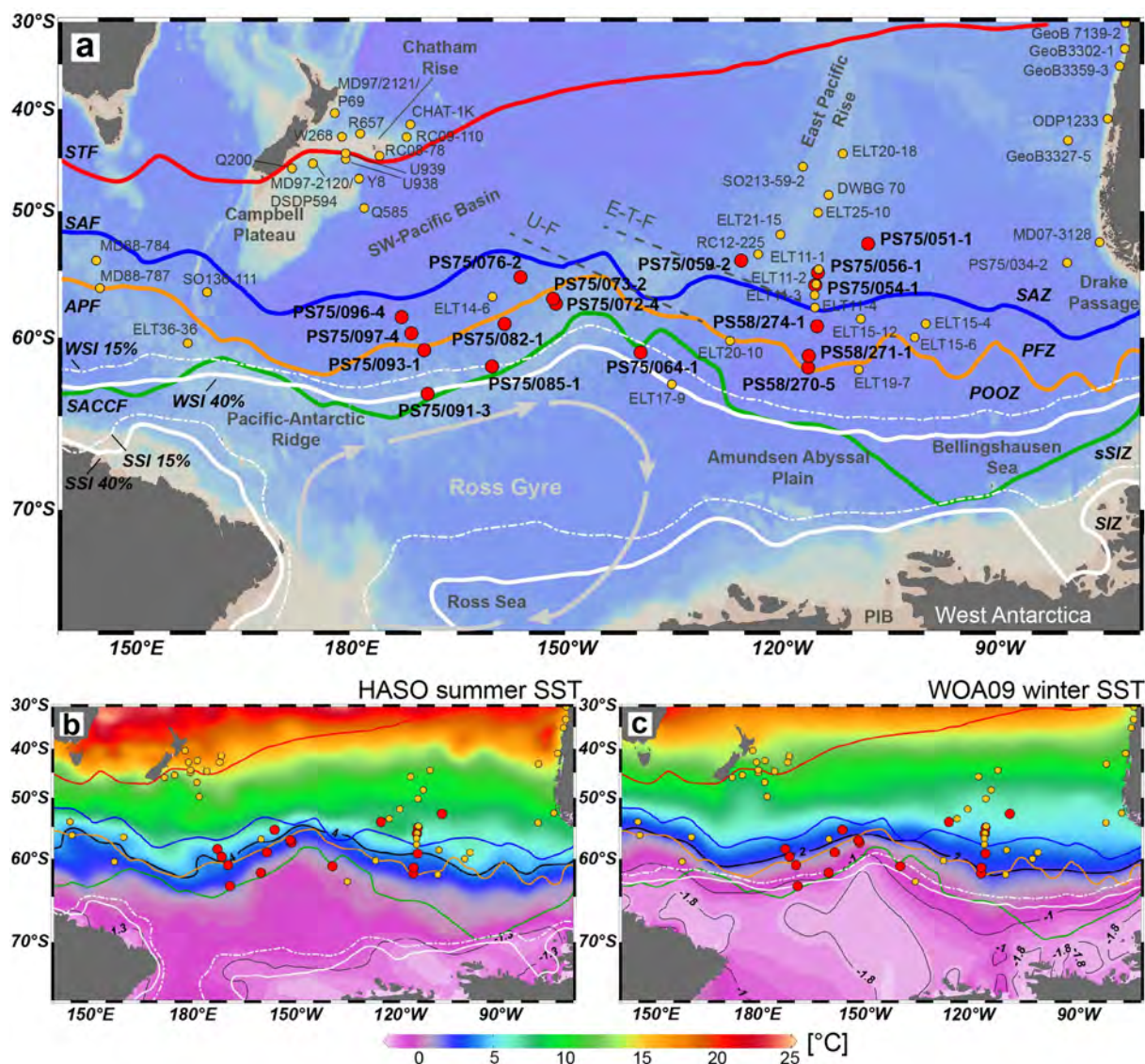
Figure 3.1: **(a)** Locations of cores analyzed in this study (red circles) and other cores discussed in the paper (yellow circles, for references see Tab. 3.1). WSI 15%/SSI 15%: modern winter/summer sea-ice edge with 15% sea-ice concentration, WSI 40%/SSI 40%: modern winter/summer sea-ice edge with 40% sea-ice concentration (Reynolds et al., 2002, 2007); E-T-F: Eltanin Tharp Fracture Zone, U-F: Udintsev Fracture Zone (Udintsev (Ed.), 2003); oceanic fronts according to Orsi et al. (1995); STF: Subtropical Front, SAF: Subantarctic Front, APF: Antarctic Polar Front, SAZ: Subantarctic Zone, PFZ: Polar Front Zone, POOZ: Permanent Open Ocean Zone, SACCF: Southern Antarctic Circumpolar Current Front, sSIZ: seasonal Sea Ice Zone, SIZ: Sea Ice Zone. **(b)** Modern summer SSTs from the Hydrographic Atlas of the Southern Ocean (HASO; Olbers et al., 1992); core locations and oceanographic fronts as in (a); 4°C and -1.3°C isotherm representing the APF and sea-ice edge respectively. **(c)** Modern winter SSTs from the World Ocean Atlas 2009 (WOA09, July-September; Locarnini et al., 2010); core locations and oceanographic fronts as in (a); 2°C and -1°C isotherm representing the APF and sea-ice edge respectively.

Related to topographic forcing, frontal positions in the ACC close to large bathymetric features (e.g. Pacific-Antarctic Ride, Udintsev Fracture Zone) remain relatively stable at seasonal and interannual time scale, whereas over abyssal plains (e.g. Amundsen-Bellingshausen Abyssal Plaines) their location appears to be fairly unstable because of mesoscale activity and atmospheric forcing (Sallée et al., 2008; Sokolov and Rintoul, 2009) (Fig. 3.1a). A prominent oceanographic feature in our study area is the cyclonic Ross Gyre. This gyre transports cold Antarctic Surface Water from the southern Ross Sea far north into the region of the Pacific-Antarctic Ridge. This results in relatively colder surface waters, a distinctly expanded winter sea-ice field and enhanced sea-ice seasonality in the western Pacific sector of the Southern Ocean (Fig. 3.1). The west-east differences in sea surface conditions in the Pacific Southern Ocean sector are also related to specific atmospheric conditions. While comparatively warm winds from the north along the Antarctic Peninsula lead to reduced sea-ice occurrence in the eastern sector, cold-air outbursts from the Antarctic ice sheet favor increased sea-ice production and northward expansion in the Ross Sea sector (Harangozo, 2004). Moreover, changes of the Southern Annular Mode (SAM) and the Amundsen Sea Low, but also tropical variability and the El Niño-Southern Oscillation (ENSO), influence the oceanographic conditions in the western and eastern Pacific Southern Ocean (Yuan, 2004; Sallée et al., 2008; Turner et al., 2009; Thompson et al., 2011). Therefore, interannual and decadal SST and sea-ice changes are amplified in the Pacific sector including for example a distinct increase in sea ice north of the Ross Sea embayment and a strong sea-ice decrease in the Bellingshausen-Amundsen Sea as documented by observational time-series (1979-2011) (Maksym et al., 2012; Stammerjohn et al., 2012). As the Pacific Sector collects the majority of the West Antarctic Ice Sheet (WAIS) drainage (Ó Cofaigh et al., 2005; Mosola and Anderson, 2006; Smith et al., 2011), it is the key region for understanding the impact of fresh water input induced by melting of the WAIS, which reacts sensitive to atmospheric and oceanographic conditions (Joughin and Alley, 2011).

3.3   Material and Methods

3.3.1   Core material

Temperature and sea-ice estimates were accomplished at a total of 17 sites sampled during R/V *Polarstern* cruises ANT-XIII/5a and ANT-XXVI/2 (Fig. 3.1, Table 3.1). The majority of cores were retrieved by piston coring (PC) with corresponding trigger cores (TC)

(Gersonde, 2011). Exceptions are cores PS75/056-1 and PS75/072-4 recovered with a gravity corer (GC) and core PS75/073-2 taken with a kasten corer (KC). The sites are located on different latitudinal transects (120°W, 150-160°W and ~170°W) in the eastern and western Pacific sector covering the Southern Ocean between the northern Antarctic Zone (AZ) and the southern SAZ (Fig. 3.1, Table 3.1).

Table 3.1 Locations of sediment cores presented and discussed in this study.

Core	Latitude	Longitude	Water depth (m)	Coring device[a]	Zone[b]	Data source
CHAT-1K	41°34.80'S	171°30.00'W	3556	KC	STZ	Barrows and Juggins, 2005; Kucera et al., 2005b
DSDP594	45°34.41'S	174°56.88'E	1204	CC	SAZ	Barrows and Juggins, 2005
DWBG 70	48°29.00'S	113°17.0'W		GC	SAZ	Luz , 1977; Moore et al., 1980
ELT11-1	54°54.42'S	114°42.18'W	3475	PC	SAZ	Luz , 1977; Moore et al., 1980; Gersonde et al., 2005
ELT11-2	56°03.60'S	115°03.60'W	3109	PC	SAZ	Luz , 1977; Moore et al., 1980; Mashiotta et al., 1999; Gersonde et al., 2005
ELT11-3	56°54.18'S	115°14.58'W	4023	PC	SAZ	Luz , 1977; Moore et al., 1980; Gersonde et al., 2005
ELT11-4	57°49.80'S	115°12.60'W	4773	PC	SAZ	Gersonde et al., 2005
ELT14-6	57°01.20'S	160°05.40'W	4520	PC	PFZ	Gersonde et al., 2005
ELT15-4	59°01.20'S	99°45.60'W	4910	PC	PFZ	Gersonde et al., 2005
ELT15-6	59°58.20'S	101°19.20'W	4517	PC	PFZ	Gersonde et al., 2005
ELT15-12	58°40.80'S	108°48.00'W	4575	PC	PFZ	Gersonde et al., 2005
ELT17-9	63°04.80'S	135°07.20'W	4848	PC	sSIZ	Gersonde et al., 2005
ELT19-7	62°09.60'S	109°05.40'W	5051	PC	POOZ	Gersonde et al., 2005
ELT20-10	60°13.20'S	127°01.08'W	4471	PC	POOZ	Gersonde et al., 2005
ELT20-18	44°33.00'S	111°19.80'W	2868	PC	SAZ	Luz , 1977; Moore et al., 1980
ELT21-15	52°01.02'S	120°01.20'W	2999	PC	SAZ	Luz , 1977; Moore et al., 1980
ELT25-10	50°06.00'S	114°46.98'W	2890	PC	SAZ	Luz , 1977; Moore et al., 1980
ELT36-36	60°23.40'S	157°37.80'E	2816	PC	POOZ	Gersonde et al., 2005
GeoB3327-5	43°14.40'S	79°59.00'W	3531	GC	SAZ	Ho et al., 2012
GeoB3302-1	33°13.01'S	72°06.00'W	1498	GC	SAZ	Kim et al., 2002
GeoB3359-3	35°13.00'S	72°48.50'W	678	GC	SAZ	Romero et al., 2006
GeoB7139-2	30°12.00'S	71°58.99'W	3267	GC	STZ	Kaiser et al., 2008
MD07-3128	52°39.57'S	75°33.97'W	1032	GPC	SAZ	Caniupán et al., 2011
MD88-784	54°11.40'S	144°47.40'E	2800	GPC	PFZ	Gersonde et al., 2005
MD88-787	56°22.80'S	145°18.00'E	3020	GPC	PFZ	Gersonde et al., 2005
MD97-2120	45°32.06'S	174°55.85'E	1210	GPC	SAZ	Pahnke et al., 2003; Pahnke and Sachs, 2006
MD97-2121	40°22.80'S	177°59.40'E	3014	GPC	STZ	Pahnke and Sachs, 2006
ODP1233	41°00.00'S	74°27.00'W	838	CC	SAZ	Kaiser and Lamy, 2010
P69	40°24.00'S	178°00.00'E	2195	GC	STZ	Barrows and Juggins, 2005
PS58/270-5	62°01.68'S	116°07.38'W	4981	PC	POOZ	**this study**
PS58/271-1	61°14.58'S	116°02.82'W	5214	PC	PFZ	**this study**; Gersonde et al., 2005; Esper and Gersonde, 2014a/b
PS58/274-1	59°12.42'S	114°53.28'W	5136	PC	PFZ	**this study**
PS75/034-2	54°22.12'S	80°05.40'W	4425	PC	SAZ	Ho et al., 2012
PS75/051-1	52°48.73'S	107°48.33'W	3949	PC	SAZ	**this study**

Table 3.1 continued

Core	Latitude	Longitude	Water depth (m)	Coring device[a]	Zone[b]	Data source
PS75/054-1	56°09.11'S	115°07.98'W	4113	PC	SAZ	**this study**
PS75/056-1	55°09.74'S	114°47.31'W	3581	GC	SAZ	**this study**
PS75/059-2	54°12.90'S	125°25.53'W	3613	PC	SAZ	**this study**
PS75/064-1	61°00.74'S	139°27.85'W	4600	PC	sSIZ	**this study**
PS75/072-4	57°33.51'S	151°13.17'W	3099	GC	POOZ	**this study**
PS75/073-2	57°12.26'S	151°36.65'W	3234	KC	POOZ	**this study**
PS75/076-2	55°31.71'S	156°08.39'W	3742	PC	PFZ	**this study**
PS75/082-1	59°02.48'S	158°51.82'W	4000	PC	POOZ	**this study**
PS75/085-1	61°56.38'S	160°07.10'W	3734	PC	sSIZ	**this study**
PS75/091-3	63°41.66'S	169°04.47'W	2940	PC	sSIZ	**this study**
PS75/093-1	60°52.33'S	169°32.89'W	3762	PC	POOZ	**this study**
PS75/096-4	58°32.86'S	172°42.06'W	5057	PC	PFZ	**this study**
PS75/097-4	59°42.02'S	171°21.44'W	4672	PC	PFZ	**this study**
Q200	46°00.00'S	172°01.80'E	1370	GC	SAZ	Barrows and Juggins, 2005
Q585	49°42.00'S	177°55.20'W	4354	GC	SAZ	Barrows and Juggins, 2005
R657	42°31.80'S	178°29.40'W	1408	GC	STZ	Sikes et al., 2002; Barrows and Juggins, 2005
RC08-78	44°46.80'S	175°46.20'W	1756	PC	STZ	Barrows and Juggins, 2005
RC09-110	42°52.20'S	172°01.20'W	1917	PC	STZ	Barrows and Juggins, 2005
RC12-225	53°40.20'S	123°06.00'W	2964	PC	SAZ	Luz , 1977; Moore et al., 1980
SO136-111	56°40.20'S	160°13.80'E	3912	GC	PFZ	Crosta et al., 2004; Gersonde et al., 2005
SO213-59-2	45°49.00'S	116°52.00'W	6161	GC	SAZ	Tapia et al., 2015
U938	45°04.80'S	179°30.00'E	2700	GC	SAZ	Sikes et al., 2002; Barrows and Juggins, 2005
U939	44°30.00'S	179.30.00'E	1300	PC	SAZ	Sikes et al., 2002; Barrows and Juggins, 2005
W268	42°51.00'S	178°58.20'E	980	PC	STZ	Sikes et al., 2002; Barrows and Juggins, 2005
Y8	46°58.25'S	178°39.40'W	1335	KC	SAZ	Lüer et al., 2009

[a] Coring devices: PC Piston Corer; GC Gravity Corer; KC Kasten Corer; GPC Giant Piston Corer; CC Composite Core; [b] Oceanographic zones: STZ Subtropical Zone; SAZ Subantarctic Zone; PFZ Polar Front Zone; POOZ Permanent Open Ocean Zone; sSIZ seasonal Sea Ice Zone

3.3.2   Sample preparation and counting of diatom slides

The preparation of sediment material and the permanent mounting of diatoms for light microscopy followed the standard methods presented by Gersonde and Zielinski (2000). Cores were sampled and analyzed at a spacing of 5 cm and the respective diatom counting was carried out according to Schrader and Gersonde (1978). On average, 400–600 diatom valves were counted in each slide using a Zeiss Axioplan 2 at x1000 magnification.

3.3.3   Diatom assemblage composition

Diatoms were identified to species or species group level and if possible to forma or variety level. The taxonomy follows primarily Hasle and Syvertsen (1996), Zielinski and Gersonde (1997), and Armand and Zielinski (2001). For temperature and sea-ice reconstructions 29, respectively 28, species and species groups were considered (Table 3.2). These species show close relationships to both environmental variables and different oceanographic zones (Zielinski and Gersonde, 1997; Armand et al., 2005; Crosta et al., 2005; Romero et al., 2005; Esper et al., 2010; Esper and Gersonde, 2014a, b). Following Zielinski and Gersonde (1997) and Zielinski et al. (1998) we combined some taxa to groups:

The *Thalassionema nitzschioides* group combines *T. nitzschioides* var. *lanceolata* and *T. nitzschioides* var. *capitulata*, two varieties with gradual transition of features between them and no significantly different ecological behavior. The species *Fragilariopsis curta* and *Fragilariopsis cylindrus* were combined as *F. curta* group taking into account their similar relation to sea ice and temperature (Zielinski and Gersonde, 1997; Armand et al., 2005). Furthermore, the *Thalassiosira gracilis* group comprises *T. gracilis* var. *gracilis* and *T. gracilis* var. *expecta* considering that characteristic pattern in the varieties are often transitional, which hampers distinct identification.

Although the two varieties *Eucampia antarctica* var. *recta* and *E. antarctica* var. *antarctica* display different biogeographical distribution (Fryxell and Prasad, 1990), they were combined to the *Eucampia antarctica* group. This group was not included in the TF as it shows no relationship to either sea ice or temperature variation (Esper and Gersonde, 2014a, b) and may cause no-analog situations due to higher glacial than modern abundances (Zielinski et al., 1998). However, the abundance pattern of the *E. antarctica* group can be used as a stratigraphic tool because it displays a pattern allowing for the detection of glacial intervals (Burckle and Cooke, 1983; Burckle, 1984a, b).

Besides the *E. antarctica* group we also discarded diatoms assembled as *Chaetoceros* spp. group from the TF-based reconstructions, following Zielinski et al. (1998) and Esper and Gersonde (2014a). This group combines mainly resting spores of a diatom genus with cosmopolitic distribution pattern that cannot be identified to species level due to the lack of morphological features. Therefore, different ecological demands of single taxa cannot be distinguished. But the *Chaetoceros* spp. group can be used as an additional stratigraphic indicator by inter-core correlation of specific abundance fluctuations in glacial and deglacial intervals.

Table 3.2 Twenty-nine diatom taxa/taxa groups of the IKM-D336/29/3q and MAT-D274/28/4an data set.

Name
Actinocyclus actinochilus (Ehrenberg) Simonsen,1982
[a]*Alveus marinus* (Grunow) Kaczmarska and Fryxell, 1996
Azpeitia tabularis (Grunow) Fryxell and Sims in Fryxell et al., 1986
Fragilariopsis curta group
[b]*Chaetoceros* spp. – not differentiated to taxon level –
[b]*Eucampia antarcita* (Castracane) Mangin 1945
Fragilariopsis doliolus (Wallich) Medlin and Sims, 1993
Fragilariopsis kerguelensis (O´Meara) Hustedt 1952
Fragilariopsis obliquecostata (Van Heurck) Heiden in Heiden and Kolbe, 1928
Fragilariopsis rhombica (O´Meara) Hustedt, 1952
Fragilariopsis ritscheri Hustedt, 1958
Fragilariopsis separanda Hustedt, 1958
Fragilariopsis sublinearis (Van Heurck) Heiden in Heiden and Kolbe, 1928
Hemidiscus cuneiformis Wallich, 1860
Nitzschia bicapitata Cleve, 1901
Porosira pseudodenticulata (Grunow) Jørgensen,1905
Pseudo-nitzschia turgiduloides (Hasle) Hasle, 1993
Rhizosolenia antennata forma *semispina* Sundström, 1986
Rhizosolenia bergonii H. Peragallo, 1892
Rhizosolenia species A Armand and Zielinski, 2001
Roperia tesselata (Roper) Grunow ex Pelletan, 1889
Stellarima microtrias (Ehrenberg) Hasle and Sims, 1986
Thalassionema nitzschioides forma 1 Zielinski and Gersonde, 1997
Thalassionema nitzschioides group
Thalassionema nitzschioides var. *parva* (Heiden) Moreno-Ruiz and Licea, 1995
Thalassiosira antarctica Comber, 1896
Thalassiosira gracilis (Karsten) Hustedt, 1958
Thalassiosira lentiginosa (Janisch) Fryxell, 1977
Thalassiosira oestrupii (Ostenfeld) Hasle, 1972
Thalassiosira oliverana (O´Meara) Makarova and Nikolajev, 1983
Thalassiothrix antarctica Schimper ex Karsten, 1905

[a]only in IKM-D336/29/3q
[b]Taxa excluded from datasets IKM-D336/29/3q and MAT-D274/28/4an

3.3.4   Reconstruction techniques

Our reconstructions include estimates of summer sea surface temperatures (SSST) and winter sea-ice (WSI) concentrations obtained with TFs developed by Esper and Gersonde (2014a, b). For SSST estimates we applied the Imbrie and Kipp Method (IKM; Imbrie and Kipp, 1971) and for WSI the Modern Analog Technique (MAT; Hutson, 1980). Statistical details and background of the methods and their performance at different application levels

and in comparison with other estimation methods are presented in Esper and Gersonde (2014a, b).

Estimates of SSSTs were accomplished using TF IKM-D336/29/3q, comprising 336 reference samples from surface sediments in the western Indian, the Atlantic and the Pacific sectors of the Southern Ocean, with 29 diatom taxa and taxa groups, and a 3 factor model calculated with quadratic regression. The SSST estimates refer to summer (January-March) temperatures at 10 m water depth averaged over a time period from <1900-1991 (Hydrographic Atlas of the Southern Ocean, HASO; Olbers, et al., 1992). The HASO was used because it represents an oceanographic reference dataset least influenced by the recent warming in the Southern Ocean (Esper and Gersonde, 2014b).

Our supra-regional TF revealed the optimum results in the comparison of different TF approaches for temperature reconstructions, achieving lower errors, better communalities, and less no-analog situations than regional TFs (Esper and Gersonde, 2014b). The root mean square error of prediction (RMSEP) for the reference data set, resulting from the standard deviation between measured and estimated temperatures, is 0.83°C (Esper and Gersonde, 2014b). IKM calculations were carried out with the software packages PaleoToolBox and WinTransfer (http://www.pangaea.de/Software/PaleoToolBox; Sieger et al., 1999).

For estimating WSI concentration we applied the TF MAT-D274/28/4an, comprising 274 reference samples from surface sediments in the western Indian, the Atlantic and the Pacific sectors of he Southern Ocean, with 28 diatom taxa and taxa groups, and an average of 4 analogs (Esper and Gersonde, 2014a). This reference data set was specifically designed for the reconstruction of sea ice. The WSI estimates refer to September sea-ice concentrations averaged over a time period from 1981-2010 at each surface sediment site (National Oceanic and Atmospheric Administration, NOAA; Reynolds et al, 2002; 2007). The reference data set is suitable for our approach as it uses a 1° by 1° grid, representing a higher resolution than previously used and results in a RMSEP of 5.52% (Esper and Gersonde, 2014a). We defined 15% concentration as threshold for maximum sea-ice expansion following the approach of Zwally et al. (2002) for the presence or absence of sea ice, and 40% concentration representing the average sea-ice edge (Gloersen et al., 1992; Gersonde et al., 2005). MAT calculations were carried out with the statistical computing program *R* (R core team, 2012). Further enhancement of the sea-ice reconstruction was obtained by consideration of the abundance pattern of the diatom sea-ice indicators allowing for qualitative estimate of sea-ice occurrence, as proposed by Gersonde and Zielinski (2000).

In contrast to CLIMAP (1976, 1981), we refrained from the estimation of winter sea surface temperatures and summer sea-ice (SSI) concentration based on TF-derived calculations. Considering that in the open modern Southern Ocean the diatom signal is primarily exported during austral summer (Abelmann and Gersonde, 1991; Fischer et al., 2002), it must be assumed that the diatom assemblages preserved in the sediment record are related to summer surface water temperatures. Statistical tests support the close relation between estimated and measured SSSTs at the reference sites (Esper and Gersonde, 2014b). In areas affected seasonally by sea ice, the summer diatom signal includes specific sea-ice diatoms that seed the spring-summer bloom after release from melting ice (Smith and Nelson, 1986; Gersonde and Zielinski, 2000; Fischer et al., 2002). The close relationship between this signal preserved in the sediment record and the occurrence of WSI represents the backbone for the sea-ice reconstruction based on statistical methods (Esper and Gersonde, 2014a). In open-ocean areas affected by perennial sea ice (e.g. in the Weddell Sea) the export of diatom indicator is too low to produce a sedimentary signal allowing for TF-based SSI reconstructions (Fischer et al., 1988; Esper and Gersonde, 2014a). Hence, we followed the approach by Gersonde and Zielinski (2000) to combine the occurrence and abundance patterns of SSI related diatom species *Fragilariopsis obliquecostata* and *Fragilariopsis sublinearis* together with strongly decreased biogenic sedimentation rates for a rough estimate of SSI distribution. For an approximation of winter SSTs we applied the modern relationship between sea ice and under sea-ice temperature, which on average is ca. -1 to -1.8°C at a >50% sea-ice cover (Locarnini et al., 2010, Fig. 3.1c).

Reconstructed variables include averaged temperature and sea-ice values for the E-LGM time slice as well as minimum (SSST) and maximum (WSI) estimates in the E-LGM time slice. Anomalies between modern and E-LGM estimates are presented for both, the averaged and minimum SSST. We chose minimum SSST and maximum WSI concentration for the presentation of glacial conditions in figures, to emphasize the differences to modern conditions. Reconstructed variables are available in the PANGAEA database (www.pangaea.de, http://doi.pangaea.de/10.1594/PANGAEA.849115). Maps, temperature and sea-ice plots have been produced with ODV (Ocean Data View; Schlitzer, 2014).

3.3.5 Dating

For the determination of the time interval equivalent to the EPILOG time LGM slice (E-LGM; 19,000–23,000 cal. yr BP) we established age models at highest possibly accuracy.

It is commonly known that the establishment of precise and high-resolution age models in the Southern Ocean is problematic due to discontinuous or lacking carbonate content which impedes the generation of continuous foraminifer-based oxygen isotope stratigraphies and AMS^{14}C dating, and/or strongly fluctuating sedimentation rates. Thus, the accuracy of our age models may not be comparable with tropical records. To allow for dating at highest possible accuracy we applied the following approach. It is based on the generation of well-constraint age models for selected stratigraphic reference cores from different sectors of the study area and a subsequent inter-core correlation using multiple sediment parameters for the dating of cores not allowing for isotope stratigraphic or AMS^{14}C-based age determination. The inter-core correlation considers element concentration and magnetic susceptibility records measured with an AVAATECH profiling X-ray Fluorescence (XRF) core-scanner at the Alfred-Wegener-Institute and with a GEOTEK Multi-Sensor Core Logger onboard R/V *Polarstern* (Gersonde, 2011), respectively. We particularly used the Fe and Ca counts and Si/Ti ratio records in combination with diatom abundance and TF-derived SSST records. Additional testing and refinement was achieved by the correlation to dust, iron (Fe) and temperature records from the EPICA Dome C (EDC) ice-core (Jouzel et al., 2007; Lambert et al., 2008; Martínez-Garcia et al., 2009), adjusted to the EDC3 age scale (Fe flux, Parrenin et al., 2007) or the AAIC12 age scale (dust and temperature; Bazin et al., 2013; Veres et al., 2013), as well as to the δ^{18}O record of the WAIS Divide ice core (WDC) (WAIS Divide Project Members, 2013) (Figs. 3.2, S3.1).

A total of 65 AMS^{14}C datings were used to establish the age models for eight reference cores (PS58/271-1, PS58/274-1, PS75/059-2, PS75/064-1, P75/072-4, PS75/073-2, PS75/085-1, PS75/093-1, Table 3.3, Fig. 3.2). Out of these, 45 datings were derived from monospecific samples of the planktic foraminifers *Neogloboquadrina pachyderma* sinistral and *Globigerina bulloides*, accomplished at the National Ocean Science Accelerator Mass Spectrometry Facility (NOSAMS) at Woods Hole Oceanographic Institution (WHOI) and the Eidgenössische Technische Hochschule (ETH, Zürich). While the minimum sample size required for the datings at NOSAMS is >1 mg carbonate, measurements carried out with the recently developed 200kV Mini radioCarbon Dating System (MICADAS) at ETH

Figure 3.2: Iron content fluctuation (red), benthic and planktic foraminifera oxygen isotope records (black), radiocarbon ages (blue triangles: foraminifera, yellow diamonds: humic acids) and sedimentation rates (grey) of reference cores compared to the LR04 stack and associated Marine Isotope Stages (MIS) 1-5 (Lisiecki and Raymo, 2005), dust and iron fluxes from the EPICA Dome C (EDC) ice core (dust: Lambert et al., 2008; iron: Martínez-Garcia et al., 2009; AICC 12 age scale: Bazin et al., 2013; Veres et al., 2013; EDC3 age scale: Parrenin et al., 2007); E-LGM: EPILOG Last Glacial Maximum time slice. Scale extended to 100 cal. kyr BP to show glacial-interglacial variability.

(http://www.ams.ethz.ch/instruments/micadas) only require <1 mg carbonate, thus allow extension of the AMS^{14}C dating to sediments with low content in foraminifers. The comparison of the MICADAS dating results with those of conventional AMS measurements obtained from two neighboring cores (PS75/072-4 and PS75/073-2) allows for testing the accuracy of the dating based on small sample sizes of foraminifera carbonate (Fig. S3.2). In general, the deglacial-Holocene dating results obtained from both approaches yield consistent results. Discrepancies occur in sections with low carbonate content as well as low time resolution and sedimentation rates during the last glacial. The dating of foraminifers selected from such sections in PS75/072-4 (111-112 cm, 171-172 cm, 176-177 cm) yields ages that are distinctly too young (Fig. S3.2) or display reversed values (PS75/073-2, 122.5-123.5 cm, 127.5-128.5 cm) (Table 3.3). This pattern may be indicative of bioturbation, which results in the displacement of single foraminiferal tests that disturb the dating of the small volume samples. As such, it can be suggested that small sample dating (<1mg carbonate) should at least be based on series of multiple down-core AMS^{14}C measurements to allow for the detection of reworking or bioturbation effects.

Twenty bulk sediment samples were processed at NOSAMS or at Leibniz-Laboratory for Radiometric Dating and Stable Isotope Research (Kiel University) for dating organic carbon from humic acid fraction at core sections with no or insufficient foraminiferal carbonate content (Table 3.3). This includes four measurements of core PS58/271-1 presented by Jacot des Combes et al. (2008). The humic acid derived dating allows for establishment of consistent age models in our reference cores (Fig. 3.2) and tests of the accuracy of this dating method supports its utility (Walker et al., 2001). However, it must be considered that such dating may be biased due to the mobility of humic acids but also by eolian input of organic carbon matter, especially during glacial periods. Here we checked the accuracy of the humic acid dating via core-core correlation using the fluctuations of sediment composition properties.

Radiocarbon ages were converted to calendar years before present (cal. yr BP; 1000yr = 1kyr) using the calibration software CALIB 7.0.2 (Stuiver and Reimer, 1993; Stuiver et al., 2005) with the MARINE13 calibration curve (Reimer et al., 2013). For the time span of the Holocene and the deglacial until 14 ^{14}C kyr BP, we applied reservoir ages between 520 and 750 yrs dependent on the latitudinal position of the cores according to Bard (1988) (Table 3.3). This approach is commonly used to approximate Southern Ocean reservoir ages (e. g. Shemesh et al., 2002; Chase et al., 2003; Bianchi and Gersonde, 2004; Tapia et al., 2015).

Table 3.3 AMS ^{14}C ages obtained of studied cores. C sources for dating are: H – humic acid fraction; F_{nps} – foraminifera *N. pachyderma sin.*; F_{bull} – foraminifera *G. bulloides*.
KIA: **Ki**el **A**ccelerator ;OS: National **O**cean **S**cience AMS Woods Hole; ETH: **E**idgenössische **T**echnische **H**ochschule Zürich.

Core	Depth (cm)	Lab ID	C source	^{14}C age (yrs BP)	Error (yrs)	Reservoir age	2σ min	2σ max	Calib. Age (cal yr BP)
PS58/271-1	14-17	KIA 16755	H	6150[b]	70	750	6025	6370	6218
	113-117	KIA 16756	H	9570[b]	100	750	9679	10232	10002
	141-144.5	KIA 23791	H	10345	60	750	10771	11146	10981
	172-176	KIA 23792	H	11370	80	750	12321	12716	12562
	212-217[a]	KIA 16757[a]	H	14480[b]	182	1200	15343	16454	15946
	271-275	KIA 23793	H	19690[b]	165	1200	21906	22695	22340
PS58/274-1	6-11	KIA 29594	H	3775	40	690	3246	3465	3368
	170-175	KIA 29595	H	11980	80	690	12968	13343	13177
	276-281	KIA 29596	H	16980	110	1200	18787	19337	19036
	419-424	KIA 29597	H	19350	140	1200	21627	22358	22002
PS75/059-2	2-3	OS-101191	F_{bull}	3900	30	520	3622	3822	3722
	17-18	OS-101192	F_{bull}	6680	45	520	6948	7197	7078
	37-38	OS-101247	F_{bull}	10650	55	520	11407	12001	11759
	47-48	OS-101250	F_{bull}	11950	45	520	13189	13415	13302
	52-53[c]	OS-101251	F_{bull}	13550	45	520	15343	15792	15599
	57-58[c]	OS-101303	F_{bull}	14500	50	1200	15311	15758	15545
	52-58[d]		*F_{bull}*						*15572*
	67-68	OS-101304	F_{bull}	25900	110	1200	28450	28989	28727
	72-73[c]	OS-101306	F_{bull}	29200	130	1200	31351	32256	31703
	77-78[c]	OS-101308	F_{bull}	29500	130	1200	31634	32702	32159
	87-88[c]	OS-101311	F_{bull}	29900	130	1200	32276	33334	32822
	72-88[d]		*F_{bull}*	*29533*	*130*	*1200*	*31671*	*32747*	*32207*
	97-98	OS-101313	F_{bull}	35400	200	1200	38286	29163	38686
PS75/064-1	6-9	OS-106097	H	2950	15	750	2198	2337	2295
	20-2	OS-106098	H	3880	25	750	3341	3491	3413
	55.5-59	OS-106099	H	7270	40	750	7333	7512	7432
	80.5-84	OS-106100	H	10650	40	750	11166	11486	11285
PS75072-4	1-2	ETH 48932.1.1	F_{nps}	1369	60	590	635	873	729
	21-22	ETH 48933.1.1	F_{nps}	2311	63	590	1548	1856	1705
	36-37	ETH 48934.1.1	F_{nps}	3332	65	590	2761	3108	2929
	51-52	ETH 48935.1.1	F_{nps}	4392	68	590	4088	4476	4291
	76-77	ETH 48936.1.1	F_{nps}	7188	96	590	7315	7658	7494
	91-92	ETH 48937.1.1	F_{nps}	9119	78	590	9441	9838	9600
	101-102	ETH 48938.1.1	F_{nps}	10194	79	590	10748	11170	10984
	111-112[e]	ETH 48939.1.1	F_{nps}	10600	86	590	11219	11871	11524
	131-132	ETH 48940.1.1	F_{nps}	12509	95	590	13529	14021	13786
	151-152	ETH 48941.1.1	F_{nps}	17279	158	1200	18968	19799	19387
	156-157	ETH 48942.1.1	F_{nps}	20001	171	1200	22342	23078	22676
	166-167	ETH 48943.1.1	F_{nps}	25596	332	1200	27769	29079	28418
	171-172[e]	ETH 48944.1.1	F_{nps}	20208	186	1200	22472	23383	22887
	176-177[e]	ETH 48945.1.1	F_{nps}	21533	225	1200	23919	25132	24464

Table 3.3 continued

Core	Depth (cm)	Lab ID	C source	^{14}C age (yrs BP)	Error (yrs)	Reservoir age	2σ min	2σ max	Calib. Age (cal yr BP)
PS75/073-2	17.5-18.5	OS-96102	F_{nps}	4060	25	590	3722	3924	3838
	25.5-26.5	OS-96101	F_{nps}	4770	25	590	4705	4853	4807
	37.5-38.5	OS-96100	F_{nps}	5870	30	590	5985	6180	6089
	52.5-53.5	OS-96109	F_{nps}	7730	35	590	7922	8102	7993
	62.5-63.5	OS-96099	F_{nps}	9260	50	590	9571	9963	9779
	73.5-74.5	OS-96098	F_{nps}	10300	50	590	10965	11227	11118
	82-83	OS-96097	F_{nps}	11100	50	590	12229	12605	12466
	103-104	OS-98711	F_{nps}	13400	50	590	15092	15480	15255
	113-114	ETH 48946.1.1	F_{nps}	14979	106	1200	16303	17005	16654
	122.5-123.5[e]	ETH 48947.1.1	F_{nps}	17805	154	1200	19620	20425	20028
	127.5-128.5[e]	ETH 48948.1.1	F_{nps}	17644	150	1200	19476	20219	19834
	146.5-147.5	OS-96096	F_{nps}	46700	4000	1200	42281	50000	47007
PS75/085-1	5.5-9	OS-106101	H	2420	40	750	1534	1759	1642
	45-49	OS-106102	H	3830	25	750	3291	3441	3364
	131.5-135.5	OS-106103	H	5350	30	750	5282	5439	5358
	185-189	OS-106281	H	6520	35	750	6496	6707	6607
	245.5-249.5	OS-106282	H	7700	40	750	7709	7917	7815
	301-305	OS-106283	H	8920	40	750	9077	9362	9214
	342.5-343.5	OS-98706	F_{nps}	9900	35	750	10274	10529	10417
	357.5-358.5[c]	OS-98721	F_{nps}	10350	35	750	10823	11130	10999
	358.5-359.5[c]	OS-98720	F_{nps}	10400	35	750	10906	11171	10062
	357.5-359.5[d]		*F_{nps}*	*10375*	*35*	*750*	*10865*	*11153*	*11032*
	552.5-553.5	OS-98719	F_{nps}	21300	130	1200	23841	24485	24162
	557.5-558.5[c]	OS-98718	F_{nps}	22900	140	1200	25693	26200	25947
	558.5-559.5[c]	OS-98708	F_{nps}	23100	150	1200	25845	26478	26117
	557.5-559.5[d]		*F_{nps}*	*23000*	*145*	*1200*	*25772*	*26354*	*26026*
PS75/093-1	26.5-27.5	OS-106674	F_{nps}	8100	35	710	8171	8340	8259
	41.5-42.5	OS-106675	F_{nps}	10100	45	710	10567	10877	10701

[a] ^{14}C age obtained by averaging values from two analysis
[b] Jacot des Combes et al., 2008
[c] samples where ^{14}C ages combined to average value
[d] ^{14}C ages obtained by averaging values from several measuements
[e] rejected due to unlikely sedimentation rates or implausibly ages

To account for higher glacial and deglacial reservoir ages, we apply an average reservoir age of 1200 yr for radiocarbon ages older than 14 ^{14}C kyr BP. This is in the range of surface water reservoir ages reported from glacial sediments in the Pacific sector (Skinner et al., 2015). We are aware that higher surface-water reservoir ages may also be applicable during the deglacial and the glacial. As summarized by Skinner at al. (2015) such ages may increase to 1300 yrs at the Chilean Margin (Siani et al. 2013), ca. 1400 yrs in the Drake Passage (Burke and Robinson, 2012), and >2500 years in the Subantarctic Atlantic (Skinner et al. 2010). The placement of the shift from glacial to post-glacial reservoir ages at 14 ^{14}C kyr BP

considers findings of Skinner et al. (2010, 2015), which show a major shift in Southern Ocean reservoir ages around this time period. The shift in reservoir ages at 14 ^{14}C kyr BP leads to uneven age assignments around this age in cores with dense sample spacing for radiocarbon dating. This is true for core PS75/059-2 where the application of different reservoir ages results in similar calibrated calendar ages at different core depth (Table 3.3). To harmonize the datings from this interval we use a calibrated age averaged from both results. In PS75/059-2 we mark 3 age determinations between 72 and 88 cm, only slightly increasing with depth. This may be related to bioturbation effects in a glacial core section with low carbonate content. To better approximate the age of this sediment interval we have averaged the dating results. Averaging was also applied for datings received from nearby samples in PS75/085-1 (intervals 357.5-359.5 cm and 557.5-559.5 cm), resulting in dating offsets of ≤200 ^{14}C years (Table 3.3). Considering the relatively low sample resolution a plateau tuning of ^{14}C ages to determine individual reservoir ages for certain time slices (Sarnthein et al., 2015) was not feasible.

The sediment composition of five cores (PS75/056-1, PS75/059-2, PS75/072-4, PS75/073-2 and PS75/085-1) allowed for the establishment of oxygen isotopic records from benthic (*Cibicidoices wuellerstorfii*) or planktic (*N. pachyderma*$_{sin.}$) foraminifers (Fig. 3.2). This includes the benthic isotope records from PS75/056-1 and PS75/059-2 presented by Lamy et al. (2014). The isotope measurements were obtained at a Thermo Finnigan MAT 253 (Kiel 4) and were aligned to the LR04 stack of Lisiecki and Raymo (2005) (Fig. 3.2). The combination of the isotope-based stratigraphy with radiocarbon ages allowed a refinement of the PS75/059-2 age model of Lamy et al. (2014) and also served as template to improve the age model of PS75/056-1. Further constraints for coherence and refinement of reference cores were obtained by inter-core correlation as well as alignment of XRF measurements and reconstructed SSST records to the equivalent EDC ice core records (Jouzel et al., 2007; Lambert et al., 2008; Martínez-Garcia et al., 2009). The cross-correlation of ^{14}C dated cores leads to slightly modifications of the PS75/093-1 age model presented by Lamy et al. (2014).

The transfer of the stratigraphic information obtained for the reference cores to other cores not allowing for AMS and oxygen isotope-based dating techniques was achieved by correlation of the physical/chemical parameters and augmented by correlation of abundance fluctuations of the diatoms species *Fragilariopsis kerguelensis, Eucampia antarctica* group and *Chaetoceros* spp. This was especially helpful for the correlation of core sections with strongly changing and/or low sedimentation rates. Due to the detailed correlation to the

reference cores, we were able to slightly refine the age model of core PS75/076-2 proposed in Lamy et al. (2014).

The correlation of cores and the calculation of resulting sedimentation rates was carried out using the AnalySeries 2.0 software (Paillard et al., 1996) with linear interpolation between pointers. Detailed information for pointers used in age models including correlation source are presented in the Supporting Information (Table S3.1).

3.3.6   Quality ranking of statistically derived estimates and age assignment

Following the approach presented by Gersonde et al. (2005), TF estimates and chronostratigraphic age assignments of the E-LGM level were quality ranked and an average quality level for each estimate was proposed (Fig. 3.3; Table 3.4). The quality ranking should serve as a guideline for the selection of estimates used for data compilations or advanced studies (e.g. data-model comparison).
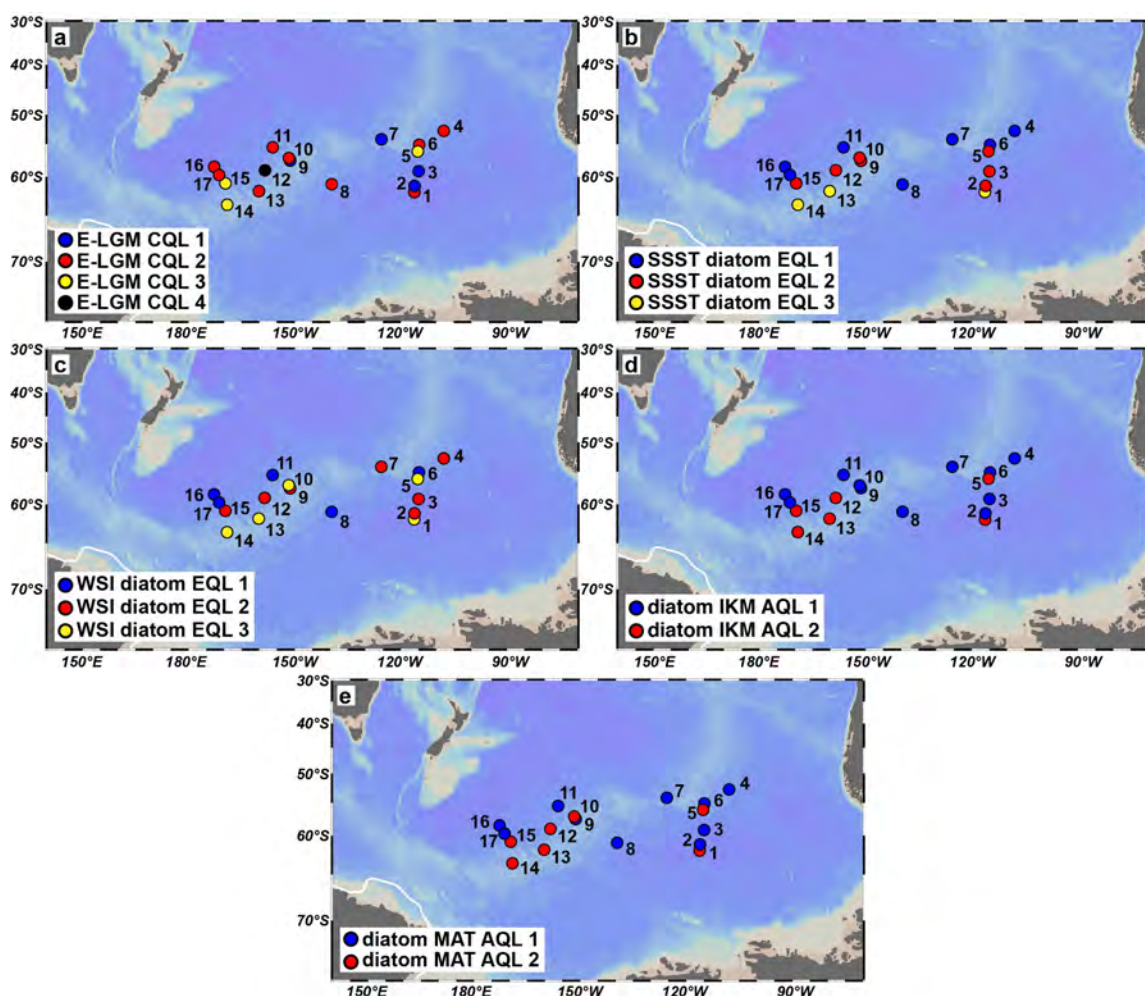

Figure 3.3: Spatial distribution of quality levels assigned to the E-LGM reconstructions. (a) Distribution of Chronostratigraphic Quality Levels (CQL). (b) Distribution of Estimated Quality Levels (EQL) for SSST. (c) Distribution of Estimated Quality Levels for WSI. (d) Distribution of SSST Average Quality Levels (IKM AQL). (e) Distribution of WSI Average Quality Level (MAT AQL).

Three estimate quality levels (EQL 1-3) are proposed for quality control of the SSSTs. The EQLs for SSST are based on the communality derived from the IKM transfer function for down-core samples. The communality expresses the total variance of all factors in a variable.

Estimate quality level 1: communality >0.8

Estimate quality level 2: communality 0.7-0.8

Estimate quality level 3: communality <0.7

Table 3.4 Preservation of diatoms in the E-LGM time slice and quality levels for SSST and WSI estimates.

	Core	E-LGM Preservation quality[a]	E-LGM CQL	EQL IKM SSST mean/min	EQL MAT WSI mean/max	AQL IKM min/ MAT max
1	PS58/270-5	4	2	3/3	3/3	2/2
2	PS58/271-1	3	1	2/2	3/2	1/1
3	PS58/274-1	3	1	2/2	2/2	1/1
4	PS75/051-1	2	2	1/1	2/2	1/1
5	PS75/054-1	3	3	2/2	3/3	2/2
6	PS75/056-1	2	2	1/1	1/1	1/1
7	PS75/059-2	2	1	1/1	2/2	1/1
8	PS75/064-1	2	2	1/1	2/1	1/1
9	PS75/072-4	3	1	2/2	2/2	1/1
10	PS75/073-2	3	2	2/2	3/3	1/2
11	PS75/076-2	2	2	1/1	1/1	1/1
12	PS75/082-1	3	4	2/2	2/2	2/2
13	PS75/085-1	4	2	3/3	3/3	2/2
14	PS75/091-3	4	3	3/3	3/3	2/2
15	PS75/093-1	3	3	2/2	2/2	2/2
16	PS75/096-4	2	2	1/1	1/1	1/1
17	PS75/097-4	2	2	1/1	1/1	1/1

[a]Preservation index: 1: good, 2: good-moderate, 3: moderate, 4: moderate-poor, 5: poor (classification according to Zielinski, 1993)

For MAT derived sea-ice concentrations the EQLs where defined by means of the dissimilarity index. This index is based on distances (squared chord distance), which defines the dissimilarity of the analogs found for the reference samples. The distance average increases with an increase in the degree of dissimilarity of the analogs. The threshold of the dissimilarity index for logarithm-transformed samples is 4.58 and good average distances are smaller than half of this threshold value (Esper and Gersonde, 2014a). Based on this threshold, three quality levels for WSI reconstructions were established.

Estimate quality level 1: threshold <2.29

Estimate quality level 2: threshold 2.29 – 4.58

Estimate quality level 3: threshold >4.58

As communality (IKM) and dissimilarity (MAT) only reflect the quality of the comparison between reference and down-core samples, effects related to changes in assemblage preservation that may divert the estimates towards implausible values remain unconsidered. Therefore the EQLs for MAT and IKM where combined with the preservation index according to the classification of Zielinski (1993) (1: good, 2: good-moderate, 3: moderate, 4: moderate-poor, 5: poor) (Table 3.4). The determining factor for the preservation quality level was the lowest preservation value in the E-LGM time slice of every core. Each original MAT and IKM EQL with preservation level moderate (3) was downgraded by one level; cores with a preservation level moderate-poor (4) were assigned to the lowest level EQL 3.

The assignment of chronostratigraphic quality levels (CQL) follows the suggestion of Mix et al. (2001) and Kucera et al. (2005a), originally proposed for the multiproxy reconstruction of the last glacial ocean surface (MARGO). Considering specific limitations concerning the dating of Southern Ocean sediment records (e.g. concerning the generation of radiometric dates and establishment of continuous $\delta^{18}O$ records), we propose the following quality levels modified from the original definition:

E- LGM Chronozone Level 1: Chronologic control based either on at least one radiometric date within the interval 19-23 cal. kyr BP, such as reservoir-corrected ^{14}C-yr dates or two bracketing radiometric dates of any kind within the interval 11 and 30 cal. kyr BP accompanied by benthic $\delta^{18}O$ records allowing for alignment to the LR04 stack.

E-LGM Chronozone Level 2: Chronologic control based on two bracketing radiometric dates of any kind within the interval 11 and 30 cal. kyr BP or by correlation of non-radiometric data ($\delta^{18}O$ stratigraphy, diatom abundance pattern, elemental parameter) to similar regional records that have been dated to match the level 1 protocol.

E-LGM Chronozone Level 3: Chronologic control based on other stratigraphic constraints (diatom abundance patterns, elemental parameter) that are correlated to similar records dated elsewhere to match the level 2 protocol.

E-LGM Chronozone Level 4: Chronologic control complicated by low sedimentation rates and less distinctive parameters for detailed correlation with records that match the level 1-3 protocols.

For general quality information of each E-LGM value, the chronostratigraphic and estimate quality level were combined following the approach of Gersonde et al. (2005) who

defined two average quality levels (AQL) (Table 3.4). AQL1 includes values with CQL and EQLs 1 or 2, whereas all other combinations are stated as AQL2. As we are using two different transfer functions, AQL levels were defined independently for both reconstructed variables. These levels concern the minimum SSST and maximum WSI concentrations as these values are as well used for the better visualization of differences concerning temperature and sea-ice reconstructions.

3.4   Results

3.4.1   Age models and sedimentation rates

The majority of the age models reach CQLs of 1 and 2, thus exhibiting a high accuracy and a very reliable assignment of the E-LGM time slice (Fig. 3.3a, Table 3.4). Overall, our age models show distinctly lower sedimentation rates during the last glacial compared to the Holocene (Fig. 3.2). Exceptions are records from the eastern Pacific sector (e.g. PS75/271-1 and PS75/274-1) with similar Holocene and last glacial sedimentation rates. The mapping of average sedimentation rates obtained for the E-LGM time slice displays a W-E gradient, with highest sedimentation rates in the eastern Pacific sector. Although local differences in sedimentation rates will depend on the specific topographic settings of the core sites, the general trend indicates increased sedimentation rates in a zone north of the E-LGM winter sea-ice edge (40% concentration) which corresponds to the modern northern POOZ and adjacent PFZ (Fig. 3.4).
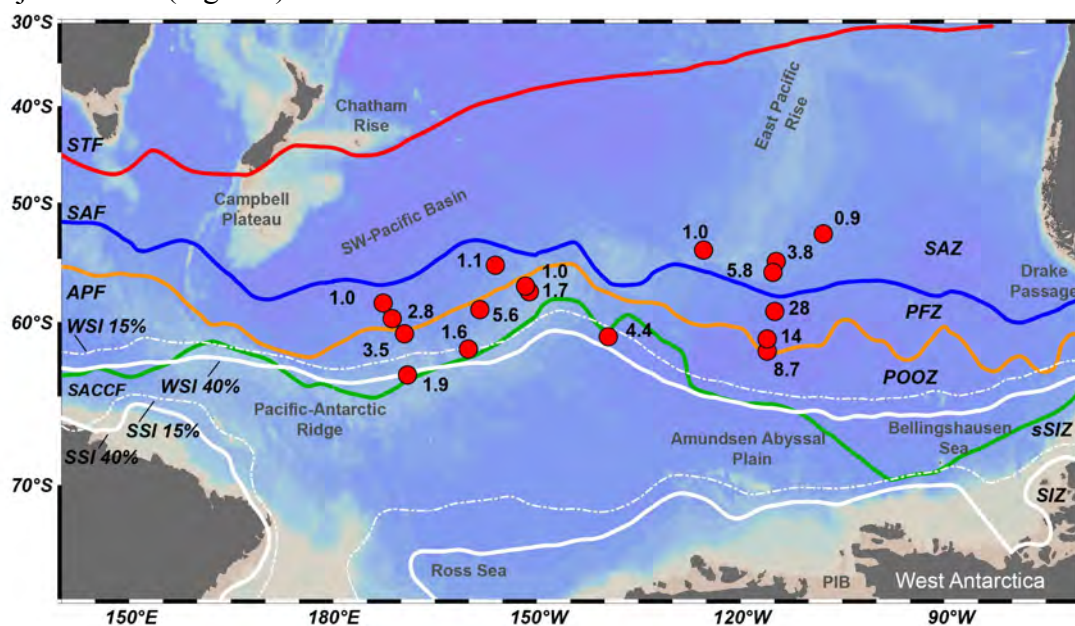

Figure 3.4: Average sedimentation rates at studied core locations during the E-LGM time slice (cm/kyr). Fronts and sea-ice edges as in Fig. 3.1.

3.4.2   EPILOG LGM summer surface conditions

The majority of SSST-estimates derived from TF IKM-D336/29/3q reach quality levels 1 and 2 (communality >0.7) (Fig. 3.3b), thus can be rated as reliable results. At 3 core sites located in the vicinity of the E-LGM WSI edge, estimates reach less reliable EQLs of 3 (Table 3.4). Estimates averaged over the E-LGM interval and obtained minimum values are presented in Table 3.5. Here we focus our SSST presentation on the minimum value estimated in the E-LGM time slice to document the maximum deviation from modern conditions. The estimates display a S-N increase in E-LGM temperatures, with lowest values estimated at the southernmost sites, located in the modern POOZ and highest SSSTs, reaching up to 5.1°C, in the modern southern SAZ (Fig. 3.5a.). However, the SSSTs obtained from the southern sites may be biased towards warmer values, as an effect of selective dissolution of diatom species resulting in a relative increase in strongly silicified taxa such as *Fragilariopsis kerguelensis* and/or *Thalassiosira lentiginosa* (Shemesh, et al., 1989). These species are prominently deposited in areas with warmer Southern Ocean surface waters (Crosta et al., 2005; Esper et al., 2010). Affected sites include PS58/270-5, PS75/085-1 and PS75/091-3 that are located south of the E-LGM winter sea-ice edge (40% concentration), according to our reconstruction (Fig. 3.6). Based on the modern relationship between summer temperature and WSI concentration (Fig. 3.1b, c), the E-LGM SSSTs at these sites probably reached ~0-1°C. Thus, the estimated temperatures at the southern sites are in the range of the TF error. Assuming colder SSSTs in the range of the modern temperatures, the anomalies are relatively stronger, yet fitting into the regional range (Table 3.5). Further north, in the modern POOZ and adjacent PFZ, the E-LGM SSST estimates range between 1 and 1.5°C, which is representative for a northward displacement of the glacial POOZ. Our new E-LGM estimates allow for an allocation of E-LGM isotherms in the Pacific sector, which can be augmented by SSST estimates from previous work (Fig. 3.5, for site numbers and reference see Tab. 3.1). This accounts especially for the area of the modern SAZ, which is not well documentable by diatom-based proxies. The enhanced data set permits for the localization of E-LGM isotherms ranging from 0°C to 4°C (Fig. 3.5a). The 4°C value corresponds to the average surface temperature at the modern Polar Front in austral summer (Fig. 3.1b). Thus, E-LGM cooling in the modern PFZ reached 2 to 3 K compared to present (Figs. 3.5b, 3.7). Strongest cooling occurred in the area of the modern SAZ reaching values close to 5 K. (Figs. 3.5b, 3.7; Table 3.5).
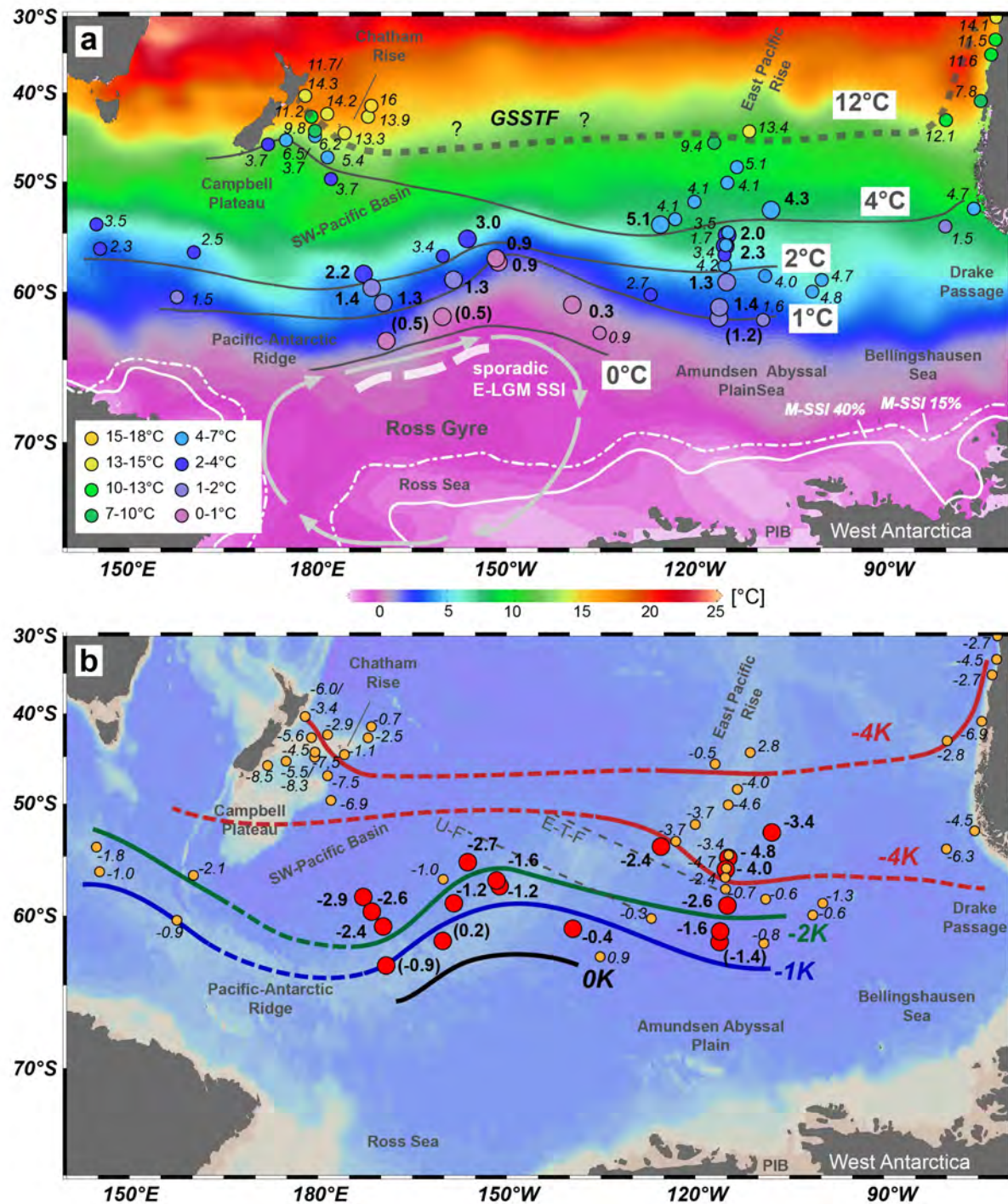
Figure 3.5: **(a)** Estimated E-LGM SSST and SSI compared to modern HASO SSST (Olbers et al., 1992) and modern SSI (Reynolds et al., 2002, 2007) with averaged reconstructed SSST isotherms (in °C). Numbers indicate minimum temperatures within the E-LGM time slice for cores in this study (bold) and from literature (italic, see Table 3.1, Table S3.2). GSSTF: Glacial Southern Subtropical Front. Color scale of core symbols represents the color code of the HASO SSST. **(b)** Averaged SSST anomaly (E-LGM/modern) isotherms (K) with single values for cores in this study (bold) and from literature (italic, see Table 3.1, Table S3.2). Values in parentheses represent probably underestimated temperatures and anomalies, respectively.

The estimation of the SSI extent is hampered by the fact that no cores allowing for suitable E-LGM reconstruction are available from offshore sites south of the studied area. This is due to very low Late Quaternary sedimentation rates not allowing for adequate

stratigraphic discrimination of the E-LGM together with the absence of microfossil records allowing for paleoceanographic reconstruction (Gersonde, 2011). Summer sea-ice indicators, such as *Fragilariopsis obliquecostata* and *Fragilariopsis sublinearis* (Gersonde and Zielinski 2000), show low abundances (<1.5%) during the E-LGM time slice in all studied cores. Hence, the relative abundance of both species in the studied southernmost cores is not indicative enough for the presence of SSI.

Table 3.5 Summary of EPILOG LGM summer SST (SSST) and sea-ice (WSI) concentration estimates derived from diatom assemblage information.

Core	E-LGM depth interval [cm]	E-LGM average sed. rate[cm]	E-LGM Sample number	Modern SSST (°C)[a]	E-LGM SSST mean (°C)	E-LGM SSST min (°C)	ΔLGM mean /mod. SSST (K)	ΔLGM min /mod. SSST (K)	E-LGM Sept. mean SI conc. (%)	E-LGM Sept. max SI conc. (%)	E-LGM Preservation quality[b]
PS58/270-5	143-173	8.7	3	2.6	1.5	1.2 (1)	-1.1	-1.4 (-1.6)	15.9	24.1	4
PS58/271-1	243-285	14	4	3.0	1.9	1.4	-1.1	-1.6	23.9	46.4	3
PS58/274-1	278-439	28	16	3.9	1.9	1.3	-2.0	-2.6	19.0	28.3	3
PS75/051-1	18-21	0.9	1	7.7	4.3	4.3	-3.4	-3.4	1.2	1.2	2
PS75/054-1	64-87	5.8	2	6.3	2.6	2.3	-3.7	-4.0	12.1	18.5	3
PS75/056-1	61-75	3.8	3	6.8	2.8	2.0	-4.0	-4.8	5.6	8.7	2
PS75/059-2	59-62	1.0	1	7.5	5.1	5.1	-2.4	-2.4	1.4	1.4	2
PS75/064-1	156-173	4.4	3	0.7	0.5	0.3	-0.2	-0.4	33.9	78.7	2
PS75/072-4	151-157	1.7	2	2.1	1.0	0.9	-1.1	-1.2	51.9	72.4	3
PS75/073-2	117-122	1.0	2	2.5	1.0	0.9	-1.5	-1.6	15.5	24.6	3
PS75/076-2	14-17	1.1	1	5.7	3.0	3.0	-2.7	-2.7	9.9	9.9	2
PS75/082-1	83-105	5.6	5	2.5	1.7	1.3	-0.8	-1.2	12.8	27.1	3
PS75/085-1	545-551	1.6	2	0.3	0.7	0.5 (0)	0.4	0.2 (-0.3)	26.2	21.3	4
PS75/091-3	187-196	1.9	2	1.4	1.0	0.5 (0)	-0.4	-0.9 (-1.4)	47.4	70.8	4
PS75/093-1	92-102	3.5	2	3.7	1.3	1.3	-2.4	-2.4	6.1	6.4	3
PS75/096-4	18-21	1.0	1	5.1	2.2	2.2	-2.9	-2.9	2.6	2.6	2
PS75/097-4	17-27	2.8	2	4.0	1.6	1.4	-2.4	-2.6	6.8	6.8	2

Values in parentheses represent suggested SSSTs interpolated from the modern temperature to sea ice concentration and corresponding anomalies.
[a]Modern SSST after Olbers et al. (1992)
[b]Preservation index: 1: good, 2: good-moderate, 3: moderate, 4: moderate-poor, 5: poor (classification according to Zielinski, 1993)

3.4.3   EPILOG LGM winter surface conditions

The most important parameter for E-LGM winter conditions is the reconstruction of the winter sea-ice extent based on TF-derived WSI concentrations. Such reconstruction of WSI concentrations with TF MAT-D274/28/4 reaches estimation quality levels 1 or 2 (MAT dissimilarity index <4.58) at the majority of the studied sites (Fig. 3.3c). At 5 locations the dissimilarities were higher and thus resulting in less reliable estimates. This includes sites in

areas at or south of the E-LGM WSI edge (40% concentration) (PS75/270-5, PS75/085-1), where biogenic opal dissolution leads to relative enrichment of strongly silicified diatom species not indicative of sea ice (e.g. *Fragilariopsis kerguelensis*) and bias the TF-estimates towards smaller concentration values (Fig. 3.6a, Tables 3.4, 3.5). At these sites E-LGM sedimentation rates are strongly reduced (Figs. 3.2, 3.4), thus showing a relation between sea-ice occurrence and open ocean biogenic sedimentation similar to modern conditions. Esper and Gersonde (2014a) show that the deposition of biogenic opal, which represents the major component of modern open ocean sediments in the Southern Ocean (Lisitzin, 1985), drops to 0-40% in areas with >75% WSI concentration.

The WSI concentration pattern displays differences between the eastern and western sector of the Pacific Southern Ocean (Figs. 3.6, 3.7; Table 3.5). In the area north of the modern Ross Gyre the WSI estimates suggest a narrow zone with decreasing concentrations from >40% (average sea-ice edge) to <15% (maximum sea-ice extent). A rather sharp drop in sea-ice concentrations marking the E-LGM sea-ice extent would be consistent with the pattern of sea-ice concentration decline at the modern Antarctic sea-ice edge (Worby and Comiso, 2004). This zone is tightly related to increased S-N gradients of the E-LGM SSSTs following the extent of a distinct underwater topographic feature, the Pacific-Antarctic Ridge (Figs. 3.1a, 3.5-3.7).

In contrast, our estimates from the eastern sector suggest no steep S-N decline in WSI concentration. North of sites indicating the average sea-ice edge (40% concentration), we observe a broader zone with concentration >15%, extending into the area of the southern East Pacific Rise (Figs. 3.1a, 3.6, 3.7). This is not interpreted to represent a broader extent of the marginal sea-ice zone, but to be indicative of increased variability in northward WSI extent during the E-LGM in this area. The zone of variable WSI extent in this area in the northern Amundsen-Bellingshausen Sea may exceed ca. 5° in latitude, thus more than 500 km (Figs. 3.6, 3.7). As such, the northward expansion of the WSI shows an E-W differentiation, with a WSI northward expansion by ca. 5° in latitude in the western Pacific sector (mirroring the extent of the Pacific-Antarctic Ridge) and a northward shift of the average WSI by ca. 5° in latitude together with an up to 10° latitudinal displacement of sporadic WSI extent in the eastern sector. The zone of sporadic extent is bounded to the north by the topographic feature of the southern East Pacific Rise (Figs. 3.1, 3.6, 3.7).

Because we refrained from the estimation of winter sea surface temperature (WSST) using the transfer function technique, we approximated the WSST in our study area assuming a
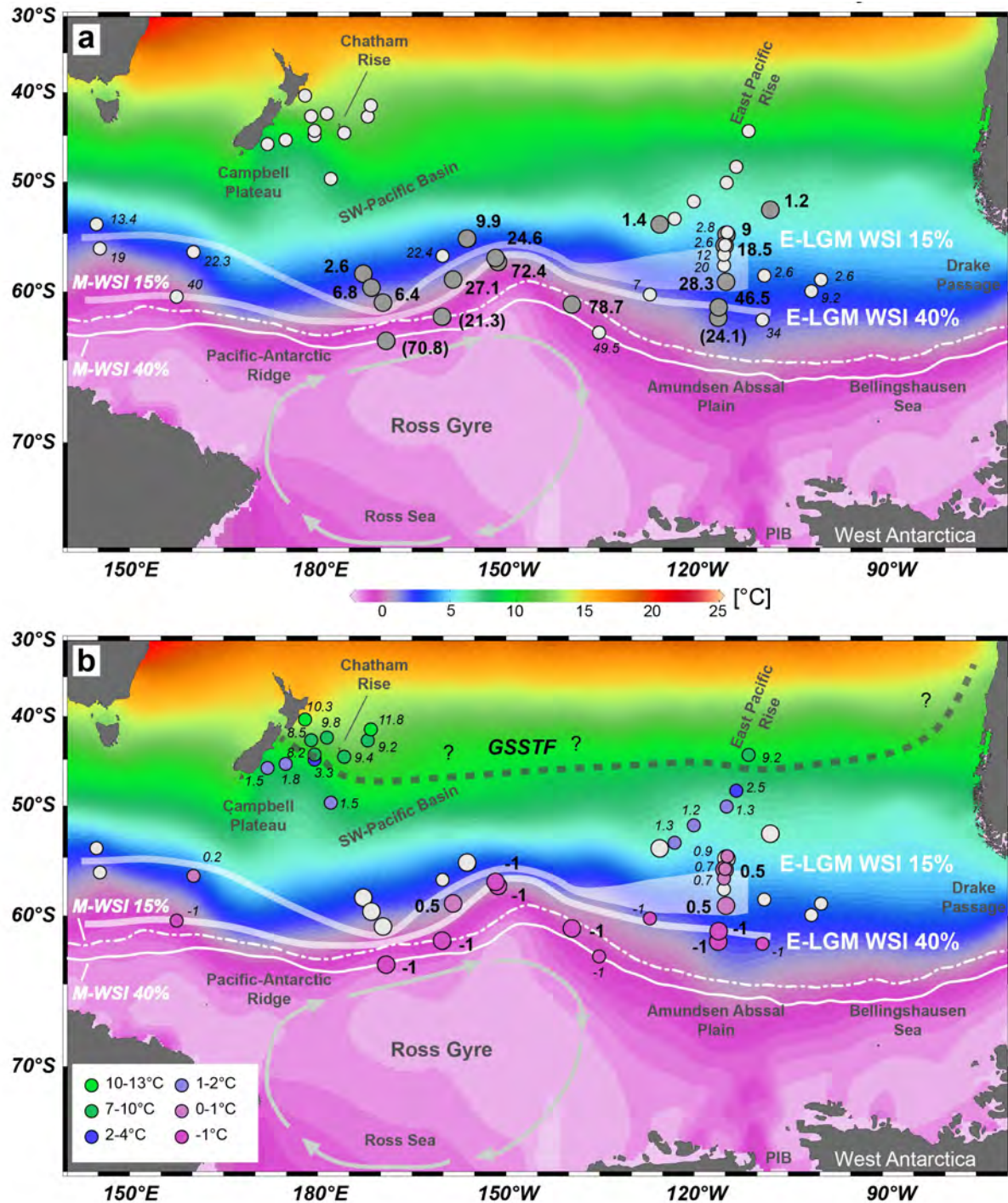
Figure 3.6: **(a)** Estimated E-LGM WSI distribution compared to modern WSI distribution and WOA09 winter SSTs. Numbers indicate maximum estimated sea-ice concentration during the E-LGM time slice from this study (bold) and the literature (italic, see Tab. 3.1, S3.2); values in parentheses represent underestimated values. **(b)** Estimated E-LGM winter SSTs from this study (bold, implied from modern day relationship between WSI and underlying temperature from this study) and literature values (italic, see Tab. 3.1, S3.2); GSSTF: Glacial Southern Subtropical Front. Color scale of core symbols represents the same color code as the WOA09 WSST. E-LGM WSI estimates include the maximum winter sea-ice extent (>15% September concentration) and the average sea-ice concentration (40% concentration). Modern winter sea-ice edges after Reynolds et al. (2002, 2007).

similar relationship between the concentrations of WSI and underlying sea surface

temperature during the E-LGM than at present. The modern relationship between WSST and

WSI at a concentration of 40% (average WSI edge) ranges from -1.5° to 0.5°C and at 15% WSI concentration between 0° and 1°C (Locarnini et al., 2010) (Fig. 3.1c). In areas affected by WSI at higher concentration the WSSTs drop to -1.8°C. Thus, we approximated average WSSTs during the E-LGM around -1°C at core sites located at the average WSI edge and ~0.5°C in the zone of the maximum sea-ice extent (Figs. 3.6, 3.7). This set of approximations for the Antarctic cold-water realm can be combined with winter temperatures derived from foraminiferal and diatom assemblages (Moore et al., 1980; Sikes et al., 2002; Crosta et al., 2004; Kucera et al., 2005b; Barrows and Juggins, 2005) to construct a broader view of the WSST regime during the E-LGM in the South Pacific sector (Fig. 3.6).

3.5   Discussion

3.5.1   Last glacial surface water temperatures in the Pacific Southern Ocean sector

A comparison of our diatom-TF derived data with results from the few previous studies in our study area shows that most of the previous results yield generally slightly warmer temperatures compared with our results. This accounts for reconstructions based on a foraminiferal TF (Moore et al., 1980) at the Eltanin core sites ELT11-1, ELT11-2 and ELT11-3 and for diatom-based TF results presented by Gersonde et al. (2005) from the same sites and other Eltanin cores (Fig. 3.5, Tables 3.5, S3.2). Part of the mismatch, which may challenge the utility of these data, may be related to the poor stratigraphic delineation of the LGM available for the Eltanin cores. However, we find strong coherence between our results and LGM SSTs from core ELT11-2 (1.7°C) derived by Mg/Ca paleothermometry from planktic foraminifers (Mashiotta et al., 1999) (Fig. 3.5, Table S3.2).

Despite potential deficiencies concerning the comparability between different reconstruction methods (e.g. alkenones, Mg/Ca, foraminifer and radiolarian transfer functions) and stratigraphic LGM determinations the combination of our new diatom-based results of E-LGM SSSTs with data from previous studies (Mashiotta et al, 1999; Sikes et al., 2002; Pahnke et al., 2003; Barrows and Juggins, 2005; Gersonde et al., 2005; Kim et al., 2002; Kucera et al., 2005b; Pahnke and Sachs, 2006; Romero et al., 2006; Kaiser et al., 2008; Kaiser and Lamy, 2010; Caniupán et al., 2011; Ho et al., 2012; Lüer et al., 2009) allows for the generation of a consistent pattern of the latitudinal zonation of surface temperatures in the Pacific sector of the Southern Ocean during the LGM (Figs. 3.5, 3.7; Table S3.2). North of the Pacific-Antarctic Ridge (around the modern APF) the 1° and 2°C-isotherms display a

narrow pattern, closely aligned to the bottom topography. Further north, in the area of the SW-Pacific Basin (representing part of the modern PFZ and SAZ), the latitudinal SSST gradients are weaker and the reconstructed surface temperatures suggest a displacement of the 4°C-isotherm as far north as the northern Campbell Plateau-Bounty Through (ca. 46°S) (Sikes et al., 2002; Pahnke et al., 2003; Barrows and Juggins, 2005; Pahnke and Sachs, 2006; Lüer et al., 2009). Such displacement would stretch the sea-ice free cold-water zone of the modern Southern Ocean from ca. 3-4° in latitude (ca. 300-450 km) (Fig. 3.1b) to more than 10° in latitude (>1000 km) in the glacial ocean in the area north of the outflow area of the Ross Gyre (Figs. 3.5a, 3.6, 3.7). Additional support for strong northward extension of the cold-water realm comes from the presence of ice rafted debris events recorded in glacial sediments from Campbell Plateau (Carter et al., 2002). Furthermore, the SST cooling in the present STZ and northern SAZ may be supported by less warm water transport to the eastern NZ coast due to a weakening of the East Australian Current (EAC), indicated by steeper temperature gradients during the LGM in the tropical south western Pacific Ocean (Felis et al., 2014). A relative cooling (by >4 K) restricted to the area north of the Ross Sea and extending to ca. 45°S was also suggested by CLIMAP (1981). However, this was based on reconstructions from a very limited number of sites and does not reach values ranging around 7-8.5 K as reported from the Campbell Plateau (Figs. 3.5, 3.7; Table S3.2).

In contrast, in the eastern sector of the Pacific Southern Ocean the displacement of the SSST-isotherms displays a more uniform pattern with a general northward shift of the 1°C-isotherm by ca. 2° in latitude, and a shift of the 2° and 4°C-isotherms by ca. 5° in latitude. The data available between 100° and 130°W indicate that the 4°C-isotherm was located around 54°S in this sector. Thus the location of the 4°-isotherm, which corresponds to the SSST at the modern APF (Dong et al., 2006, Fig. 3.1b), was closely related to the topographic feature of the Eltanin-Tharp Fracture Zone, which bounds the East Pacific Rise to its South (Figs. 3.5b, 3.7). Only little information is available on LGM temperatures in the open South Pacific corresponding to the warmer modern SAZ. This curtails extensive LGM reconstructions from that zone. However, SST estimates generated by Luz (1977), Moore et al. (1980) and Tapia et al. (2015) suggests a distinct S-N LGM-temperature increase around ca. 47° in latitude at the East Pacific Rise (Figs. 3.5a, 3.7; Table S3.2). North of this zone with enhanced SST gradients, LGM-estimates indicate only minor SST cooling or even slight SST warming compared with modern conditions (Figs. 3.5, 3.7, Table S3.2). Similarly, a temperature increase by >4 K is reported from a narrow zone off the South Island of New Zealand (NZ) located around 44°-43°S (Figs. 3.5a, 3.7), as presented by Sikes et al.
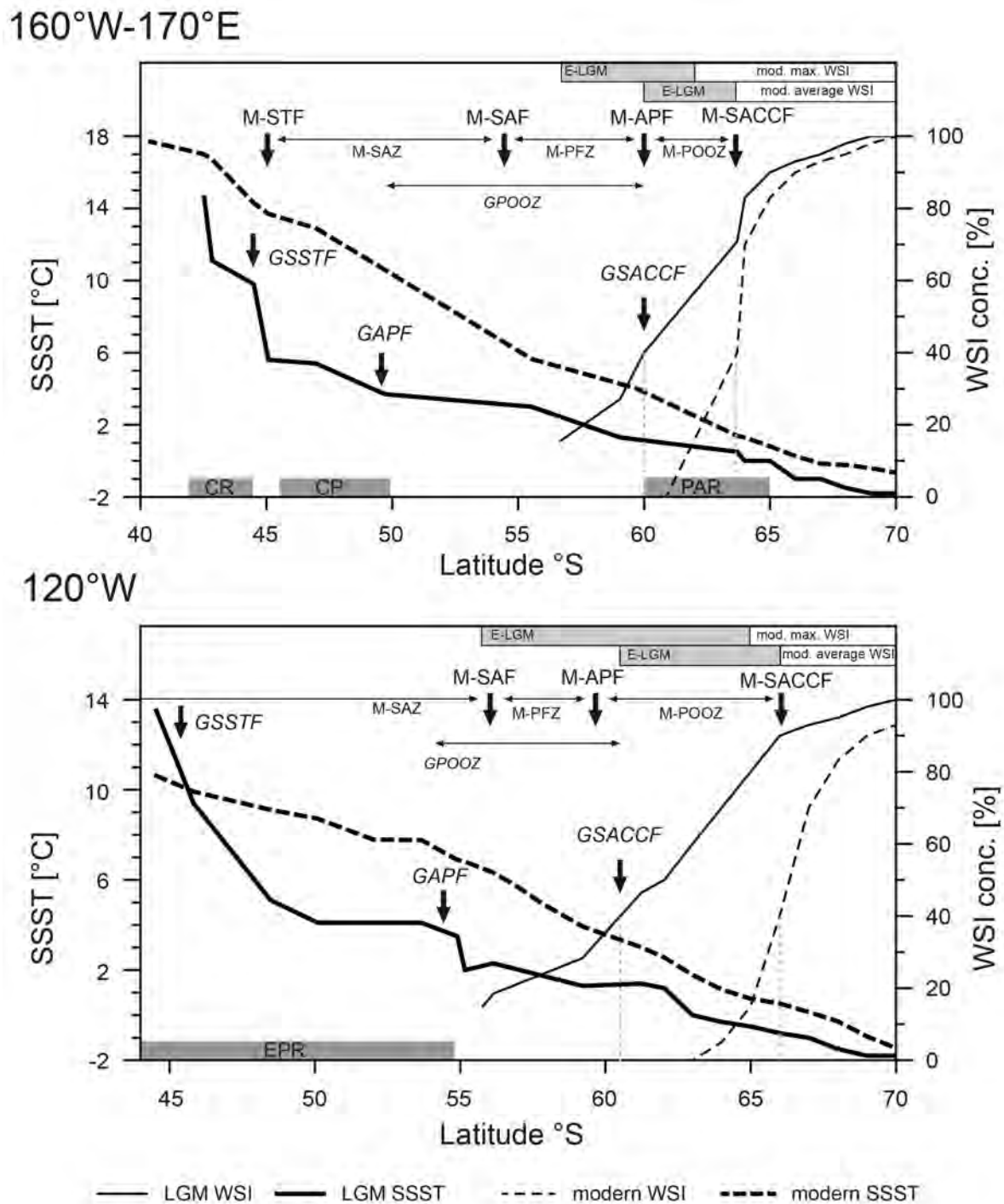
Figure 3.7: Schematic representation of modern SSST and WSI variations (Olbers et al., 1992, Reynolds et al., 2002, 2007) and E-LGM SSST and WSI variations on two meridional transects at 120°W and from 160°W to 170°E. Indicated are the locations of the oceanic fronts and ACC zones at modern conditions (according to Orsi et al., 1995) and estimated for the E-LGM together with the maximum and average winter sea-ice extent. The glacial fronts and zones represent conditions associated with the corresponding modern equivalents. Prefix M indicates modern front or zone, prefix G indicates glacial front or zone: APF, Antarctic Polar Front (~4°C); SAF, Subantarctic Front, STF, Subtropical Front; PFZ, Polar Front Zone; SAZ, Subantarctic Zone; POOZ Permanent Open Ocean Zone; SACCF, Southern Antarctic Circumpolar Current Front; GSSTF, Glacial Southern Subtropical Front; PAR, Pacific-Antarctic Ridge; CP, Campbell Plateau; CR, Chatham Rise; EPR, East Pacific Rise.

(2002), Barrows and Juggins (2005), Kucera et al. (2005b), and Pahnke and Sachs (2006) (Table S3.2). Such enhanced SST gradients have been described from the modern oceanic fronts, e.g. the STF and SAF in different sectors of the Southern Ocean (Graham and De Boer, 2013), a pattern that is however not clearly discernible in SST compilations integrating data primarily collected during 40-50 years of observation (Olbers et al., 1992; Locarnini et al., 2010) (Fig. 3.1b, c) due to the inter-annual variability of the location of fronts that may vary over 5° in latitude (e.g. Moore et al. 1999; Graham and De Boer, 2013). The >4 K SST cooling reconstructed for the area off the NZ South Island (Fig. 3.5b, Table S3.2) is in the range of the LGM temperature depression of 6-6.5 K required to match high-resolution simulations of the NZ Southern Alps LGM ice field with geological field data (Golledge et al. 2012). As such the glaciation of the NZ South Island during the LGM is related to the stretching of the cold-water zone north of the outflow area of the Ross Gyre, which reduced air temperatures over the South Island, and potentially led to modest reduction in atmospheric moisture (Golledge et al., 2012). The effect of potential feedbacks between the NZ ice field and the surface ocean temperatures around NZ await further numerical simulations. In contrast to the data and model-based evidence for distinct cooling during the last glacial on and around the NZ South Island, Neil et al. (2004) suggested the presence of a stable warm water pool located in the center of the Campbell Plateau, although they admit that waters around this pool were distinctly colder. Surface water temperatures were derived from the $\delta^{18}O$ record at two sites with very low sedimentation rates located on the plateau interior. In the light of later studies from the area off NZ (Barrow and Juggins, 2005; Pahnke and Sachs, 2006; Lüer et al., 2009) the presence of such an isolated warm surface water pool with temperatures exceeding Holocene SSTs seems rather unlikely.

Prominent LGM-cooling was also reported from sediment cores recovered in the area straddled by the Humboldt Current, which flows north along the west coast of South America (Fig. 3.5). The Humboldt Current links antarctic waters with the subtropical-tropical realm and exerts strong control on the climate in western South America. The cooling with temperature reductions by up to 7°C (ODP1233, Kaiser and Lamy, 2010) is most likely the result of enhanced northward deflection of water masses imprinted with up to 4°C cooler SSSTs than today, as presented here for the first time based on a more extensive set of LGM-data from the area of the modern ACC in the Pacific sector. It represents a strong extension of the polar Pacific cold-water realm along western South America during the E-LGM. The impact of the enhanced northward advection of polar cold water is most noticeable in the

Eastern Equatorial Pacific cold tongue, where it contributed to significant cooling during the E-LGM (Feldberg and Mix, 2002; Kucera et al., 2005b; Morey et al., 2005; Dubois et al., 2009). Interestingly, colder LGM temperatures off the South American coast were already reconstructed by CLIMAP (1981), yet the overestimation of SSSTs in the eastern Pacific sector prohibited the link between the high- and low-latitude cooling. Similar to the glaciation off the NZ South Island, the pronounced cooling off the Chilean coast can be associated with growth of the Patagonian ice sheet during the LGM (Kaiser and Lamy et al., 2010).

While estimates of LGM-WSST from our study represent an approximation assuming a similar relationship between the reconstructed concentration of WSI and underlying sea surface temperature during the E-LGM and at present (thus can only be generated for areas affected by sea ice), TF-based LGM-WSSTs are available from the modern Subantarctic area, all generated from planktic foraminifer records (Luz, 1977; Sikes et al., 2002; Barrows and Juggins, 2005, Kucera et al; 2005b) (Fig. 3.6b, Table S3.2). Although representing only small data sets, the combination of both yields a consistent pattern of LGM-WSST suggesting a distinct northward expansion of the Antarctic cold-water realm in both, the western and eastern Pacific sectors of the Southern Ocean. The TF-based LGM-WSSTs imply that the location of the zone of enhanced SST gradients recorded in close relation to the northern Campbell Plateau-Bounty Trough area and around 45°S at the East Pacific Rise remained stable during LGM summer and winter. Considering the apparent seasonal stability of its location and the related distinct SST shift from ca. 4-5°C to ca. 12-16°C in LGM summer and from ca. 2-3°C to ca. 8-12°C in LGM winter we propose to name the zone the Glacial Southern Subtropical Front (GSSTF). Although the modern STF, characterized by a SST shift from ca. 11° to 18°C (Belkin and Gordon, 1996; also see Fig 3.1b, c for SST-STF relationship) is placed north of our GSSTF, according to Orsi et al. (1995) (Fig. 3.1), we think that the distinct increase from values characteristic of temperatures around the modern APF to SSTs >11°C warrants such designation. South of the GSSTF, in the glacial POOZ, the SST-seasonality is assumed to range between 2 and 3°C, which is similar to the SST seasonality in the modern POOZ (Fig. 3.1b, c). Around the glacial WSI edge the SST-seasonality displays lower values, that do not exceed 2°C, resembling the seasonality in the modern seasonal Sea Ice Zone.

3.5.2   Last glacial sea ice in the Pacific Southern Ocean sector

Our reconstruction of E-LGM-WSI concentration substantiates former reconstructions of the WSI extent during the LGM, which were based on a smaller and less representative set of sample sites and less established dating (CLIMAP, 1981; Cooke and Hays, 1982; Crosta et al., 1998a, b; Gersonde et al., 2005). In general, our findings are close to the former reconstructions placing the maximum extent of the LGM winter sea-ice field to a latitude north of 60°S in the western Pacific sector and to ca. 60°S in the eastern sector (Gersonde et al., 2005) (Figs. 3.6a, 3.7). However, our reconstructions document more precisely the distribution of the average sea-ice edge during the last glacial winter locating this edge around 60°S, and suggest a close relationship with bottom topography in the area of the Pacific-Antarctic Ridge. Our interpretation of a rather variable extent of the WSI in the northern Amundsen-Bellingshausen Sea is supported by former data presented by Crosta et al. (1998a, b) and summarized in Gersonde et al. (2005). The finding of a northward expansion of the LGM-WSI field by ca. 5° in latitude, relative to modern conditions (Fig. 3.6), is corroborated by bromine depletion measurements from the Talos Dome ice core (TALDICE) recovered in the Ross Sea sector of East Antarctica (72°49´S, 159°11´E) interpreted to indicate a ~500 km farther north located sea-ice edge (Spolaor et al., 2013).

Our study does not provide new data concerning the extent of the LGM-SSI which hampers estimations of LGM sea-ice seasonality in the Pacific Southern Ocean sector as this has been proposed for the Atlantic and Indian sectors (Gersonde et al., 2005). The yet only estimation of LGM-SSI extent in the Pacific sector was presented by CLIMAP (1981) suggesting that perennial sea-ice field covered the Pacific Southern Ocean during the LGM as far north as 60°S. CLIMAP (1981) reconstructed the SSI extent using the boundary between silty diatomaceous clay and diatom ooze, assumed to mirror the 0°C isotherm (Hays et al., 1976). However, such relationship is not supported by findings of Burckle et al. (1982) who related the shift in sedimentary facies with the late spring sea-ice extent, a pattern supported by the comparison of sea-ice extent data and biogenic opal deposition in surface sediments showing a close relationship to the extent of the winter-spring sea-ice field (Geibert et al., 2005). The CLIMAP (1981) scenario would imply that seasonal variability in sea-ice extent was strongly decreased or nearly absent during the LGM, thus in strong contrast to modern conditions. Decreased or absent sea-ice variability would not be in favor of the generation of deep and bottom water in the SO, assumed to be mainly generated by sea-ice related salt injection during the glacial (Schmittner, 2003; Shin et al., 2003). Although we have no clear

data on the LGM-SSI extent in the Pacific sector, the scenario proposed by CLIMAP (1981) appears unlikely and it would be in contrary to findings from the Atlantic and Indian sectors, which point to distinctly increased seasonal variability in the LGM sea-ice extent (Gersonde et al., 2005).

Interestingly, we observe in last glacial sediments, recovered at the Pacific-Antarctic Ridge from water depths between ~2900-3800 m (PS75/072-4, PS75/073-2, PS75/085-1) (Fig. 3.1), the presence of well-preserved planktic foraminifers (*N. pachyderma*$_{sin}$). This occurrence is reflected by increased calcite counts in the XRF-records (Fig. S3.3). The sites were affected by seasonal sea ice during the LGM and glacial sedimentation rates are strongly decreased (Figs. 3.2, 3.6). Since the foraminifers from the glacial sections allowed the establishment of decent oxygen isotope records and AMS^{14}C measurements (Fig. 3.2, Table 3.3), it appears unlikely that they have been reworked from older sediments. *Neogloboquadrina pachyderma*$_{sin}$ is the only known foraminifer adapted to dwell in or close to sea ice (e.g. Spindler and Dieckmann, 1986), thus potentially presents an additional indicator of past sea-ice occurrence. Specimens recorded from antarctic sea ice comprise specific morphotypes. They mainly represent juvenile and subadult *N. pachyderma*$_{sin}$ stages, lacking typical adult morphological features such as compact, thick walled tests with more or less quadrate shape (Spindler and Dieckmann, 1986; Berberich, 1996). Microscopic inspection reveals that the specimens preserved in our records are typical adult stages, thus lack the morphological features, indicative for specimen retrieved from sea ice. As such, the preserved *N. pachyderma*$_{sin}$ cannot be used as indicator of sea-ice occurrence, however it cannot be excluded that the specimen were part of the sea-ice community at an earlier stage of their life cycle.

3.5.3   The Pacific sector as part of the glacial Southern Ocean and beyond

Our new set of data from the Pacific sector fills a critical gap in the documentation of Southern Ocean surface parameters (temperature and sea ice) during the LGM, as requested e.g. by Gersonde et al. (2005). This allows for a more detailed evaluation of Southern Ocean basin-basin differentiations and exchange pattern, mechanisms controlling surface ocean parameters and their distribution, as well as the discussion of the impacts on southern-low latitude exchange processes and atmosphere-ice related impacts or feedbacks. The new data are also useful to further validate LGM scenarios derived by numerical modeling.

The combination of our Pacific SST data compilation with the data presented by Gersonde et al. (2005) from the Atlantic and Indian sectors of the Southern Ocean reveals a distinct cooling in all Southern Ocean sectors during the last glacial. This is in contrast to Gersonde et al. (2005), who assumed that the LGM cooling was less developed in the Pacific sector, a view that was however based on a limited number of data. Circum-Antarctic cooling was strongest (>4 K) in the area of the modern SAZ, except for the Indian sector where strongest cooling extends into the area of the modern Subtropical Zone (Fig. 3.8). The 4°C isotherm, which represents the SSST at the modern APF, was shifted northward by >10° in latitude north of the Ross Sea, reaching a latitude close to 45°S in the area of Campbell Plateau, straddled at present by the STF (Fig. 3.1). This locates the 4°C isotherm at a latitude similar to the Atlantic and Indian sectors, but in both sectors this area is in the vicinity of the modern SAF or the southern SAZ (Gersonde et al., 2005). Such pattern suggests that the strongest northward stretching of the Antarctic cold-water realm (SSST <4°C) during the LGM occurred in the sector north of the Ross Sea. In the eastern Pacific sector of the Southern Ocean the 4°C isotherm is located further to the south, around 55°S (Fig. 3.5a). Such asymmetric pattern of the LGM-ACC in the Pacific sector is comparable to modern conditions in the SE Atlantic sector, where the northward extension of the Malvinas-Falkland Current yields a distinct protrusion of antarctic colder waters belonging to the Subantarctic Zone temperature regime (Orsi et al., 1995; Sokolov and Rintoul, 2009).

In the Pacific sector the northward enlargement of the winter sea-ice field (concentration >40%) by ca. 4 – 5° in latitude was less developed compared to the displacement of the average winter sea-ice edge in the Atlantic and Indian sectors, where the data presented by Gersonde et al. (2005) suggest a shift by up to 10° in latitude (e.g. in the Indian sector) during the LGM. Also CLIMAP (1981) presented stronger winter sea-ice expansion in the Atlantic and Indian sectors. Considering that the CLIMAP (1981) estimate of the last glacial extent summer sea-ice field is rather unlikely, the seasonal SIZ was strongly expanded during the LGM, as documented by Gersonde et al. (2005), Allen et al. (2011) and Collins et al. (2012).

The Southern Ocean areas governed by large clockwise circulating cold-water gyres, the Ross Gyre in the Pacific sector and the Weddell Gyre in the Atlantic sector, display a similar cooling pattern (Fig. 3.7). For the Atlantic sector, Gersonde et al. (2005) postulated a (sporadical) extended summer sea-ice field related to an extended LGM Weddell Gyre. Potentially, but not proved by data, a similar pattern was also established in the Ross Sea sector.

Because of the lack of appropriate sediment records our study cannot include data on sea surface temperature and sea-ice extent in the Drake Passage. Such data are critical because the Drake Passage represents the connection pathway between the Pacific and the Atlantic sector and constitutes, besides the deep Tasmanian pathway, the second bottleneck of antarctic circumpolar circulation shaping the structure of the ACC, which plays a crucial role in global overturning circulation. However, our data from the east Pacific together with findings from the Scotia Sea (Collins et al., 2012) allow for a rough assessment of the SST and sea-ice regime established during the last glacial in this region, thus the ACC structure during the last glacial. Considering that maximum temperatures of surface water entering the Drake Passage do not exceed 4°C it can be suggested that the ACC did not include surface waters with temperatures exceeding those established during austral summer at the modern APF. This is in contrast to modern conditions with ACC surface temperatures including the PFZ temperature regime and beyond. Considering the presence of cold surface temperatures (<4°C) and the extended winter and summer sea-ice fields in the Scotia Sea (Collins et al., 2012), it can be speculated that the LGM winter sea-ice field covered a large portion, but not the entire Drake Passage. The winter sea-ice edge may have been related to the extent of a zone (reaching up to 58°S) with LGM flow speeds lower than present, while north of this zone LGM flow speeds were similar or slightly faster compared with modern conditions (McCave et al., 2014). A larger expansion with possibly total coverage of the Drake Passage during winter can be deduced from the sea-ice reconstructions in the Scotia Sea (Collins et al., 2012) for a period pre-dating the LGM (31 – 23.5 cal. kyr BP), which falls into the period of strongest last glacial southern high-latitude cooling according to ice core (EPICA Community Members, 2004; WAIS Divide Project Members, 2013) and marine (Gersonde et al. 2003a, b; Crosta et. al., 2004) records.

The northward deflection of waters >4°C into the coastal current (Humboldt Current) off western South America led to distinct colder ACC temperatures compared with the temperature regime governing the modern ACC. It can be speculated that the enhanced cooling observed in the Atlantic and Indian sectors is closely related to the injection of colder waters via the Drake Passage, which intensified the thermal isolation and cooling of the Southern Ocean and Antarctic continent during the last glacial.

Sea surface temperature reconstructions have been used to delineate past locations and displacements of specific oceanic fronts, such as the APF and the SAF, assuming that the temperature settings of past frontal systems is similar to modern settings (e.g. Govin et al., 2009; Bostock et al., 2013; Ho et al., 2012). Such reconstruction may lead to questionable

results because (1) the proper definition of modern fronts is not only related to water temperature or temperature gradients at the oceans surface (e.g. Orsi et al., 1995; Belkin and Gordon, 1996; Sokolov and Rintoul, 2009), (2) the relatively low sample spacing makes it difficult to depict accurately SST gradients in the paleorecord, especially in regions were the location of frontal systems is subject to strong seasonal or interannual variability, and (3) past oceanic fronts may be characterized by parameters different from modern conditions. However, these restrictions do not preclude estimations of the occurrence and location of past
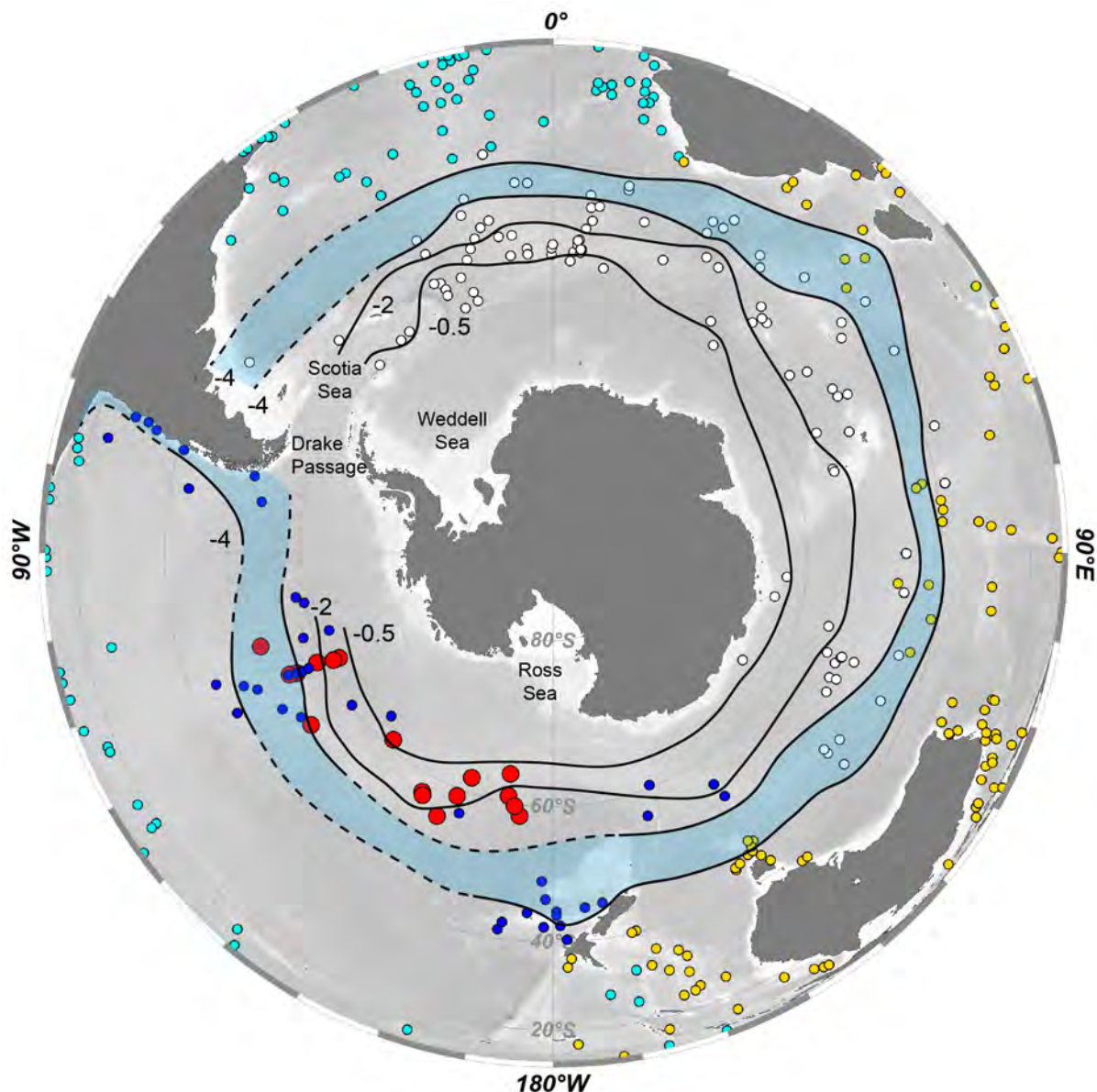

Figure 3.8: Compilation of available reconstructed SSST anomalies (E-LGM/modern) in the Southern Ocean and adjacent lower latitude areas (red: new data presented in this study; dark blue: see Tab. 3.1, S3.2; yellow: Barrows and Juggins, 2005; light blue; Kucera et al., 2005b; white: Gersonde et al., 2005). Isotherms in °C; areas with anomalies >4 K shaded in blue.

oceanic fronts, e.g. when zones of enhanced SST-gradients can be pinpointed, when isotherms are closely related to bottom topography or when sedimentological records allow for the identification of zones with different flow speeds. Hypothetically we suggest the presence of an oceanic front close to the winter sea-ice edge where SSST range around 1°C, and a front at the northern boundary of the glacial ACC, where SSST are on average 4°C (Figs. 3.5, 3.6, 3.7). The front close to the glacial sea-ice edge would be comparable to the modern SACCF, which bounds the Antarctic sea-ice field to its north. Similar to the modern APF, which is in the area of the glacial SACCF, its location in the western Pacific Southern Ocean sector would be relatively stable as a result of topographic forcing (Pacific-Antarctic Ridge). In the eastern sector the front would cross the abyssal plain of the Amundsen and Bellingshausen seas and the lack of topographic forcing could infer stronger dependency on atmospheric forcing, making its location less stable. Such pattern is documented by our data, suggesting a rather stable location of the WSI edge in the area affected by topographic forcing and a more instable edge in the eastern sector (Fig. 3.6). In the Drake Passage and the southern Scotia Sea the glacial SACCF could be related to the zone of changing ACC flow speed reported by McCave et al. (2014). In the Atlantic sector of the Southern Ocean and to less extent also in the Indian sector a glacial front comparable to the modern SACCF would be located at a more northern latitude considering the pattern of the glacial winter sea-ice edge as reported by Gersonde et al. (2005). The northern boundary of the glacial ACC should also be represented by an oceanographic front, as it is true for the modern ACC bounded to its north by the SAF (Orsi et al. 1995; Sokolov and Rintoul, 2009). The surface water temperature regime at such front can be placed around 4°C, which is equivalent to the SSST at the modern APF. While in the Pacific sector the 4°C summer isotherm is well separated spatially from the northern sea-ice edge (Figs. 3.5, 3.6), reconstructions from the Atlantic and Indian sectors (Gersonde et al., 2005) suggest a closer occurrence of both surface ocean parameters. This may infer stronger meridional and seasonal temperature gradients in the Atlantic and Indian zone adjacent to the Antarctic winter sea-ice field compared to the Pacific sector in the last glacial. The occurrence of a front characterized by SSSTs similar to that of the modern APF may be interpreted as indication of a northward displacement of the APF during the glacial. Such displacement has been corroborated by an experiment with a fully coupled global atmosphere-ocean general circulation model (AOGCM) resulting in a latitudinal shift of 5-7° in latitude in the glacial Atlantic sector (Abelmann et al., 2015). The experiment defined the front as 2°C isotherm of the averaged temperature between 100-300 m of water, which represents a commonly used oceanographic definition of the modern APF

(Belkin and Gordon, 1996). Our data suggest a similar displacement in the eastern Pacific sector (Figs. 3.5, 3.7). In the western sector a stronger displacement would place the 4°C front as far north as into the area of Campbell Plateau. Reaching its northernmost location in the glacial Southern Ocean the 4°C front would abut on the GSSTF which marks the boundary to warmer subtropical surface waters in the glacial ocean. A similar cold-water protrusion with cold and warmer water frontal systems narrowing each other can be observed in the modern Southern Ocean in the area of the Falkland Plateau (Orsi et al., 1995; Sokolov and Rintoul, 2009). The glacial expansion of the Antarctic cold-water sphere resulted in enhanced temperature gradients in the zone, which adjoins the warm Southern Hemisphere subtropical gyres. Although these gyres were slightly contracted during the glacial, their position remained relatively stable and they experienced only minor cooling by <2 K (e.g. in the South Atlantic) or became even warmer than present (by 1-2 K) in the South Pacific as suggested by the few available data points (MARGO Project Members, 2009). While in the Pacific sector we could delineate the presence of a glacial front, the GSSTF, characterized by SST gradient of ca. 5-10°C during summer (Fig. 3.5), in the Atlantic and Indian sectors such front was not discerned based on the available data (Gersonde et al. 2005). However, also in these SO sectors the SST gradients in the zone south of the gyres driven by subtropical highs were distinctly increased during the last glacial (Gersonde et al., 2005). Such steepening in gradients may enhance atmospheric flow and thus ocean current velocities in this zone. Modeling of the last glacial Southern Hemisphere wind fields (four PMIP2 simulations) provides mixed results for surface wind speeds compared with modern (pre-industrial) conditions (Rojas et al., 2009). Two simulations suggest an overall decrease in summer and winter surface wind speeds (HadCM3, IPSL), one shows no change or a slight increase (MIROC3.2.2) and one (CCSM3) results in an increase, especially during austral winter (up to 5 m/s). Interestingly, the CCSM3 simulation is the only one that considers a pattern of glacial SSST anomalies (up to 5°C cooling in the modern subantarctic realm) similar to the anomalies reconstructed with proxies (Fig. 3.8). However the CCSM3-based WSI concentration presents a slightly overestimated sea-ice extent in comparison with our proxy data.

As outline above, in areas with absent bottom topographic forcing, e.g. over abyssal plains in the eastern Pacific Southern Ocean sector, mesoscale activity (e.g. eddies, filaments) and atmospheric forcing may impact the location and variability of frontal systems (Sallée et al., 2008; Sokolov and Rintoul, 2009) and the extent of the sea-ice field. Wind fields, oceanic frontal systems, circulation, upwelling and sea-ice variability in the modern Southern Ocean

are closely linked to the SAM and ENSO, presenting most important modes of atmospheric forcing over the Southern Hemisphere (e.g. Thompson and Wallace, 2000; Yuan, 2004; Lefebvre et al., 2004; Sallée et al., 2008; Turner et al., 2009; Thompson et al., 2011). While SAM explains up to 30% of atmospheric pressure variability in the Southern Hemisphere (Thompson and Wallace, 2000) the tropical Pacific phenomenon ENSO exerts its impact via teleconnections (Trenberth et al., 1998). Although numerical simulations suggest an overall weaker SAM amplitude during the LGM, which would entrain a weaker Southern Hemisphere vortex and Southern Westerly Winds (Kim et al., 2014), we suggest that the variability in winter sea-ice extent observed in the eastern Pacific sector (Fig. 3.6) may be related to fluctuating atmospheric forcing mechanisms, such as the SAM. Indeed, the model-derived assumptions of weaker SAM variability and related weaker ACC velocity during the LGM are contrasted by proxy data on the ACC flow speed indicating similar or faster ACC flow north of the glacial winter sea-ice field (McCave et al., 2014). However, most recent data indicate a strong decrease of the northernmost (subantarctic) ACC pathway entering the Drake Passage during the glacial (Lamy et al., 2015).

Another mechanism having potential to stimulate an enlargement of the sea-ice field in the eastern Pacific Southern Ocean is linked to effects by cold ENSO (La Niña) events (Yuan, 2004). However, estimates of ENSO variability in the LGM yield contrasting results. For instance, model and proxy-based reconstructions show either increased (e.g. Otto-Bliesner et al., 2003) or decreased ENSO variability (e.g. Leduc et al., 2009; Ford et al., 2015), as well as indications for more El Niño-like (e.g. Koutavas et al., 2002) or La Niña-like conditions (e.g. Rincón-Martínez et al., 2010; Staines-Urías et al., 2015). Our reconstruction of advection of cold waters from the ACC via the Humboldt Current to the eastern equatorial Pacific represents a feasible mechanism for a more La Niña-like state in LGM.

In the glacial Atlantic sector the zone of maximum opal deposition ("opal belt") is shifted northward and deposition rates remain to modern deposition (Frank et al. 2000). This pattern suggests a northward displacement of the Ekman upwelling zone and thus of the glacial Southern westerlies. A similar northward shift of the westerlies in the South Pacific realm is in line with proxy-based studies e.g. by Stuut and Lamy (2004), Heusser et al. (2006) and summarized by Kohfeld et al. (2013), who suggest either the strengthening or an equatorward shift of the Southern Westerlies as the most likely glacial scenarios. Our data do not allow to trace the pattern of biogenic opal deposition in the glacial Pacific sector in detail, but previous work based on ^{230}Th-normalized biogenic opal flux rates documents a decrease

in glacial opal flux in the zone south of the modern APF (Chase et al., 2003; Bradtmiller et al., 2009), thus in the zone affected by glacial winter sea ice (Fig. 3.6). Enhanced glacial opal burial is reported from the area north of the modern APF (Chase et al., 2003; Bradtmiller et al., 2009, Lamy et al., 2014). The sedimentation rates in our cores (Figs. 3.2, 3.4) indicate a distinct glacial increase in the area north of the average winter sea-ice edge in the eastern Pacific sector (Figs. 3.2, 3.4) which is in concert with increased opal flux data presented by Bradtmiller et al. (2009) from the same area. In contrast, cores located in the modern POOZ generally display reduced or strongly decreased sedimentation rates (Figs. 3.2, 3.4). This provides indication of a northward shifted opal belt during the glacial, but in contrast to the Atlantic sector, the available flux data point to a relative decrease in glacial opal burial in the Pacific sector (Chase et al., 2003; Bradtmiller et al., 2009). This finding has been related to decreased glacial iron fertilization in the Pacific sector as well as to ice cover and the related length of the growing season (Chase et al., 2003). Bradtmiller et al. (2009) speculate that the relatively low opal burial is indicative of a mechanism called "Silicic Acid Leakage Hypothesis" (SALH), which predicts that during glacial excess silicic acid was exported from the Southern Ocean to lower latitudes. In the absence of satisfactory evidence that silica originating in the Southern Ocean has been buried in equatorial sediments, Bradtmiller et al (2009) suspect that the silica export is possibly mirrored in continental margin deposits. Indeed, the study of sediment cores from sites off Chile (southern Humboldt current) points to increased glacial deposition of biogenic silica, interpreted to reflect enhanced availability of silicic acid (e.g. Hebbeln et al., 2002; Romero et al., 2006; Chase et al., 2014). However, a stable isotope-based evaluation of the nature of opal deposition off Peru is not supportive of a glacial advection of silicic acid from the Southern Ocean as far north as the Pacific equatorial latitudes (Ehlert et al., 2013).

Numerical simulations of last glacial SST and sea-ice conditions in the Pacific sector of the Southern Ocean result in a large range of scenarios. While some simulation match relatively well our proxy-based results, others display pictures that are less realistic, when compared with our data. Out of four PMIP2 simulations presented by Rojas et al. (2009), three show generally too warm temperatures in the Pacific sector of the Southern Ocean resulting in lower LMG/modern anomalies than the proxy records. The simulation with CCSM3 reproduces well the strongest summer cooling (>4 K) in the modern SAZ, which is close to the cooling inferred from proxy data (Fig. 3.8). However, the CCSM3 glacial winter SSTs display in part unrealistic data. A cooling up to 5 K in the glacial SIZ thus in an area with modern winter SSTs between -1° to -1.8°C (Fig. 3.1b, c) is not feasible. Another model-

data synthesis reveals a similar distribution of strongest cooling areas as CCSM3 (Annan and Hargreaves, 2009). However, the simulation with a fully coupled global atmosphere-ocean general circulation model (AOGCM) by Zhang et al. (2013) represent the most reliable reconstruction compared to our results, displaying a well established zonal cooling in the modern SAZ and the cold-water deflection along the South American continent. The simulated sea-ice concentrations by Paul and Schäfer-Neth (2005) reveal a qualitatively similar pattern as our diatom-based reconstructions with a more northward extent of WSI in the eastern Pacific sector and a sea-ice edge following the topography in the western sector. Nevertheless, the expansion of the average WSI edge (40% concentration) is overestimated by ~5° in latitude. The estimated SSI extent may be in line with the latitudinal 5° shift of the cold-water realm during the LGM summer. Coupled climate model studies of sea-ice extent in both seasons reveal strongly variable results among the applied models. In general, the different studies based on the same model configurations show relatively similar results (Rojas et al., 2009; Roche et al., 2012; Goosse et al., 2013). However, the estimations obtained with different simulation techniques range from massive overestimation of WSI and SSI (e.g. FGOALS, LCM12, CCSM) to sea-ice field simulations that are close to the proxy results (IPSL, HADCM). Yet, small deviations are obvious in the Pacific sector. While the WSI reconstructions of Goosse et al. (2013) mirror well the influence of topography in the western Pacific sector, the simulations presented by Roche et al (2012) strongly overestimate the sea-ice extent in the eastern sector. The most recent sea-ice simulations presented by Zhang et al. (2013, AOGCM) and Ballarotta et al. (2013, OGCM NEMO) show a similar overestimation of the WSI edge, especially in the eastern Pacific sector and the Drake Passage. For example, the reconstructed 90% WSI edge from Zhang et al. (2013) is coherent with our proxy based 40% WSI edge. The simulation in Ballarotta et al. (2013) shows an almost identical SSI and WSI extent, similar to the outcome of four models (FGOALS, CCSM, LCM12, ECBILT) presented by Roche et al. (2012). Our SSST estimates for the area with SSI coverage according to the model results show discrepancies e.g. SSI at SSST >0°C which make the model-based reconstruction rather unrealistic. The overestimation of sea ice in models might be related to problems in reproducing the stability and stratification of the water column necessary for sea-ice formation (Goosse et al., 2013). Also crucial for modeled sea-ice results is the resolution to precisely represent the dynamical interactions between ocean and atmosphere as well as the model simulation of winds that drive sea-ice distribution (Roche et al., 2012).

3.6   Conclusions

Our study of diatom-derived summer sea surface temperature and winter sea-ice concentrations from the Pacific sector of the Southern Ocean contributes to a coherent circum-Antarctic picture of temperature and sea-ice distribution during the LGM. Combined with previous studies from the Pacific Southern Ocean, our reconstructions show a consistent pattern of latitudinal zonation that mirrors similar findings from the Atlantic and Indian sectors. The northward shift of the cold-water realm and the associated deflection of water masses >4°C into the Humboldt Current eventually led to distinct cooling in the modern Antarctic Zone. The transport of such cold-water masses (<4°C) through the Drake Passage resulted in significant cooling of the Atlantic and Indian Southern Ocean sectors. This finding shows that the glacial cooling in the Southern Ocean was particularly influenced by the water masses of the ACC and the signal propagation via the exchange routes between the different Southern Ocean sectors.

Our results indicate that the influence of topographic forcing documented by the isotherm and sea-ice trends during the LGM inhibits the determination of frontal movement solely based on colder SSTs. As such, the frontal system in the ACC was most likely characterized by different physical parameters compared to its modern equivalent. Definite frontal assignments in the LGM may thus only be possible in zones with distinct latitudinal temperature gradients or in areas with significant boundary conditions like the sea-ice edge. In the latter case, the Glacial Southern Antarctic Circumpolar Current Front (GSACCF) represents further the southern limit of the glacial opal belt, indicating enhanced glacial opal deposition in the Pacific sector at a more northern position, similar to the Atlantic sector. This displacement is probably induced by equatorward shifted Westerlies and corresponding Ekman upwelling.

Though closing a prominent gap in Southern Ocean LGM reconstructions, more information has to be gained from the Indian sector, the Drake Passage and the Pacific Subantarctic Zone. Furthermore, despite the availability of a transfer function for summer sea-ice concentration (Esper and Gersonde, 2014a), the reconstruction is still hampered by dissolution and low sedimentation rates. Better knowledge of LGM sea-ice seasonality would enhance our understanding of deep and bottom water formation and its impact on CO_2 sequestration in the glacial Southern Ocean. Besides some relatively congruent modeled LGM reconstructions compared to the proxy estimates, most available coupled climate models show distinct discrepancies. The new data and reconstructions provide an improved

database to test the reliability of future coupled climate models focusing on E-LGM temperature and sea-ice concentration. Our estimates may also be helpful for improved modeling of the Southern Westerly Wind belt and the associated changes in ACC flow speed. As such, velocity data from the ACC in the Southern Ocean are urgently needed to decipher ocean-atmosphere feedbacks.

3.7　Acknowledgments

Supplementary data to – Last Glacial Maximum sea surface temperature and sea-ice extent in the Pacific sector of the Southern Ocean
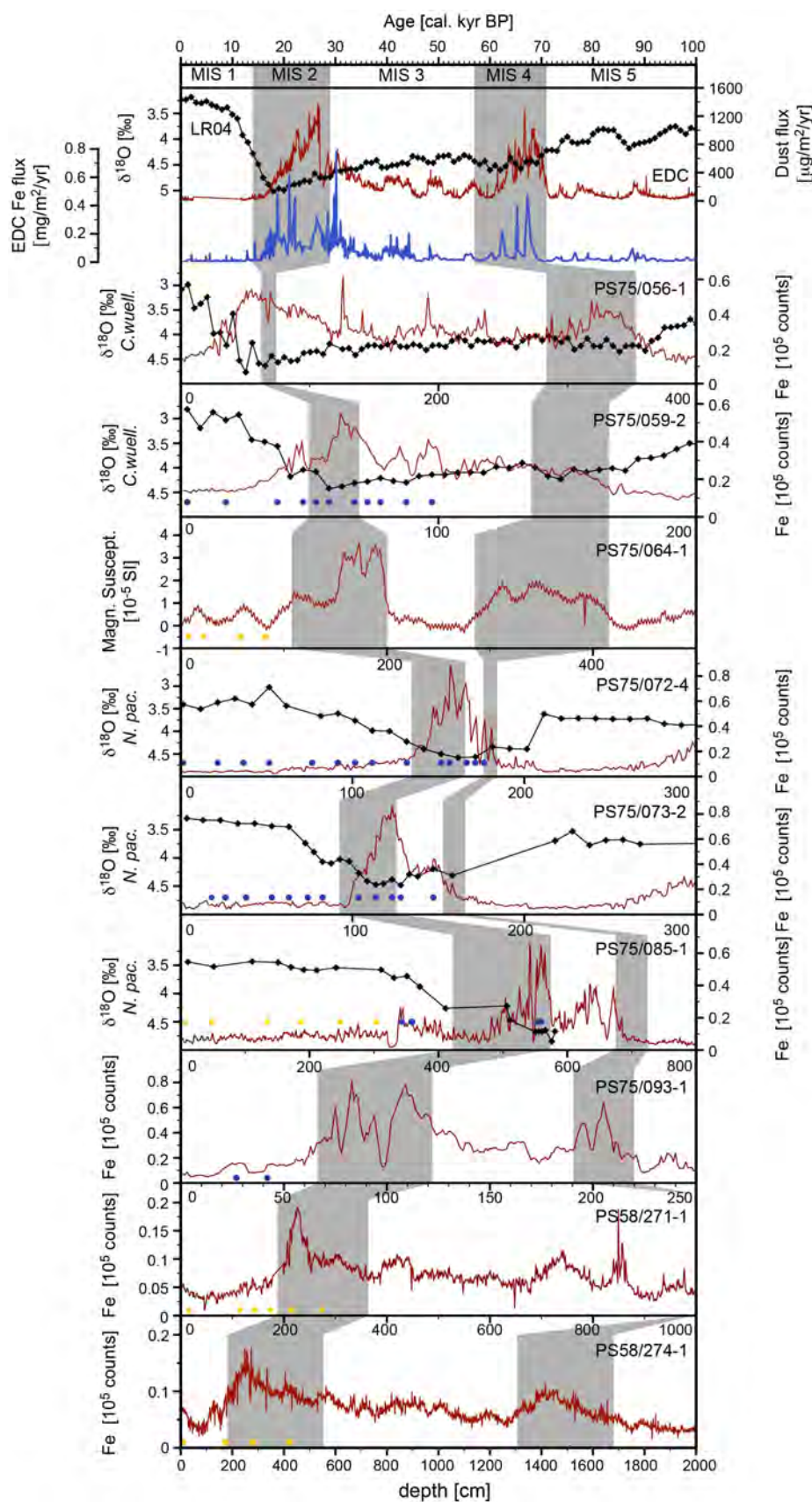
Figure S3.1: Unaligned iron content fluctuations (red), benthic and planktic oxygen isotope records (black) and depths of radiocarbon measurements (yellow circles: humic acids, blue circles: foraminifera) of reference cores compared to the LR04 stack and associated Marine Isotope Stages (MIS) 1-5 (Lisiecki and Raymo, 2005), dust and iron fluxes from the EPICA Dome C (EDC) ice core (dust: Lambert et al., 2008; iron: Martínez-Garcia et al., 2009; AICC12 age scale: Bazin et al., 2013; Veres et al., 2013; EDC3 age scale: Parrenin et al., 2007); E-LGM: EPILOG Last Glacial Maximum time slice. Scale extended to 100 cal. kyr BP to show glacial-interglacial variability.
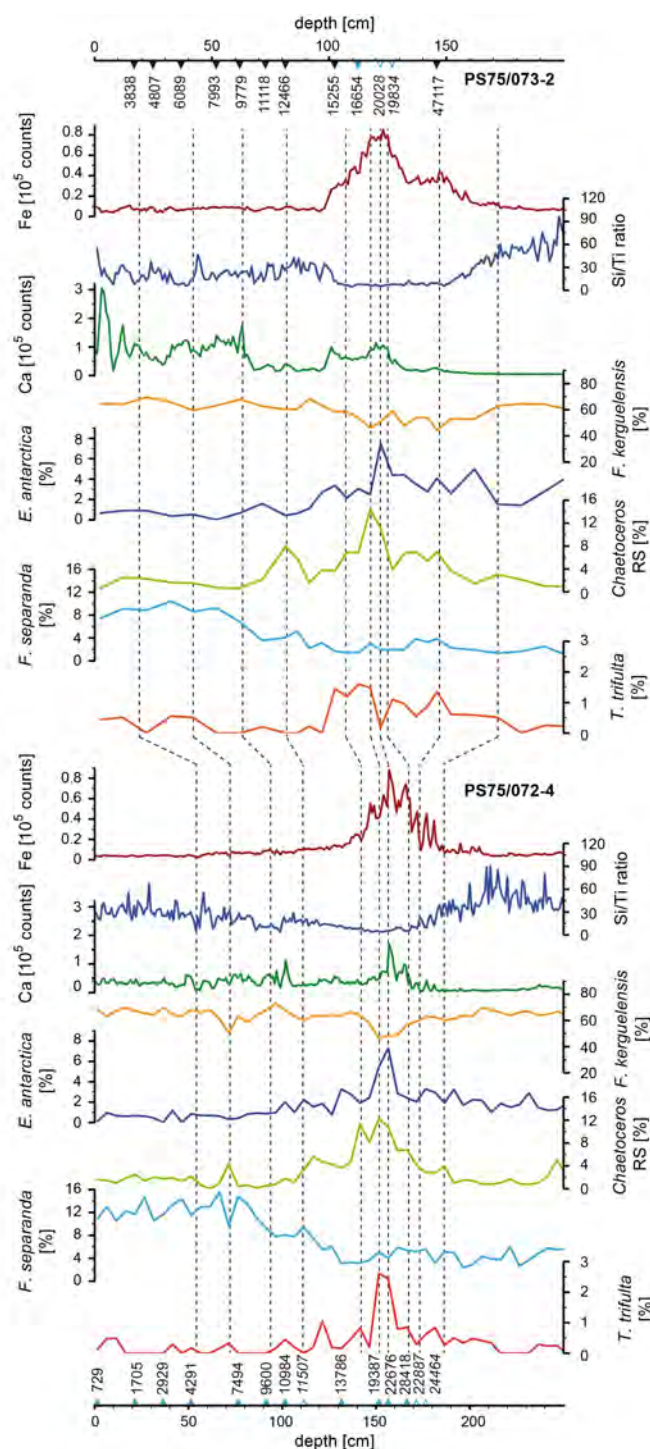
Figure S3.2: Correlation of core PS75/072-4 (lower panels) to PS75/073-2 (upper panels) on depth scale with correlation lines based on XRF element analysis and diatom percentages with corresponding calibrated ^{14}C ages obtained from conventional AMS^{14}C datings (black triangles) and small sample datings (blue triangles).

The age model of core PS75/072-4 based on small sample datings resembled the core-to-core correlation. Thus AMS^{14}C datings with less than 100μg carbon from foraminiferal carbonate serve as alternative to conventional AMS^{14}C datings in diatomaceous sediments with less carbonate concentration. Open triangles and italic numbers represent datings that where rejected due to unreliable ages based on the depth correlation as well as on unlikely high sedimentation rates (see Table 3.3). In core PS75/073-2 the oldest obtained age at 147 cm (47117 cal. kyr BP) exhibits a large error (4000 yrs, see Table 3.3) yet is not completely deviant as Marine Isotope Stage (MIS) 2 is highly condensed. This is particularly visible in the Si/Ti ratio that is indicative for less opal productivity and/or burial. The increasing Si/Ti rate in core PS75/073-2 at ~160 cm and in core PS75/072-4 at ~190 cm depth together with a distinct decrease in the iron counts is indicative for MIS 5.1.
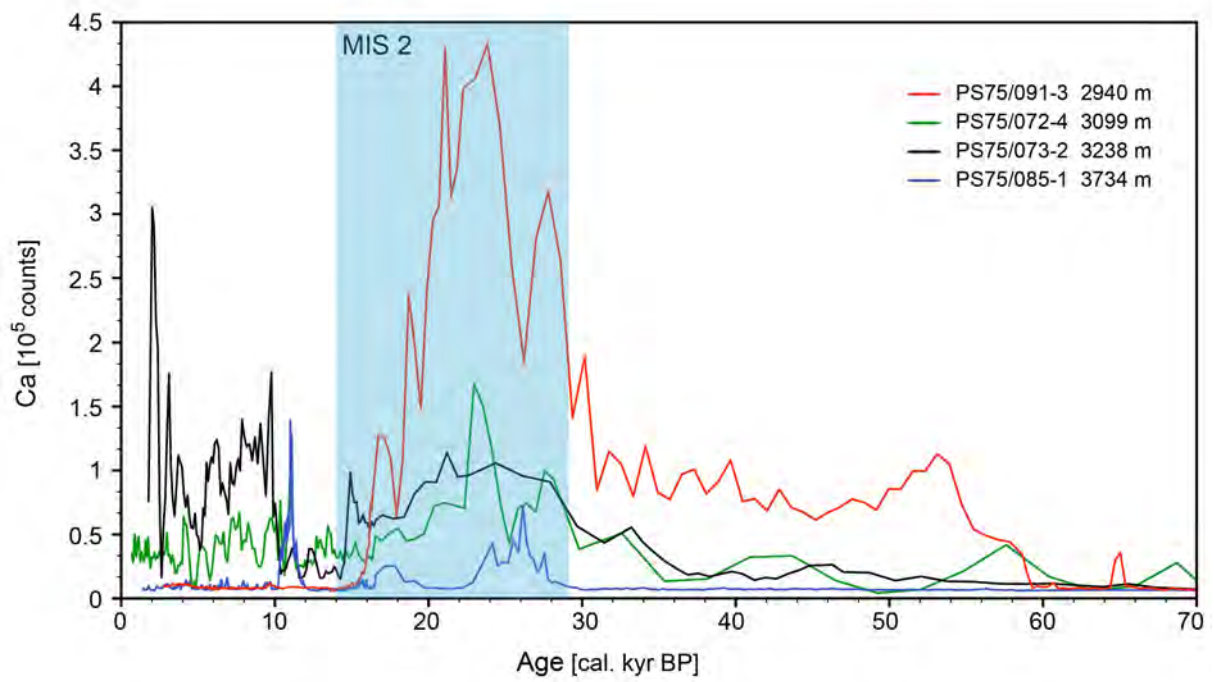
Figure S3.3: XRF Ca counts from 4 cores located at the Pacific Antarctic Ridge exhibiting higher carbonate content in Marine Isotope Stage (MIS) 2.

Table S3.1 Startigraphic age control points; Fe, Ca, Si/Ti: Fe-Area, Ca-Area, Si/Ti ratio of XRF element analysis; Fkerg: *F. kerguelensis*; Eanta: *E. antarctica*; Chaet: *Chaetoceros* resting spores; SSST: summer sea surface temperature; LR04: Lisiecki & Raymo (2005); Mag.sus: Magnetic suceptibility; LOD: last occurence date; FOD: first occurence date. Biostratigraphy according to Zielinski and Gersonde (2002); EDC: EPICA Dome C ice core.

PS58/270-5

Core depth (cm)	Age (kyr)	Correlation
4	5.857	Fe with Fe PS58/271-1
67	7.264	Fe with Fe PS58/271-1
112	12.461	SSST with SSST PS58/271-1
142	18.923	Eanta/Fkerg with Eanta/Fkerg PS58/271-1
172	22.818	Eanta with Eanta PS58/271-1
248	30.626	Fe with Fe PS58/271-1
363	61.520	Fe with Fe PS58/271-1
391	66.985	Fe with Fe PS58/271-1
523	96.092	Fe with Fe PS58/271-1
602	113.140	Fe with Fe PS58/271-1
652	117.564	Fe with Fe PS58/271-1
692	124.928	Fe with Fe PS58/271-1
712	128.931	SSST with SSST PS58/271-1
742	132.212	LOD Rouxia leventerae
932	189.558	LOD Hemidiscus karstenii
1302	245.059	SSST with EDC δT
1412	280.805	LOD Rouxia constricta
1702	326.617	SSST with EDC δT
1832	342.103	SSST with EDC δT
1942	381.849	LOD Actinocyclus ingens
2012	404.900	SSST with EDC δT
2142	428.065	SSST with EDC δT
2282	470.337	SSST with EDC δT

PS58/271-1

Core depth (cm)	Age (kyr)	Correlation
15.5	6.218	[14]C humic acids
115	10.002	[14]C humic acids
142.75	10.981	[14]C humic acids
174	12.562	[14]C humic acids
215	15.946	[14]C humic acids
273	22.340	[14]C humic acids
391	28.613	Fe with EDC dust
690	39.558	Fe with EDC dust
902	45.750	Fe with EDC dust
1252	63.384	Fe with EDC dust
1369	70.908	Fe with EDC dust
1613	87.005	Fe with EDC dust
1962	113.215	SSST with EDC δT
2290	129.425	SSST with EDC δT
2370	139.093	SSST with EDC δT

Table S3.1 continued

PS58/274-1

Core depth (cm)	Age (kyr)	Correlation
8.5	3.368	[14]C humic acids
172.5	13.177	[14]C humic acids
278.5	19.036	[14]C humic acids
421.5	22.002	[14]C humic acids
566	30.329	Fe with EDC dust
677	35.070	Fe with EDC dust
1331	61.450	Fe with EDC dust
1585.8	71.714	Fe with EDC dust
2013	82.000	Fe with EDC dust
2065	84.575	Fe with EDC dust

PS75/051-1

Core depth (cm)	Age (kyr)	Correlation
5	7.780	Fkerg with Fkerg PS75/059-2
20	20.834	SSST/Fe with SSST/Fe PS75/059-2
35	42.231	Fe with Fe PS75/059-2
49	66.725	Fe/Ca with Fe/Ca PS75/059-2
73	77.418	Fe/Ca with Fe/Ca PS75/059-2
93	93.752	Fe with Fe PS75/059-2
163	137.868	Fe with Fe PS75/059-2
219	174.656	Fe with Fe PS75/059-2
259	192.839	Fe with Fe PS75/059-2
319	253.862	Fe with Fe PS75/059-2
373	277.335	Fe with Fe PS75/059-2
401	302.135	Fe with Fe PS75/059-2
443	349.441	Fe with Fe PS75/059-2
464	361.023	Fe with Fe PS75/059-2
575	408.117	Fe with Fe PS75/059-2
614	425.026	Fe with Fe PS75/059-2
629	430.717	Fe/Ca with Fe/Ca PS75/059-2
691	471.059	Fe with EDC dust
774	534.180	Fe with EDC dust
1391	628.550	Fe with EDC dust
1703	740.025	Fe with EDC dust
1788	795.225	Fe with EDC dust

PS75/054-1

Core depth (cm)	Age (kyr)	Correlation
1	9.314	Fe with Fe PS75/056-1
8	11.232	Fe with Fe PS75/056-1
25	12.514	Fe with Fe PS75/056-1
36	13.053	Fe with Fe PS75/056-1
52	17.070	Eanta/Chaet with Eanta/Chaet PS75/056-1
92	23.759	Eanta/Chaet with Eanta/Chaet PS75/056-1
232	34.068	Eanta with Eanta PS75/056-1

Table S3.1 continued

PS75/054-1

Core depth (cm)	Age (kyr)	Correlation
302	36.637	Fe with Fe PS75/056-1
611	40.747	Fe with Fe PS75/056-1
636	41.517	Fe with Fe PS75/056-1
744	45.755	Fe with Fe PS75/056-1
963	58.432	Fe with Fe PS75/056-1
1114	64.938	Fe with Fe PS75/056-1
1369	74.891	Fe with Fe PS75/056-1
1466	79.955	Fe with Fe PS75/056-1
1619	86.160	Fe with Fe PS75/056-1
1748	95.130	Fe with Fe PS75/056-1
1857	99.525	Fe with Fe PS75/056-1
2029	110.193	Fe with Fe PS75/056-1
2105	113.834	Fe with Fe PS75/056-1
2121	121.993	Fe with Fe PS75/056-1
2130	127.771	Fe with Fe PS75/056-1
2146	134.065	Fe with Fe PS75/056-1
2161	138.194	Fe with Fe PS75/056-1
2182	146.450	Fe with Fe PS75/056-1
2205	154.036	Fe with Fe PS75/056-1
2228	160.100	Fe with Fe PS75/056-1

PS75/056-1

Core depth (cm)	Age (kyr)	Correlation
3.75	5.512	SSST with SSST PS75/059-2
13.75	10.121	Fe/SSST/Chaet/$CaCO_3$ with PS75/059-2
26	12.299	Fe/Chaet/Fkerg/$CaCO_3$ with PS75/059-2
43.75	14.210	Eanta/Chaet/Fkerg with PS75/059-2
68.75	21.360	SSST/Eanta/Chaet with PS75/059-2
108.75	30.954	Eanta/Chaet with PS75/059-2
226	46.012	$\delta^{18}O$ with $\delta^{18}O$ PS75/059-2
359	72.232	$\delta^{18}O$ with $\delta^{18}O$ PS75/059-2
491	88.945	$\delta^{18}O$ with $\delta^{18}O$ PS75/059-2
581	103.594	$\delta^{18}O$ with $\delta^{18}O$ PS75/059-2
628	114.289	$\delta^{18}O$ with $\delta^{18}O$ PS75/059-2
690.5	131.485	$\delta^{18}O$ with $\delta^{18}O$ PS75/059-2
755.5	153.847	$\delta^{18}O$ with $\delta^{18}O$ PS75/059-2
836	184.354	$\delta^{18}O$ with $\delta^{18}O$ PS75/059-2
904	221.124	$\delta^{18}O$ with $\delta^{18}O$ PS75/059-2
963	251.833	$\delta^{18}O$ with $\delta^{18}O$ PS75/059-2
1001	256.759	$\delta^{18}O$ with $\delta^{18}O$ PS75/059-2

PS75/059-2

Core depth (cm)	Age (kyr)	Correlation
0	0	$\delta^{18}O$ with LR04
2.5	3.722	^{14}C F_{bull}
17.5	7.078	^{14}C F_{bull}

Table S3.1 continued

PS75/059-2

Core depth (cm)	Age (kyr)	Correlation
37.5	11.759	^{14}C F$_{bull}$
47.5	13.302	^{14}C F$_{bull}$
55	15.572	^{14}C F$_{bull}$
67.5	28.727	^{14}C F$_{bull}$
80	32.207	^{14}C F$_{bull}$
97.5	38.686	^{14}C F$_{bull}$
140	58.774	Fe with EDC dust (Lamy et al., 2014)
163	70.203	Fe with EDC dust (Lamy et al., 2014)
238	87.114	Fe with EDC dust (Lamy et al., 2014)
316	104.967	Fe with EDC dust (Lamy et al., 2014)
344	115.408	Fe with EDC dust (Lamy et al., 2014)
395	130.385	Fe with EDC dust (Lamy et al., 2014)
412	137.868	Fe with EDC dust (Lamy et al., 2014)
442	149.604	Fe with EDC dust (Lamy et al., 2014)
695	251.833	Fe with EDC dust (Lamy et al., 2014)
796	281.102	Fe with EDC dust (Lamy et al., 2014)
821	297.446	Fe with EDC dust (Lamy et al., 2014)
866	309.857	Fe with EDC dust (Lamy et al., 2014)
905	334.303	Fe with EDC dust (Lamy et al., 2014)
962	355.875	Fe with EDC dust (Lamy et al., 2014)
1048	379.175	Fe with EDC dust (Lamy et al., 2014)
1092	391.584	Fe with EDC dust (Lamy et al., 2014)
1225	411.043	Fe with EDC dust (Lamy et al., 2014)
1283	424.394	Fe with EDC dust (Lamy et al., 2014)
1307	431.981	Fe with EDC dust (Lamy et al., 2014)
1342	452.646	Fe with EDC dust (Lamy et al., 2014)
1387	472.435	Fe with EDC dust (Lamy et al., 2014)

PS75/064-1

Core depth (cm)	Age (kyr)	Correlation
7.5	2.295	^{14}C humic acids
22	3.413	^{14}C humic acids
57.25	7.432	^{14}C humic acids
82.25	11.285	^{14}C humic acids
119	15.517	Mag.Sus/Fkerg with Fe/Fkerg PS75/072-4
154	18.690	Fkerg with Fkerg PS75/072-4
175	23.473	Fkerg with Fkerg PS75/072-4
199	31.292	Fkerg with Fkerg PS75/072-4
215	38.456	Mag.Sus with EDC dust
225	41.900	Mag.Sus with EDC dust
296	59.429	Mag.Sus with EDC dust
413	70.679	Mag.Sus with EDC dust
832	110.258	Mag.Sus with Fe PS75/072-4
1120	130.579	Mag.Sus with EDC dust
1418	187.402	Mag.Sus with EDC dust
1530	194.838	Mag.Sus with EDC dust

Table S3.1 continued

PS75/072-4

Core depth (cm)	Age (kyr)	Correlation
1.5	0.729	^{14}C F$_{nps}$
21.5	1.705	^{14}C F$_{nps}$
36.5	2.929	^{14}C F$_{nps}$
51.5	4.291	^{14}C F$_{nps}$
76.5	7.494	^{14}C F$_{nps}$
91.5	9.600	^{14}C F$_{nps}$
101.5	10.984	^{14}C F$_{nps}$
131.5	13.786	^{14}C F$_{nps}$
136.5	14.480	SSST with EDC δT
146.5	16.666	SSST with EDC δT
151.5	19.387	^{14}C F$_{nps}$
156.5	22.676	^{14}C F$_{nps}$
166.5	28.418	^{14}C F$_{nps}$
181.5	70.106	CRS with CRS PS75/072-3
186.5	71.804	CRS with CRS PS75/072-3
266.5	84.992	δ^{18}O with LR04
326.5	90.619	δ^{18}O with LR04
646.5	128.506	δ^{18}O with LR04
666.5	130.158	δ^{18}O with LR04
706.5	135.711	LOD Rouxia leventerae
736.5	190.837	LOD Hemidiscus karstenii
761.5	199.926	δ^{18}O with LR04
855	217.380	Fe with EDC dust
877	224.337	Fe with EDC dust
911.5	244.057	LOD Rouxia constricta
941.5	291.058	Rouxia constricta and Hemidiscus karstenii
958	305.000	Fe with EDC dust

PS75/073-2

Core depth (cm)	Age (kyr)	Correlation
18	3.838	^{14}C F$_{nps}$
26	4.807	^{14}C F$_{nps}$
38	6.089	^{14}C F$_{nps}$
53	7.993	^{14}C F$_{nps}$
63	9.779	^{14}C F$_{nps}$
74	11.118	^{14}C F$_{nps}$
82.5	12.466	^{14}C F$_{nps}$
103.5	15.255	^{14}C F$_{nps}$
113.5	16.654	^{14}C F$_{nps}$
122	22.603	Ca with Ca PS75/072-4
128	33.213	Ca with Ca PS75/072-4
147	47.007	^{14}C F$_{nps}$
160	68.943	Si/Ti vs EDC δT
162	70.500	Fe with EDC dust
251	84.411	δ^{18}O with LR04, Fe with EDC dust
325	88.984	δ^{18}O with LR04, Fe with EDC dust

Table S3.1 continued

PS75/076-2

Core depth (cm)	Age (kyr)	Correlation
1	13.319	Chaet with Chaet PS75/072-4
8	14.411	Fe with Fe PS75/072-4
28	32.587	Fe with Fe PS75/072-4
63	63.292	Fe with EDC dust (Lamy et al., 2014)
85	70.544	Fe with EDC dust (Lamy et al., 2014)
110	75.019	Fe with Fe PS75/072-4
147	87.571	Fe with Fe PS75/072-4
214	104.175	Fe with Fe PS75/072-4
248	110.805	Fe with Fe PS75/072-4
271	131.755	Fe with Fe PS75/072-4
301	148.074	Fe with EDC dust (Lamy et al., 2014)
336	157.393	Fe with EDC dust (Lamy et al., 2014)
432	187.372	Fe with EDC dust (Lamy et al., 2014)
458	200.476	Fe with EDC dust (Lamy et al., 2014)
553	235.687	Fe with EDC dust (Lamy et al., 2014)
573	250.638	Fe with EDC dust (Lamy et al., 2014)
601	259.743	Fe with EDC dust (Lamy et al., 2014)
650	269.764	Fe with EDC dust (Lamy et al., 2014)
754	296.044	Fe with EDC dust (Lamy et al., 2014)
828	326.874	Fe with EDC dust (Lamy et al., 2014)
858	345.455	Fe with EDC dust (Lamy et al., 2014)
889	358.636	Fe with EDC dust (Lamy et al., 2014)
1048	389.362	Fe with EDC dust (Lamy et al., 2014)
1167	431.806	Fe with EDC dust (Lamy et al., 2014)
1202	451.633	Fe with EDC dust (Lamy et al., 2014)
1265	470.823	Fe with EDC dust (Lamy et al., 2014)
1335	533.996	Fe with EDC dust (Lamy et al., 2014)
1373	557.817	Fe with EDC dust (Lamy et al., 2014)
1467	627.597	Fe with EDC dust (Lamy et al., 2014)
1587	687.732	Fe with EDC dust (Lamy et al., 2014)
1619	718.543	Fe with EDC dust (Lamy et al., 2014)
1649	737.138	Fe with EDC dust (Lamy et al., 2014)
1686	747.302	Fe with EDC dust (Lamy et al., 2014)
1758	796.453	Fe with EDC dust (Lamy et al., 2014)
1782	818.970	Fe with ODP 1090 (Lamy et al., 2014)
1842	873.931	Fe with ODP 1090 (Lamy et al., 2014)
1886	901.709	Fe with ODP 1090 (Lamy et al., 2014)
1904	908.185	Fe with ODP 1090 (Lamy et al., 2014)
1936	923.276	Fe with ODP 1090 (Lamy et al., 2014)
1988	966.207	Fe with ODP 1090 (Lamy et al., 2014)
2033	981.297	Fe with ODP 1090 (Lamy et al., 2014)

PS75/082-1

Core depth (cm)	Age (kyr)	Correlation
12	6.889	Fe/SSST with Fe/SSST PS75/093-1
35	9.561	SSST with SSST PS75/093-1

Table S3.1 continued

PS75/082-1

Core depth (cm)	Age (kyr)	Correlation
40	11.106	Chaet/SSST with Chaet/SSST PS75/093-1
55	15.509	Chaet/Fkerg/Fe with Chaet/Fkerg/Fe PS75/093-1
70	16.751	Chaet/Fkerg/Fe with Chaet/Fkerg/Fe PS75/093-1
100	21.997	Chaet/Fkerg/Fe with Chaet/Fkerg/Fe PS75/093-1
125	26.540	Chaet/Eanta with Chaet/Eanta PS75/093-1
160	34.764	Fkerg/SSST with Fkerg/SSST PS75/093-1
175	36.605	Eanta with Eanta PS75/093-1
346	48.756	Fe with Fe PS75/093-1
444	67.138	Fe with Fe PS75/093-1
517	79.185	Fe with Fe PS75/093-1
600	88.910	Fe with Fe PS75/093-1
683	102.135	Fe with Fe PS75/093-1
754	111.415	Fe with Fe PS75/093-1
806	132.159	Fe with Fe PS75/093-1
896	161.662	Fe with Fe PS75/093-1
967	185.075	Fe with Fe PS75/093-1
1007	193.599	Fe with Fe PS75/093-1
1035	206.975	Fe with Fe PS75/093-1
1055	217.720	Fe with Fe PS75/093-1
1085	228.904	Fe with Fe PS75/093-1

PS75/085-1

Core depth (cm)	Age (kyr)	Correlation
7.25	1.642	[14]C humic acids
30	2.514	Chaet with Chaet PS75/072-4
47	3.364	[14]C humic acids
90	4.281	Chaet with Chaet PS75/072-4
133.5	5.358	[14]C humic acids
187	6.607	[14]C humic acids
247.5	7.815	[14]C humic acids
303	9.214	[14]C humic acids
343	10.417	[14]C humic acids
358.5	11.032	[14]C humic acids
429.5	14.480	SSST with EDC δT
541	16.557	Fe with Fe PS75/072-4
553	24.162	[14]C humic acids
558.5	26.026	[14]C humic acids
650	47.422	Fe with Fe PS75/072-4
668	55.269	Fe with Fe PS75/072-4
682	59.213	Fe with Fe PS75/072-4
684	68.936	Fe with Fe PS75/072-4
967	84.198	Fe with Fe PS75/072-4
1354	103.769	Ca with Ca PS75/072-4
1413	109.318	Ca with Ca PS75/072-4
1522	118.292	Ca with Ca PS75/072-4
1590	128.686	Ca with Ca PS75/072-4

Table S3.1 continued

PS75/085-1

Core depth (cm)	Age (kyr)	Correlation
1617	130.368	Ca with Ca PS75/072-4
1642	132.327	Ca with Ca PS75/072-4
1653	133.166	Ca with Ca PS75/072-4
1661	147.474	Fe with Fe PS75/072-4
1673	157.841	Fe with Fe PS75/072-4
1679	164.752	Fe with Fe PS75/072-4
1684	183.045	Fe with Fe PS75/072-4
1686	194.576	Fe with Fe PS75/072-4
1891	224.383	Fe with Fe PS75/072-4
1966	243.250	Fe with Fe PS75/072-4

PS75/091-3

Core depth (cm)	Age (kyr)	Correlation
5	3.014	Fkerg with Fkerg PS75/085-1
25	4.068	SSST with SSST PS75/085-1
50	5.510	Fkerg with Fkerg PS75/085-1
75	6.210	Fkerg/SSST with Fkerg/SSST PS75/085-1
95	7.266	Fkerg/Eanta/Chaet with Fkerg/Eanta/Chaet PS75/085-1
110	8.382	Fkerg with Fkerg PS75/085-1
120	9.425	Chaet with Chaet PS75/085-1
130	10.026	Fkerg/Eanta/Chaet with Fkerg/Eanta/Chaet PS75/085-1
135	11.105	Fkerg/SSST with Fkerg/SSST PS75/085-1
145	14.480	Fkerg/Eanta/Chaet with Fkerg/Eanta/Chaet PS75/085-1
155	14.862	Fkerg/Eanta/Chaet with Fkerg/Eanta/Chaet PS75/085-1
170	15.793	Fkerg with Fkerg PS75/085-1
180	16.352	Fkerg/Chaet/SSST with Fkerg/Chaet/SSST PS75/085-1
195	22.261	SSST with SSST PS75/085-1
241	58.649	Fe with Fe PS75/085-1
320	85.210	Fe with Fe PS75/085-1
341	90.419	Fe with Fe PS75/085-1
503	106.214	Fe with Fe PS75/085-1
542	111.459	Fe with Fe PS75/085-1
737	129.932	Fe with Fe PS75/085-1
778	132.861	Fe with Fe PS75/085-1
806	152.657	Fe with Fe PS75/085-1
941	220.398	Fe with Fe PS75/085-1
962	228.838	Fe with Fe PS75/085-1
1003	268.641	Fe with EDC Dust
1034	280.118	Fe with EDC Dust
1060	342.540	Fe with EDC Dust
1085	385.200	Fe with EDC Dust
1128	430.760	Fe with EDC Dust
1166	471.668	Fe with EDC Dust
1217	534.180	Fe with EDC Dust
1248	555.412	Fe with EDC Dust
1278	629.047	Fe with EDC Dust

Table S3.1 continued

PS75/091-3

Core depth (cm)	Age (kyr)	Correlation
1297	667.833	Fe with EDC Dust

PS75/093-1

Core depth (cm)	Age (kyr)	Correlation
10	4.932	Fkerg with Fkerg PS75/072-4
27	8.259	[14]C Fnps
42	10.701	[14]C Fnps
70	14.480	SSST with SSST PS75/085-1
80	16.538	Fe with Fe PS75/085-1
95	19.726	Fe with Fe PS75/085-1
120	31.082	Fe with Fe PS75/085-1
196	59.066	Fe with EDC dust (Lamy et al., 2014)
205	65.701	Fe with EDC dust (Lamy et al., 2014)
238	77.553	Fe with EDC dust (Lamy et al., 2014)
288	85.715	Fe with EDC dust (Lamy et al., 2014)
361	93.238	Fe with EDC dust (Lamy et al., 2014)
461	103.465	Fe with EDC dust (Lamy et al., 2014)
488	108.044	Fe with EDC dust (Lamy et al., 2014)
584	132.937	Fe with Fe PS75/072-4
610	152.625	Fe with Fe PS75/072-4
690	185.486	Fe with Fe PS75/072-4
957	244.035	Fe with Fe PS75/072-4
996	281.000	Fe with EDC dust
1125	347.000	Fe with EDC dust
1183	423.000	Fe with EDC dust
1198	459.400	Fe with EDC dust
1208	468.650	Fe with EDC dust
1279	528.375	Fe with EDC dust

PS75/096-4

Core depth (cm)	Age (kyr)	Correlation
1	10.121	Fkerg with Fkerg PS75/059-2
10	12.993	Eanta/Chaet with Eanta/Chaet PS75/059-2
20	21.360	Eanta/Chaet with Eanta/Chaet PS75/059-2
24	26.622	Eanta with Eanta PS75/059-2
59	34.243	Eanta/Chaet with Eanta/Chaet PS75/059-2
126	40.340	Fe with Fe PS75/059-2
474	77.418	Fe/Si/Ti with Fe/Si/Ti PS75/059-2
588	104.967	Fe/Si/Ti with Fe/Si/Ti PS75/059-2
668	136.107	Fe/Si/Ti with Fe/Si/Ti PS75/059-2
772	173.040	Fe with Fe PS75/059-2
870	189.203	Fe with Fe PS75/059-2
1079	231.630	Fe with Fe PS75/059-2
1180	251.833	Fe with Fe PS75/059-2
1294	277.335	Fe with Fe PS75/059-2

Table S3.1 continued

PS75/096-4

Core depth (cm)	Age (kyr)	Correlation
1367	291.562	Fe with Fe PS75/059-2
1489	345.657	Fe with Fe PS75/059-2
1760	393.632	Fe/Si/Ti with Fe/Si/Ti PS75/059-2
1904	431.349	Fe/Si/Ti with Fe/Si/Ti PS75/059-2

PS75/097-4

Core depth (cm)	Age (kyr)	Correlation
1	11.291	Fe with Fe PS75/059-2
20	20.834	Chaet with Chaet PS75/059-2
60	32.207	Chaet with Chaet PS75/059-2
129	39.868	Fe with Fe PS75/059-2
145	44.122	Fe with Fe PS75/059-2
210	69.706	Fe with Fe PS75/059-2
335	112.798	Fe with Fe PS75/059-2
405	131.265	Fe with Fe PS75/059-2
435	142.562	Fe with Fe PS75/059-2
486	173.444	Fe with Fe PS75/059-2
582	192.031	Fe with Fe PS75/059-2
717	232.034	Fe with Fe PS75/059-2
830	252.123	Fe with Fe PS75/059-2
911	259.947	Fe with Fe PS75/059-2
1097	275.886	Fe with Fe PS75/059-2
1208	290.908	Fe with Fe PS75/059-2
1358	345.278	Fe with Fe PS75/059-2
1463	356.959	Fe with Fe PS75/059-2
1682	379.175	Fe with Fe PS75/059-2

Table S3.2 E-LGM minimum SSTs, anomalies and sea-ice concentration from published foraminiferal (f), diatom (d) and alkenone (a) records.

Core	mod. SSST (°C)[a]	E-LGM SST (°C)	Season[b]	ΔLGM/ mod. SSST (K)	E-LGM Sept SI conc. (%)	E-LGM WSST (°C)[c]	Seasonal Range[d] (°C)	Reference
CHAT-1K	16.7	15.7 f	Ts	-1.0		11.3 f	4.4	Barrows and Juggins, 2005
CHAT-1K	16.7	16.3 f	Ts	-0.4		12.2 f	4.1	Kucera et al., 2005b
DSDP594	12.0	3.7 f	Ts	-8.3		1.8 f	1.9	Barrows and Juggins, 2005
DWBG 70	9.1	5.1 f (M)	Ts	-4.0		2.3 f (M)/ 2.6 f (L)	2.8 (M)/ 2.5 (L)	(M) Moore et al., 1980; (L)Luz, 1977
ELT11-1	6.9	3.5 f (M)	Ts	-3.4		1.0 f(M)/ 0.7 f (L)	2.5 (M)/ 2.8 (L)	(M) Moore et al., 1980; (L)Luz, 1977
ELT11-1	6.9	5.7 d	Ts	-1.2	2.8			Gersonde et al., 2005
ELT11-2	6.4	3.4 f(M)	Ts	-3.0		0.8 f(M)/ 0.6 f (L)/	2.6 (M)/ 2.8 (L)	(M) Moore et al., 1980; (L)Luz, 1977
ELT11-2	6.4	1.7 f	Tann	-4.7				Mashiotta et a., 1999
ELT11-2	6.4	5.5 d	Ts	-0.9	2.6			Gersonde et al., 2005
ELT11-3	5.8	3.4 f(M)	Ts	-2.4		0.8 f (M)/ 0.6 f (L)	2.6 (M)/ 2.8 (L)	(M) Moore et al., 1980; (L)Luz, 1977
ELT11-3	5.8	3.4 d	Ts	-2.4	12.0			Gersonde et al., 2005
ELT11-4	4.9	4.2 d	Ts	-0.7	20.0			Gersonde et al., 2005
ELT14-6	4.4	3.4 d	Ts	-1.0	22.4			Gersonde et al., 2005
ELT15-12	4.6	4.0 d	Ts	-0.6	2.6			Gersonde et al., 2005
ELT15-4	6.0	4.7 d	Ts	-1.3	2.6			Gersonde et al., 2005
ELT15-6	5.4	4.8 d	Ts	-0.6	9.2			Gersonde et al., 2005
ELT17-9	0.0	0.9 d	Ts	0.9	49.2			Gersonde et al., 2005
ELT19-7	2.4	1.6 d	Ts	-0.8	34.0			Gersonde et al., 2005
ELT20-10	3.0	2.7 d	Ts	-0.3	7.0			Gersonde et al., 2005
ELT20-18	10.6	13.4 f (M)	Ts	2.8		9.2 f(M)/ 9.2 f (L)	4.2 (M)/ 4.2 (L)	(M) Moore et al., 1980; (L)Luz, 1977
ELT21-15	7.8	4.1 f (M)	Ts	-3.7		1.2 f (M)/ 1.1 f (L)	2.9 (M)/ 3.0 (L)	(M) Moore et al., 1980; (L)Luz, 1977
ELT25-10	8.7	4.1 f (M)	Ts	-4.6		1.5 f (M)/ 1.1 f (L)	2.6 (M)/ 3.0 (L)	(M) Moore et al., 1980; (L)Luz, 1977
ELT36-36	2.4	1.5 d	Ts	-0.9	40.0			Gersonde et al., 2005
GeoB3327-5	14.9	12.1 a	Tann	-2.8				Ho et al., 2012
GeoB3302-1	16.0	11.5 a	Tann	-4.5				Kim et al., 2002
GeoB3359-3	14.3	11.6 a	Tann	-2.7				Romero et al., 2006
GeoB7139-2	16.8	14.1 a	Tann	-2.7				Kaiser et al., 2008
MD07-3128	9.2	4.7 a	Tann	-4.5				Caniupán et al., 2011
MD88-784	5.3	3.5 d	Ts	-1.8	13.4			Gersonde et al., 2005
MD88-787	3.3	2.3 d	Ts	-1.0	19.0			Gersonde et al., 2005
MD97-2120	12.0	6.5 a	Tann	-5.5				Pahnke and Sachs, 2006
MD97-2120	12.0	6.4 f	Tann	-5.6				Pahnke et al., 2003
MD97-2121	17.7	11.7 a	Tann	-6.0				Pahnke and Sachs, 2006
ODP1233	14.7	7.8 a	Tann	-6.9				Kaiser and Lamy, 2010
P69	17.7	14.3 f	Ts	-3.4		10.3 f	4.0	Barrows and Juggins, 2005
PS75/034-2	7.8	1.5 a	Tann	-6.3				Ho et al., 2012
Q200	12.2	3.7 f	Ts	-8.5		1.5 f	2.2	Barrows and Juggins, 2005

Table S3.2 continued

Core	mod. SSST (°C)[a]	E-LGM SST (°C)	Season[b]	ΔLGM/ mod. SSST (K)	E-LGM Sept SI conc. (%)	E-LGM WSST (°C)[c]	Seasonal Range[d] (°C)	Reference
Q585	10.6	3.7 f	Ts	-6.9		1.5 f	2.2	Barrows and Juggins, 2005
R657	17.0	14.6 f	Ts	-2.4		10.5 f	4.1	Barrows and Juggins, 2005
R657	17.0	11.7 a	Tann	-5.3				Sikes et al., 2002
R657	17.0	13.7 f	Ts	-3.3		9.0 f	4.7	Sikes et al., 2002
RC08-78	14.4	13.3 f	Ts	-1.1		9.4 f	3.9	Barrows and Juggins, 2005
RC09-110	16.4	13.9 f	Ts	-2.5		9.2 f	4.7	Barrows and Juggins, 2005
RC12-225	7.8	4.1 f (M)	Ts	-3.7		1.5 f (M)/ 1.1 f (L)	2.6 (M)/ 3.0 (L)	(M) Moore et al., 1980; (L)Luz, 1977
SO136-111	4.6	2.2 d	Ts	-2.4	22.3			Gersonde et al., 2005
SO136-111	4.6	2.8 d	Ts	-1.8		0.2 d	2.6	Crosta et al., 2004
SO213-59-2	9.9	9.4 f	Tann	-0.5				Tapia et al., 2015
U938	13.7	5.6 f	Ts	-8.1		2.8 f	2.8	Barrows and Juggins, 2005
U938	13.7	6.5 a	Tann	-7.2				Sikes et al., 2002
U938	13.7	6.8 f	Ts	-6.9		3.8 f	3.0	Sikes et al., 2002
U939	14.3	9.8 f	Ts	-4.5		8.2 f	1.6	Barrows and Juggins, 2005
U939	14.3	7.6 a	Tann	-6.7				Sikes et al., 2002
W268	16.7	11.2 f	Ts	-5.6		8.5 f	2.7	Barrows and Juggins, 2005
W268	16.7	12.3 a	Tann	-4.4				Sikes et al., 2002
Y8	12.9	5.4 r	Ts	-7.5				Lüer et al., 2009

[a] Modern SSST after Olbers (1992)
[b]Season = Sea surface temperature (SST) estimate representing summer SST (Ts, February or JFM) or mean annual SST (Tann)
[c]Winter sea surface temperature (WSST) estimate representing JAS (Barrows and Juggins, 2005) or August (Crosta et al., 2004)
[d] Seasonal Range = seasonality of SST
Temperature values for visualization in Figures 5 and 6 were averaged at core sites with two estimates from the same fossil group. Where temperatures from different fossil group are reconstructed, the estimate of a more representative reference data set was preferred as well as a summer estimate was preferred to an annual estimate.

Chapter 4 – Last glacial to early Holocene sea surface temperature and sea-ice variability in the Pacific sector of the Southern Ocean

Verena Benz[*][a,b], Oliver Esper [a,b], Rainer Gersonde [a,b], Frank Lamy [a,b], Ralf Tiedemann [a]

[a]Alfred-Wegener-Institut Helmholtz-Zentrum für Polar- und Meeresforschung, Am Alten Hafen 26, 27568 Bremerhaven, Germany
[b]MARUM - Zentrum für Marine Umweltwissenschaften der Universität Bremen, Leobener Str. 28359 Bremen, Germany

to be submitted to Paleoceanography

Abstract

The last glacial to interglacial transition is marked by interhemispheric decoupling of climate events associated with the bipolar seesaw. Our reconstructions of diatom-derived sea surface temperatures and sea-ice concentration from the Pacific sector of the Southern Ocean, so far underrepresented regarding paleoceanographic studies, aims to decipher deglacial differences between Southern Ocean basins on millennial time scales. Most prominent is the spatial decoupling of the onset of deglacial warming, with early warming and sea-ice retreat starting at ca. 22,000 years before present (yr BP) in the eastern Pacific sector, which is closely aligned to warming at the West Antarctic Ice Sheet. Such an early onset of deglaciation was probably triggered via simultaneously rising insolation for about 1000 years in both hemispheres. However, the early warming was not propagated into the adjacent Atlantic sector, where an early response may have been overprinted by changes in the Atlantic Meridional Overturning Circulation. As such the atmospheric CO_2 concentration is primarily governed by the deglacial changes in the Atlantic sector. The following deglacial development in the Pacific sector shows gradual warming towards a first warm optimum around 15,000 yr BP, the thermal reversal between 14,000 and 12,000 yr BP and a Holocene climatic optimum centered at 10,000-11,000 yr BP revealing typical "Antarctic timing". Differences in the occurrence and magnitude of these events in the eastern and western Pacific sectors were influenced by the interplay of bottom topography and changes in the strength and intensity of westerly winds and the Southern Annular Mode.

4.1   Introduction

The last deglaciation (Termination I, TI) represents the most promising interval to study processes driving and amplifying Earth´s climate development from a full glacial to a full interglacial state. Multiple records from all ocean basins and continents, including continental ice core records, allow for global-scale documentation of the processes shaping the last deglacial development. This provides a keystone for the understanding of past climate-related processes needed to test and improve numerical climate simulations and, subsequently, the development of realistic projections of future conditions. Exceptional records from Greenland and antarctic ice cores document Termination I at highest (up to seasonal) resolution and allow for precise synchronization of Northern and Southern hemisphere climate records at high precision. The synchronization relies on atmospheric CH4 records, a terrestrial biosphere signal (Brook et al. 2000), that displays in-phase variability in Greenland and antarctic ice cores. Based on the synchronization is was possible to depict the sequence of warmings and coolings during TI characterized by abrupt changes on the Northern Hemisphere and more smooth variability on the Southern Hemisphere that occur out of phase (Blunier et al. 1998; EPICA Community Members 2006). The underlying mechanisms, highlighted as "bipolar seesaw" (Broecker 1998; Stocker and Johnson 2003), are recognized to be intimately related to changes in Atlantic Meridional Overturning Circulation (AMOC), potentially triggered by events in the North Atlantic (Broecker et al., 1985; Jansen and Veum, 1990), but also in the Southern Ocean (Stocker 2003). Relying on simulations with a three-dimensional oceanic circulation model, Knorr and Lohmann (2003) suggested that the gradual warming in the Southern Ocean, which predates the strong deglacial warming in the northern Atlantic by several thousand of years during the last glacial, induced an abrupt consumption of the Thermohaline Circulation from a near shut-down to a full interglacial mode. The resulting dramatic shift from glacial to interglacial conditions in the Northern Hemisphere, well documented by multiple proxy records (e.g. Thornalley et al., 2011) entrained a massive ice-sheet collapse resulting in a sea level rise of about 14-18 m in less than 500 years (Weaver et al., 2003; Deschamps et al., 2012). This event, originally recognized by Fairbanks et al. (1989) and named meltwater pulse 1A (MWP-1A), marks the abrupt onset of the Bølling warming on the Northern Hemisphere around 14,400 years ago. The analysis of Atlantic (Barbados) and Pacific (Tahiti) sea-level records (Deschamps et al., 2012) supports the suggestion of Weaver et al. (2003) that MWP-1A was predominantly caused by a rapid reduction of antarctic ice volume. Primary

candidates for such decay are the marine based sectors of the Antarctic ice sheet, mainly comprising the West Antarctic Ice Sheet (WAIS) (Gomez et al., 2010). According to numerical simulations (Mikolajewicz, 1998; Weaver et al., 2003), massive meltwater shedding into the major drainage area of the WAIS, the Pacific sector of the Southern Ocean, would cause surface ocean cooling in this sector and in opposite lead to warming the North Atlantic via the "bipolar seesaw" effect. Such process would represent an alternate or additional Southern Hemisphere-sourced mechanism driving the fast warming at the onset of the Bølling in the Northern Hemisphere. A promising approach to rate the likelihood of model-based scenarios is the comparison of the numerical simulations with data gathered from marine proxy records. An impressive effort to map the variability of marine climate records from all ocean basins in combination with ice core records between the last glacial and the present interglacial has been presented by Shakun et al. (2012). They conclude from the analysis of 80 proxy records that the antiphased hemispheric temperature variability in response to "bipolar seesaw" mechanisms superimposed on globally in-phase warming driven by increasing atmospheric CO_2 concentrations explains much of the temperature change during the last deglaciation. According to their data set deglacial warming started initially in the Northern Hemisphere between 21,500 and 19,000 years ago, thus predates the onset of warming and atmospheric CO_2 increase in the Southern Hemisphere around 18,000 years ago as documented in East Antarctic ice cores. Such time relationship would preclude a Southern Hemisphere trigger of the last deglacial warming as a response to changes in antarctic insolation, which increase the duration of Southern Hemisphere summer (Huybers and Denton, 2008). However, the latter mechanism is corroborated by more recent results obtained from a West Antarctic ice core, which display the onset of deglacial warming in West Antarctica between 22,000-20,000 years ago (WAIS Divide Project Members, 2013). The initial WAIS retreat in the Amundsen sector suggested to occur prior to between 22,400 and 21,000 years ago (Smith et al., 2011; Klages et al., 2014), thus close to the early warming date documented in the WAIS ice core, to o. Such timing would decouple the onset of atmospheric CO_2 increase found to occur synchronously in both, East and West Antarctic ice cores around 18,000 years ago (Marcott et al., 2014), from the temperature development in the Pacific Antarctic sector. Although modeling results, ice core records and the WAIS climate history point to specific processes that shape the last deglacial development in the Pacific Antarctic sector, only a limited number of climate records exists, which document the deglacial temperature development of the Southern Ocean in the Pacific sector. Open ocean records include three surface water temperature records from cores recovered in the southern

and the central Subantarctic Zone in the eastern sector (E11-2, Mashiotta et al., 1999; SO213-59-2, Tapia et al., 2015), and from the Polar Front Zone south of Campbell Plateau (SO136-111, Crosta et al., 2004). Additionally, sea-ice records are available from SO136-111 and E27-23, the latter retrieved from the northern Antarctic Zone southwest of SO136-111 (Ferry et al., 2015b) (Fig. 4.1). Other temperature records derive from near-shore sites off New Zealand located north and south of the Subtropical Front (MD97-2120, Pahnke et al., 2003; MD97-2121, Pahnke and Sachs, 2006; Marr et al. 2013) and from subantarctic sites off Chile (ODP 1233, Kaiser and Lamy, 2010).

To significantly augment the knowledge of the paleoceanographic development in the Pacific sector, we here present 17 new Pacific paleoclimate records which document the transition from the last glacial to the modern interglacial (past 30 kyr, 1000 yr = 1kyr) at highest possible time resolution. The records represent diatom-transfer function-based sea surface temperature and sea-ice concentration estimates interpreted in combination with diatom indicator species, allowing to trace the extent of the winter and summer sea-ice field and specific diatom productivity regimes. The studied sites are located between 100°W and 180°E and document past conditions in a broad zone extending from the Southern Antarctic Circumpolar Current Front (SACCF) and the modern winter sea-ice edge (40% concentration), respectively, in the South to the southern Subantarctic Zone (SAF) in the North (Fig. 4.1). This zone is in the core of the Antarctic Circumpolar Current (ACC) where Southern Westerlies driven Ekman upwelling generates increased nutrient advection, which enhances the deposition of biogenic opal (Geibert et al., 2005) and CO_2 outgassing (Lovenduski et al., 2007). The position of the Southern Westerlies, the intensity of the Southern Annular Mode (SAM) and the El Niño Southern Oscillation (ENSO) influence the extent of sea ice in the studied zone (Yuan, 2004; Thompson et al., 2011). Age control of the studied cores is outlined in detail in *Benz et al.* (*a; under rev.*), a paper that focuses on Last Glacial Maximum conditions in the Pacific sector. To further broaden the view based on our records we combine and compare them with other marine records available from the Pacific sector together with selected high-resolution records from the Atlantic sector as well as Greenland and antarctic ice core records.

Major goals of our study are (1) to depict the timing of the onset of the last deglaciation as indicated by sea surface temperature increase and sea-ice retreat to investigate the nature of an offset of the deglacial initiation between the West and the East Antarctic realm and (2) to test whether and to what extent deglacial warming in the Pacific sector is decoupled from the global atmospheric CO_2 increase to study underlying mechanisms for

such decoupling. (3) To study the physical and biological processes in the Pacific sector that impact ocean/atmosphere exchange during the last deglaciation. (4) To test the model-based hypothesis that the decay of the West Antarctic Ice Sheet represents a major contribution to MWP-1A, which should be accompanied by a distinct surface ocean cooling in the Pacific sector. (5) To reveal the impact of AMOC versus Pacific processes on the pattern and timing of the deglacial evolution in the Pacific sector. (6) To document the deglacial evolution of the ACC surface water temperature regime in the Pacific and discuss implications for the development of the "cold water route" across the Drake passage, which affects the heat/salinity transport in the Atlantic sector and thus development of thermohaline circulation (e.g. Knorr and Lohmann, 2003).

4.2   Material and Methods

4.2.1   Sediment material and oceanographic setting

The 17 studied cores for the reconstruction of Summer Sea Surface Temperature (SSST) and Winter Sea Ice (WSI) concentration were recovered during the R/V Polarstern expeditions ANT-XIII5a and ANT-XXVI/2 (Fig. 4.1, Table 4.1) (http://doi:10.1594/PANGAEA.60007; Gersonde, 2011). Deployed devices include piston, gravity and kasten corer.

Our study area is located in the Pacific sector of the Southern Ocean between 180°E and 100°W (Fig. 4.1, Table 4.1). The studied cores document the changes of the environmental conditions of the Antarctic Circumpolar Current (ACC) covering the area between the modern southern Subantarctic Zone (SAZ) and the northern Antarctic Zone (AZ), between ca. 50°S and 65°S (Orsi et al., 1995). Here modern summer surface water temperatures range between ca. 0 and 8°C in summer (Olbers et al., 1992). Sediment facies deposition varies between calcareous nannofossil ooze containing varying diatom and foraminifera content and nannofossil-diatom ooze in the SAZ and in vicinity of the Subantarctic Front (SAF) (Gersonde, 2011). Sediments from the Polar Front Zone (PFZ) and the Permanent Open Ocean Zone (POOZ) south of the Antarctic Polar Front (APF) consist mainly of diatom ooze with highest opal content of 50-80%. From the seasonal Sea Ice Zone (SIZ) less opal deposition is reported (10-50%; Lisitzin, 1985). The burial area of pure diatom ooze is coincident with the expansion of the opal belt between the northern SAZ and the PFZ (Geibert et al., 2005; Bradtmiller et al., 2009).

The frontal system in the ACC is strongly related to topographic forcing. Thus, fronts remain relatively stable at seasonal and interannual time scales close to large bathymetric features, whereas over abyssal plains their location appears to be fairly unstable (Sokolov and Rintoul, 2009). The cyclonic Ross Gyre transports cold Antarctic Surface Water from the southern Ross Sea far north into the region of the Pacific Antarctic Ridge. Thus, in the western Pacific sector of the Southern Ocean, relatively colder surface water, a distinctly expanded WSI field and enhanced sea-ice seasonality are prevailing (Fig. 4.1).
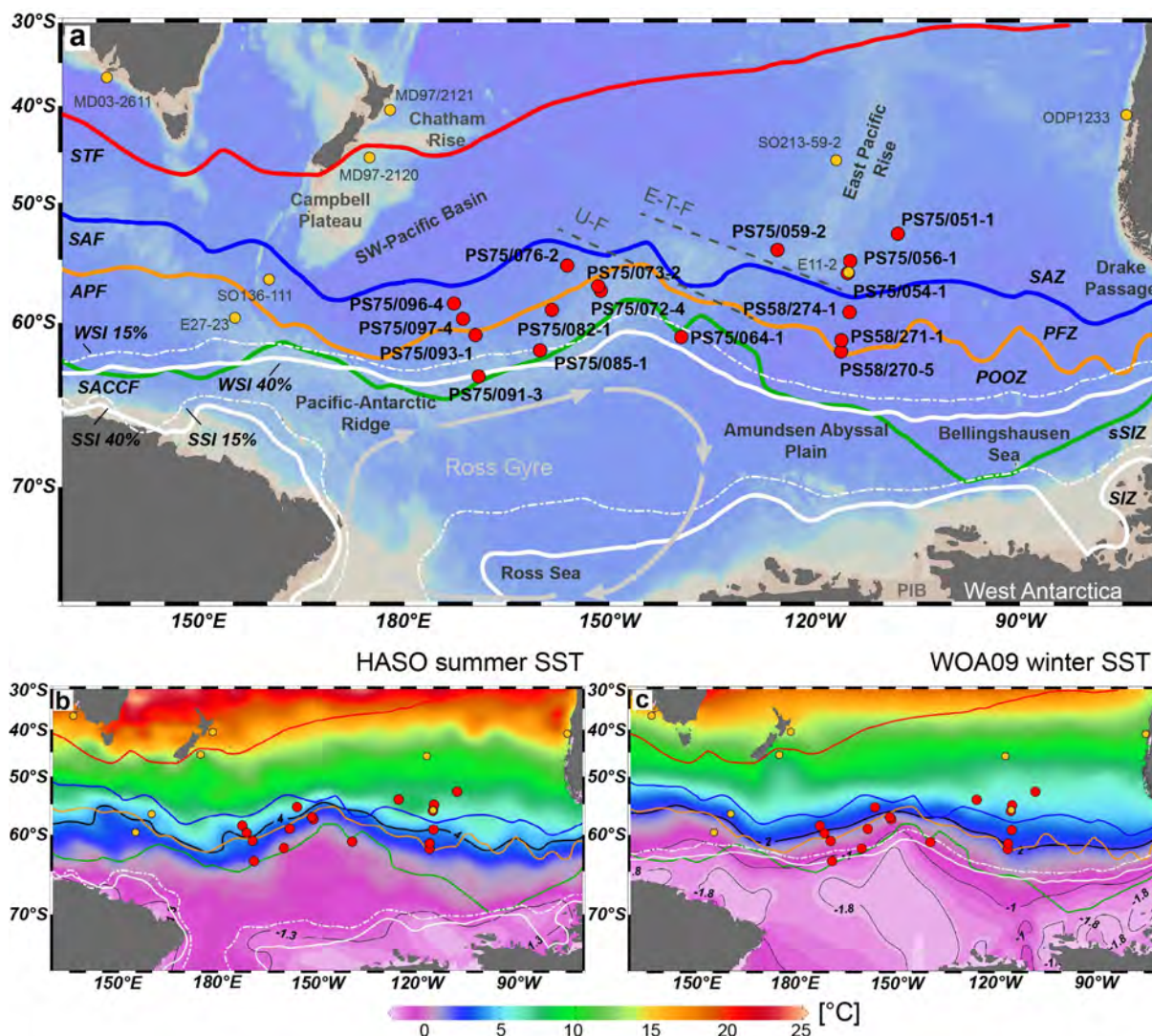
Figure 4.1: **(a)** Locations of cores analysed in this study (red circles) and other cores discussed in the paper (yellow circles, for references see Table 4.1). WSI 15%/SSI 15%: modern winter/summer sea-ice edge with 15% sea-ice concentration, WSI 40%/SSI 40%: modern winter/summer sea-ice edge with 40% sea-ice concentration (Reynolds et al., 2002, 2007); E-T-F: Eltanin Tharp Fracture Zone, U-F: Udintsev Fracture Zone (Udintsev (Ed.), 2003); oceanic fronts according to Orsi et al. (1995); STF: Subtropical Front, SAF: Subantarctic Front, APF: Antarctic Polar Front, SACCF: Southern Antarctic Circumpolar Current Front; SAZ: Subantarctic Zone, PFZ: Polar Front Zone, POOZ: Permanent Open Ocean Zone, (s)SIZ: (seasonal) Sea Ice Zone, **(b)** Modern summer SSTs from the Hydrographic Atlas of the Southern Ocean (HASO; Olbers et al., 1992); core locations and oceanographic fronts as in (a); 4°C and -1.3°C isotherm representing the APF and sea-ice edge respectively. **(c)** Modern winter SSTs from the World Ocean Atlas 2009 (WOA09, July-September; Locarnini et al., 2010); core locations and oceanographic fronts as in (a); 2°C and -1°C isotherm representing the APF and sea-ice edge respectively.

Table 4.1 Locations of sediment cores presented and discussed in this study.

Core	Latitude	Longitude	Water depth (m)	Coring device[a]	Zone[b]	Data source
ELT11-2	56°03.60'S	115°03.60'W	3109	PC	SAZ	Mashiotta et al., 1999
ELT27-23	59°73.1'S	155°14.3'E	3182	PC	POOZ	Ferry et al., 2015b
MD03-2611	36°44.00'S	136°33.00'E	2420	GC	STZ	Calvo et al., 2007
MD97-2120	45°32.6'S	174°55.85'E	1210	GPC	SAZ	Pahnke et al., 2003; Pahnke and Sachs, 2006
MD97-2121	40°22.80'S	177°59.40'E	3014	GPC	STZ	Pahnke and Sachs, 2006
ODP1233	41°00.00'S	74°27.00'W	838	CC	SAZ	Kaiser and Lamy, 2010
ODP 1094	53°10.8'S	5°07.8'W	2807	CC	POOZ	Bianchi and Gersonde, 2004
PS58/270-5	62°01.68'S	116°07.38'W	4981	PC	POOZ	**this study**
PS58/271-1	61°14.58'S	116°02.82'W	5214	PC	PFZ	**this study;** Esper and Gersonde, 2014a/b
PS58/274-1	59°12.42'S	114°53.28'W	5136	PC	PFZ	**this study**
PS75/051-1	52°48.73'S	107°48.33'W	3949	PC	SAZ	**this study**
PS75/054-1	56°09.11'S	115°07.98'W	4113	PC	SAZ	**this study**
PS75/056-1	55°09.74'S	114°47.31'W	3581	GC	SAZ	**this study**
PS75/059-2	54°12.90'S	125°25.53'W	3613	PC	SAZ	**this study**
PS75/064-1	61°00.74'S	139°27.85'W	4600	PC	sSIZ	**this study**
PS75/072-4	57°33.51'S	151°13.17'W	3099	GC	POOZ	**this study**
PS75/073-2	57°12.26'S	151°36.65'W	3234	KC	POOZ	**this study**
PS75/076-2	55°31.71'S	156°08.39'W	3742	PC	PFZ	**this study**
PS75/082-1	59°02.48'S	158°51.82'W	4000	PC	POOZ	**this study**
PS75/085-1	61°56.38'S	160°07.10'W	3734	PC	sSIZ	**this study**
PS75/091-3	63°41.66'S	169°04.47'W	2940	PC	sSIZ	**this study**
PS75/093-1	60°52.33'S	169°32.89'W	3762	PC	POOZ	**this study**
PS75/096-4	58°32.86'S	172°42.6'W	5057	PC	PFZ	**this study**
PS75/097-4	59°42.2'S	171°21.44'W	4672	PC	PFZ	**this study**
SO136-111	56°40.20'S	160°13.80'E	3912	GC	PFZ	Crosta et al., 2004; Ferry et al., 2015b
SO213-59-2	45°49.00'S	116°52.00'W	6161	GC	SAZ	Tapia et al., 2015

[a] Coring devices: PC Piston Corer; GC Gravity Corer; KC Kasten Corer; CC Composite Core; [b] Oceanographic zones: STZ Subtropical Zone; SAZ Subantarctic Zone; PFZ Polar Front Zone; POOZ Permanent Open Ocean Zone; sSIZ seasonal Sea Ice Zone

Specific atmospheric conditions further influence the west-east differences in sea surface conditions in the Pacific sector. While cold-air outbursts from the Antarctic ice sheet favor increased sea-ice production and northward expansion in the Ross Sea sector, comparatively warm winds from the north along the Antarctic Peninsula lead to reduced sea-ice occurrence in the eastern sector (Harangozo, 2004). In addition, changes of the SAM and the Amundsen Sea Low as well as tropical variability and the ENSO strongly influence the oceanographic conditions in the western and eastern Pacific sector (Yuan, 2004; Turner et al., 2009; Thompson et al., 2011). Furthermore, the Pacific Sector is the key region to understand the impact of fresh water injection triggered by melting of the (WAIS), as it collects the

majority of the WAIS drainage (Ó Cofaigh et al., 2005; Mosola et al., 2006; Smith et al., 2011).

4.2.2   Age constraints

The age models of the sediment cores used in this studies result from a combined chronostratigraphic approach, including Accelerator Mass Spectrometry (AMS) ^{14}C datings, foraminifer-based oxygen isotope stratigraphy and inter-core correlations using changes in physical sediment parameters and diatom abundance patterns (Table 4.2; *Benz et al., a; under rev.*).

The ^{14}C radiocarbon ages were derived from monospecific samples of the planktic foraminifers *Neogloboquadrina pachyderma* sinistral and *Globigerina bulloides* as well as from bulk sediment samples for dating organic carbon from the humic acid fraction. The majority of samples were measured at the National Ocean Science Accelerator Mass Spectrometry Facility (NOSAMS) at Woods Hole Oceanographic Institution (WHOI). Specifically small foraminifera samples were additionally measured at the Eidgenössische Technische Hochschule (ETH, Zürich) (*Benz et al., a; under rev.*). Applied reservoir ages for Marine Isotope Stage (MIS) 1 vary between 520 – 750 yr dependent on the latitudinal core position according to Bard (1988). For MIS 2 a reservoir age of 1200 yr was chosen considering the existent higher reservoir ages in the glacial and early deglacial found in several areas of the Southern Ocean (Burke and Robinson, 2012; Siani et al., 2013, Skinner et al., 2010; 2015). The raw ages were converted to calibrated years before present (cal. kyr BP) using the calibration software CALIB 7.0.2 (Stuiver and Reimer, 1993; Stuiver et al., 2005) with the MARINE13 calibration curve (Reimer et al., 2013).

Together with oxygen isotopic records from five cores, age models for eight reference cores were established (*Benz et al., a; under rev.*). These age models were further constrained and refined by inter-core correlation and additional alignment of X-ray fluorescence (XRF) measurements and reconstructed SSST records to the equivalent EDC ice core records (Jouzel et al., 2007; Lambert et al., 2008; Martínez-Garcia et al., 2009). The XRF-derived parameter together with abundance fluctuations of prominent diatom species were used to transfer the stratigraphic information of the reference cores to other cores lacking AMS and oxygen isotope-derived dating (*Benz et al., a; under rev.*).

The correlation of cores and the resulting sedimentation rates were established using the AnalySeries 2.0 software (Paillard et al., 1996) with linear interpolation between tie points.

Table 4.2 Depth assignment (depth in cm) for discussed time slices[a]

Core	Time slice (cal. kyr BP)				
(depth in cm)	MIS1/2 (14)	AHO (9-12)	ACR (12.5-14.5)	LGM (19-23)	MIS2/3 (29)
PS58/270-5	120	83–108	112–122	143–173	233
PS58/271-1	192	89–163	174–198	243–285	402
PS58/274-1	188	103–152	162–197	278–439	543
PS75/051-1	12.5	7.5–10	10.5–13	18–21	26
PS75/054-1	40	0-18	25–42	64–87	164
PS75/056-1	42	11.5–24	28–45	61–75	101
PS75/059-2	50	26–39	43–51	59–62	69
PS75/064-1	106	68–88	93–111	156–173	192
PS75/072-4	133	88–112	118–137	151–157	167
PS75/073-2	94	59–80	83–98	117–122	126
PS75/076-2	6	–	0–8	14–17	25
PS75/082-1	50	31–43	45–52	83–105	136
PS75/085-1	420	295–378	389–431	545–551	572
PS75/091-3	144	116–137	139–146	187–196	204
PS75/093-1	67	32–51	56–70	92–102	116
PS75/096-4	11.5	0–6	9–12	18–21	35
PS75/097-4	7	0–2	4–8	17–27	49

[a] Stratigraphy derived from the sources referenced in the text. MIS: Marine Isotope Stage; AHO: Antarctic Holocene Optimum, ACR: Antarctic Cold Reversal; LGM: Last Glacial Maximum.

4.2.3   Sample preparation and diatom analysis

Cores were sampled and analyzed at a spacing of 5 or 10 cm dependent on the time resolution. Preparation of material and permanent mounts of diatoms for light microscopy followed the standard method developed by Gersonde and Zielinski (2000). The diatom counting was carried out according to Schrader and Gersonde (1978). An average of 400 – 600 diatom valves was counted in each slide using a Zeiss Axioplan 2 at x1000 magnification.

Diatoms were identified to species or species group level and if possible to forma or variety level. The taxonomy followed Hasle and Syvertsen (1996), Zielinski and Gersonde (1997), and Armand and Zielinski (2001). For temperature and sea-ice reconstructions 29, respectively 28, species and species groups were used (Esper and Gersonde 2014a, b). The selected species show direct dependency to both environmental variables and different oceanographic zones (Zielinski and Gersonde, 1997; Armand et al., 2005; Crosta et al., 2005; Romero et al., 2005; Esper et al., 2010; Esper and Gersonde, 2014a, b). Following Zielinski and Gersonde (1997) and Zielinski et al. (1998) some species were combined to groups (details see *Benz et al., a; under rev.*).

The most prominent diatom species for comparison of all cores are *Fragilariopsis kerguelensis*, *Eucampia antarctica*, *Chaetoceros* spp. resting spores and *Thalassiosira lentiginosa*. The relative abundance patterns of these diatom species serve as indicator of certain oceanographic conditions and helped constraining the age models. The species *F. kerguelensis* is the most abundant and strongly silicified diatom species in the entire dataset and sediments within the ACC, and its abundance fluctuation between glacials and interglacials mirrors biogenic opal export in the ACC (Esper et al., 2010). Another prominent contributor to the biogenic opal content in sediments is *T. lentiginosa*, representing another strongly silicified and thus robust specimen. Although it is a more temperate species (Esper et al., 2010) and generally its abundance increases towards interglacials, at core sites affected by selective dissolution a significant increase of *T. lentiginosa* occurs (Shemesh et al., 1989). The *E. antarctica* abundance is mainly important as stratigraphic tool supporting the assignment of glacial periods (Burckle and Cooke, 1983; Burckle, 1984a, b). Resting spores of *Chaetoceros* spp. show a direct dependency to meltwater induced freshwater lenses stratifying the upper water column as well as to the release of iron into the water column both favoring their growth (Crosta et al., 1997). Hence this genus is a good indicator for glacial intervals as they show high abundances in the seasonal SIZ directly at the sea-ice edge as well as in open ocean areas influenced by higher iron input due to increased dust transport during the glacial (Abelmann et al., 2006; Esper et al., 2010). On the other hand, *Chaetoceros* spp. peaks occurring in the early deglaciation may be indicative for prominent meltwater events with significant release of snow-settled dust and/or the reorganization of the deep-water circulation and increased nutrient supply to surface waters (Spero and Lea, 2002; Abelmann et al., 2006).

4.2.4   Reconstruction techniques

The reconstruction of summer sea surface temperature and winter sea-ice concentration was obtained with the Imbrie and Kipp (IKM; Imbrie and Kipp, 1971) transfer function (TF) for SSST and the Modern Analog Technique (MAT) for WSI concentration. In particular, we applied the recently developed TFs by Esper and Gersonde (2014a, b). Considering the results of the comparison of different statistical methods and their performances, the TF IKM-D336/29/3q was used for SSST and the TF MAT-D274/28/4 for WSI, supported by the abundance pattern of diatom sea-ice indicators *F. curta* and F. cylindrus (Gersonde and Zielinksi, 2000). The root mean square error of prediction (RMSEP)

for SSST and WSI is 0.83°C and 5.52%, respectively (Esper and Gersonde, 2014a, b). For both TFs species relative abundances were used as logarithm transformed values to enhance the weight of less abundant taxa. IKM calculations were carried out with the software packages PaleoToolBox and WinTransfer (http://www.pangaea.de/Software/PaleoToolBox; Sieger et al., 1999); MAT values were calculated with the statistical computing software package R (R Core Team, 2012). The new SSST and WSI TFs were further used to recalculate the temperature estimates for core ODP1094 (Bianchi and Gersonde, 2004) and to estimate for the first time WSI concentration on the basis of the published diatom counts.

Problems in the reconstruction of both parameters arise from selective dissolution of cold-water and sea-ice indicating diatom species that are relatively weakly silicified, leading to the enrichment of strongly silicified taxa like *F. kerguelensis* and *T. lentiginosa* (Shemesh, et al., 1989). Thus, SSST results during cold periods may be biased towards warmer values preferentially in the vicinity of the sea-ice edge, where dissolution is enhanced due to low sedimentation rates and less productivity. For WSI reconstruction the selective dissolution leads to biased TF-estimates towards lower concentration values.

Additionally, we performed a Principal Component Analysis (PCA) of the SSST records. As the SSST estimates from the western cores were often biased by selective dissolution and showed too high temperatures during the glacial, the PCA was estimated for eastern cores only to exclude the noise over data ratio. For the eastern pacific sector the temperature estimates of 7 cores covering the time span from 30 to 13.5 cal. kyr BP were rescaled to interpolate data points for every 500 yr step using the software AnalySeries 2.0 (Paillard et al., 1996). The PCA was performed with the statistical software package R (R Core Team, 2012) and hereby, it was possible to filter the noise of every single core and get a general temperature trend over the deglacial in the eastern Pacific sector of the Southern Ocean. Due to lacking Holocene temperature estimates in a number of cores, the PCA was only performed for the mentioned time slice. Further analyses with fewer cores but for longer time periods were excluded to maintain the highest possible dataset. For WSI concentrations no PCA was accomplished, as this parameter shows no linear trend suitable to calculate a general trend. For better visualization in maps and figures, the minimum (maximum) SSSTs (WSI concentration) were selected for the Antarctic Cold Reversal (ACR), whereas for the Antarctic Holocene Optimum (AHO) the maximum (minimum) SSSTs (WSI concentration) were chosen. Reconstructed variables and analyses are available in the PANGAEA database (www.pangaea.de). Maps, temperature and sea-ice plots were generated using the ODV software (Ocean Data View; Schlitzer, 2014).

4.3   Results

4.3.1   Sedimentation rates

Estimated sedimentation rates of the studied cores situated in the different oceanographic zones show comparable patterns, yet with differences between western and eastern sector (Fig. 4.2). During the glacial the sedimentation rates of the majority of cores range between 1 and 5 cm/kyr (Fig. 4.2a-m). However, at core sites located in the PFZ of the Amundsen Abyssal Plain sedimentation rates during the glacial reached distinctly higher values of 10-30 cm/kyr in average (Fig. 4.2o-q).
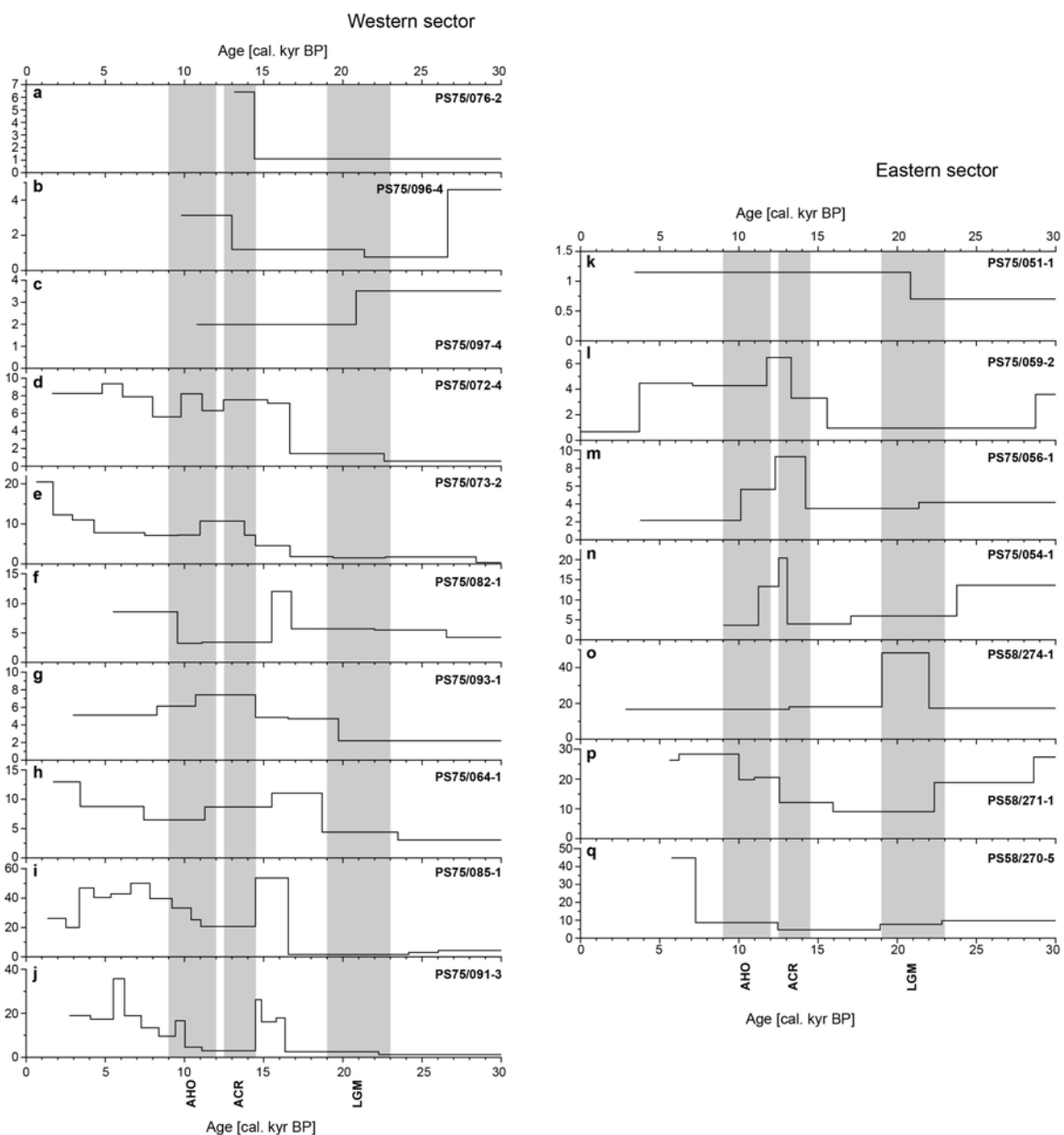
Figure 4.2: Sedimentation rates (y-axis) of studied cores in the Pacific sector of the Southern Ocean plotted against age. AHO: Antarctic Holocene Optimum, ACR: Antarctic Cold Reversal, LGM: Last Glacial Maximum.

From ~19 kyr on the sedimentation rate in all studied cores varies dependent on their location in the different oceanographic zones and the influence of WSI. Whereas cores situated in the PFZ (Fig. 4.2a-c, o-q) and the SAZ (Fig. 4.2k-n) show relatively stable sedimentation rates in the early deglacial (ca. 19-15 cal. kyr BP), the sedimentation rates in the POOZ (Fig. 4.2d-g) and the modern seasonal SIZ (Fig. 4.2h-j) display distinct increases. Most prominent is the change from relatively low glacial to high deglacial sedimentation rates in cores located on the Pacific-Antarctic Ridge at ca. 16.5 cal. kyr BP (Fig. 4. 2d, c, f, i, j). The southernmost cores, lying south of the modern maximum WSI edge (15% concentration), together with a high-resolution core from the APF (Fig. 4.2f, i, j) show a distinct drop of sedimentation after 1-2 kyr that is not pronounced in other cores from the POOZ and the seasonal SIZ. Cores that are located in deeper water depth do not display such a prominent pattern, yet show an early increase in sedimentation rates between 20-18 cal. kyr BP and a rather stable behavior over Termination I (Fig. 4.2g, h).

At ~15 cal. kyr BP sedimentation rates in the western PFZ and eastern SAZ start to rise simultaneously with the drop in the western POOZ and the seasonal SIZ. (Fig. 4.2a, l, m). Two cores from these zones show a first increase in deglacial sedimentation rates not before 13 cal. kyr BP (Fig. 4.2 c, n). Yet a newly drop is visible in the majority of cores from the SAZ around 12 to 10 cal. kyr BP.

After 12 cal. kyr BP the majority of cores depict rather stable sedimentation rates with exceptions from the eastern PFZ showing rising sedimentation rates from 10 kyr BP on (Fig. 4.2p, q). Generally, cores south of the SAF the eastern and south of the APF in the western Pacific sector show higher average sedimentation rates throughout the studied time period.

4.3.2   Diatom assemblage

The diatom composition in all cores show a clear trend from the last glacial to the early Holocene (Figs. 4.3, 4.4). During the glacial the abundance of *F. kerguelensis* shows a N-S gradient in cores from the eastern Pacific sector. Whereas cores in the PFZ depict abundances of ~60-70% (Fig. 4.3o-q), the abundance in the SAZ decreases gradually from 55 to 30% northward (Fig. 4.3k-n). In the western sector such a distinct pattern is not that pronounced showing *F. kerguelensis* abundances around 55% in the majority of cores with a slight decrease in the northernmost cores from the PFZ (Fig. 4.3a-j). With the start of the deglacial, the abundance of *F. kerguelensis* increases in the majority of the studied cores reaching eventually highest values in the eastern PFZ of ca. 80% (Fig. 4.3o-q). Yet, distinct

drops in its abundance during cold events such as the ACR are visible especially in the eastern SAZ and northern PFZ (Fig. 4.3l-o) as well as the seasonal SIZ (Fig. 4.3h-i).
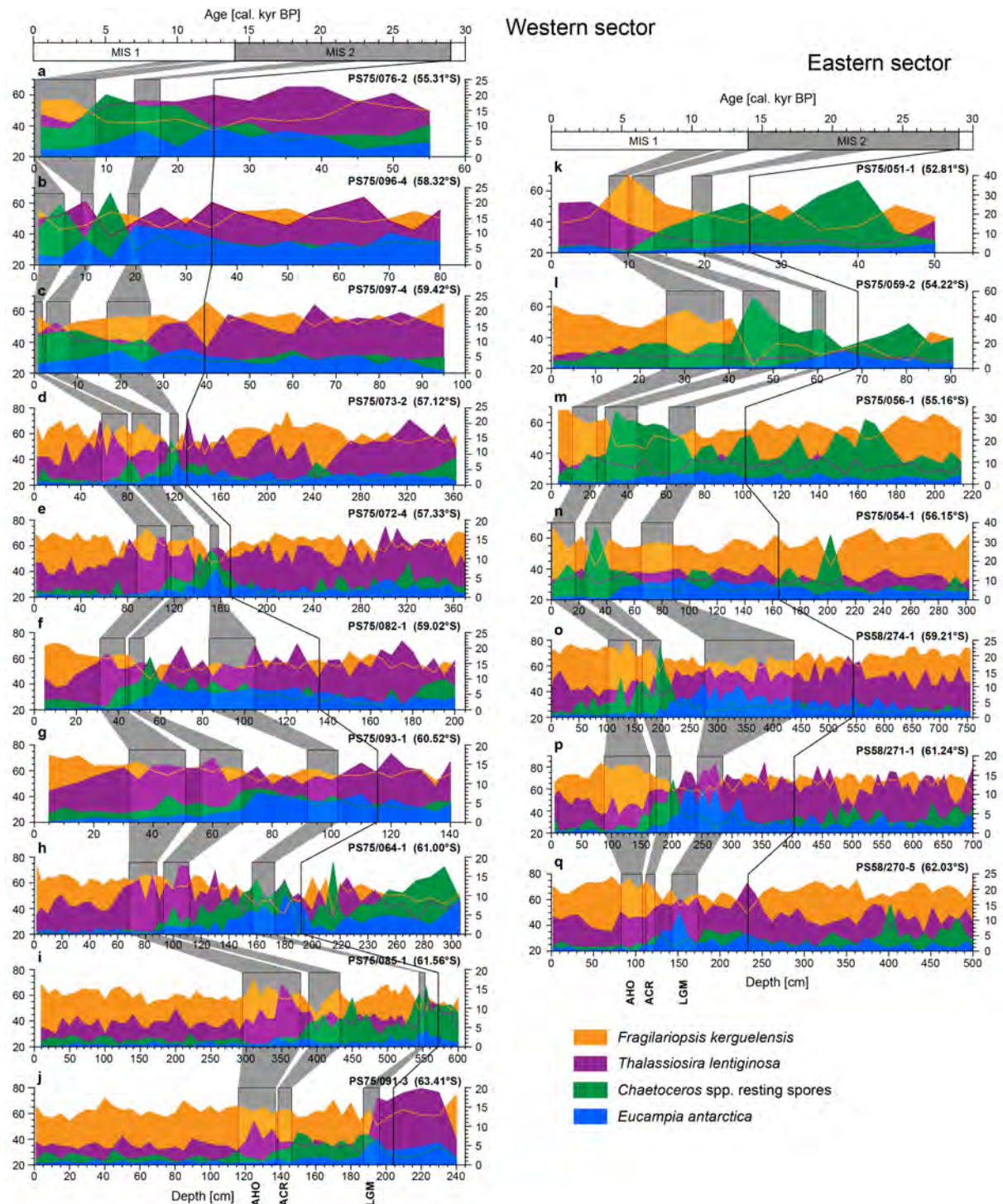

Figure 4.3: Relative abundances of relevant diatom species plotted against depth. Left y-axis: *F. kerguelensis*; right y-axis: *T. lentiginosa*, *Chaetoceros* spp. resting spores, *E. antarctica*. Grey bars represent the assignment to the time slices AHO, ACR and LGM. Black line indicates the end of Marine Isotope Stage (MIS) 2 at 29 kyr BP. AHO: Antarctic Holocene Optimum, ACR: Antarctic Cold Reversal, LGM: Last Glacial Maximum.

An opposite trend is visible in the abundance of *Chaetoceros* spp. resting spores. In the eastern sector the abundances increase northward from relatively low values of around 5% in the PFZ to up to 20% in the SAZ (Fig. 4.3k-q) during the glacial. The pattern in the western sector is not only controlled by a N-S difference but also from the location of the cores in relation to the Pacific Antarctic Ridge and their proximity to the WSI edge. As such, cores from all oceanographic zones located at the Pacific Antarctic Ridge display abundances of up to 15% (Fig. 4.3a, d, e, h-j). The other cores from the POOZ and the PFZ show *Chaetoceros* spp. resting spores in average of ca. 7% (Fig. 4.3b, c, f, g). After the glacial the *Chaetoceros* abundances increase significantly in almost all cores from the Eastern sector and reach peak values of up to 15-55%. Similar to the glacial period, there is an increasing south to north gradient, where cores from the SAZ reach their peak values within the ACR time slices, slightly later than those from the PFZ (Fig. 4.3l-p). The *Chaetoceros* abundance peaks mirror the distinct drops of *F. kerguelensis*. After the peaks, the average values of *Chaetoceros* throughout the Holocene drops to under 10%.

The strongly silicified diatom species *E. antarctica* that is a relatively good indicator for colder climate states shows abundances of maximum 10% in the western as well as in the eastern sector in all oceanographic zones (Fig. 4.3a-q). Generally the peak values are reached during the LGM time slice and the early deglacial. In all cores the *E. antarctica* abundances decrease before the ACR time slice and only minor values around 1% in the early Holocene.

Another robust and strongly silicified diatom species in Southern Ocean sediments is *Thalassiosira lentiginosa* with a rather wide temperature range (Esper et al., 2010) that primarily indicates open ocean conditions (Esper and Gersonde, 2014b). However, in our cores it is a strong indicator for selective dissolution as its abundance reach high values of up to 20% in cores south of the modern and/or glacial average winter sea-ice edge (Fig. 4.3i, j, q).

The specific cold-water and sea-ice diatom taxa *Fragilariopsis curta* and *Fragilariopsis cylindrus* (combined to the *F. curta* group) as well as *F. obliquecostata* show only minor abundances in the northernmost cores from the PFZ in the western and the SAZ in the eastern sector. In those cores the values of both sea-ice indicators do not reach 1% in average (Fig. 4.4a-c, k-n). Yet the pattern displays generally higher abundance of sea-ice taxa during the glacial period, followed by a strong decrease over Termination I. From cores located in the eastern PFZ slightly higher abundances are reported, showing a similar pattern with higher occurrence during the glacial and a decrease during the deglacial (Fig. 4.4o-q). However, in these cores, selective dissolution may take place, especially at the southernmost position (Fig. 4.4q). During the ACR two cores show a minor increase of the *F. curta* group
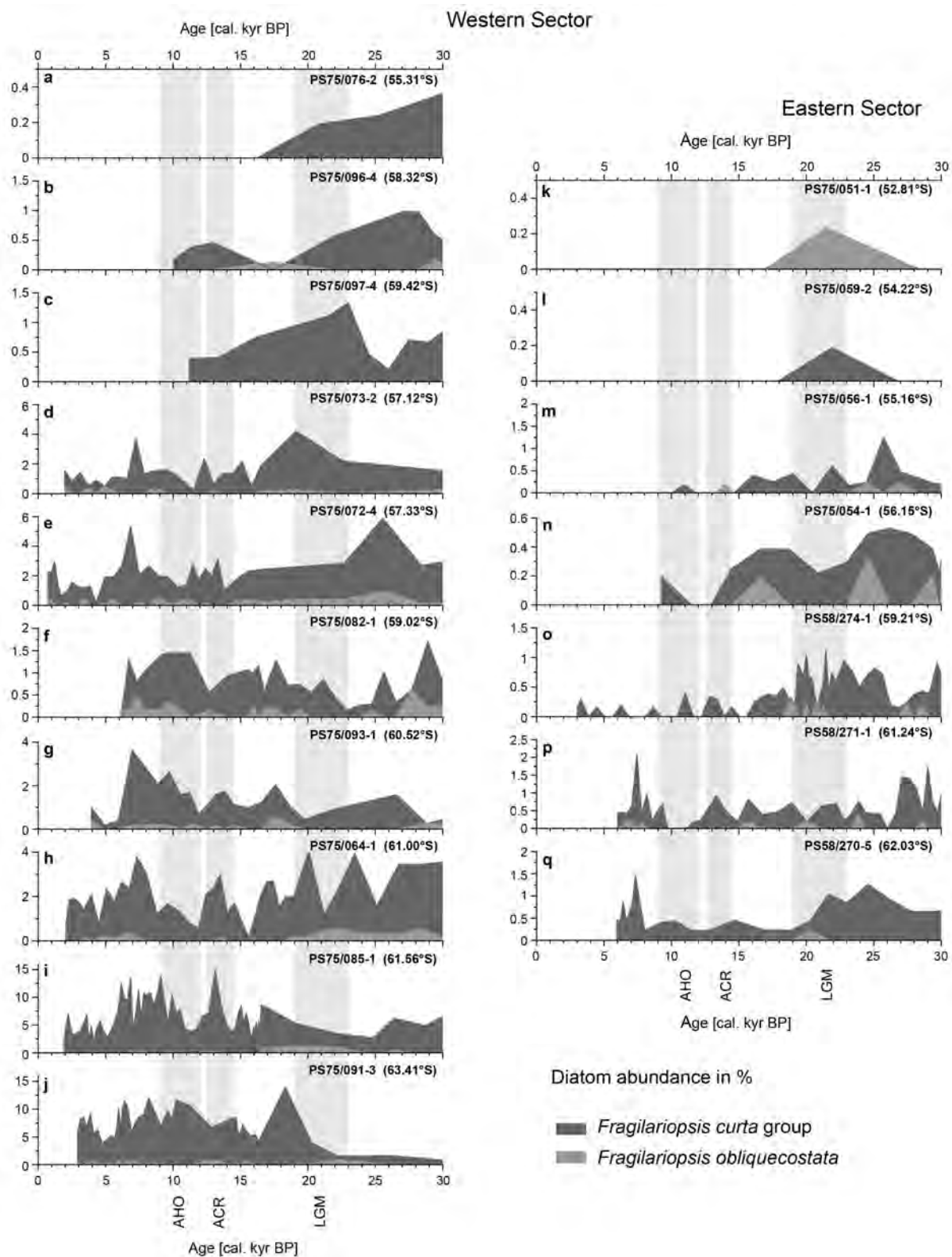
Figure 4.4: Relative abundance of sea-ice indicating diatom species *F. curta* group and *F. obliquecostata* (left y-axis), used as additional variable for the estimation of sea-ice extent plotted against age. AHO: Antarctic Holocene Optimum, ACR: Antarctic Cold Reversal, LGM: Last Glacial Maximum.

with a subsequent drop during the following AHO and presumably re-occurring cold conditions after 8 kyr (Fig. 4.4o-q). Highest abundances of the *F. curta* group up to 15% occur in the western POOZ and seasonal SIZ (Fig. 4.4d-j). Significant dissolution of this slightly silicified diatom taxa is visible in cores from the seasonal SIZ and also from the POOZ where highest abundances are exclusively found during deglacial and Holocene (Fig. 4.4d, f, g, i, j). Similar to the eastern sector, in cores from the POOZ and the seasonal SIZ the *F. curta* group shows an increase during the ACR followed by a drop of abundances during the AHO and a newly rise around 8 kyr (Fig. 4.4d, e, g-i).

In general, all studied cores show a distinct change in diatom composition from a cold glacial to a warmer climate with abundance patterns of specific cold-water and more temperate diatom species supporting the TF estimates of SSST and WSI. Although not used for the reconstruction of the latter parameters, the abundances of *Chaetoceros* resting spores and *E. antarctica* can favor the interpretation of oceanographic and atmospheric changes over Termination I. The anomalous occurrence of specific diatoms like *T. lentiginosa* during glacial periods points to selective dissolution of weakly silicified diatoms and thus helps with the interpretation of biased temperature results.

4.3.3 SSST and WSI reconstruction

Glacial SSST estimates show values of ~0.2° in the modern seasonal SIZ, 0.3 to 2°C in the modern POOZ, around 1-2.5°C in the PFZ and 2-5°C in the modern SAZ. Yet at some core sites (Fig. 4.5e, n-s) SSSTs estimated for the LGM time slice do not represent the coldest temperatures for the last glacial. Similarly, the WSI concentration at those sites showed slightly higher values before 23 cal. kyr BP (Fig. 4.5e, p-s)

The initial rise of SSST after the LGM displays some differences between the eastern and western Pacific sector of the Southern Ocean. While cores at 120°W show a gradual rise of SSSTs starting around 20–22 cal. kyr BP (Fig. 4.5m-o, q, s), the initial rise towards warmer temperatures in the western cores started around 18-19 kyr BP (Fig. 4.5a-j). Concomitant with the rise of SSSTs the winter sea-ice field in both sectors declined. However, temperatures and sea-ice records reconstructed in cores from the seasonal SIZ that were covered by approximately 40% WSI during the glacial (Fig. 4.5d, e, i, j), are highly biased towards warmer SSST and less than expected WSI due to selective dissolution.
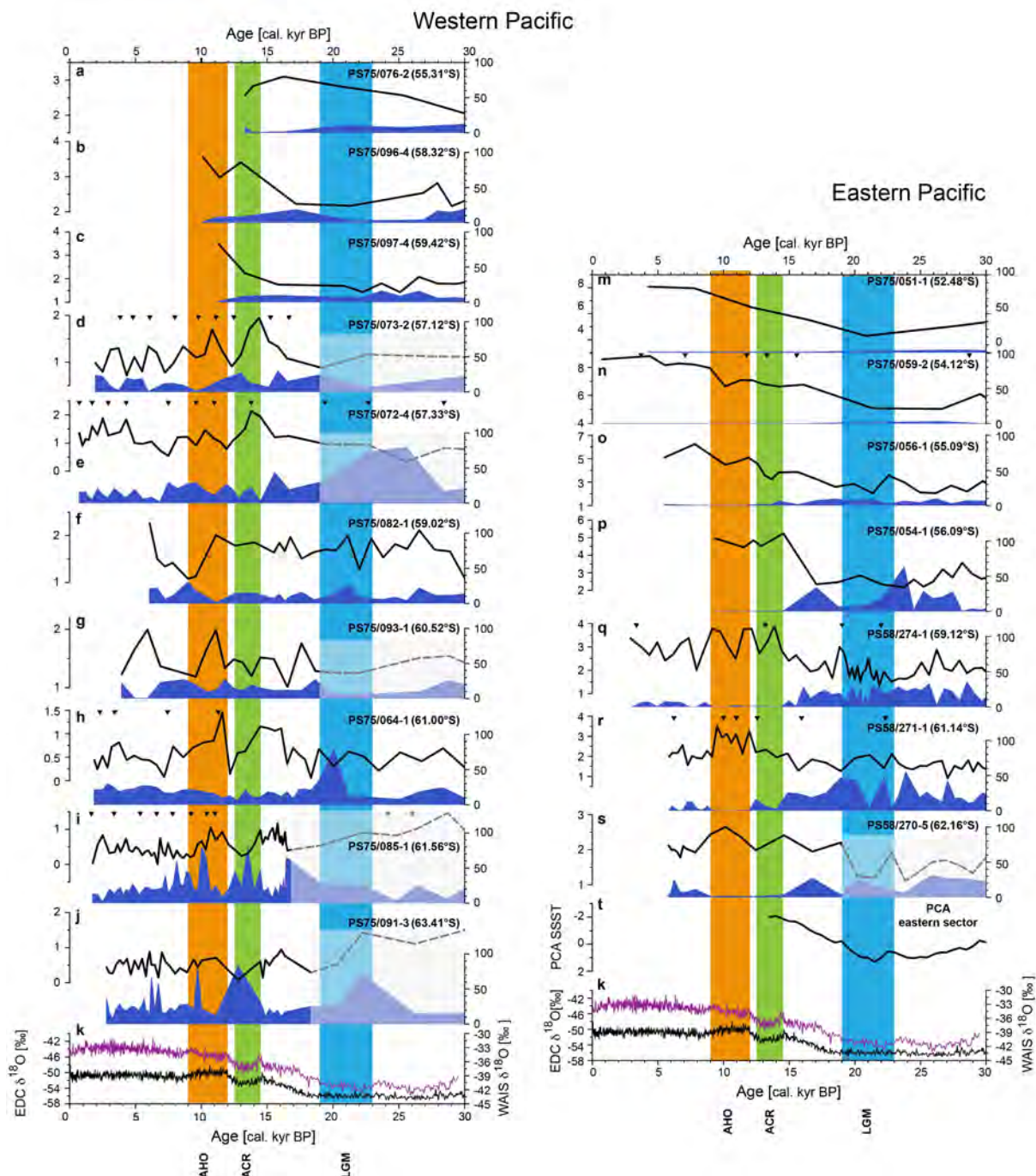
Figure 4.5: SSST and WSI estimates and PCA results from the Pacific sector of the Southern Ocean compared to the Antarctic ice cores EDC δ¹⁸O (Stenni et al., 2006; AICC12 time scale) and WAIS δ¹⁸O (WAIS Divide Project Members, 2013). Left y-axis: diatom-derived SSST; right y-axis: diatom-derived WSI concentration. AHO: Antarctic Holocene Optimum, ACR: Antarctic Cold Reversal, LGM: Last Glacial Maximum.

The first warming step towards a temporary optimum from 16 to 14 cal. kyr BP was steeper in the eastern cores and thus those cores depict a greater temperature range towards the first warm optimum (Fig. 4.5m-s). In the western Pacific sector the SSSTs reached this first optimum after a shallower rise depicting temperatures of 1°C to 2°C at 16 cal. kyr BP, best documented in cores that were previously south of the averaged WSI edge (Fig. 4.5d, e,

h-k. Although an optimum is visible in both sectors, in the western sector this temperature plateau is more pronounced due to its previous and following cooling. At the northernmost core sites in both sectors the temperature remained rather stable with no significant warm optimum over Termination I (Fig. 4.5a-c, m-n). After the temporal warming, at almost all sites the temperature decreased between 12-14.5 cal. kyr BP coincident with a re-advance of WSI at sites south of 57°S (Fig. 4.5d-j, o-s). This cooling event was more pronounced in the western and southern cores by up to 1.6°C temperature difference. Cores at the APF and north of it only show minor decrease (ca. 0.6°C) (Fig. 4.5f, g, r).

A second optimum is reached after a steep rise of SSSTs between 9 and 12 cal. kyr BP with maximum temperatures of up to 7.1°C in the modern SAZ and around 2.5-4°C in the present PFZ of both sectors. In the modern POOZ the temperatures of this optimum reach ~2°C, whereas estimates from core locations in the modern seasonal SIZ range from 0.5-1.5°C. The temporal warming expressed particularly at sites south of the SAF in the eastern sector and south of the APF in the western sector was accompanied by the retreat of winter sea ice (Fig. 4.5d-j, q-s). After ca. 1-2 cal. kyr BP, the temperature drops again significantly. The cold temperatures remain in the POOZ, but rise again or remain stable in the SAZ and PFZ.

The general trend of temperature development in the eastern Pacific sector over Termination I is best expressed by a Principal Component Analysis (PCA) (Fig. 4.5t). During the glacial period from 30 to 22 cal. kyr BP only small-scale variations can be observed, diminishing the signals of coldest temperatures in the pre-LGM time period. Yet, the PCA corroborates the early start of warming from ca. 22 cal. kyr BP on and a constant rise of PCA values until ~14 cal. kyr BP. Later than 14 cal kyr BP the PCA seems to show apattern of decreasing temperatures that can not be further traced due to the low data coverage in the last 13.5 kyr.

4.4 Discussion

4.4.1 Glacial conditions and start of Southern Ocean warming

4.4.1.1 Glacial conditions

The glacial period in the Pacific sector of the Southern Ocean was characterized by continuously colder than present SSSTs of up to -5K leading to a northward expansion of the cold-water realm by in average 5° in latitude accompanied by a similar northward advance of

sea ice by up to 5-10° latitude. Yet both parameters show an east-west gradient, including the extent of the maximum WSI ice edge (15% concentration) reaching to 56°S in the eastern and 60 to 57°S in the western sector (*Benz et al., a; under rev.*). Although relatively distinct temperature variations occur in single cores (e.g. Fig. 4.5f, p, q), the general trend that is supported by the performed PCA (Fig. 4.5t) shows low SSST variability throughout the glacial. The northward extent of the WSI field, leading to distinctly less opal burial and stronger dissolution, is in line with extremely low sedimentation rates at core sites south of the glacial seasonal SIZ (*Benz et al., a; under rev.*). Furthermore the higher sedimentation rates found especially in the eastern modern PFZ and SAZ corroborate a shift of the opal burial zone by approximately 5° in latitude as proposed by different authors (Chase et al. 2003, Bradtmiller et al., 2009).

Interestingly, we find indications that the period of coldest Southern Ocean SSSTs occurred pre-LGM. Accompanied by colder SSSTs, also the WSI concentrations were slightly higher in this pre-LGM period especially in the eastern Pacific sector (Fig. 4.5p-s) that is additionally corroborated by the slightly higher abundances of sea-ice diatoms (Fig. 4.4m-q). The dissolution-biased records from the western sector do not show this specific pattern. The maximum WSI edge probably extended pre-LGM around 1-2° in latitude further northward to 59°S in the western sector and multiple events of sea-ice advance in the eastern sector may have occurred. These results show a good agreement with previous temperature and sea-ice reconstructions from the central and westernmost Pacific sector of the Southern Ocean (Fig. 4.6d, i; Crosta et al., 2004; Tapia et al., 2015), off southern New Zealand (Fig. 4.6c, 4.7h; Pahnke and Sachs, 2006), as well as from the Atlantic sector (Fig., 4.7j; e.g. Bianchi and Gersonde, 2004; Gersonde et al., 2005; Collins et al., 2012; Abelmann et al., 2015). The SSSTs and sea-ice estimates reconstructed from the Atlantic sector (Bianchi and Gersonde, 2004; Gersonde et al., 2005; Collins et al., 2012) also display coldest temperature values and a farther sea-ice extent around 25 cal. kyr BP. Likewise the maximum extent of Patagonian glaciers is found prior to ~22 cal. kyr BP and they show only minor advances until 19 cal. kyr BP or even a slight retreat of ice extent (Kaplan et al., 2008; Kilian and Lamy, 2012). Although the variations in ice core temperatures during the last glacial are minor, the lowest temperatures were also recorded from ca. 29-26 cal. kyr BP from the East and West Antarctic ice sheet (WAIS Divide Project Members, 2013).
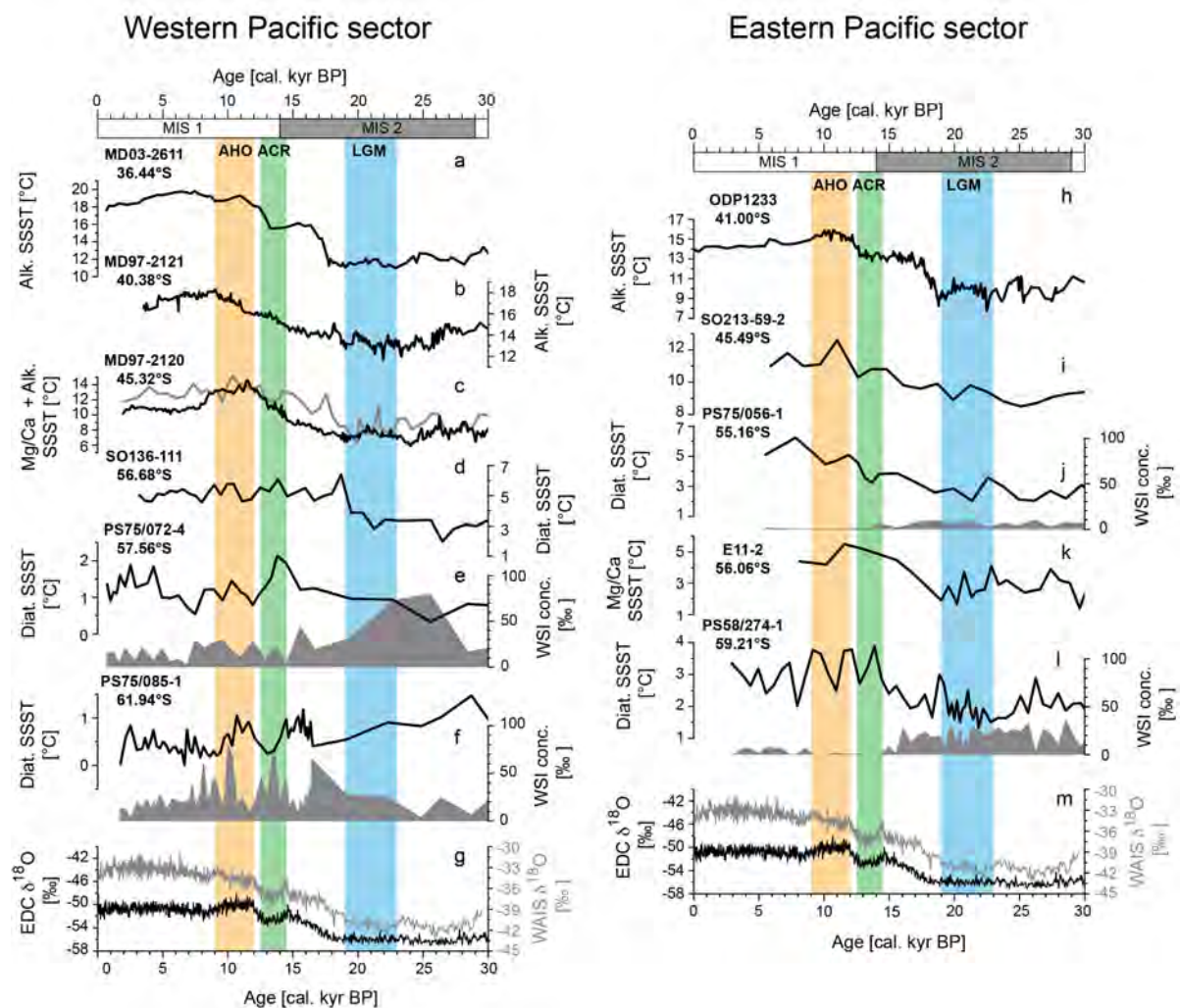
Figure 4.6: SSST and WSI records from the western and eastern Pacific sector of the Southern Ocean (for references see Table 4.1) compared to EDC δ18O and WDC δ18O (Stenni et al., 2006; AICC12 time scale; WAIS Divide Project Members, 2013). MIS1/2: Marine Isotope Stage 1 and 2; AHO: Antarctic Holocene Optimum; ACR: Antarctic Cold Reversal; LGM: Last Glacial Maximum.

In general, the extent of sea ice together with the huge expansion of the cold-water realm during the glacial significantly influenced the ACC. The export of cold-water masses led to distinct cooling along the Humboldt Current system and subsequently in the eastern equatorial Pacific as well as in the Atlantic and Indian sectors due to the colder than present throughflow via the Drake Passage (*Benz et al., a; under rev.*). Furthermore, steep temperature gradients at the Glacial Southern Subtropical Front (GSSTF) point to a contraction of the Subtropical Gyre with minor to almost no cooling in its interior similar to the Atlantic sector (MARGO Project Members, 2009). Overall, during the last glacial, the behavior of the different Southern Ocean sectors is comparable in the magnitude of strongest cooling (>4K in the SAZ) and the average northward expansion of the winter sea-ice extent. Resulting from the severe cooling in the SAZ and the deflection of >4°C water masses the

Antarctic continent and its surrounding Southern Ocean seems strongly thermally isolated south of ~55°S.

Diatom-derived TF-estimates of glacial SSST are alone not solely indicative for frontal displacement in the Southern Ocean due to the strong topographic forcing that steers ocean currents in the ACC. Most likely the fronts where only characterized by colder SSSTs during the LGM (*Benz et al., a; under rev.*). The huge WSI expansion in the Pacific sector contributes to a circum-Antarctic WSI extent that is probably twice as large as modern (Gersonde et al., 2005) maintaining deep and bottom water formation due to brine release during sea-ice formation (Schmittner et al., 2003; Shin et al., 2003). This process might have led to a large drop in atmospheric CO_2 due to salt transport into the deep ocean (Bouttes et al., 2010) that caused, together with the inhibited outgassing of CO_2 by extensive sea-ice cover, the increase of old, less ventilated water masses in the Southern Ocean during the glacial (e.g. Burke and Robinson, 2012; Skinner et al., 2015).

4.4.1.2 Start of deglacial warming

The rise of temperature after the LGM displays a similar gradient between eastern and western Pacific sector as during the glacial (*Benz et al., a; under rev.*). While in the eastern sector an increase of SSSTs started as early as 22 cal. kyr BP (Fig. 4.5m-o, p, s) the western sector starts with a temperature rise from 18 cal. kyr BP on (Fig. 4.5d, h, j). Though, due to the biased temperatures in several cores from the western sector as well as a relatively low time resolution in cores from the western PFZ (Fig. 4.5a-c) a probable early deglacial warming in the western sector can not be excluded. As most of the cores with an early deglacial are beyond the glacial sea-ice edge, the WSI concentration gives only minor hints for a possible early retreat (Fig. 4.5m-q). However, especially cores from the SAZ show a simultaneous increase of the *Chaetoceros* spp. resting spores together with a decline of the cold-water diatom *E. antarctica* (Fig. 4.3l-n) indicating surface water stratification

Figure 4.7: Selected SSST and WSI records from the Pacific sector of the Southern Ocean (for references see Table 4.1) compared to an Atlantic record, orbital parameter, midsummer insolation as well as arctic and antarctic ice core parameters for revealing interhemispheric relationship. Precession and obliquity (Laskar et al., 2004); ice-volume equivalent sea level (esl, Lambeck et al., 2014); daily northern and southern midsummer insolation (Laskar et al., 2004), OT: Onset of Termination after Schulz and Zeebe (2006); NGRIP $\delta^{18}O$ (NGRIP Members, 2004; GICC05 time scale); deep-water ventilation ages (benthic foraminifera to atmosphere) from core MD07-3076 (Skinner et al., 2010); PCA Pacific SSST (this study); EDC and WDC non-sea salt Na (Fischer et al., 2007; WAIS Divide Project Members, 2013); EDC and WDC CO_2 (Lüthi et al., 2008, AICC12; Marcott et al., 2014); EDC $\delta^{18}O$ and WDC $\delta^{18}O$ (Stenni et al., 2006, AICC12; WAIS Divide Project Members, 2013). AMOC: Atlantic Meridional Overturning Circulation; AHO: Antarctic Holocene Optimum; AIM 1: Antarctic Isotope Maximum; 1ACR: Antarctic Cold Reversal; B/A: Bølling/Allerød; H1: Heinrich stadial 1; LGM: Last Glacial Maximum; PCA: Principal Component Analysis; YD: Younger Dryas.
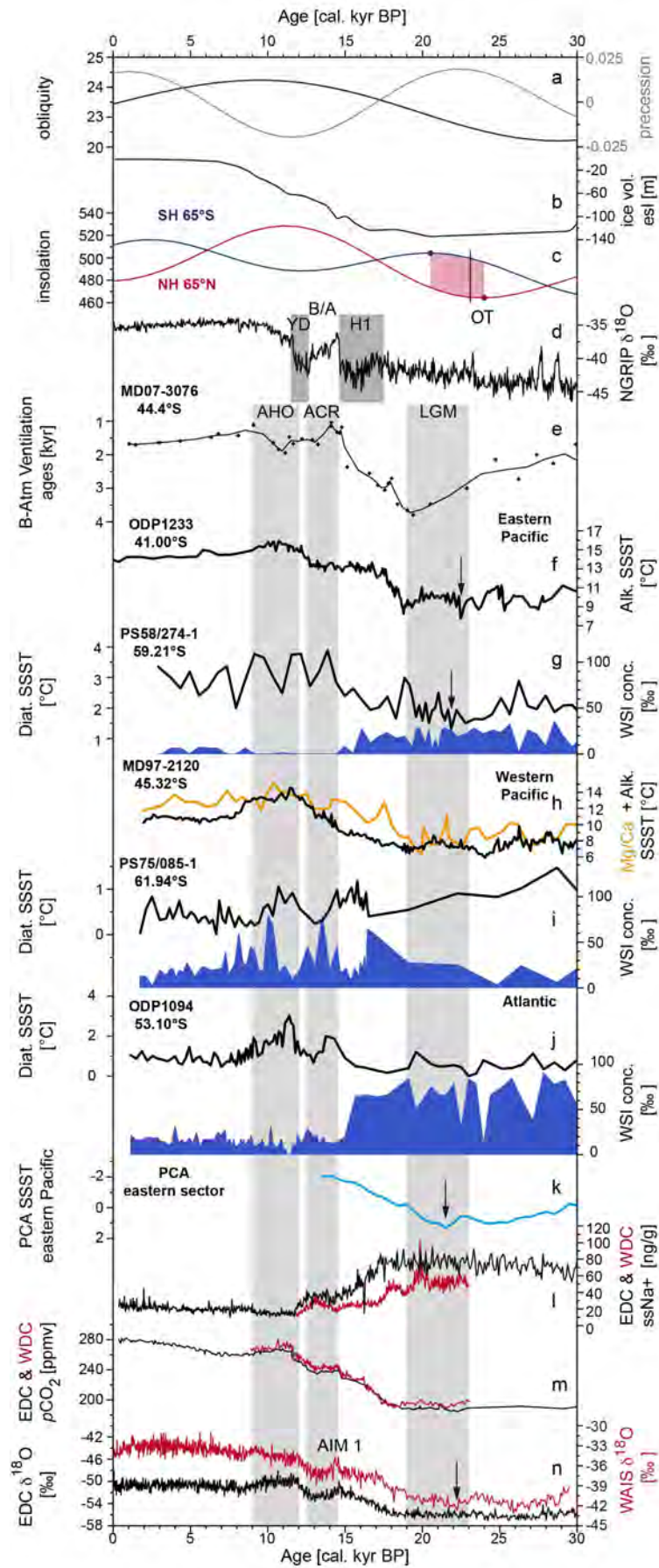
due to melting sea ice and favoring bioproductivity. At core sites from the Pacific Antarctic Ridge, the *Chaetoceros* spp. abundances that were continuously high throughout the glacial show peak abundances directly at the end of the LGM at 19 cal. kyr BP. This pattern implies significant discharges of meltwater at the end of the LGM exceeding the seasonal meltwater input throughout the LGM. The sedimentation rates at these time slices do however not show a clear pattern associated with an early or late warming (Fig. 4.2).

The pattern of an early start of deglacial warming was not yet in the focus of other temperature reconstructions in the Pacific sector of the Southern Ocean. However, there are indications that the rise of temperature starting as early as 23-21 cal. kyr BP can be also observed in previous studies (Pahnke et al., 2003; Pahnke and Sachs, 2006; Romero et al., 2006; Kaiser et al., 2008; Kaiser and Lamy, 2010; Tapia et al., 2015). Temperature records from core sites off the Chile margin show an early warming step at ~22.5 cal. kyr BP with a subsequent significant rise of SST from 18-19 cal. kyr BP on (Figs. 4.6h; 4.7f; Kim et al., 2002; Kaiser and Lamy, 2010) or a steady warming over Termination I (Romero et al., 2006, Kaiser et al., 2008). Such pattern is also visible at core locations in the central Pacific sector (Fig. 4.6i; Tapia et al., 2015), and in the STZ off NZ (Fig. 4.6b; Pahnke and Sachs, 2006). However, temperature records off southern New Zealand and the Australian bight show the first distinct warming step between 17-19 cal. kyr BP (Fig. 4.6a, c; Pahnke et al., 2003; Pahnke and Sachs, 2006; Calvo et al., 2007). Previous studies from the SAZ around 120°W (Fig. 4.6k; Mashiotta et al., 1999) do also not corroborate the early temperature rise found in our cores at the same latitude, yet further north around 45°S, foraminiferal temperature reconstructions show an early warming from 20 cal. kyr BP (Fig. 4.6j; Tapia et al., 2015). Sea-ice retreat from the Scotia Sea and the westernmost Pacific sector as early as 21-20 cal. kyr BP (Crosta et al., 2004; Collins et al., 2012) is further in line with the early warming in the Pacific sector, and directly influenced areas through the exchange via the cold-water route though the Drake Passage. Additionally, δ^{15}N records in the central and eastern Pacific sector, indicating nutrient supply and utilization in surface waters, show an early rise between 21-22 kyr cal. BP (Verleye et al., 2013). This rise in δ^{15}N corresponds to a decrease of dinoflagellate cysts that has been interpreted as a poleward shifting ACC (Verleye and Louweye, 2010).

Available temperature records from the westernmost Pacific sector resemble the early warming around 21.5 cal. kyr BP (Fig. 4.6d; Crosta et al., 2004), whereas in the Atlantic sector the SSST estimates do not show any significant warming step prior to 19-18 cal. kyr BP (Fig. 4.7j; Bianchi and Gersonde, 2004;). Yet, a retreat of sea ice in the Atlantic sector

starting around 22-21 cal. kyr BP is observable from two cores in the eastern Atlantic, located in the PFZ and POOZ (Abelmann et al., 2015). In a recent study on the deglacial temperature rise and its starting point in the different world oceans, the South Pacific SST stack do not show any early warming (He et al., 2013). Instead it resembles the trend from the Atlantic sector, resulting in an SH Ocean stack, that shows the temperature rise from 19 cal. kyr BP on. Yet, a significant difference to our comparison of new data with earlier studies from the Pacific sector is that the different stacks starts from 21 cal. kyr BP on, not including the entire LGM time slice. Therefore, the early warming that can be seen in cores used by He et al. (2013) is not fully included in the stacks from the Southern Ocean. Furthermore, the six cores that generate the Pacific stack are all situated north of 45°S in the northern SAZ or STZ and at continental margins and/or plateaus. As such the SH stack may lack signals that are directly associated with the ACC from the open ocean and the proximity of the Antarctic continent. Such stack must be extended with reconstructions from the Antarctic zone of the Pacific sector and on a longer time scale.

The observed differences in the temperature pattern of the Atlantic and Pacific sectors are highly comparable to antarctic ice core records from the different drilling sites in the SO catchment areas (Petit et al., 1999; Blunier and Brook, 2001; Brook et al., 2005; EPICA Community Members, 2006; Jouzel et al., 2007; Stenni et al., 2011; WAIS Divide Project Members, 2013). In several antarctic ice core records an early warming can be observed especially at core locations on the WAIS together with an early retreat of sea ice (Byrd ice core; Blunier and Brook, 2001; Siple Dome, Brook et al., 2005; WAIS Divide Project Members, 2013). The WAIS Divide Project Members (2013) stated in their study that by sea-ice retreat in the Pacific SO, triggered by insolation changes, the WDC warms before 18 cal. kyr BP as the WAIS is directly influenced by the adjacent ocean. Such feedback mechanism between the ocean and the marine-based ice sheet is not recorded from ice sheets, of East Antarctica, where the influence of sea ice and ocean temperature plays an inferior role. This hypothesis is supported by a study of Schulz and Zeebe (2006), proposing a mechanism called the "insolation canon", where a synchronous, prolonged (≥1000 yr) increase of Northern Hemisphere (NH) and Southern Hemisphere (SH) insolation triggers the termination. The onset of Termination I (OT) is dated to 23.1 cal. kyr BP, lying between the NH minimum and the SH maximum insolation (Fig. 4.7c). Therefore, the authors also suggest a lead of the SH warming around a termination. An alternative scenario also sees the high SH insolation as trigger of warming but the continuing rise of temperature as a result of reaching maximum obliquity which results in prolonged and higher total summer energy

(Fig. 4.7a; Drysdale et al., 2009). The early warming recorded from the WDC ice core is further corroborated by studies of glacier retreat in the Amundsen Sea Embayment where the deglaciation of the outer shelf occurred as early as ~22 cal. kyr BP (Smith et al., 2011; Klages et al., 2014) consistent with the retreat from the outer Ross Sea shelf (~25 cal. kyr BP, Mosola and Anderson, 2006) and the Bellingshausen Sea (25.5 cal. kyr BP, Hillenbrand et al., 2010). Significant ice sheet retreat is coincident with rising sea level after the minimum lowstand around 21 cal. kyr BP (Fig. 4.7b; Lambeck et al., 2014) that further influence the marine-based WAIS.

As signals in the Southern Ocean are further propagated via the export routes, the lag of sea-ice retreat and temperature rise in the Atlantic sector with regard to the Pacific sector may have been the result of an overprinting bipolar seesaw in the Atlantic Ocean. As already indicated by the different signals in ice cores associated with the different ocean sectors (Fig. 7l-n), the marine data as well show a decoupling regarding the initial start of the termination in the different SO basins. However, the CO_2 records from the WDC and EDC ice cores show remarkable similarity with a simultaneous rise starting between 19-18 cal. kyr BP (Lüthi et al., 2008; Marcott et al., 2014). As such, the early warming in the eastern Pacific together with the sea-ice retreat may have no significant impact on the upwelling of CO_2 enriched deep water. However, latest reconstructions of ventilation ages and $\Delta^{14}C$-values of the last 30 kyr in the Pacific sector of the Southern Ocean show an early weakening of glacial stratification and a transfer of old carbon into the intermediate-water level (Ronge, 2014). The carbon release from the deeper ocean may have been coupled to the early warming in the West Antarctic region and the retreat of WSI in the eastern Pacific sector. Yet, as no significant changes in the sedimentation rates of cores located in the modern SAZ is visible in the late glacial (Fig. 4.5m-o), no distinct change in the rate of bioproductivity and subsequent opal burial might have occurred (Fig. 4.2k-n). As such, the carbon release from deep waters was probably buffered in intermediate waters until significant upwelling and sea-ice retreat took place also in the western Pacific as well as the Atlantic sector. As the CO_2 rise in the EDC ice core record occurred synchronous with the temperature rise (Parrenin et al., 2013) the early warming and the sea-ice retreat reported from the eastern Pacific sector was not directly propagated to the Atlantic sector. A probable mechanism for the lag of the Atlantic sector is the shutdown of the Atlantic Meridional Overturning Circulation (AMOC) at ca. 18 kyr (McManus et al., 2004) together with the southward shifting Intertropical Convergence Zone (ITCZ) and SH westerlies (De Decker et al., 2012). The already warmed SH coupled with the cooling in the NH eventually leads to significant warming in the Atlantic sector

initiating the sea-ice retreat in this sector and vigorous upwelling, thus outgassing of CO_2. Such a late start of CO_2 outgassing via the Atlantic sector is further corroborated by the decrease of ventilation ages in the Atlantic sector beginning at 19 cal. kyr BP (Fig. 4.7e; Skinner et al., 2010). Though the essential contribution to the beginning of the atmospheric CO rise is governed by the Atlantic sector in response to the NH, the Pacific sector points to an active role of the SH in triggering the last deglaciation.

4.4.2 Termination I

4.4.2.1 Early deglacial (Heinrich I)

After the different onset of warming in the eastern and western Pacific sector, all cores show a relatively steady rise of temperature during the early deglacial (18-16 cal. kyr BP). In the eastern sector the abundances of sea-ice indicating diatoms diminished throughout this time period to <0.5% (Fig. 4.4k-q) indicating rapid sea-ice retreat that is further accompanied by WSI concentration values under 20% (Fig. 4.5 m-s). Hence, in this Pacific sector the maximum WSI edge may have reached to ~61°S, representing an expansion of ca. 3° in latitude. Although sea ice is still present, it is distinctly less expanded than in the western sector, mirroring the modern sea-ice distribution in the Pacific sector. Despite a significant WSI retreat in the western sector especially obvious in cores covered by >40% sea ice (Fig. 4.5d, e, h-j), the maximum WSI edge probably still reached, similar to the glacial expansion, to ca. 57°S and follows the trend of the Pacific Antarctic Ridge, where values of up to 40% are present accompanied by sea-ice indicating diatom abundances of ~3% (Fig. 4.4d-j). Additionally the SSST change in the early deglacial in these cores are only minor about ca. 0.5-1°C. As the total variance of cores from modern SSSTs in the range of 1-2°C is generally relatively low, a significant warming during the deglacial is predominantly visible in cores from the PFZ (Fig. 4.5a-c) and the northernmost POOZ (Fig. 4.5d-e).

Differences between the eastern and western sector are further indicated through abundance changes of the other diatom taxa. In the eastern modern SAZ the *Chaetoceros* spp. resting spores show rather constant values during the early deglacial (Fig. 4.3l-n) whereas the abundances in the modern PFZ exert a steep increase towards the late deglacial (Fig. 4.3o-p). In the modern SAZ *Chaetoceros* spp. abundances were significantly high, whereas in the modern PFZ *F. kerguelensis* abundance showed a constant increase. However, the sedimentation rates in the eastern Pacific sector do not indicate changes in the biological pump efficiency usually reflected by high *F. kerguelensis* abundances (Smetacek et al., 2004)

Apart from small-scaled changes in cores from the modern PFZ, the sedimentation rates remained constant during the early deglacial (Fig. 4.2k-q). The only distinct rise in sedimentation rates occurred around 16 cal. kyr BP in core PS75/059-2 (Fig. 4.2l). In contrast, the western Pacific cores that are influenced by the retreating sea ice and thus meltwater intrusion, that fuels prominent diatom blooms (Arrigo and Thomas, 2004), show a first rise in sedimentation rates around 19 cal. kyr BP (Fig. 4.2g-h) and a second more significant step between 17-16 cal. kyr BP (Fig. 4.2d-f, i-j). The second increase in sedimentation rates occur together with an increase of *F. kerguelensis* abundances (Fig. 4.3d-e, h-j).

Nevertheless, the general trend of rising temperature and retreating sea ice at all core sites around 19-18 cal. kyr BP (Figs. 4.6, 4.7) resembles that of antarctic ice core temperature and sea salt Na (ssNa) concentration results (Fig. 4.7l, n; Fischer et al., 2007; WAIS Divide Project Members, 2013). The pattern is also consistent with SST reconstructions from the westernmost Pacific sector (Fig. 4.6d), off New Zealand (Fig. 4.6a, b), from the Chilean margin (Fig. 4.6h, 4.7f) and the Atlantic sector of the Southern Ocean (Fig. 4.7j). Additionally, the majority of deglaciation in New Zealand and Australia occurred from 17 cal. kyr BP on (Schaefer et al., 2006) mirroring the glacier retreat in Patagonia (Kaplan et al., 2008). Thus the marine circum-Antarctic evolution of the deglacial temperature rise towards the Holocene displays a comparable pattern. Generally, the distinct SST rise starting around 19 cal. kyr BP is steeper at core sites covered previously by winter sea ice south at or south of the APF (e.g. SO136-111, PS75/064-1, Figs. 4.5h, 4.6d). Further north in the central Pacific or off NZ the temperature shows a more gradual increase. However, at the core site south off Australia, that is influenced by strong temperature gradients associated with frontal positions a steep SST increase is visible (Fig. 4.6a; MD03-2611, Calvo et al., 2007). Especially in the Humboldt Current System the warming of the SH leads to an abrupt SST rise as the deflection of cold water along the South American coast declines with increasing temperatures reaching almost modern values in the eastern Pacific sector.

The distinct deglacial temperature rise, occurring in records from all Southern Ocean sectors is concomitant with the cold Heinrich I event in the NH (H1; 18-15 cal. kyr BP) when outbursts of meltwater and icebergs led to the shutdown/reduction of the AMOC after 18 cal. kyr BP (McManus et al., 2004). The slowdown of the AMOC favored the storage of heat in the SH (Knorr and Lohmann, 2003). Additionally, the ITCZ was pushed southward due to WSI advances in the NH, leading to poleward shifting southern westerlies (De Deckker et al., 2012). The southerly position of the wind belt in turn favored eventually the circum-Antarctic

retreat of sea ice due to wind-driven upwelling of warmer Circumpolar Deep Water (CDW) (Denton et al., 2010). Ultimately, the outgassing of CO_2, that started not before the AMOC shutdown and was probably induced by increased upwelling, accelerated the warming of the SH (Toggweiler et al., 2006; Anderson et al., 2009). Coupled climate models further produce changes in the sea level pressure in mid- and high-latitudes under increasing atmospheric CO_2 (Cai et al., 2003) expressed by a trend of the SAM to a high index state where negative anomalies over Antarctica intensify the polar vortex and strengthen the westerlies (Thompson and Wallace, 2000). The SAM upward trend and changing wind stress curl in the mid-latitudes strengthened the East Australian Current and subsequently the South Pacific subtropical gyre and led to a southward shift of an inter-basin super gyre (Cai et al., 2005). This poleward shift might have further increased the warming in the Pacific sector of the Southern Ocean. An increased inflow of Subtropical water associated with a strengthened South Pacific Gyre is corroborated by foraminiferal studies from the Chatham Rise and Campbell Plateau during the early deglacial (Marr et al., 2013).

4.4.2.2 Antarctic Isotope Maximum I (AIM I)

The deglacial rise of SSST induced by the bipolar seesaw reached a temporal optimum especially at core sites in the western sector between 16 and 14 cal. kyr BP, which was accompanied by a drop in sea-ice concentration (Fig. 4.5d-e, i-j). The winter sea-ice occurrence was significantly reduced placing the sea-ice edge approximately at its present position. Concomitant with a decrease of sea-ice diatom abundances (Fig. 4.4d-e, g-j) the *Chaetoceros* spp. abundances increased at core sites in the AZ (Fig. 4.3d-f, i-j). Despite the more distinct occurrence of the first temporal optimum in the western sector, the coincidence of the sea-ice diatom decrease and *Chaetoceros* spp. increase is also observable in the modern eastern PFZ. These high abundances of *Chaetoceros* spp. in cores from the western AZ and eastern PFZ indicates higher productivity probably induced by melt water due to sea-ice retreat or iceberg discharge and thus stratification in the upper water column (Fig. 4.3d-f, i-j, o-q). The rise of *Chaetoceros* abundances and *F. kerguelensis* abundances at this time interval (Fig. 4.4d-f, i-j) is further in line with the significant increase of sedimentation rates in the western modern AZ especially in those cores covered by >40% WSI during the LGM (Fig. 4.4d-f, i-j). In the eastern sector the sedimentation rates do not show a significant change since the glacial except for core site PS75/059-2, that exhibit a slight increase around 15.5 cal. kyr BP (Fig. 4.2l).

The timing of the warm optimum is in accordance with other Pacific Southern Ocean records (Fig. 4.6; Calvo et al., 2007; Kaiser and Lamy, 2010; Tapia et al., 2015) as well as with records from the Atlantic sector (Fig. 4.7j; Bianchi and Gersonde 2004). Despite uncertainties regarding the reservoir ages during the deglacial due to upwelling of old carbon-rich deep waters (e.g. Siani et al., 2013), the timing of the temporal optimum is broadly consistent with the Antarctic Isotope Maximum 1 (AIM1) found in antarctic ice cores (Fig. 4.7n; WAIS Divide Project Members, 2013).

The steady warming during the early deglacial especially in the eastern Pacific sector indicates a shrinking extent of the cold-water realm compared to the huge northward expansion during the glacial. This leads to a reorganization of the ACC zonal system regarding the maximum opal productivity and burial zones as well as the associated SSSTs of the frontal system. Compared to the LGM, the maximum opal export and burial thus shifts southward, corroborating the maximum opal fluxes during the deglaciation found in the western Pacific sector (Chase, et al., 2003; Anderson et al., 2009; Bradtmiller et al., 2009). The higher productivity and opal burial south of the modern APF is further favored by the upwelling of nutrient-rich deep water (Anderson et al., 2009). Due to the general southward shift of the wind system together with the shift of the cold-water realm and the retreat of sea ice, the strong export of probably nutrient rich antarctic surface water into the Humboldt Current was decreased in the early deglacial. Hence, along the South American coast, the productivity and opal burial that was high during the LGM is reduced (Hebbeln et al., 2002; Ehlert et al., 2013; Chase et al., 2014). The transition from full glacial to deglacial conditions may have been governed by once upwelling of silicid acid depleted Subantarctic Mode Water (SAMW) (Ehlert et al., 2013) or by a poleward shift of the SWW similar to LGM conditions subsequently leading to less precipitation and eventually less glacial erosion delivering additional silicon (Chase et al., 2014).

The increasing SSSTs during the deglacial in the Pacific sector of the Southern Ocean influenced the exchange of water masses with the Atlantic sector through the Drake Passage. Together with the retreat of the WSI cover and the rising temperatures the water masses transported into the Atlantic sector were imprinted with SSSTs comparable to the modern PFZ water temperatures. Hence, the warmer water transported into the Scotia Sea may have influence on the retreat of WSI in this area from ~17 cal. kyr BP on (Collins et al., 2012). Additionally, the enhanced warm water transport supports eventually the deglacial warming in the Atlantic and Indian Ocean sectors, comparable to the cooling in the LGM (*Benz et al., a; under rev.*). Furthermore, as surface water with SSSTs warmer than 4°C are not entirely

deflected along the South American coast, the isolation of the Southern Ocean that is visible during the LGM strongly decreases.

4.4.2.3 Antarctic Cold Reversal (Bølling-Allerød)

The warming trend observed at the majority of studied core sites was interrupted by reoccurring colder conditions starting between 15 and 14 cal. kyr BP and lasting for approximately 2-3 kyr (Fig. 4.5d-j, n-s, 4.8a). The cold water realm was shifted northward with an average displacement of 3° in latitude of the 4°C isotherm. In contrast to the LGM reconstruction (*Benz et al., a; under rev.*), this isotherm, that approximates the SSST at the modern APF, did not reach to the Campbell Plateau but largely follows the Pacific Antarctic Ridge. All reconstructed isotherms resemble the bottom topography, which led to stronger temperature gradients in the western than in the eastern sector (Fig. 4.8a). Hence, in the eastern sector the 2°C isotherm resembles approximately its modern position around 62°S whereas in the western sector it is shifted northward by ca. 3° in latitude. The decrease of SSSTs is concomitant with a re-advance of the average sea-ice edge to the Pacific Antarctic Ridge at core sites from the western sector (Figs. 4.5i-j, 4.8b, Table 4.3). However, in both sectors the maximum WSI edge expands northward about 2-3° in latitude resembling the trend of the modern WSI edge, resulting from topographic forcing. Event-like advances in the eastern sector seem not to occur regarding the distinct NS gradient of the WSI concentration values (Fig. 4.8b). This gradient is further mirrored by absent or extremely low abundances of the *F. curta* group in the SAZ and northern PFZ (Figs. 4.4k-o, 5 m-q). The relative position of the WSI in the western sector is further concomitant with increasing abundances of sea-ice diatom species (Fig. 4.4d-e, g-j). At core sites from the western modern PFZ the low time resolution inhibits further implications on the exact behavior at this time period. Where a slight re-advance of sea ice is visible together with a drop in temperature (Fig. 4.5a) the sea-ice indicating diatom species are negligible (Fig. 4.4a), whereas at core sites with a newly increase of sea-ice diatoms (Fig. 4.4b) the SSST drop is displayed ca. 1.5 kyr later (Fig. 4.5b). Similar to core sites from the SAZ and northern PFZ in the eastern sector, at core sites from the SW-Pacific Basin may not experience a distinct cold reversal.

Differences in the *Chaetoceros* pattern between eastern and western Pacific sector (Fig. 4.3) may probably result from sea-ice/iceberg transport by westerly winds into the eastern sector, as it is observed today (Assmann et al., 2005), inducing prominent *Chaetoceros* blooms during the cold reversal in the southern SAZ (Fig. 4.3l-n). The ice

transport into the eastern or central Pacific sector is further in accordance with increasing lithogenic fluxes from west to east (Bradtmiller et al., 2009) hence resulting in higher iron
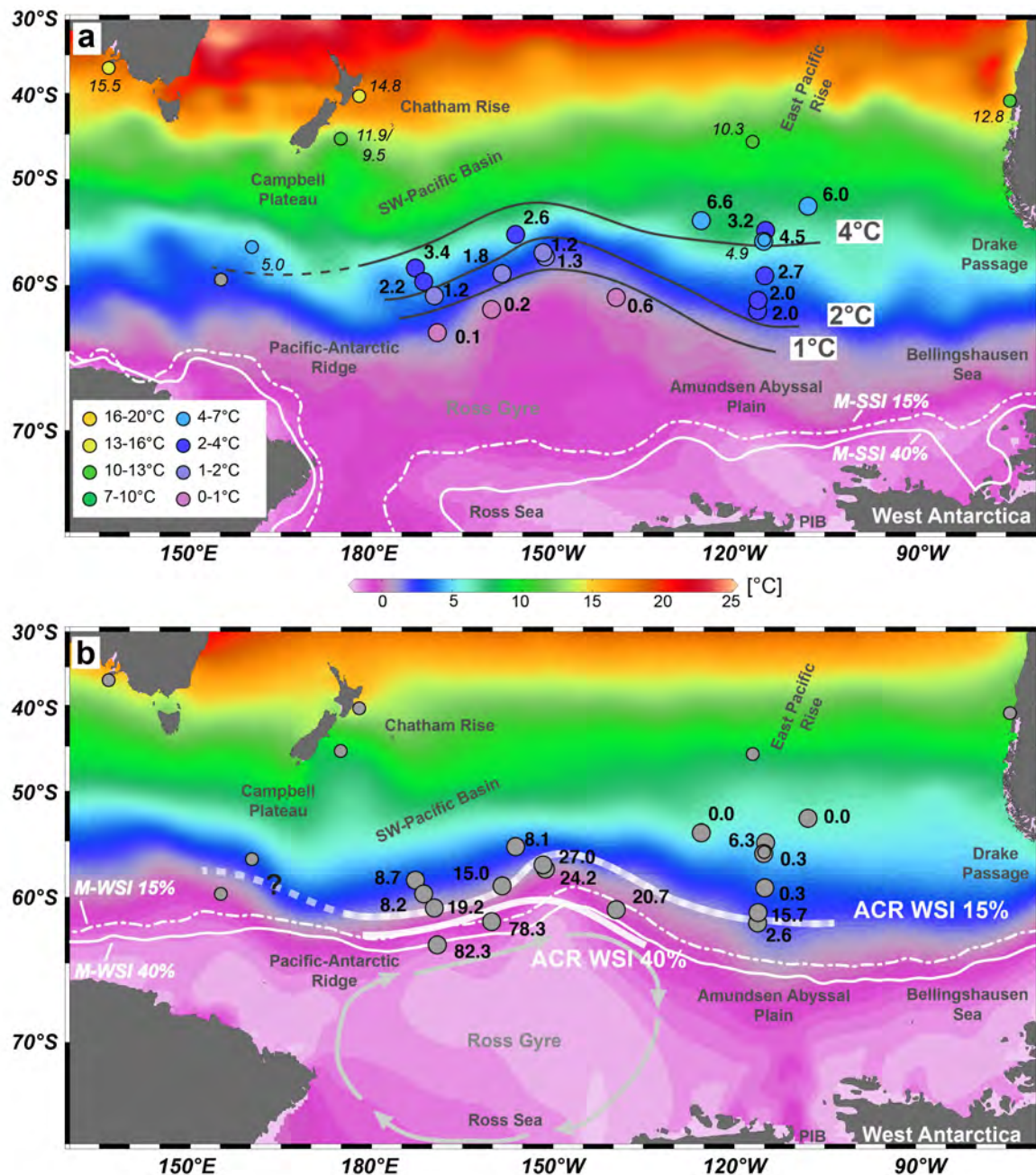

Figure 4.8: **(a)** Estimated ACR SSST compared to modern HASO SSST (Olbers et al., 1992) and modern SSI (Reynolds et al., 2002, 2007) with averaged SSST isotherms (in °C). Numbers indicate minimum temperatures within the ACR time slice for cores in this study (bold) and from literature (italic, see Tables 4.1, 4.3); Color scale of core symbols represent color code of the HASO SSST. **(b)** Estimated ACR WSI distribution compared to modern WSI distribution and WOA09 winter SSTs. Numbers indicate maximum estimated sea-ice concentration during the ACR time slice from this study (see Table 4.3). ACR WSI estimates include the maximum winter sea-ice extent (>15% September concentration). Modern winter sea-ice edges after Reynolds et al. (2002, 2007).

availability. In contrast, recurrence of sea ice in the western sector is also accompanied by an increase of *Chaetoceros* spp., yet not as significant as during the glacial period or in the eastern SAZ (Fig. 4.3h-i). In general, this is in line with decreasing iron contents in marine and antarctic ice cores during the deglaciation (Martínez-Garcia et al., 2009; Lamy et al., 2014). As new peaks in *Chaetoceros* spp. abundances occur partly at the beginning of the second rise of temperature after the cold reversal in the western and eastern sector, this pattern points to meltwater-induced diatom blooms due to probably more stratified surface water conditions around 13-12 cal. kyr. BP (Fig. 4.3d-e, o-p). The *Chaetoceros* spp. peak abundances in the modern SAZ occurred together with decreased *F. kerguelensis* abundance but increasing sedimentation rates in the same cores (Fig. 4.2l-n). Similar to the deglacial less biogenic opal burial is found in the modern SAZ (Lamy et al., 2014), and the high sedimentation rates probably represent a shift from a diatom dominated to a carbonate facies (e.g. core description of PS75/059-2 in Gersonde, 2011). Significant sedimentation changes took further place in cores from the seasonal SIZ, where the sedimentation rate drops simultaneously with a renewed cooling and the recurrence of WSI (Figs. 4.2 and 4.5 i-j).

Previous studies from the Pacific sector of the Southern Ocean do not show a pronounced cold reversal as observed in the southernmost open ocean cores (Fig. 4.6a-d, h, i, k). The majority of SST estimates show rather stable conditions during this time slice e.g. ODP1233, Fig. 4.6a, d, h) or a further steady rise of temperature (Fig. 4.6b, c, i, k). However, the still relatively cold SSTs at the Chilean coast compared to modern indicate a similar northward deflection of colder water masses as in the LGM. However, such huge northward expansion as seen in the western Pacific sector during the LGM time slice does not occur.

In the westernmost Pacific sector, temperatures from the modern PFZ (Fig. 4.6d) resemble their modern value around 5°C, placing the 4°C-isotherm at its present position. This result is consistent with a lack of WSI at this core site after ca. 15 cal. kyr BP (Crosta et al., 2004). Yet, new sea-ice reconstructions from this core sites established with the Generalized Additive Model (GAM) and MAT indicate sea-ice presence during the ACR (Ferry et al., 2015a, b). However, as the established RMSEP ranges for both methods between 14 and 28%, the estimations remain relatively weak. Thus the assignment of the 15% maximum winter sea-ice edge remains unclear. The occurrence of the ACR in Southern Ocean cores may generally be influenced by the proximity of the core location in relation to the influence of cold surface waters transported northward by the cold-water gyre or within the pathway of the ACC. This is corroborated by the significantly stronger development of the ACR in the western Pacific cores in the AZ, influenced by cold water from the Ross Gyre

and the vicinity to the modern WSI edge. In the Atlantic sector, available temperature estimations show similar results for the cold reversal between ca. 14 – 12 cal. kyr BP with a simultaneous recurrence of sea ice into the modern POOZ to approximately 53°S (Gersonde et al., 2003; Bianchi and Gersonde, 2004; Divine et al., 2010). The SSST values of ca. 1-3°C recorded from the modern Atlantic POOZ are in line with our estimates from the modern western POOZ and partly from the southern modern PFZ in the eastern sector. Furthermore, the maximum extent of sea ice and the cold-water realm is farther north considering latitude than in the Pacific sector, yet the relative latitudinal expansion of ca. 3° is highly comparable.

Table 4.3 AHO maximum and ACR minimum SSTs, anomalies and AHO minimum and ACR maximum sea-ice concentration from mapped foraminiferal (f), diatom (d) and alkenone (a) records.

Core	mod. SSST (°C)[a]	AHO SST max. (°C)	ΔAHO/mod. SSST (K)	AHO Sept. min SI conc. (%)	ACR SST min. (°C)	ACR Sept. max SI conc (%)	Referenz
ELT11-2	6.4	5.5 f	-0.9	--	4.9 f	--	Mashiotta et al., 1999
MD03-2611	17.9	19.3 a	3.0	--	15.5 a	--	Calvo et al., 2007
MD97-2120	12.0	15.2 f	3.2	--	11.9 f	--	Pahnke et al., 2003
MD97-2120	12.0	14.6 a	2.6	--	9.5 a	--	Pahnke and Sachs, 2006
MD97-2121	17.7	18.2 a	0.5		14.8 f		Pahnke and Sachs, 2006
ODP1233	14.7	16.0 a	1.3	--	12.8 a	--	Kaiser and Lamy, 2010
PS58/270-5	2.6	2.6 d	0.0	0.3	2.0 d	2.6	**this study**
PS58/271-1	3.0	3.5 d	0.5	0.0	2.0 d	15.7	**this study;** Esper and Gersonde, 2014a/b
PS58/274-1	3.9	3.8 d	-0.1	0.0	2.7 d	0.3	**this study**
PS75/051-1	7.7	7.2 d	-0.5	0.0	6.0 d	0.0	**this study**
PS75/054-1	6.3	5.0 d	-1.3	0.0	4.5 d	0.3	**this study**
PS75/056-1	6.8	5.1 d	-1.7	0.0	3.2 d	6.3	**this study**
PS75/059-2	7.5	7.1 d	-0.4	0.0	6.6 d	0.0	**this study**
PS75/064-1	0.7	1.5 d	0.8	9.7	0.6 d	20.7	**this study**
PS75/072-4	2.1	1.5 d	-0.6	11.1	1.3 d	24.2	**this study**
PS75/073-2	2.5	1.7 d	-0.8	1.6	1.2 d	27.0	**this study**
PS75/076-2	5.7	--	--	--	2.6 d	8.1	**this study**
PS75/082-1	2.5	2.0 d	-0.5	1.3	1.8 d	15.0	**this study**
PS75/085-1	0.3	1.1 d	0.8	9.0	0.2 d	78.3	**this study**
PS75/091-3	1.4	0.7 d	-0.7	11.9	0.1 d	82.3	**this study**
PS75/093-1	3.7	2.0 d	-1.7	9.9	1.2 d	19.2	**this study**
PS75/096-4	5.1	3.6 d	-1.5	1.3	3.4 d	8.2	**this study**
PS75/097-4	4.0	3.5 d	-0.5	1.2	2.2 d	8.7	**this study**
SO136-111	4.6	5.8 d	1.2	0.0[b]	5.0 d	0.0[b]	Crosta et al., 2004
SO213-59-2	9.9	12.6 f	2.7	--	10.3 f	--	Tapia et al., 2015

[a] Modern SSST after Olbers et al. (1992);
[b] Values representing sea-ice duration per month/per yer instead of concentrations.

The timing of the marine cold reversal is broadly consistent with recurring colder conditions and glacier advances in South Patagonia (Sugden et al., 2005; Moreno et al., 2009) and the New Zealand Alpes (Putnam et al., 2010; Newnham et al., 2012). Despite the mentioned uncertainties of reservoir ages in the Southern Ocean, the timing of the marine cold reversal is within the range of the ACR reported from antarctic ice cores (EPICA Community Members, 2006; WAIS Divide Project Members, 2013). Concomitant with lower antarctic temperatures in the time slice from 14.5-12.5 cal. kyr BP, the sea-ice proxy ssNa also indicates a wider circum-Antarctic sea-ice expansion (Fig. 4.7l; Fischer et al., 2007; WAIS Divide Project Members, 2013) that is confirmed by studies from all Southern Ocean sectors (Gersonde et al., 2003; Bianchi and Gersonde, 2004; Divine et al., 2010; Ferry et al., 2015b).

The repeated of cold surface water during the ACR together with the new advance of winter sea ice especially in the western Pacific sector is similarly to the LGM influenced by topographic and atmospheric forcing. Whereas the distinct bottom topography in the western sector favors the development of relatively significant ACR representing downscaled glacial-like conditions, the temperature and sea-ice trend over the Amundsen Abyssal Plain in the eastern sector seems to be more influenced by atmospheric changes. The shift to a more positive SAM index during the deglacial, that is associated with enhanced CO_2 outgassing (Lovenduski and Gruber, 2005; Cai et al., 2005), resulted in extremely low sea-level pressure over the Amundsen-Bellingshausen Sea (e.g. Lefebvre et a., 2004). Such conditions led to reduced sea-ice advance in this region and stronger advance of sea ice in the Ross Sea area (Fig. 4.8b). This pattern closely resembles the modern distribution of sea ice that is related to positive SAM years and probably more La Niña-like conditions (Koutavas et al., 2002) or at least weaker El Niño-like activity (Stainer-Urias et al., 2015).

Furthermore, the changes of atmospheric conditions may include a renewed equatorward shift of the westerly wind belt during the ACR similar to the shift during the last glacial, but not as significant to cause a temperature reversal at core sites from the lower latitudes (Fig. 4.6h, 4.7f; e.g. Lamy et al., 2007). Wind driven upwelling may be shifted slightly north in the northern Ross Sea area, leading to an associated shift of the maximum opal burial zone and decreasing opal flux south of the present APF after ca. 15 cal. kyr BP (Anderson et al., 2009). This is in line with distinct drops in sedimentation rates in the southernmost western cores (Fig. 4.2i-j). In contrast, cores from the eastern modern SAZ show higher sedimentation rates during the ACR (Fig. 4.2 l-n), yet not due to enhanced opal deposition (Bradtmiller et al., 2009; Lamy et al., 2014) but probably higher export of

carbonate. After reduced diatom productivity off the Peruvian coast during the early deglacial, the availability of silicic acid via upwelling increased as indicated by higher diatom productivity (Ehlert et al., 2013). Nutrient supply via upwelling is also visible in cores off the Chilean coast until 35°S, where the relative abundance of species associated with upwelling increases significantly after 15.5 cal. kyr BP (Romero, et al. 2006). Further south, recurring higher absolute abundances of coccoliths between 14 and 10 cal. kyr BP after a deglacial decrease are linked to a renewed ACC nutrient supply (Saavedra-Pellitero et al., 2011). The divergence between upwelling and ACC surface water induced higher productivity was already suggested by Romero et al. (2006) with an approximate boundary around 35°S. Such a change is concomitant with cold subantarctic water of ca. 4°C that is deflected into the Humboldt Current (Fig. 4.8a) similarly as during the LGM (*Benz et al., a; under rev.*) yet with less northward extent of the cold water tongue.

There is ongoing debate about the contribution of the Antarctic ice sheets to meltwater pulse 1A (MWP-1A) around 14.5 cal. kyr BP that may have been caused by the rapid warming in the SH and probably triggered the reactivation of the AMOC and thus the Bølling warming and ACR cooling (Weaver et al., 2003; Deschamps et al., 2012). Coupled climate models suggest an important role of especially the WAIS inducing significant cooling of the adjacent ocean by meltwater injection (e.g. Weaver et al., 2003). Despite a growing body of evidence, that the Antarctic ice sheet probably contributed half of the ~14 m sea level rise during the MWP-1A (Deschamps et al., 2012), an exclusive of the WAIS responsible for the meltwater event can not be verified (Hillenbrand et al., 2010). Recent studies imply that the WAIS, retreating to the mid- and inner shelf not before ca. 14.5 cal. kyr BP (Anderson et al., 2002; Smith et al., 2011), only contributed ~9 m until present to the global sea level thus representing an unlikely source for this meltwater event. It is probable that the meltwater pulse and the concomitant sea level rise triggered the reduction of the WAIS due to increased basal melt (Mackintosh et al., 2011). Additionally, our SSST records especially from the eastern Pacific sector do not confirm the proposed cooling by up to 7°C resulting from meltwater injection from the WAIS (Weaver et al., 2003) as they show a steady rise of temperatures instead of a distinct cooling. A similar behavior is recorded from the ice sheet in the Ross Embayment, that also contributed not significantly to the MWP-1A associated sea level rise (Anderson et al., 2014). And although the western Pacific records show cooling associated with the ACR after ~14.5 cal. kyr BP, the magnitude of around 1°C is not as significant as model data suggested for the MWP-1A (Weaver et al., 2003; Fig. 4.5).

4.4.3   Antarctic Holocene Optimum

The second rise of temperature after the ACR reaches a maximum around 12-9 cal. kyr BP. Compared to modern conditions, reconstructed SSSTs at the studied core sites display still colder or similar values (Figs. 4.5b-g, j, m-q, 4.9b). Only at a few sites in vicinity of the modern winter sea-ice edge the temperatures exceed modern SSSTs by up to ~1°C (Figs. 4.5h-i, 4.9b Table 4.3). The warming is further accompanied by minimum winter sea-ice expansion not reaching the modern WSI edge (Fig. 4.9c) as well as in general low abundances or total absence of sea-ice diatoms in the majority of cores (Fig. 4.4a-e, g-i, k-q). The core sites in the western PFZ and POOZ generally exhibit a shorter warm period compared to the sites from the eastern PFZ zone, yet its occurrence is more concise (Fig. 4.5d, g-i). Thus close to 9-10 kyr years the southernmost cores exhibit a newly advance of winter sea ice to ~62°S (Fig. 4.5i-j). The differences between the warmer SSSTs south and still colder SSSTs north of the present WSI edge may result from the position of the Antarctic divergence during this warm optimum. Subsequently, the upwelling of comparatively cold intermediate and deep water that was deflected northward by the Ekman drift at ca. 60°S may have led to colder SSSTs than observed south of 60°S (Lovenduski and Gruber, 2005). It may also be possible, that the distinct warming in the SH that was induced by the shutdown of the AMOC during the Younger Dryas significantly influenced the southern core sites, whereas the more northernmost sites reacted more slowly and with a further temperature rise during the Holocene. The shorter duration of the warm optimum at the southern cores sites may additionally be influenced by the significant retreat of sea ice and the WAIS around 12 cal. kyr BP (e.g. Das and Alley, 2008). The possible intrusion of meltwater may have led to abrupt surface-water cooling.

The northward shift of the 4°C isotherm during the warming is only slightly less compared to present in the western sector than during the ACR, resulting from the still colder than modern SSSTs at the northern core sites (Fig. 4.9a). However, in the eastern sector, although cores from the SAZ show negative anomalies, the SSSTs in the PFZ reaveal only minor deviations from modern SSSTs (~0.5°K, Fig. 4.9a). While this difference leads to the location of the 4° isotherm at its present position only in the eastern sector the 2° isotherm resembles its modern position in the entire study area (Fig. 4.10a).

Although the exact timing varies slightly from one site to another, the temperature optimum between roughly 12-9 cal. kyr BP is evident in the majority of cores in the Pacific sector of the Southern Ocean (Fig. 4.6, Table 4.3). Simultaneously with higher temperatures,
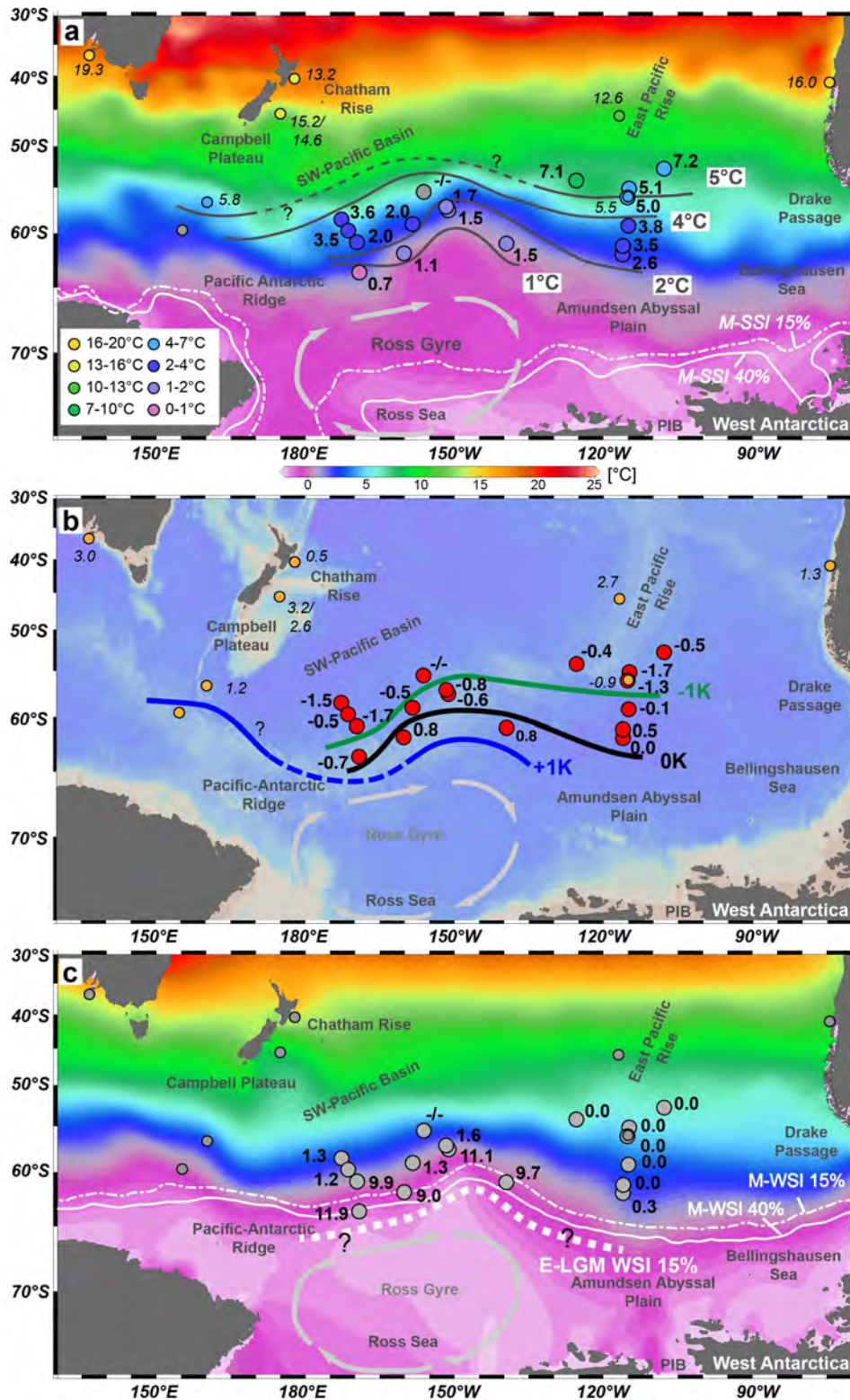
Figure 4.9: **(a)** Estimated AHO SSST compared to modern HASO SSST (Olbers et al., 1992) and modern SSI (Reynolds et al., 2002, 2007) with averaged SSST isotherms (in °C). Numbers indicate maximum temperatures within the AHO time slice for cores in this study (bold) and from literature (italic, see Table 4.1, 4.3); Color scale of core symbols represent color code of the HASO SSST. **(b)** Averaged SSST anomaly (AHO/modern) isotherms (in K) with single values for cores in this study (bold) and from literature (italic, see Table 4.1, 4.3). **(c)** Estimated AHO WSI distribution compared to modern WSI distribution and WOA09 winter SSTs. Numbers indicate minimum estimated sea-ice concentration during the AHO time slice from this study (bold) and the literature (italic, see Table 4.3). AHO WSI estimates include the maximum winter sea-ice extent (>15% September concentration). Modern winter sea-ice edges after Reynolds et al. (2002, 2007).

records from NZ and Chile indicate a progressive retreat of the glaciers (Schaefer et al., 2009, Kaplan et al. 2010) as well as increasing humid conditions resulting from higher precipitation and intensified westerlies (Barrell et al., 2012; Kilian and Lamy, 2012). The temperature optimum is further documented at core sites from the Atlantic sector (Fig. 4.7j; Gersonde et al., 2003; Bianchi and Gersonde, 2004). Although the optimum at all studied and compared core sites do not always exceed modern SSST values, it displays a marine circum-Antarctic warm optimum that is in agreement with the commonly called Antarctic Early Holocene Optimum (AHO; Masson et al., 2000) documented in antarctic ice cores (WAIS Divide Project Members, 2013). Based on the revised age models of the EDC ice core and associated temperature shifts (AICC12, Bazin et al., 2013; Veres et al., 2013) as well as on the marine records, we define the AHO from 12-9 cal. kyr BP. Although the AHO is visible in all antarctic ice cores, proxy records of the ice cores located in West Antarctica show further rising temperatures throughout the Holocene (Figs. 4.6g, 4.7n; WAIS Divide Project Members, 2013). This is similar to the SSST trend visible at marine core sites from the SAZ in the eastern Pacific sector (Fig. 4.5m-o). Similar to the development of the early deglacial, the steady rising SH insolation (Fig. 4.7c) towards the Late Holocene may have had a stronger impact on the eastern Pacific area with a direct implementation of the signal. The records from the western area as well as the other Southern Ocean sectors follow more closely the NH insolation (Fig. 4.7c) trend with a cooling during the Late Holocene.

Generally, the distinct temperature rise after the ACR and the following AHO are related to the ongoing interhemispheric changes associated with the bipolar seesaw. As such, the AHO is probably induced by the cold Younger Dryas, starting at ca. 12 kyr BP in the NH and a reduced AMOC storing heat in the SH (McManus et al., 2004). Additionally, strengthened westerlies during this time period (Lamy et al., 2010) favored intensified upwelling contributing to rising atmospheric CO_2 (Mayr et al., 2013) (Fig. 4.7m). Mirroring the development of the early deglacial the retreat of sea ice concomitant with a rise in atmospheric CO_2 after the ACR may have amplified each other (Cai et al., 2003), leading to significantly warmer temperatures and reduced sea-ice cover. Moreover, during the temperature rise towards the AHO strengthened El Niño-like conditions (Rein et al., 2005; Stainer-Urias et al., 2015) resulted in atmospheric heat flux into the Subantarctic Pacific, therebyenhancing the retreat of sea ice and warmer SSSTs (Yuan et al., 2004) (Fig. 4.9b, 4.10b).

The restored upwelling of older water masses and eventually the enhanced supply of nutrients during the AHO is accompanied by higher opal fluxes (Anderson et al., 2009),

coincident with increasing sedimentation at core locations from the eastern PFZ that are in line with maximum *F. kerguelensis* abundances (Figs. 4.2p, 4.3o-q). However, as the eastern Pacific sector experienced distinct warming after the ACR and the 4°C isotherm approximates its present position, low amounts of cold, nutrient rich water were transported northward along the Humboldt Current system, leading to a decrease in primary productivity and accompanied accumulation of diatoms, dinoflagellates and coccoliths (Romero et al., 2006; Verleye and Louwye, 2010; Saavedra-Pellitero et al., 2011).
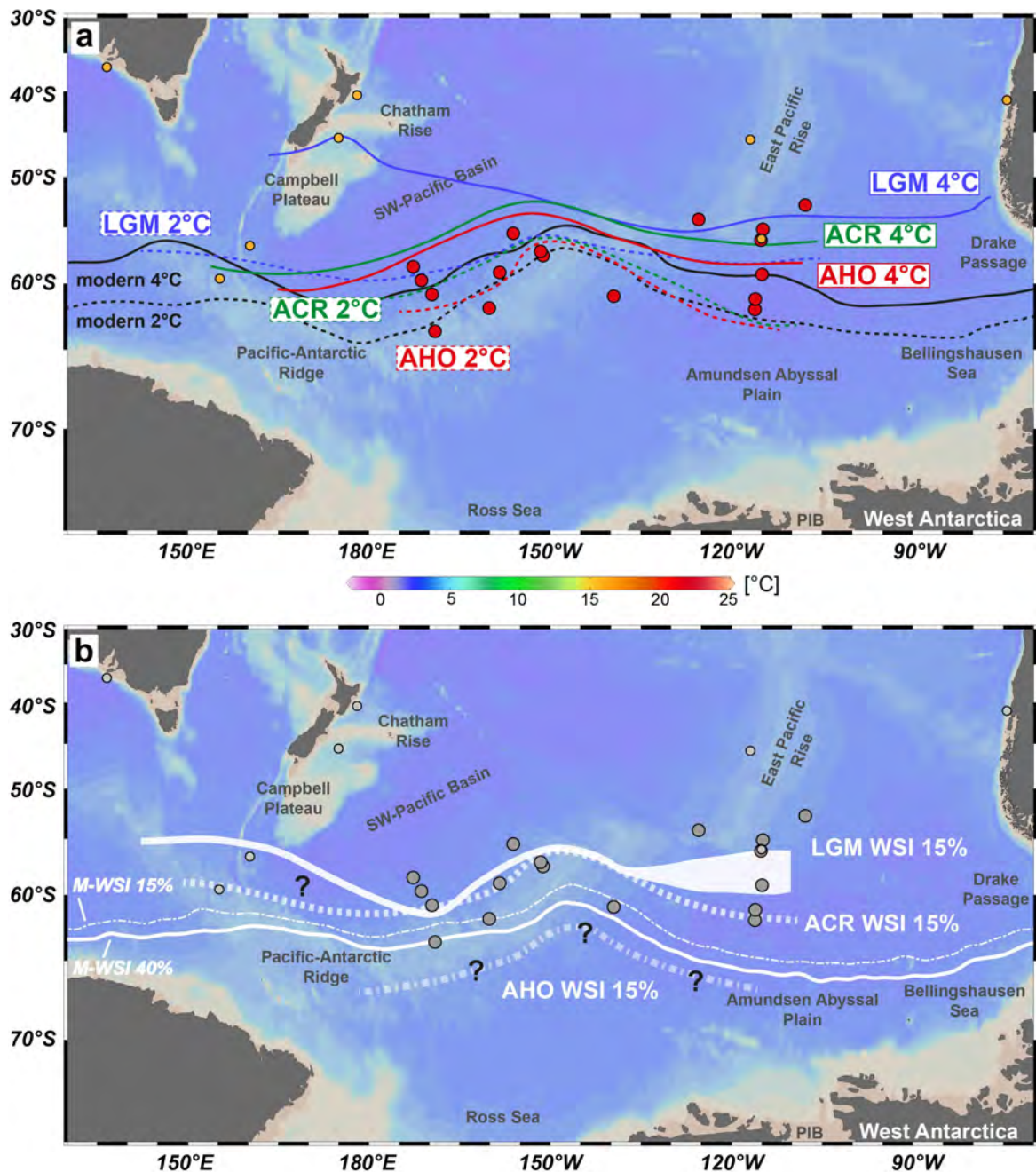
Figure 4.10: **(a)** Averaged 2° and 4°C isotherms for the time slices LGM, ACR and AHO compared to the modern 2° and 4° isotherm derived from HASO SSSTs (Olbers et al., 1992). **(b)** Estimated 15% WSI extent for the time slices LGM, ACR and AHO compared to modern 15% and 40% WSI extent (Reynolds et al., 2002; 2007).

4.4   Synthesis

The deglacial history in the Pacific sector of the Southern Ocean mainly displays the "Antarctic timing" pattern (after Lamy et al., 2004) known from continental margins (e.g. Kilian and Lamy, 2012), the Atlantic sector (e.g. Bianchi and Gersonde, 2004) and from antarctic ice cores (e.g. WAIS Divide Project Members, 2013). However, differences occur between the different Southern Ocean sectors regarding the onset of the deglaciation and its direct influence on CO_2 release after the glacial.

During the glacial significant WSI expansion (Fig. 4.11a) led to reduced air-sea-gas exchange, that favored the storage of CO_2 in the deep ocean (Fig. 4.11b). Additionally, the large seasonal change of sea-ice cover maintained the production of AABW via brine release during sea-ice formation, as the shelf areas, the primary modern AABW formation regions (Fig. 4.11a), were entirely covered by ice sheets. The northward shift of the SWW and increased dust supply during the glacial resulted in an equal northward shift of the main opal burial areas with opal flux comparable to modern conditions (Fig. 4.11b).

The "Antarctic timing" over the glacial/interglacial transition includes the deglacial warming in the Southern Hemisphere triggered by changing insolation in both hemispheres and orbital parameter variations (Schulz and Zeebe, 2006) and eventually the shutdown of the AMOC via freshwater input in the North Atlantic during Heinrich 1 (McManus et al., 2004). Though the eastern and western Pacific sectors exhibit a different timing concerning the initial start of warming between 23 and 18 cal. kyr BP, the rise of temperature reaches in both sectors a first warm optimum correspondent to the AIM 1. The increasing SSST during the early deglacial (18-15 cal. kyr BP) favors sea-ice reduction together with a poleward shift of the SWW that led to CO_2 outgassing via enhanced wind-driven upwelling. The input of nutrient repleted deep water governs increased bioproductivity and subsequent opal burial (Fig. 4.11c).

The strong warming in the SH ultimately resulted in enhanced antarctic ice sheet melting and enhanced water mass transport via the cold and warm water routes that fed back to the NH by resuming the AMOC and leading to a subsequent warming during the B/A (Knorr and Lehmann, 2003). Rather simultaneously the SH warming slowed down or even reversed documented in the marine and ice core records as the ACR (Fig. 4.11d, e.g. Stenni et al., 2011). In the eastern Pacific sector a less pronounced cooling led to almost modern conditions regarding the 2°C isotherm, whereas in the western Pacific sector, which is stronger influenced by the cold-water gyre in the Ross Sea similar conditions as during the

glacial occur (Fig. 4.10a). Biogenic opal burial shifted slightly north concomitant with the cold-water realm and the sea-ice edge and decreased compared to the deglacial (Anderson et al., 2009).
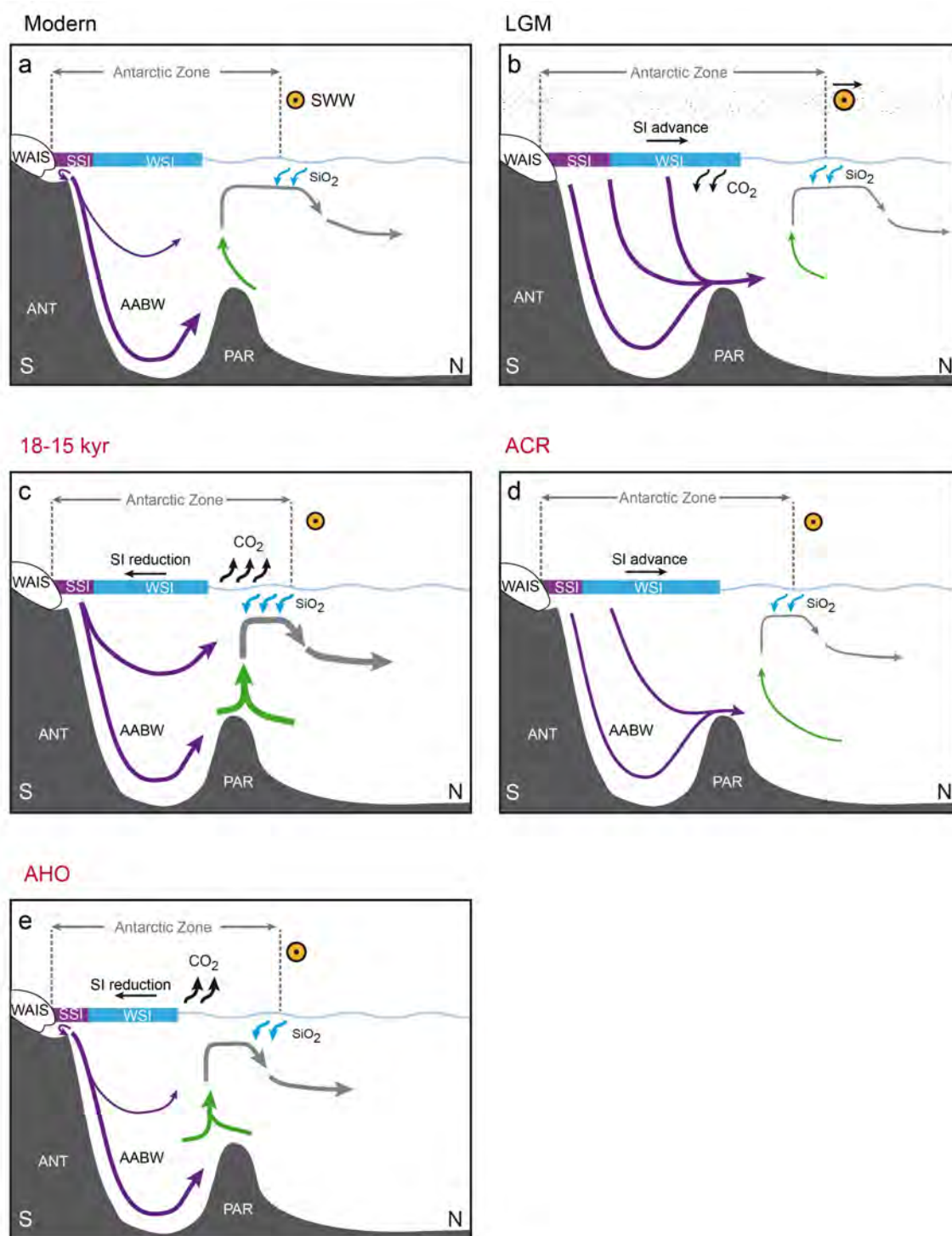

Figure 4.11: Schematic illustration of climate development in the LGM-Holocene Pacific sector of the Southern Ocean. **(a)** Modern conditions; **(b)** 23-19 kyr, LGM: Last Glacial Maximum; **(c)** 18 – 15 kyr; **(d)** 14.5 – 12.5, ACR: Antarctic Cold Reversal; **(e)** 12 – 9 kyr, AHO: Antarctic Holocene Optimum. AABW: Antarctic Bottom Water; PAR: Pacific Antarctic Ridge; SSI: Summer Sea Ice; SWW: Southern Westerly Winds; WAIS: West Antarctic Ice Sheet; WSI: Winter Sea Ice.

During the AHO (Fig. 4.11e) at the majority of core locations a significant thermal optimum occurred after a distinct rise of temperature, that mirrors the climate records of antarctic ice cores and the atmospheric CO_2 concentration (WAIS Divide Project Members, 2013, Marcott et al., 2014). In the SAZ of the eastern Pacific sector modern conditions were reached concerning the position of the 4 and 2°C isotherms (Figs. 4.10a, 4.11e). Yet, the maximum WSI extent probably did not extend as far north as seen at present (Fig. 4.10b). The rise of CO_2 is closely aligned to vigorous upwelling of deep-water masses that resulted from intensified westerlies and a positive SAM index (Cai et al., 2005; Lovenduski et al. 2007). Such upwelling of nutrient-rich waters promoted higher and subsequently resulted in higher opal export.

4.5   Conclusions

The temperature and sea-ice reconstructions from the Pacific sector of the Southern Ocean corroborate the common view of a relatively congruent circum-Antarctic pattern of Termination I. The temperature development generally appears to be characterized by in-phase changes, at least regarding the overall trends. However, there is strong evidence that the Southern Hemisphere insolation influenced an early sea surface temperature rise and sea-ice retreat especially in the Pacific sector of the Southern Ocean adjacent to the marine-based WAIS during the LGM time slice. Although this phenomenon appears to have a more regional impact, this result is essential for the interpretation of the signal propagation between the Southern Ocean sectors and the sensitivity of single areas. As atmospheric CO_2 concentrations are unaffected by the early warming as well as the sea-ice retreat, the huge outgassing via upwelling of deep water masses is primarily governed by deglacial changes in the Atlantic sector. The start of the AMOC may have been the eventual trigger for massive CO_2 release. To achieve significant evidence for the probably incomplete outgassing of CO_2 occurring at the early deglaciation more research has to be done concerning stratification of the water column based on diatom- and radiolarian-derived oxygen isotopic studies. Such proxies may decipher a possible buffering of radiocarbon depleted deep water in intermediate depths during the late LGM.

Our reconstructions further indicate that the WAIS triggered MWP-1A is unlikely concerning the minor temperature drops that would be associated with such massive cold meltwater intrusion into the surface ocean. Generally, the Antarctic timing of the deglaciation events is closely related to the bipolar seesaw, yet the trends in temperature and

sea-ice extent are further linked to the atmospheric changes induced by the glacial to interglacial shifts of the SAM and the strength of the ENSO

4.6   Acknowledgments

Chapter 5 – Holocene climate variability in the high-latitude western South Pacific based on diatom-derived sea surface temperatures and sea-ice estimates

Verena Benz[*][a,b], Oliver Esper [a,b], Rainer Gersonde [a,b], Frank Lamy [a,b], Ralf Tiedemann [a,b]

[a]Alfred-Wegener-Institut Helmholtz-Zentrum für Polar- und Meeresforschung, Am Alten Hafen 26, 27568 Bremerhaven, Germany
[b]MARUM - Zentrum für Marine Umweltwissenschaften der Universität Bremen, Leobener Str. 28359 Bremen, Germany

Abstract

We used diatom-based transfer functions to estimate summer sea surface temperatures and winter sea-ice concentrations in the Antarctic Zone of the western Pacific sector south of 56°S to assess paleoceanographic changes during the Holocene. The most prominent finding is the cooling between ~10,000 – 8,000 years before present that occurs circum-Antarctic wide after the Antarctic Holocene Optimum. This cooling is most likely induced by meltwater shedding from the West Antarctic Ice Sheet and is associated with an equatorward expansion of the Southern Westerly Winds. However, the strong cooling in the Pacific's Antarctic Zone is contrasted by persistent warming in the Subantarctic Zone. Until approximately 5,000 years before present, the western Pacific temperatures remained relatively cold, mirroring conditions from other Southern Ocean areas. This cold period is further followed by a warming that lasts for approximately 3,000 years. This subsequent Late Holocene warming was presumably triggered by increasing insolation and higher solar activity, causing more frequent El Niño events and eventually warming the western Pacific sector of the Southern Ocean. The Holocene signal variability in the Pacific was propagated via the Drake Passage into the western Atlantic sector. However, local changes of temperature and sea-ice trends were highly dependent on the proximity and latitudinal position of paleoclimate archives to the atmospheric and oceanographic mechanisms, and might have overprinted a common Holocene temperature trend in the Southern Hemisphere.

5.1   Introduction

Mechanisms that are responsible for climate change during the Holocene in the Southern Hemisphere are of special interest regarding the recent warming and its associated feedbacks like ice-sheet loss, sea-level rise and ocean-atmosphere interaction (IPCC, 2014). The Holocene period started at about 11,000 years before present (yr BP) in the Southern Hemisphere with relatively warm conditions almost mirroring the present climate state. However, until the recent rapid warming, the Holocene climate in the Southern Ocean (SO) has shown high variability with distinct cool and warm periods (e.g. Mayewski et al., 2004; Bentley et al., 2009; Kilian and Lamy, 2012). Most prominent is a SO wide cooling after the Antarctic Holocene Optimum at ~8 kyr BP (1 kyr = 1000 yr) that is accompanied by new sea-ice advance (e.g. Bianchi and Gersonde, 2004; Divine et al., 2010) and an atmospheric CO_2 decrease recorded in antarctic ice cores (Lüthi et al., 2008). Preceding to that cooling a significant retreat of the West Antarctic Ice Sheet (WAIS; Larter et al., 2014) resulted in meltwater shedding into the adjacent ocean basins (Das and Alley, 2008; Mathiot et al., 2013) and contributed to a sea-level rise between ~11.4 and 8.2 kyr BP (Lambeck et al., 2014). Coupled climate model simulations of significant freshwater input from the WAIS (+100 milli-Sverdrup) into the Pacific sector suggested distinct cooling in the Antarctic Zone south of 60°S of up to 1.5°C that is propagated into the Atlantic and to a lesser extent into the Indian sector (Mathiot et al., 2013). During the Mid-Holocene several records show partially opposite results with either relatively stable cool conditions (e.g. Bianchi and Gersonde, 2004; Pahnke and Sachs, 2006; Divine et al., 2010) or a renewed warming during the so-called Hypsithermal (e.g. Hodell et al., 2001; Crosta et al., 2004; Crosta et al., 2008). Over the course of the Late Holocene similar heterogeneous trends are detected at different sites in the SO (e.g. Hodell et al., 2001; Bentley et al., 2009; Strother et al., 2015) that are, as well as during the Mid-Holocene, probably related to different time constraints or the influence of strong regional variability of the following atmospheric mechanisms. In general, the majority of studies assign the variability of their records to changes within the strength and latitudinal position of the Southern Westerly Winds (SWW) (e.g. Bentley et al., 2009; Divine et al., 2010; Kilian and Lamy, 2012), intensity and frequency changes of the El Niño Southern Oscillation (ENSO) (Moy et al., 2002) as well as the Southern Annular Mode (SAM) and feedbacks within those atmospheric mechanisms (e.g. Varma et al., 2011; Gomez et al., 2013; Rees et al., 2015). Local climate variability caused by non-uniform response to the mentioned mechanism inhibits the assignment of a common Holocene climate trend in the SO.

From the Pacific sector of the SO high resolved Holocene records are relatively rare despite from continental margin (Pahnke and Sachs, 2006; Kilian and Lamy, 2012). Most exceptional records with annual to seasonal resolution are available from the western Ross Sea sector and off Adélie Land (East Antarctica) (Cunningham et al., 1999; Denis et al., 2006; Crosta et al., 2008). However, sediment cores retrieved from the open marine environment have by the majority moderate to low sedimentation rates (2-9 cm/kyr in average) and large parts of the Holocene are missing often (e.g. Mashiotta et al, 1999; Tapia et al., 2015; *Benz et al., b; in prep.).*

Here, we present five well-dated, highly resolved sediment records documenting the Holocene, putting an emphasis on the Mid- to Late Holocene on the basis of diatom-based transfer function estimates of summer sea surface temperature (SSST) and sea-ice concentration from the western Pacific sector of the SO. Highly resolved estimates from this area are yet missing in the marine record and play a significant role in deciphering the Holocene mechanisms and environmental development in the understudied high-latitude South Pacific. As the Pacific sector of the SO is mainly characterized by the eastward flowing Antarctic Circumpolar Current (ACC) that connects the different sectors of the SO, the investigated region is of special importance to study the propagation of temperature and water mass signals to the Atlantic and Indian sectors of the SO. The exchange of heat from the Pacific to the Atlantic sector is maintained via the so-called "cold-water route" through the Drake Passage. Thus, significant sea surface cooling or warming, stimulated by variation in intensity and/or frequency of the SWW and the ENSO or by freshwater intrusion, is transferred into the Atlantic and Indian sectors. Furthermore, the bifurcation of the ACC in the eastern Pacific sector into the Humboldt-Chile Current favors the export of cold-water masses far north into the Eastern Equatorial Current. Via the combination of our new, relatively high resolved records and several selected other marine records from the western Pacific and Atlantic sectors we can address questions concerning the Holocene climate development on a circum-Antarctic view.

The objectives of our study are primarily (1) to document the Holocene temperature trend in the western Pacific in relation to previously documented climate change in this basin and the adjacent sectors, (2) to test the simulated sea surface cooling between 8 and 10 kyr BP, its possible origin from the WAIS and the related heat transport to the Atlantic sector, and (3) to identify possible drivers of the cooling and warming sequence in the Southern Hemisphere and its feedbacks between the ocean and the atmosphere.

5.2   **Material and Methods**

Holocene sea surface temperature and sea-ice reconstructions were accomplished at five sediment cores covering the western Pacific sector of the SO between the Antarctic Polar Front (APF) and the average winter sea-ice (WSI) edge between 135° and 170°W (Fig. 5.1, Table 5.1). During R/V Polarstern cruise ANTXXVI/2 all cores have been recovered using piston, gravity or kasten coring devices (Table 5.1, Gersonde, 2011). All cores are situated in the Permanent Open Ocean Zone (POOZ) that is bounded to the north by the Antarctic Polar Front (APF) and to the south by the WSI edge that is roughly coincident with the Southern ACC Front (SACCF) (Fig. 5.1). The study area is predominantly influenced by the northward transport of cold surface waters via the Ross Gyre and the vicinity to the WSI edge. The sediment facies of the studied time slice consists mainly of diatom ooze with minor contributions of foraminifers, terrigenous mud and nannofossils.
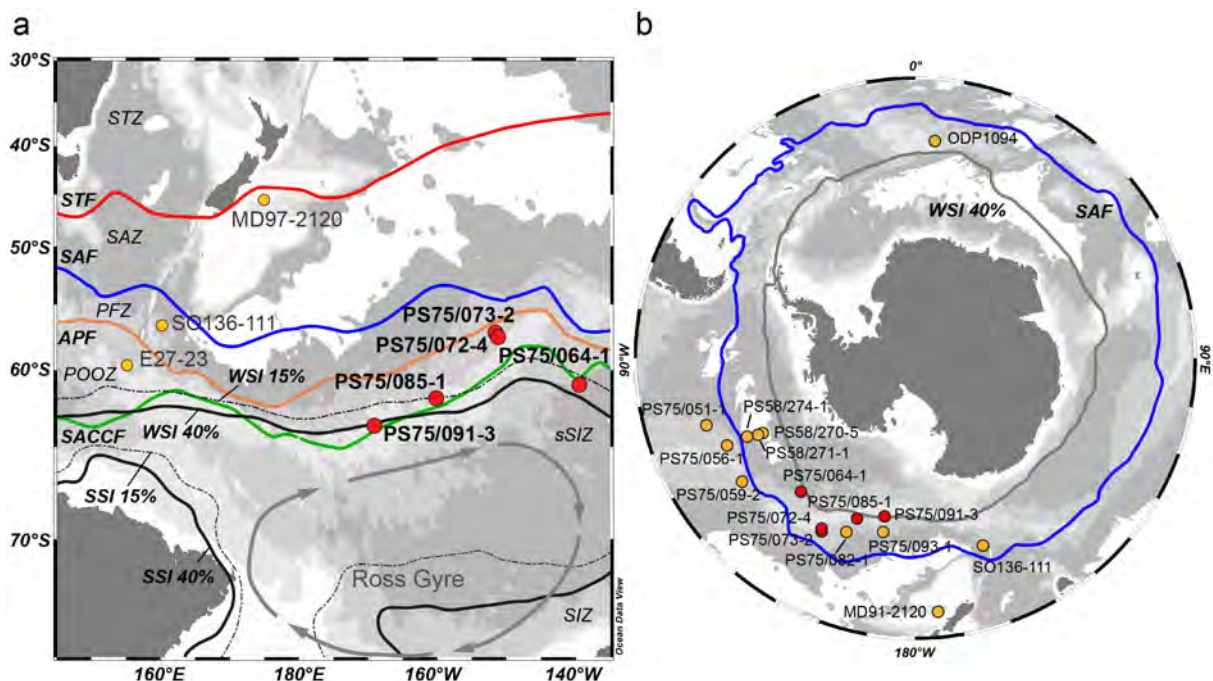

Figure 5.1: **(a)** Location of studied cores (red circles) and discussed cores (yellow circles) from the Holocene time slice (see Table 5.1). **(b)** Location of studied cores (red circles) and discussed cores (yellow circles) for sea surface temperature anomaly between 8-10 cal. kyr BP (Fig. 5.4; Table 5.1). WSI/SSI: modern winter/summer sea-ice edge each for 15% (dashed: 40%) sea-ice concentration (Reynolds et al., 2002, 2007); Oceanographic fronts according to Orsi et al. (1995); STF: Subtropical Front, SAF: Subantarctic Front, APF: Antarctic Polar Front, SAZ: Subantarctic Zone, PFZ: Polar Front Zone, POOZ: Permanent Open Ocean Zone, SACCF: Southern Antarctic Circumpolar Current Front, sSIZ: seasonal Sea Ice Zone, SIZ: Sea Ice Zone.

All cores were sampled on a spacing of 5 cm, except for core PS75/85-1 that was sampled every 10 cm. Preparation of the retrieved material for quantitative diatom slides for light microscopy was done according to the standard methods developed by Gersonde and

Zielinski (2000). Diatoms slides were analyzed using a Zeiss Axioplan 2 at x1000 magnification and respective counting of an average of 400-600 diatom valves per sample was carried out according to the counting standards proposed by Schrader and Gersonde (1987). The counted diatoms were identified to species or species group level following the taxonomy of Hasle and Syvertsen (1996), Zielinski and Gersonde (1997), and Armand and Zielinski (2001). The 29 (28) diatom species and species groups considered for the reconstruction of SSST (WSI) were chosen in accordance to their relationship to both environmental variables and oceanographic zones (Esper and Gersonde, 2014 a, b).

Table 5.1 Locations of sediment cores presented and discussed in this study

Core	Latitude	Longitude	Water depth (m)	Coring device[a]	Zone[b]	Data source
ELT27-23	59°73.1'S	155°14.3'E	3182	PC	POOZ	Ferry et al., 2015b
MD97-2120	45°32.06'S	174°55.85'E	1210	GPC	SAZ	Pahnke et al., 2003; Pahnke and Sachs, 2006
PS58/270-5[c]	62°01.68'S	116°07.38'W	4981	PC	POOZ	*Benz et al., b; in prep.*
PS58/271-1[c]	61°14.58'S	116°02.82'W	5214	PC	PFZ	*Benz et al., b; in prep.*
PS58/274-1[c]	59°12.42'S	114°53.28'W	5136	PC	PFZ	*Benz et al., b; in prep.*
PS75/051-1[c]	52°48.73'S	107°48.33'W	3949	PC	SAZ	*Benz et al., b; in prep.*
PS75/056-1[c]	55°09.74'S	114°47.31'W	3581	GC	SAZ	*Benz et al., b; in prep.*
PS75/059-2[c]	54°12.90'S	125°25.53'W	3613	PC	SAZ	*Benz et al., b; in prep.*
PS75/064-1	61°00.74'S	139°27.85'W	4600	PC	sSIZ	**this study**; *Benz et al., b; in prep.*
PS75/072-4	57°33.51'S	151°13.17'W	3099	GC	POOZ	**this study**; *Benz et al., b; in prep.*
PS75/073-2	57°12.26'S	151°36.65'W	3234	KC	POOZ	**this study**; *Benz et al., b; in prep.*
PS75/082-1[c]	59°02.48'S	158°51.82'W	4000	PC	POOZ	*Benz et al., b; in prep.*
PS75/085-1	61°56.38'S	160°07.10'W	3734	PC	sSIZ	**this study**; *Benz et al., b; in prep.*
PS75/091-3	63°41.66'S	169°04.47'W	2940	PC	sSIZ	**this study**; *Benz et al., b; in prep.*
PS75/093-1[c]	60°52.33'S	169°32.89'W	3762	PC	POOZ	*Benz et al., b; in prep.*
SO136-111	56°40.20'S	160°13.80'E	3912	GC	PFZ	Crosta et al., 2004 Ferry et al., 2015b
ODP 1094	53°10.08'S	5°07.08'W	2807	CC	POOZ	Bianchi and Gersonde, 2004

[a] Coring devices: PC Piston Corer; GC Gravity Corer; KC Kasten Corer; CC Composite Core;
[b] Oceanographic zones: STZ Subtropical Zone; SAZ Subantarctic Zone; PFZ Polar Front Zone; POOZ Permanent Open Ocean Zone; sSIZ seasonal Sea Ice Zone.
[c] Cores studied only for the 8-10 kyr SSST anomaly (see Fig. 5.4)

The reconstruction of summer sea surface temperatures (SSST) and winter sea-ice (WSI) concentration were accomplished using transfer-function (TF) derived estimates. For SSST the Imbrie and Kipp Method (IKM; Imbrie and Kipp, 1971) was used and the Modern Analog Technique (MAT; Hutson, 1980) for WSI concentrations. The applied TFs were recently developed by Esper and Gersonde (2014a, b) and obtain the best results in comparison to different TF approaches.

For SSST estimates the TF IKM-D336/29/3q was applied, comprising 336 reference samples from surface sediments in the Atlantic, the western Indian and the Pacific sectors of the SO, with 29 selected diatom taxa and taxa groups and a 3-factor model calculated with quadratic regression. As reference for modern SSSTs (January-March) serve the temperatures at 10m water depths from the Hydrographic Atlas of the SO (HASO; Olbers, et al., 1992). Averaged over a time period from ~1900-1991 these SSSTs represent the least influenced dataset by recent warming in the SO. The root mean squared error of prediction (RMSEP) of the applied TF is 0.83°C (Esper and Gersonde, 2014b). IKM calculations were carried out with the software packages PaleoToolBox and WinTransfer (http://www.pangaea.de/Software/PaleoToolBox; Sieger et al., 1999).

Estimates for WSI concentration were carried out, using the TF MAT-D274/28/4an, with 274 reference samples from surface sediments in the Atlantic, the western Indian and the Pacific sectors of the SO, including 28 diatom taxa and taxa groups, and an average of 4 analogs (Esper and Gersonde, 2014a). The WSI concentrations of the reference dataset were derived from the September sea-ice concentrations averaged over a time period from 1981-2010 at each surface site (National Oceanic and Atmospheric Administration, NOAA; Reynolds et al, 2002; 2007). The application of this TF results in a RMSEP of 5.52% (Esper and Gersonde, 2014a). A concentration of 15% is defined as threshold for the maximum sea-ice extent (Zwally et al., 2002), indicating the absence or presence of sea ice. Following the approach of Gloersen et al. (1992) and Gersonde et al. (2005), the average sea-ice edge is represented by 40% concentration. MAT calculations were carried out with the statistical computing program *R* (R core team, 2012). Additional information about the winter sea-ice cover comes from the abundance fluctuations of the diatom species *Fragilariopsis cylindrus* and *Fragilariopsis curta*. These two species exhibit a similar relationship to sea ice and temperature and thus were combined to the *F. curta* group (Zielinski and Gersonde, 1997; Armand et al., 2005).

The new SSST and WSI TFs were additionally used to recalculate the temperature estimates for core ODP1094 (Bianchi and Gersonde, 2004) and to estimate its WSI concentration. Reconstructed variables are available in the PANGAEA database (www.pangaea.de, doi in progress). Maps, temperature and sea-ice plots have been produced with ODV (Ocean Data View; Schlitzer, 2014).

5.3 Age constraints

The age models of the five studied cores have been primarily established by radiocarbon dating of monospecific foraminifer samples (*Neogloboquadrina pachyderma* sinistral) from cores P75/072-4, PS75/073-2 and PS75/085-1 and the humic acid fraction of the bulk sediment from cores PS75/064-1 and PS75/085-1 (Table 5.2; *Benz et al., a; under rev.*).

Table 5.2 AMS[14]C ages for studied Holocene time slice. Carbon sources for dating are: H – humic acid fraction; F –foraminifera *N. pachyderma sin.* OS: National **O**cean **S**cience AMS Woods Hole; ETH: **E**idgenössische **T**echnische **H**ochschule Zürich.

Core	Depth (cm)	Lab ID	C source	[14]C age (yrs BP)	Error (yrs)	Reservoir age	2σ min	2σ max	Calib. Age (cal yr BP)
PS75/064-1	6-9	OS-106097	H	2950	15	750	2198	2337	2295
	20-2	OS-106098	H	3880	25	750	3341	3491	3413
	55.5-59	OS-106099	H	7270	40	750	7333	7512	7432
	80.5-84	OS-106100	H	10650	40	750	11166	11486	11285
PS75072-4	1-2	ETH 48932.1.1	F	1369	60	590	635	873	729
	21-22	ETH 48933.1.1	F	2311	63	590	1548	1856	1705
	36-37	ETH 48934.1.1	F	3332	65	590	2761	3108	2929
	51-52	ETH 48935.1.1	F	4392	68	590	4088	4476	4291
	76-77	ETH 48936.1.1	F	7188	96	590	7315	7658	7494
	91-92	ETH 48937.1.1	F	9119	78	590	9441	9838	9600
	101-102	ETH 48938.1.1	F	10194	79	590	10748	11170	10984
PS75/073-2	17.5-18.5	OS-96102	F	4060	25	590	3722	3924	3838
	25.5-26.5	OS-96101	F	4770	25	590	4705	4853	4807
	37.5-38.5	OS-96100	F	5870	30	590	5985	6180	6089
	52.5-53.5	OS-96109	F	7730	35	590	7922	8102	7993
	62.5-63.5	OS-96099	F	9260	50	590	9571	9963	9779
	73.5-74.5	OS-96098	F	10300	50	590	10965	11227	11118
PS75/085-1	5.5-9	OS-106101	H	2420	40	750	1534	1759	1642
	45-49	OS-106102	H	3830	25	750	3291	3441	3364
	131.5-135.5	OS-106103	H	5350	30	750	5282	5439	5358
	185-189	OS-106281	H	6520	35	750	6496	6707	6607
	245.5-249.5	OS-106282	H	7700	40	750	7709	7917	7815
	301-305	OS-106283	H	8920	40	750	9077	9362	9214
	357.5-359.5[a]	OS-98721/OS-98720	F	10375	35	750	10865	11153	11032

[a] [14]C ages obtained by averaging values from several measurements (see *Benz et al., a; under rev.*)

The Accelerator Mass Spectrometry (AMS) ^{14}C datings were measured at the National Ocean Science Accelerator Mass Spectrometry Facility (NOSAMS) at Woods Hole Oceanographic Institution (WHOI) and the Eidgenössische Technische Hochschule (ETH, Zürich). All radiocarbon ages were converted to calendar years before present (cal. yr. BP, further referred to as kyr BP; 1000yr = 1kyr) using the calibration software CALIB 7.0.2 (Stuiver

and Reimer, 1993; Stuiver et al., 2005) with the MARINE13 calibration curve (Reimer et al., 2013). Applied reservoir ages for the Holocene time period vary between 590 and 750 years dependent on the latitudinal position of the core sites (Bard, 1988) (Table 5.2). For further coherence and refinement of the radiocarbon ages we used oxygen isotopic results from cores PS75/072-4, PS75/073-2 and PS75/085-1 (*Benz et al., a; under rev.*). The age model of core PS75/091-3 is based on the correlation of diatom abundance fluctuation to core PS75/085-1.

The inter-core correlation and the calculation of corresponding sedimentation rates was achieved using the AnalySeries 2.0 software (Paillard et al., 1996) with linear interpolation between pointers.

5.4   Results

The SSSTs in the western Pacific sector throughout the Holocene show a relatively homogenous trend (Fig. 5.2a). After significantly warm SSSTs during the Antarctic Holocene Optimum (AHO; ~12-9 kyr BP), almost reaching to or even exceeding modern values at some core locations the temperatures drop at all core sites between 0.5 and 1°C, reaching lowest values between 9-7 kyr BP (Fig. 5.2a). Thereafter, relatively stable cold conditions occur in the majority of the cores with small-scale variations within the TF error. One exception is core PS75/091-3, showing distinct millennial variations from 8 kyr BP on, not consistent to the overall cold time period. An new temperature rise, especially visible in cores PS75/072-4 and PS75/085-1, occurred around 5 kyr BP. This warm period lasted for approximately 2-3 kyr representing a second warm Holocene optimum. After 2 kyr BP SSSTs decrease again by ~0.5 to 1°C.

Concomitant with the changes in SSSTs, the WSI concentrations change as well in different magnitude (Fig. 5.2a). A distinct increase of sea-ice concentration occurs in cores PS75/072-4 and PS75/085-1 from 10 to 7 kyr BP. Only a slight and gradual increase is visible in core PS75/064-1 and PS74/073-2, whereas the southernmost core PS75/091-3 shows several reoccurring peaks, yet with values up to 80%. The maximum sea-ice edge may thus have reached up to 57°S in the first cooling phase after 10 kyr BP. During the following warm phase, starting after 5 kyr BP, sea ice remained relatively stable at ~20% in core PS75/064-1, whereas the northernmost cores (PS75/072-4 and PS75/073-2) as well as PS 75/085-1 show decreasing values. Overall, the three cores covered today by the maximum WSI expansion (Fig. 5.1) display continuously >15% WSI concentration throughout the last 10 kyr BP.

Significant changes of the diatom assemblage in the studied time slice occur mainly in the sea-ice related *F. curta* group abundance (Fig. 5.2b). In the majority of cores the *F. curta* group shows relatively low abundances during the AHO. An exception is core PS75/091-3 that lies south of the present WSI edge and probably is the most affected by the cold Ross Gyre. Towards 8-7 cal. kyr BP a twofold increase of the *F. curta* group abundance is visible, that remains relatively stable especially in the southernmost cores for approximately 2 to 3 kyr. The temperature rise starting around 5-4 cal. kyr BP (Fig. 5.2a) leads to a decrease in the abundance of sea-ice diatom species. However, similar to the pattern displayed during the AHO, the relative abundance of the *F. curta* group varies between cores influenced by cold surface water masses in the vicinity of the Ross Gyre. After 2 cal. kyr BP a second rise of the *F. curta* group indicates renewed cold water and WSI influence.
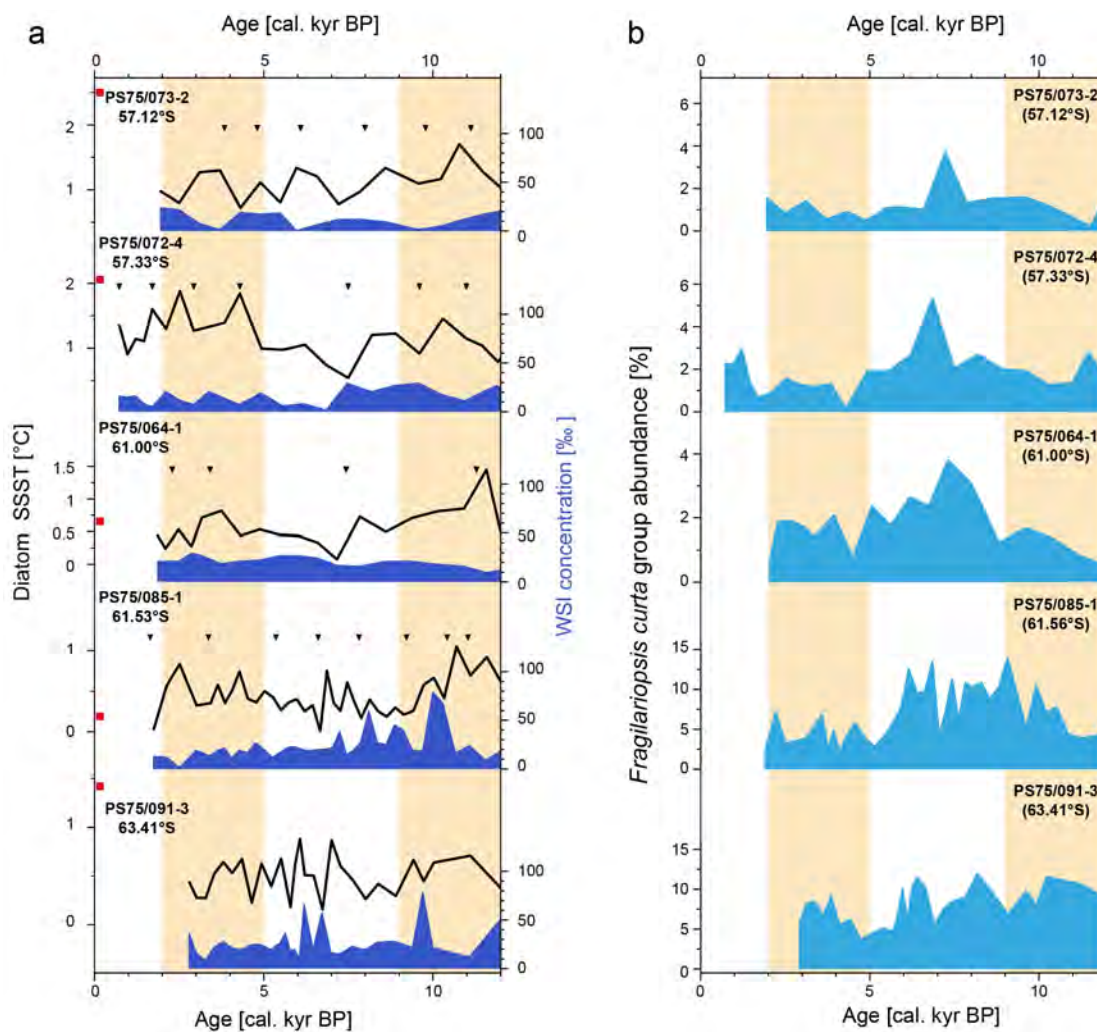
Figure 5.2: **(a)** Sea surface temperature (SSST) and winter sea-ice (WSI) concentration of studied cores for the Holocene time slice against age. **(b)** Diatom abundances of sea-ice indicating species and species groups of studied cores for the Holocene time slice against age. Black triangles: radiocarbon datings (see Table 5.2), red squares: modern SSST at core locations (see Table 5.1).

5.5   Discussion

5.5.1   Early Holocene (11.5 – 9 kyr BP)

The warm temperatures in the Early Holocene were accompanied by low WSI concentration a distinctly low abundances of sea-ice related diatoms at the majority of core sites (Fig. 5.2; *Benz et al., b; in prep.*). The SSST pattern in the western Pacific, showing similar or only slightly colder temperatures than modern, resulted in the establishment of almost modern frontal positions similar to the eastern Pacific sector (*Benz et al., b; in prep.*). Generally the AHO is a circum-Antarctic wide occurring temperature optimum that is also represented in antarctic ice cores (e.g. Bianchi and Gersonde, 2004; Pahnke and Sachs, 2006; WAIS Divide Project Members, 2013).

As all investigated core sites are influenced by WSI presence during the Antarctic Cold Reversal (*Benz et al., b; in prep.*), the shorter duration of the warm optimum compared to results from the northern SAZ (Fig. 5.3; Pahnke and Sachs) might be caused by an earlier reinforcement of the Ross Gyre. The strengthening of the gyre itself might have been influenced by the rapid retreat of the WAIS in the Ross Sea as well as the Amundsen and Bellingshausen Seas between 15 and 10 kyr BP (e.g. Anderson et al., 2014; Larter et al., 2014 and references therein). This retreat was most likely accompanied by widespread meltwater intrusion and might have contributed to a global sea-level rise between ~11.4 – 8.2 kyr BP (Fig. 5.3; Lambeck et al., 2014).

In general, the Early Holocene climate is suggests to be dominated by the position and intensity of the SWW and a positive SAM (Rees et al., 2015). The SWW are characterized by more modern summer-like conditions with stronger core and weaker marginal intensities (Lamy et al., 2010; Kilian and Lamy, 2012). The significant retreat and meltwater intrusion of the WAIS during the Early Holocene is most likely the result of amplification between rising temperatures, strengthened and more poleward oriented SWWs (Lamy et al., 2010) and associated intensified upwelling contributing to higher atmospheric CO_2 concentrations recorded in antarctic ice cores (Fig. 5.3; Mayr et al., 2013).

Figure 5.3: Western Pacific sea surface temperature (SSST) and winter sea-ice (WSI) concentration of studied cores in comparison with additional temperature records from the Subantarctic an Antarctic Pacific and Atlantic sector (see Table 5.1) together with ice core and orbital parameters: obliquity and precession after Laskar et al. (2004); ice-volume equivalent sea level (esl, Lambeck et al., 2014); daily northern and southern midsummer insolation (Laskar et al., 2004); ENSO warm events (Moy et al., 2002); MD97-2120 (Pahnke and Sachs, 2006); SO136-111 (Crosta et al., 2004; Ferry et al., 2015b); E27-23 (Ferry et al., 2015b); ODP1094 (Bianchi and Gersonde, 2004); EDC non-sea salt Na (Fischer et al., 2007); EDC and WDC CO_2 (Lüthi et al., 2008, AICC12; Marcott et al., 2014); EDC $\delta^{18}O$ and WDC $\delta^{18}O$ (Stenni et al., 2006, AICC12 time scale: Veres et al., 2013; Bazin et al., 2013; WAIS Divide Project Members, 2013). Arrows indicate cooling after the Antarctic Holocene optimum and warming around 5 kyr BP; black triangles: radiocarbon datings (see Table 5.2).
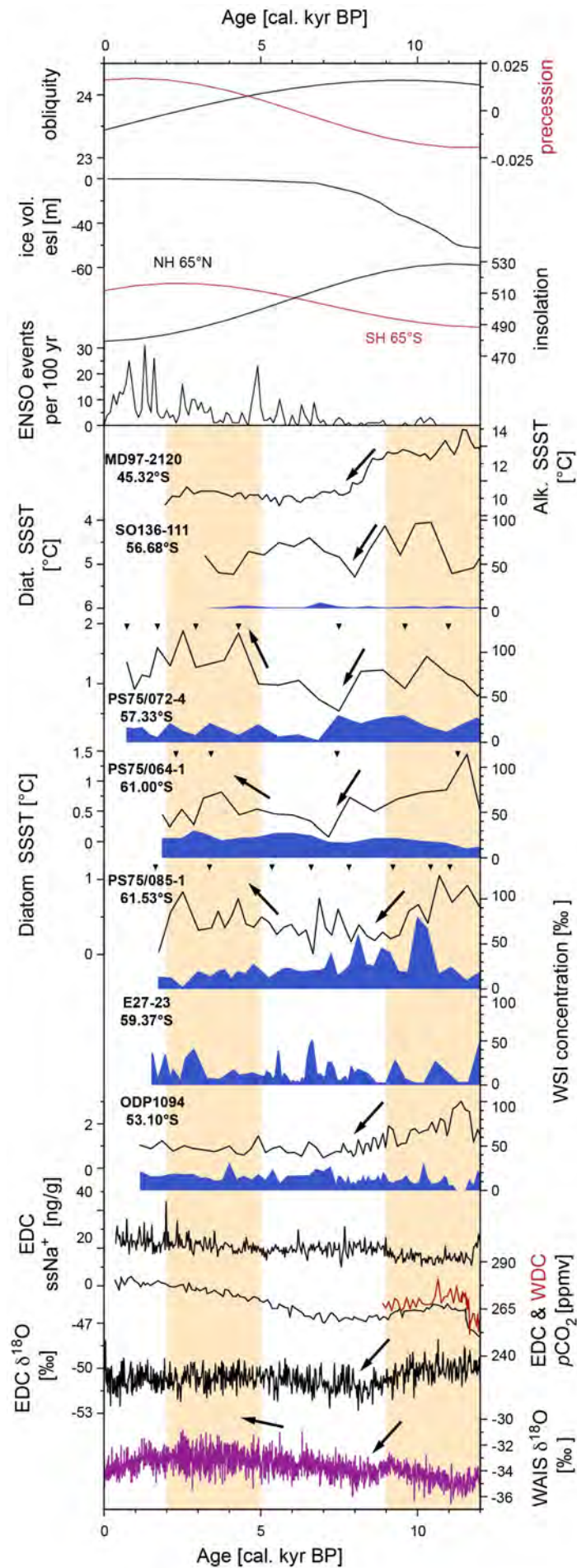
5.5.2   Mid-Holocene (9–5 kyr BP)

The SSST and WSI estimates from the western Pacific sector of the SO reveal a significant cooling period following the AHO roughly between 9 and 7 kyr BP and lasting until ~5 kyr BP. This cooling was further accompanied by a WSI advance up to 57°S resulting in a latitudinal expansion compared to the AHO by approximately 3-5°. The concentration estimates are consolidated by distinct increases of the sea-ice related diatom *F. curta* group (Fig. 5.2). The different timing of the initial cooling may result from the location of the core sites. Therefore, the southernmost cores display a relatively short early warm period due to their vicinity to the Ross Gyre and the proximity to the WSI edge (Figs. 5.1, 5.3). In contrast to our new records, the previous temperature reconstruction from the western SAZ do not show a persistent cooling after 8 kyr BP, but a temperature increase lasting until 5 kyr BP (Fig. 5.3; SO136-111; Crosta et al., 2004). Similar differences are also visible in diatom-based reconstruction of the Ross Sea sector and off Adélie Land. Diatom abundances point to a shorter cooling of ~2 kyr after 9 kyr BP with following warmer conditions until 4 kyr BP (Cunningham et al., 1999; Crosta et al., 2008). However, a cooling pattern in the Early to Mid-Holocene similar to our estimates is known from records off New Zealand (Fig. 5.3; Pahnke and Sachs, 2006) as well as from the Antarctic Peninsula area (Bentley, et al. 2009; Shevenell, et al., 2011; Etourneau, et al., 2013) and the Atlantic sector of the SO (Fig. 3; Bianchi and Gersonde, 2004; Divine et al., 2010). Additionally, the re-advance of WSI to a more northern location of the maximum sea-ice edge in the Pacific sector is corroborated by recently published WSI estimates from the southwest Pacific indicating relatively higher WSI concentrations in the vicinity of the APF after 8 cal. kyr BP (Fig. 5.3; Ferry et al., 2015b). Yet, the renewed sea-ice expansion did probably not reach into the PFZ, as WSI concentrations at core site SO136-111 did not exceed 10%, taking into account the comparable large error of the reconstruction technique (~20%; Ferry et al., 2015a). Cooling of up to 2 K was further reconstructed from cores located in the Humboldt-Chile Current area and the Eastern Equatorial Pacific, suggested to have been induced by advected cold water from the SO (Kilian and Lamy, 2010; Kalansky et al., 2015). Furthermore, pronounced cooling is also reported from all antarctic ice cores (Masson et al., 2000; WAIS Divide Project Members, 2013), which is accompanied by higher sea salt transport and thus farther sea-ice expansion (Fig. 5.3; Fischer et al., 2007). Contrasting results occur north of 35°S off the Chilean coast where the temperature development in the Holocene period is contrary to the records studied by Kilian and Lamy (2010) showing colder SSTs during the AHO and a

significant warming at ca. 8 kyr BP (Kim et al., 2002) similar to the increasing diatom-derived SSSTs at core site SO136-111 (Fig. 5.3; Crosta et al., 2004).

Possible reasons for the widespread cooling trend in the Mid-Holocene were recently simulated from various proxy results together with a coupled climate model (ATMosphere and Fresh Water Flux, ATMFWF), resulting in the most plausible cause of increased fresh water release due to melting of the WAIS (Mathiot et al., 2013). Such widespread meltwater intrusion is in line with the retreating WAIS during the Early Holocene (Anderson et al., 2014; Larter et al., 2014). The simulation of freshwater shedding into the Pacific sector between 10 and 8 kyr BP resulted in a cooling of approximately 0.5-1.5 K south of 59°S
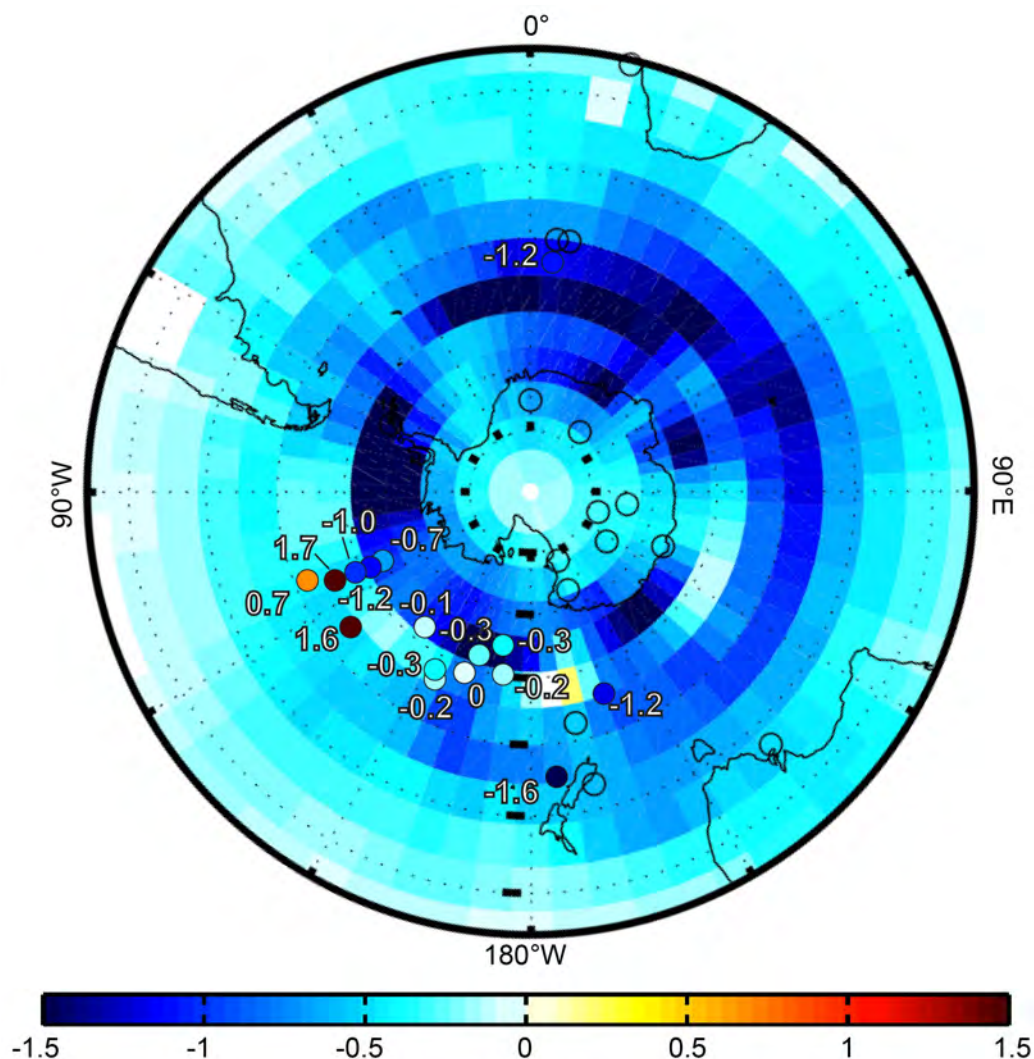

Figure 5.4: Anomaly between 8 and 10 kyr BP (8-10) at studied and discussed cores (Fig. 5.1; Table 5.1), Temperature anomaly in K (Table 5.3). Map modified after Mathiot et al. (2013).

whereas north of 59°S also warming up to 0.3 K is estimated (Mathiot et al., 2013). Stronger cooling in the Antarctic Zone (AZ) is also evident in SSST anomalies (8-10 kyr BP) estimated at core sites from the eastern and western Pacific sector (Fig. 5.4, Table 5.3; *Benz*

et al., b; in prep.). However, the absolute values between proxy records and modeling approach differ considerably between each other especially in the present SAZ. Where the coupled climate model suggest cooling of up to 0.5°C, the TF estimates show a warming of up to 1.7°C (Fig. 5.4). Such a discrepancy between proxy and model data may result only few proxy data used in the simulation. However, the WAIS retreat and associated meltwater input is still a possible driver of the cooling occurring in all SO sectors. Although the cooling is less transferred into the SAZ, directly influenced areas, like the eastern Pacific sector and the Ross Sea, show stronger cooling. It is further transferred through the Drake Passage into the Atlantic and by less extent to the Indian sector (Fig. 5.4). A reason causing less cooling north of ~59°S in the eastern sector may be the relationship between the core sites and the establishment of the modern frontal system during the Early Holocene (*Benz et al., b; in prep.*). This circumstance may have led to less northern cold-water transport, whereas the eastern transport via the Drake Passage propagated the cooling into the Atlantic and with lesser extent to the Indian sectors of the SO. However, the equatorial cooling that is suggested to be triggered by the upwelling of cold Subantarctic Mode Water (SAMW) as well as cooling off the Chilean coast (Kilian and Lamy, 2010; Kalansky et al., 2015) may further be possible. Formation of SAMW via downwelling of water masses at the SAF would thus include the cold surface water from south of ca. 59°S. In the present SAZ however, the surface water may be still influenced by increased heat transport occurring during the preceding AHO due to a strengthened South Pacific Gyre (Marr et al., 2013). Off the Chilean coast, the deflection of the ACC into the Humboldt-Chile Current favored the transport of cold surface water to core sites situated at the continental margin, similar to the cold water tongue established during the glacial period (*Benz et al., a; under rev.*). Northern advection of cold water from the SO however may have not reached as far north to influence SSTs at core sites north of 35°C where no cooling between 8 and 10 kyr BP can be observed (Kim et al., 2002).

During the Mid-Holocene the position and intensity of the SWW changes to more-winter like conditions between 12.5 – 8.5 kyr BP, represented by reduced zonal winds in the core zone and further northward expansion (Lamy et al., 2010). The authors propose a main control of sea surface temperature on the position and strength of the SWW. Thus, the cooling in the SO caused by freshwater shedding from the WAIS presumably might have governed the shift to a more latitudinal expanded and transitional weaker SWW (Kilian and Lamy, 2012). The persistence of these conditions over the next ~3 kyr mirrored the cooler Mid-Holocene period recorded in the western Pacific sector. A northward migration or

weakening of the SWW is further suggested to cause less upwelling of Circumpolar Deep Water onto the West Antarctic Peninsula shelf favoring cooler conditions necessary for new sea-ice formation (Peck et al., 2015). However, as circum-Antarctic records partly show contrasting results regarding the intensity and length of the cooler Mid-Holocene, the change of the SWW is presently not consistent with all proxy results (e.g. Kim et al., 2002; Crosta et al., 2004; Divine et al., 2010).

Additionally to changes in the SWW the climate system in the SO especially in the Pacific sector is strongly controlled by increasing ENSO frequency since the Mid-Holocene (Etourneau et al., 2013; Rees et al., 2015). Generally, the feedback to ENSO events is strongly influenced by the Antarctic Dipole, whose characteristic is the formation of a high (low) sea level pressure anomaly over the Amundsen Bellingshausen Seas simultaneous with a low (high) sea level pressure over the Weddell Sea. During warm ENSO events this sea level pressure anomaly is characterized by high pressure over the eastern Pacific sector, resulting in higher temperatures and less sea ice in the Pacific center. In contrast, more frequent El Niño events might have led to a cooler climate state with more sea ice in the Weddell Sea (Yuan, 2004). The Mid-Holocene is generally characterized as a transitional period between SWW and ENSO controlled climates (Rees et al., 2015). Generally, more frequent ENSO events starting in the Mid-Holocene (Fig. 5.3), suggested to be forced by insolation changes (Moy et al., 2002), are in broad consistency with a orbitally induced rise of Southern Hemisphere summer insolation (Fig. 5.3; Laskar et al., 2004). However, as a complete shift to an ENSO controlled regime is not yet completed, less warm El Niño events in the Mid-Holocene are consistent with the cooler temperature regime in the SO documented in the majority of marine records (Fig. 5.3; e.g. Pahnke and Sachs, 2006; Divine et al., 2010; Kilian and Lamy, 2012) and less retreat of the WAIS between 8.8 and 6.6 kyr BP (Das and Alley, 2008).

With respect to the bipolar seesaw mechanism, the "8.2 kyr BP event", a prominent cooling in the Northern Hemisphere caused by freshwater outbursts (Alley et al., 1997), should have resulted in a warming in the Southern Hemisphere (Rohling and Pälike, 2005). But although this event has been observed in paleoclimate records from almost worldwide (Mayewski et al., 2004), a distinct response in the Southern Hemisphere cannot be identified. Simulations of the 8.2 kyr BP event with a coupled atmosphere-ocean general circulation model show a general cooling in the Northern Hemisphere with a southward shift of the Intertropical Convergence Zone (ITCZ) (Alley and Ágústsdóttir, 2005). Such a shift during the deglacial was previously associated with also southward shifted westerlies, resulting in

warming of the SO (De Decker et al., 2012). As the comparison of Southern Hemisphere records show neither a prominent cooling nor a warming it seems rather likely that such small-scale event lasting for roughly two centuries (Kobashi et al., 2007) did either not influence the SO or that only very high resolved records are capable to picture such event.

5.5.3   Late Holocene (5–0 kyr BP)

The temperature and sea-ice concentration estimates from the southwestern Pacific in the Late Holocene show a short term warming interval starting between 5 and 4 kyr BP that lasts approximately until 2-3 kyr BP. The total temperature change ranges between 0.5 and 1°C (Figs. 5.2a). Concomitant with the rise of SSSTs sea-ice related diatom abundances in all studied cores decrease but still depict abundances high enough for the presence of WSI at the modern average WSI edge (Fig. 5.2a, b). As the estimated WSI concentration did not decrease in the same magnitude as temperatures rise, the summer season was probably more sensitive to climate changes during this time period than the winter season. Increasing temperatures as depicted in the AZ of the western Pacific sector (Fig. 5.2a) are also documented from the SAZ off New Zealand (Fig. 5.3; MD97-2120; Pahnke and Sachs, 2006), from terrestrial records of the Antarctic Peninsula region (Bentley et al., 2009) and from ice cores located in the West Antarctic (Fig. 5.3; Masson et al., 2000; WAIS Divide Project Members, 2013). However, diatom-derived SSSTs from core site SO136-111 (Fig. 5.3; Crosta et al., 2004) and diatom assemblages from the Antarctic continental margin (Denis et al., 2006; Crosta et al., 2008) show the opposite trend with a temperature drop at 4.5 kyr BP similar to the contrasting results during the Mid-Holocene. This cooling is roughly in line with the onset of the so-called "Neoglacial" that is recorded also in the Atlantic sector (Divine et al., 2010), marine and terrestrial records South America (Kilian and Lamy, 2012) and Dronning Maud Land (EPICA Community Members, 2006). Although not referring to a "Neoglacial", additional Atlantic marine records from the Antarctic Zone show relatively stable cold conditions throughout the late Holocene (Fig. 5.3; Bianchi and Gersonde, 2004). Despite the similar signals of the eastern Atlantic records to East Antarctic ice core results, pollen records from South Georgia closely resemble the Pacific temperature records implying warmer conditions between 4.5 – 2.8 kyr BP (Strother et al., 2015). Situated in the western Atlantic and directly in the pathway of the cold-water route, the islands' climate may picture the pattern recorded from the Pacific sector rather than from the eastern Atlantic.

As described above, changes of the SSSTs and the sea-ice expansion in the Pacific sector are strongly connected to the variability of atmospheric conditions like the SAM and ENSO. As suggested by Rees et al. (2015), the Holocene climate after 5 kyr BP is controlled by ENSO activity that is characterized by a higher frequency of warm El Niño-events (Fig. 5. 3). More frequent El Niño events are associated with increasing insolation, higher solar activity and poleward-shifted SWW (Moy et al., 20o2; Varma et al., 2011). The feedback mechanism to El Niño events in the Pacific sector (Yuan et al., 2004) resulted in less WSI concentration and higher SSSTs between 2-5 kyr BP. Largest congruence between atmospheric forcing and environmental results occurred around 2.5 kyr BP when highest SSSTs in the Pacific sector coincide with highest WAIS δ^{18}O values (WAIS Divide Project Members, 2013), distinct ENSO activity intensity (Fig. 5.3; Moy et al., 2002) and the maximum Southern Hemisphere insolation (Fig. 5.3; Laskar et al., 2004). However, as recorded from lake sediments in Tasmania, the predominant dry El Niño events were regularly interrupted by wet La Niña phases, which in turn favor cooler conditions and more sea ice in the Pacific sector of the Southern Ocean (Yuan, 2004). Therefore, higher sea-ice related diatom abundances and WSI concentration peaks during the warm interval at the beginning of the Late Holocene (Fig. 5.2) might have been responses to La Niña events. Further the distance of the studied cores to the influence of the cold water from the Ross Gyre and the average WSI edge influences the length of the warming and early WSI advance especially in the southernmost and westernmost Pacific cores (Figs. 5.2a, 5.3; Ferry et al., 2015b).

The warm period in the studied cores ended latest at 2 kyr BP when the temperature dropped again (Figs. 5.2a, 5.3) similar to temperature decreases off the southern island of New Zealand (Fig. 5.3; Pahnke and Sachs, 2006), South Georgia (Strother et al., 2015) and West Antarctic ice cores (WAIS Divide Project Members, 2013). An exact range of cooling in the western Pacific sector cannot be predicted as the last 1-2 kyr of the Holocene are missing in the majority studied as well as published cores. The available estimates call for a cooling of up to 1°C with new advances of the maximum WSI extent up to ca. 60°S thus mirroring approximately modern conditions. However, SSSTs only reached modern values in the vicinity of the maximum WSI edge, whereas at the APF, cooler conditions of <1°C were still present (Fig. 5.2). Cooler Late Holocene conditions and a gradual increase of sea ice are also reported from the coast off Adélie Land and the Ross Sea sector (Cunningham et al., 1999; Crosta et al., 2008; Denis et al., 2006). Although a return to cold conditions started

already around 4 kyr BP, indicated by increasing abundances of sea-ice related diatom species and less open ocean species the cooling trend seemed persistent throughout the Late Holocene in the Pacific Sector.

5.6   Conclusions

Our SSST and WSI reconstructions of the Holocene from the western Pacific sector of the Southern Ocean reveal a climate development similar to other Pacific basin records as well as records from the Atlantic sector. The most influencing mechanism responsible for cooling between Early and Mid-Holocene is the freshwater input from the retreating WAIS, further accompanied my shifting westerlies. However, coupled climate model simulations miss the total variance of cooling and warming between 8 and 10 kyr BP most likely due to less proxy data. Although a general climate trend in the Southern Ocean is difficult to distinguish, the western Pacific records show high similarity to climate records from the Pacific basin as well as from the Atlantic sector and antarctic ice cores.

The change from an SWW to ENSO driven climate in the Pacific Ocean is reflected in the western Pacific Sector as consequent warming in response to more frequent El Niño events. Contrasting results between different latitudes and ocean basins are presumably influenced by the variable distance to the forcing mechanisms as well as to signal propagation via long distances.

Our open ocean Holocene records emphasize the role of the WAIS as freshwater source and associated cooling in the Pacific sector as well as the strong regional feedback on changing atmospheric forcing mechanisms. Furthermore future model simulations will be enhanced by the new proxy data from open marine environments to better fit the paleoceanographic reconstructions.

5.7   Acknowledgements

Chapter 6 – Conclusions and Outlook

6.1   Conclusions

The overall aim of this thesis was the analysis of Late Quaternary climate variability in the Pacific sector of the Southern Ocean to fill an important gap in paleoceanographic research. To achieve this objective, diatom assemblages of 17 cores from the (sub)antarctic Pacific realm, covering the last 30 kyr, were investigated. Combining the new TF-derived SSST and WSI estimates with previously published records, the environmental conditions during the LGM have been studied and a continuous circum-Antarctic reconstruction of this cold climate as well as its influence on interbasin relation and ocean/atmosphere feedbacks have been established (*Chapter 3*). The subsequent transition into the present interglacial and the Holocene period were investigated to reveal potential Southern Ocean interbasin offsets indicated by antarctic ice cores and to decipher the response of SSST and WSI distribution to atmospheric mechanisms and their feedbacks (*Chapters 4, 5*). Based on the presented temperature and sea-ice estimates from the southern SAZ and AZ and the comparison to the relevant published records from the Pacific, Atlantic and Indian sectors (see *Chapter 1.2.3*) this thesis achieves decisive results concerning the raised research questions (*Chapter 1.5*):

The compilation of Pacific temperature and sea-ice records enlarged by the diatom-derived results presented in this thesis shows an average northward expansion of the Southern Ocean cold-water realm and the WSI extent by ~5° during the LGM. Though exhibiting a strong east-west gradient expressed in farther WSI expansion and steeper temperature gradients in the western sector and higher sea-ice and SST variability in the eastern sector, the Pacific sector shows a coherent latitudinal zonation mirroring results from the Atlantic and Indian sectors of the Southern Ocean. An evenly distributed zone of strongest cooling (>4 K) in the present SAZ contradicts the suggestion of a non-uniform circum-Antarctic cooling (Gersonde et al., 2005). Strong topographic forcing, predominantly causing the east-west gradient, further inhibits the definite assignment of glacial frontal positions solely based on SSTs. Considering a similar glacial as modern frontal system, imprinting of fronts with colder temperatures is strongly suggested in areas without significant SST gradients and prominent topography. The overall northward shift of cold surface water and the sea-ice edge eventually led to an associated displacement of the opal belt, an expanded area for CO_2 sequestration and the thermally intensification of the cold water route via the Drake Passage. Considerably cold surface water that deviates northward into the Humboldt Current System pinpoints

Subantarctic Surface Water as source for eastern equatorial LGM cooling. However, glacial advection of silicic acid via the Humboldt Current System might have had a less northward extent not reaching latitudes above 20°S. Coupled climate model results estimating glacial sea-ice extent might be able to match with proxy results, but the majority of models tend to overestimate especially the WSI extent around Antarctica. Atmospheric forcing mechanisms such as the Southern Westerly Winds (SWW), the Southern Annular Mode (SAM) and the El Niño Southern Oscillation (ENSO) are further significantly influencing the temperature and sea-ice pattern in the Pacific sector. Feedback mechanisms between low and high sea level pressure systems over the high and low latitudes result in intensity and frequency changes of the mentioned mechanisms. During the LGM comparatively weakened/equatorward expanded westerlies favored a wide sea-ice expansion, that might have been intensified by cold ENSO events and a positive SAM index.

The Pacific intrabasin E-W gradient did not only impact the environmental conditions during the LGM but also the subsequent deglaciation (*Chapter 4*). Although SST and sea-ice reconstructions over Termination I do show in-phase changes relative to a common antarctic sequence, the onset of deglacial warming and sea-ice retreat preceded in the eastern Pacific sector by roughly 3 kyr. Such early warming, recently detected in WAIS ice cores, was most probably triggered by simultaneous interhemispheric insolation increase, subsequently warming the surface ocean and eventually leading to ice sheet disintegration. However, deglacial warming in the western Pacific sector started simultaneously with the Atlantic sector around 19-18 kyr BP marked by the slowdown of the AMOC and additional storage of heat in the SH. Once the deglaciation in all Southern Ocean sectors started, the bipolar seesaw mechanism resulted in distinct two-step circum-Antarctic warming interrupted by the ACR between 14 and 12 kyr BP and culminating from 12-9 kyr BP in the AHO. Sea ice gradually retreated during the early deglacial SST increase, recurred during the ACR and showed its minimum extent during the AHO. During the deglacial evolution, strengthened and poleward shifted SWW enhanced upwelling of old nutrient-rich water masses that raised bioproductivity and increased CO_2 outgassing. Despite the early deglacial onset in the eastern Pacific sector, atmospheric CO_2 ultimately rose after the slowdown of the AMOC, and thus may have been primarily governed by the climate changes in the Atlantic sector. Our minor ACR cooling further suggests the WAIS as unlikely source of meltwater pulse 1A.

In comparison to the ACR, a significantly larger SST decrease occurred after the AHO between 8 and 10 kyr BP, recorded in all Southern Ocean sectors (*Chapter 5*). This distinct drop of temperatures is generated in atmosphere-ocean models by freshwater intrusion

originating from the West Antarctic. Such meltwater shedding is plausible from rapid retreat of the WAIS during the preceding thermal optimum. Strongest cooling is suggested to have taken place in the Pacific Antarctic Zone, propagating the signal into the adjacent sectors. However, the latitudinal extent of the cooling and the absolute values of model and proxy results show discrepancies that might result from insufficient reference data for the model setup. During the Mid- to Late Holocene a general trend in Southern Ocean records is hardly to determine. It seems evident that western Pacific SSSTs react very sensitive to the shift of SWW- to ENSO-governed climate whereas records in the vicinity of the Antarctic continent show high regionally influenced variability.

Although climate variability of the last 30 kyr BP in the Pacific sector of the Southern Ocean seems to closely mirror those from Atlantic marine and antarctic ice core records, our last glacial to present interglacial reconstructions point to a highly sensitive ocean sector that is most important for initiating prominent climate changes and the propagation of signals via the ACC. Besides the well-studied control of Northern Hemisphere changes on the AMOC and subsequently the Atlantic sector of the Southern Ocean, feedback mechanisms between ice, ocean and atmosphere in the Pacific, reflected in sea surface parameters, might forecast circum-Antarctic conditions.

6.2   Outlook

The results of glacial and deglacial climate evolution in the Pacific sector presented in this thesis close a prominent gap in Southern Ocean research. However, although the generated data provide a good basis for paleoceanographic implications in the discussed time slices, further studies are needed, to refine certain hypotheses. Despite the good correlation of diatom abundances and physical parameters, the establishment of age models with higher precision in the Southern Ocean is hampered by insufficient carbonate concentrations and uncertainties concerning surface reservoir ages. Despite occurrent problems within the measurements of distinctly small foraminifer contents regarding extremely low resolved time periods, the fairly new established MICADAS dating achieves good results compared to conventional techniques. Thus, for Southern Ocean sediments this method is of great advantage to achieve highest accuracy for the establishment of age models in the future especially with respect to a precise definition of a possible preceding of deglacial warming. Low amounts of material ($<$ 1mg carbonate) would allow for denser sampling strategies, enabling high resolved ^{14}C measurements and precise predictions. Although the warming is visible at several of the

investigated core sites and at previously published ones, additional ^{14}C measurements from cores in the southern SAZ would clarify the exact onset of the deglaciation. In the light of improved dating strategies, future radiocarbon research in the Pacific sector of the Southern Ocean has to focus on the establishment of reliable surface reservoir ages especially for the glacial and deglacial. Recent studies by Ronge (2014) indicate an early deglacial upwelling of deep and carbon-rich water in the southern Subantarctic Zone, probably resulting in distinctly higher reservoir ages. If such upwelling might have happened as well south of the Subantarctic and Antarctic Polar Front, we definitely need further investigation to resolve these issues.

The upwelling of carbon-rich deep water as observed by Ronge (2014) did not result in complete outgassing of CO_2. Thus, possible stratification in the eastern Pacific sector might have occurred during the glacial and early deglacial until CO_2 outgassing started simultaneously in all Southern Ocean sectors. Recent studies from the subarctic North Pacific, using diatom-derived $\delta^{18}O$ and $\delta^{30}Si$, showed the potential to decipher surface water stratification on millennial time scales (Maier et al., 2013, 2015). As the North Pacific represents a similar High Nutrient-Low Chlorophyll regime as the Southern Ocean, the application of this proxy on the same set of cores investigated in this thesis to detect possible surface water stratification, would be promising.

Further research in the Southern Ocean has to be done concerning the investigation of the ACC flow speed. Such velocity data would help to derive ACC feedbacks with the SWW, hence would provide additional data for model simulations of past wind speeds. As available climate models show ambiguous results concerning the intensity of the SWW, the majority of associated temperature gradients do not fit the proxy results. Although just recently efforts have been made to shed light on the intensity of the "cold-water route" (Lamy et al., 2015), additional velocity data of the ACC in the Pacific sector might help to unravel if the thermal intensification via the Drake Passage was accompanied by more or less water mass transport.

Most important for future research in the Southern Ocean and with respect to SST and sea-ice reconstructions on important time slices like the LGM, is the establishment of a continuous circum-Antarctic data collection. Although, large parts of the Indian Ocean areas have been studied yet (e.g. Barrows and Juggins, 2005), the Antarctic Zone south of 60°S is a blank page in Southern Ocean research. Providing similar sediment conditions as in the Atlantic and Pacific sector, the Antarctic Indian Ocean is predestinated for diatom assemblage studies and should be on the agenda of future scientific expeditions and research activities.

Data handling

All data presented in this thesis are stored electonically and will be available online in the PANGAEA database after publication or on personal request (http://www.pangaea.de).

References

Abelmann, A., Gersonde, R., 1991. Biosiliceous particle flux in the Southern Ocean. Marine Chemistry 35, 503-536, doi: 10.1016/S0304-4203(09)90040-8.

Abelmann, A., Gersonde, R., Cortese, G., Kuhn, G., Smetacek, V., 2006. Extensive phytoplankton blooms in the Atlantic sector of the glacial Southern Ocean, Paleoceanography, 21, PA1013, doi:10.1029/2005PA001199.

Abelmann, A., Gersonde, R., Knorr, G., Zhang, X., Chapligin, B., Maier, E., Esper, O., Friedrichsen, H., Lohmann, G., Meyer, H., Tiedemann, R., 2015. The seasonal sea ice zone in the glacial Southern Ocean as a carbon sink. Nature Communications, 6(8136), 1-12, doi:10.1038/ncomms9136.

Allen, C.S., Pike, J., Pudsey, C.J., 2011. Last glacial–interglacial sea-ice cover in the SW Atlantic and its potential role in global deglaciation. Quaternary Science Reviews, 30(19-20), 2446-2458, doi:10.1016/j.quascirev.2011.04.002.

Alley, R.B., Ágústsdóttir, A.M., 2005. The 8k event: cause and consequences of a major Holocene abrupt climate change. Quaternary Science Reviews, 24, 1123-1149, doi:10.1016/j.quascirev.2004.12.004.

Alley, R.B., Mayewski, P.A., Sowers, T., Stuiver, M., Taylor, K.C., Clark, P.U., 1997. Holocene climatic instability: A prominent, widespread event 8200yr ago. Geology, 25(6), 483-486, doi:10.1130/0091-7613(1997)025<0483:HCIAPW>2.3.CO;2.

Anderson, J.B., Shipp, S.S., Lowe, A.L., Wellner, J.S., Mosola, A.B., 2002. The Antarctic Ice Sheet during the Last Glacial Maximum and its subsequent retreat history: a review. Quaternary Science Reviews, 21(1), 49-70, doi: 10.1016/S0277-3791(01)00083-X.

Anderson, J.B., Conway, H., Bart, P.J., Witus, A.E., Greenwood, S.L., McKay, R.M., Hall, B.L., Ackert, R.P., Licht, K., Jakobsson, M., Stone, J.O., 2014. Ross Sea paleo-ice sheet drainage and deglacial history during and since the LGM. Quaternary Science Reviews, 100, 31-54, doi: 10.1016/j.quascirev.2013.08.020.

Anderson, R.F., Ali, S., Bradtmiller, L.I., Nielsen, S.H.H., Fleisher, M.Q., Anderson, B.E., Burckle, L.H., 2009. Wind-driven upwelling in the Southern Ocean and the deglacial rise in atmospheric CO_2. Science, 323(5920), 1443-1448, DOI: 10.1126/science.1167441.

Annan, J.D., Hargreaves, J.C., 2013. A new global reconstruction of temperature changes at the Last Glacial Maximum. Climate of the Past, 9(1), 367-376, doi:10.5194/cp-9-367-2013.

Armand, L., Zielinski, U., 2001. Diatom Species of the Genus Rhizosolenia from Southern Ocean Sediments: Distribution and Taxonomic Notes. Diatom Research, 16(2), 259-294, doi:10.1080/0269249X.2001.9705520.

Armand, L.K., Crosta, X., Romero, O., Pichon, J.J., 2005. The biogeography of major diatom taxa in Southern Ocean sediments: 1. Sea ice related species. Palaeogeography, Palaeoclimatology, Palaeoecology, 223, 93–126, doi:10.1016/j.palaeo.2005.02.015.

Arrigo, K.A., Thomas, D.N., 2004. Large scale importance of sea ice biology in the Southern Ocean. Antarctic Science, 16(4), 471-486, doi:10.1017/S0954102004002263.

Arrigo, K.R., Worthen, D., Schnell, A., Lizotte, M.P., 1998. Primary production in Southern Ocean waters. Journal of Geophysical Research, 103, 15587-15600, doi:10.1029/98JC00930.

Arrigo, K.R., Worthen, D.L., Robinson, D.H., 2003. A coupled ocean-ecosystem model of the Ross Sea: 2. Iron regulation of phytoplankton taxonomic variability and primary production. Journal of Geophysical Research, 108, 3231, doi:10.1029/2001JC000856.

Arrigo, K.R., van Dijken G.L., Bushinsky, S., 2008. Primary production in the Southern Ocean, 1997–2006, Journal of Geophysical Research, 113, C08004, doi:10.1029/2007JC004551.

Assmann, K.M., Hellmer, H.H., Jacobs, S.S., 2005. Amundsen Sea ice production and transport. Journal of Geophysical Research, 110, C12013, doi:10.1029/2004JC002797.

Bamber, J.L., Riva, R.E., Vermeersen, B.L.A., LeBrocq, A.M., 2009. Reassessment of the Potential Sea-level Rise from a Collapse of the West Antarctic Ice Sheet. Science, 324, 901, doi:10.1126/science.1169335.

Ballarotta, M., Brodeau, L., Brandefelt, J., Lundberg, P., Döös, K., 2013. Last Glacial Maximum world ocean simulations at eddy-permitting and coarse resolutions: do eddies contribute to a better consistency between models and palaeoproxies?. Climate of the Past, 9, 2669-2686, doi:10.5194/cp-9-2669-2013.

Bard, E., 1988. Correction of Accelerator Mass Spectrometry [14]C Ages Measured in Planktonic Foraminifera: Paleoceanographic Implications. Paleoceanography, 3(6), 635-645, doi:10.1029/PA003i006p00635.

Barrell, D., Almond, P.C., Vandergoes, M.J., Lowe, D.J., Newnham, R.M. A Composite Stratotype for Regional Comparison of Climatic Events in New Zealand Over the Past 30,000 Years (NZ-INTIMATE project), Quaternary Science Reviews, 74, 4-20, doi:10.1016/j.quascirev.2013.04.002.

Barrows, T.T., Juggins, S., 2005. Sea-surface temperatures around the Australian margin and Indian Ocean during the Last Glacial Maximum. Quaternary Science Reviews, 24(7-9), 1017-1047, doi:10.1016/j.quascirev.2004.07.020.

Bazin, L., Landais, A., Lemieux-Dudon, B., Toyé Mahamadou Kele, H., Veres, D., Parrenin, F., Martinerie, P., Ritz, C., Capron, E., Lipenkov, V., Loutre, M.F., Raynaud, D., Vinther, B., Svensson, A., Rasmussen, S.O., Severi, M., Blunier, T., Leuenberger, M., Fischer, H., Masson-Delmotte, V., Chappellaz, J., Wolff, E., 2013. An optimized multi-proxy, multi-site Antarctic ice and gas orbital chronology (AICC2012): 120–800 ka. Climate of the Past, 9(4), 1715-1731, doi:10.5194/cp-9-1715-2013.

Belkin, I.M., Gordon, A.L., 1996. Southern Ocean fronts from the Greenwich meridian to Tasmania, Journal of Geophysical Research, 101(C2), 3675–3696, doi:10.1029/95JC02750.

Bentley, M.J., Hodgson, D.A., Smith, J.A., Ó Cofaigh, C., Domack, E.W., Larter, R.D., Roberts, S.J., Brachfeld, S., Leventer, A., Hjort, C., Hillenbrand, C.-D., Evans, J., 2009: Mechanisms of Holocene palaeoenvironmental change in the Antarctic Peninsula region. The Holocene, 19 (1), 51-69, doi:10.1166/0959683608096603.

Benz, V., Esper, O., Gersonde, R., Lamy, F., Tiedemann, R., a. Last Glacial Maximum sea surface temperature and sea-ice extent in the Pacific sector of the Southern Ocean. Quaternary Science Reviews (under review).

Benz, V., Esper, O., Gersonde, R., Lamy, F., Tiedemann, R., b. Last glacial to early Holocene sea surface temperature and sea ice variability in the Pacific sector of the Southern Ocean. (In preparation for Paleoceanography).

Berberich, D., 1996. The planktonic foraminifere Neogloboquadrina pachyderma (Ehrenberg) in the Weddell Sea, Antarctica. Berichte zur Polarforschung (Reports on Polar Research) 195, pp. 198.

Bianchi, C., Gersonde, R., 2004. Climate evolution at the last deglaciation: the role of the Southern Ocean. Earth and Planetary Science Letters 228(3), 407-424, doi:10.1016/j.epsl.2004.10.003.

Bintanja, R., Van Oldenborgh, G.J., Katsman, C.A., 2015. The effect of increased fresh water from Antarctic ice shelves on future trends in Antarctic sea ice. Annals of Glaciology, 56 (59), doi:10.3189/2015AoG69A001.

Birks, C.J.A., Koç, N., 2002. A high-resolution diatom record of late-Quaternary sea-surface temperatures and oceanographic conditions from the eastern Norwegian Sea. Boreas, 31.323-344, doi:, 10.1111/j.1502-3885.2002.tb01077.x.

Birks, H.J.B., 2003. Quantitative paleoenvironmental reconstructions from Holocene biological data. IN: Mackay, A., Battarbee, R.W., Birks, H.J.B., Oldfield, F. (Eds.), Global Change in the Holocene. Arnold, London, pp.107-123.

Birks, H.J.B., Line, J.M., Juggins, S., Stevenson, A.C., ter Braak, C.J.F., 1990. Diatoms and pH reconstruction. Philosophical Transactions of the Royal Society of London Series B, 327, 263–278, doi:10.1098/rstb.1990.0062.

Blunier, T., Brook, E.J., 2001. Timing of Millennial-Scale Climate Change in Antarctica and Greenland During the Last Glacial Period, Science, 291(5501), 109-112, doi:10.1126/science.291.5501.109.

Blunier, T., Chappellaz, J., Schwander, J., Dällenbach, A., Stauffer, B., Stocker; T.F., Raynaud, D., Jouzel, J., Clausen, H.B., Hammer, C.U., Johnsen, S.J., 1998. Asynchrony of Antarctic and Greenland climate change during the last glacial period. Nature 394, 739-743, doi:10.1038/29447.

Bostock, H.C., Barrows, T.T., Carter, L., Chase, Z., Cortese, G., Dunbar, G.B., Ellwood, M., Hayward, B., Howard, W., Neil, H.L., Noble, T.L., Mackintosh, A., Moss, P.T., Moy, A.D., White, D., Williams, M.J.M., Armand, L.K., 2013. A review of the Australian–New Zealand sector of the Southern Ocean over the last 30 ka (Aus-INTIMATE project). Quaternary Science Reviews, 74, 35-57, doi:10.1016/j.quascirev.2012.07.018.

Bouttes, N., Paillard, D., Roche, D.M., 2010. Impact of brine-induced stratification on the glacial carbon cycle. Climate of the Past, 6(5), 575-589, doi:10.5194/cp-6-575-2010.

Bradtmiller, L.I., Anderson, R.F., Fleisher, M.Q., Burckle, L.H., 2009. Comparing glacial and Holocene opal fluxes in the Pacific sector of the Southern Ocean. Paleoceanography, 24, PA2214, doi:10.1029/2008PA001693.

Brandon, M.A., Cottier, F.R., Nilsen, F., 2010. Sea Ice and Oceanography, In: Thomas, D.N., Dieckmann, G.S. (Eds.), Sea Ice (second edition). Wiley-Blackwell, 79-111.

Broecker, W.S., 1998. Paleocean circulation during the last deglaciation: A bipolar seesaw?. Paleoceanography, 13(2), 119-121, doi: 10.1029/97PA03707.

Broecker, W.S., Peteet, D.M., Rind, D., 1985. Does the ocean-atmosphere system have more than one stable mode of operation) Nature, 315, 21-26, doi:10.1038/315021a0.

Brook, E.J., Harder, S., Severinghaus, J., Steig, E.J., Sucher, C.M., 2000. On the irigin and timing of rapid changes in atmospheric methane during the last glacial period. Global Biogeochemical Cyces, 14(2), 559-572, doi:10.1029/1999GB001182.

Brook, E.J., White, J.W.C., Schilla, A.S.M., Bender, M.L., Barnett, B., Severinghaus, J.P., Taylor, K.C., Alley, R.B., Steig, E.J., 2005. Timing of millennial-scale climate change at Siple Dome, West Antarctica, during the last glacial period, Quaternary Science Reviews, 24(12–13), 1333-1343, doi:10.1016/j.quascirev.2005.02.002.

Burckle, L.H., 1972. Diatom Evidence Bearing on the Holocene in the South Atlantic. Quaternary Research, 2, 323-326, doi:10.1016/0033-5894(72)90052-X.

Burckle, L.H., 1983. Diatom dissolution patterns in sediments of the Southern Ocean. Geological Society of American Journal, 15, 536-537.

Burckle, L.H., 1984a. Ecology and paleoecology of the marine diatom *Eucampia antarctica* (Castr.) Mangin. Marine Micropaleontology, 9: 77-86.

Burckle, L.H., 1984b. Diatom distribution and paleoceanographic reconstruction in the Southern Ocean - present and last glacial maximum. Marine Micropaleontology, 9, 241-261.

Burckle, L.H., Cooke, D.W., 1983. Late Pleistocene *Eucampia antarctica* abundance stratigraphy in the Atlantic Sector of the Southern Ocean. Micropaleontology, 29, 6-10.

Burckle, L.H., Robinson, D., Cooke, D.W., 1982. Reappraisal of sea-ice distribution in Atlantic and Pacific sectors of the Southern Ocean at 18,000 yr BP. Nature, 229, 435-437, doi:10.1038/299435a0.

Burckle, L.H., Jacobs, S.S., McLaughlin, R.B., 1987. Late Austral spring diatom distribution between New Zealand and the Ross Ice shelf, Antarctica: hydrographic and sediment correlations. Micropaleontology, 33(1), 284-297, doi:10.2307/1485528.

Burke, A., Robinson, L.F., 2012. The Southern Ocean's role in carbon exchange during the last deglaciation. Science 335(6068), 557-561, doi:10.1126/science.1208163.

Cai, W., Whetton, P.H., Karoly, D.J., 2003. The response of the Antarctic Oscillation to increasing and stabilized atmospheric CO2. Journal of Climate, 16(10), 1525-1538, doi:10.1175/1520-0442-16.10.1525.

Cai, W., Shi, G., Cowan, T., Bi, D., Ribbe, J., 2005. The response of the Southern Annular Mode, the East Australian Current, and the southern mid-latitude ocean circulation to global warming, Geophysical Research Letters, 32, L23706, doi:10.1029/2005GL024701.

Calvo, E., Pelejero, C., De Deckker, P., Logan, G. A., 2007. Antarctic deglacial pattern in a 30 kyr record of sea surface temperature offshore South Australia. Geophysical Research Letters, 34(13), doi:10.1029/2007GL029937.

Caniupán, M., Lamy, F., Lange, C.B., Kaiser, J., Arz, H., Kilian, R., -Urrea, O., Aracena, C., Hebbeln, D., Kissel, C., Laj, C., Mollenhauer, G., Tiedemann, R., 2011. Millennial-scale sea surface temperature and Patagonian Ice Sheet changes off southernmost Chile (53°S) over the past ~60 kyr. Paleoceanography, 26, PA3221, doi:10.1029/2010PA002049.

Carter, L., Neil, H.L., Northcote, L., 2002. Late Quaternary ice-rafting events in the SW Pacific Ocean, off eastern New Zealand. Marine geology, 191(1), 19-35, doi:10.1016/S0025-3227(02)00509-1.

Chase, Z., Anderson, R.F., Fleisher, M.Q., Kubik, P.W., 2003. Accumulation o biogenic and lithogenic material in the Pacific sector of the Southern Ocean during the past 40,000 years. Deep-Sea Research Part. II: Topical Studies in Oceanography, 50(3,4), 799-832, doi:10.1016/S0967-0645(02)00595-7.

Chase, Z., McManus, J., Mix, A.C., Muratli, J., 2014. Southern-ocean and glaciogenic nutrients control diatom export production on the Chile margin. Quaternary Science Reviews, 99, 135-145, doi:10.1016/j.quascirev.2014.06.015.

Clark, P.U., Dyke, A.S., Shakun, J.D., Carlson, A.E., Clark, J., Wohlfarth, B., Mitrovica, J.X., Hostetler, S.W., McCabe, A.M., 2009. The Last Glacial Maximum. Science, 325(5941), 710-714, doi:10.1126/science.1172873.

Climate: Long-Range Investigation, Mapping, and Prediction (CLIMAP) Project Members, 1976. The surface of the Ice Age Earth. Science, 191, 1131-1137.

Climate: Long-Range Investigation, Mapping and Prediction (CLIMAP) Project Members, 1981. Seasonal reconstructions of the Earth's surface at the Last Glacial Maximum. Geological Society of American Map Chart Series MC-36, 1-18.

Collins, L.G., Pike, J., Allen, C.S., Hodgson, D.A., 2012. High-resolution reconstruction of southwest Atlantic sea-ice and its role in the carbon cycle during marine isotope stages 3 and 2. Paleoceanography, 27, PA3217, doi:10.1029/2011pa002264.

Comiso, J.C., 2010. Variability and trends of the global sea ice cover. In: Thomas, D.N, Dieckmann, G.S. (Eds.), Sea ice (second edition). Wiley-Blackwell, 205-246.

Cortese, G., Abelmann, A., Gersonde, R., 2007. The last five glacial-interglacial transitions: A high-resolution 450,000-year record from the subantarctic Atlantic. Paleoceanography, 22, PA4203, doi:10.1029/2007PA001457.

Cooke, D.W., Hays, J.D., 1982. Estimates of Antarctic Ocean seasonal ice-cover during glacial intervals In: Craddock, C. (Ed.), Antarctic Geoscience, IUGS, Ser. B no. 4, 1017-1025.

Crosta, X., Pichon, J.-J., Labracherie, M., 1997. Distribution of *Chaetoceros* resting spores in modern peri-Antarctic sediments. Marine Micropaleontology, 29, 283-299, doi:10.1016/S0377-8398(96)00033-3.

Crosta, X., Pichon, J.-J., Burckle, L.H., 1998a. Application of Modern Analog Technique to Marine Antarctic Diatoms: Reconstruction of Maximum Sea-Ice Extent at the Last Glacial Maximum. Paleoceanography, 13(3), 284-297, doi:10.1029/98pa00339.

Crosta, X., Pichon, J.-J., Jacques, Burckle, L.H., 1998b. Reappraisal of Antarctic seasonal sea-ice at the Last Glacial Maximum. Geophysical Research Letters, 25(14), 2703-2706, doi:10.1029/98gl02012.

Crosta, X., Sturm, A., Armand, L., Pichon, J.-J., 2004. Late Quaternary sea ice history in the Indian sector of the Southern Ocean as record by diatom assemblages. Marine Micropaleontology 50, 209–223, doi:10.1016/S0377-8398(03)00072-0.

Crosta, X., Romero, O., Armand, L.K., Pichon, J.-J., 2005. The biogeography of major diatom taxa in Southern Ocean sediments: 2. Open ocean related species. Palaeogeography, Palaeoclimatology, Palaeoecology, 223, 66– 92, doi:10.1016/j.palaeo.2005.03.028.

Crosta, X., Denis, D., Ther, O., 2008. Sea ice seasonality during the Holocene, Adélie Land, East Antarctica. Marine Micropaleontology, 66, 222-232, doi:10.1016/j.marmicro.2007.10.001.

Crundwell, M., Scott, G., Naish, T., Carter, L., 2008. Glacial–interglacial ocean climate variability from planktonic foraminifera during the Mid-Pleistocene transition in the temperate Southwest Pacific, ODP Site 1123. Palaeogeography, Palaeoclimatology, Palaeoecology 260, 202-229, doi:10.1016/j.palaeo.2007.08.023.

Cunningham, W.L., Leventer, A., Andrews, J.T., Jennings, A.E., Licht, K.J., 1999. Late Pleistocene-Holocene marine conditions in the Ross Sea, Antarctica: evidence from the diatom record. The Holocene, 9(2), 129-139, doi: 0.1191/095968399675624796.

Das, S.B., Alley, R.B., 2008. Rise in frequency of surface melting at Siple Dome through the Holocene: Evidence for increasing marine influence on the climate of West Antarctica. Journal of Geophysical Research, 113, D02112, doi:10.1029/2007JD008790.

De Deckker, P., Moros, M., Perner, K., Jansen, E., 2012. Influence of the tropics ans southern westerlies on glacial interhemispheric asymmetry. Nature Geoscience, 5, 266-269, doi:10.1038/ngeo1431.

DeFelice, D.R., 1979. Relative diatom abundance as tool for monitoring winter sea ice fluctuations in southeast Atlantic. Antarctic Journal of the United States, 14, 105-106.

Denis, D., Crosta, X., Zaragosi, S., Romero, O., Martin, B., Mas, V., 2006. Seasonal and subseasonal climate changes recorded in laminated diatom ooze sediments, Adelie Land, East Antarctica. The Holocene, 16(8), 1137-1147, doi:10.1177/0959683606069414.

Denton, G.H., Anderson, R.F., Toggweiler, J.R., Edwards, R.L., Schaefer, J.M., Putnam, A.E. 2010. The last glacial termination. Science, 328(5986), 1652-1656, doi: 10.1126/science.1184119.

Deschamps, P., Durand, N., Bard, E., Hamelin, B., Camoin, G., Thomas, A.L., Henderson, G. M., Okuno, J., Yokoyama, Y., 2012. Ice-sheet collapse and sea-level rise at the Bolling warming 14,600 years ago. Nature, 483(7391), 559-564, doi:10.1038/nature10902.

de Vernal, A., Eynaud, F., Henry, M., Hillaire-Marcel, C., Londeix, L., Mangin, S., Matthiessen, J., Marret, F., Radi, T., Rochon, A., Solignac, S., Turon, J.-L., 2005. Reconstruction of sea-surface conditions at middle to high latitudes of the Northern Hemisohere during the Last Glacial Maximum (LGM) based on dinoflagellate cyst assemblages. Quaternary Science reviews, 24, 897-924, doi:10.1016/j.quascirev.2004.06.014.

Diekmann, B., 2007. Sedimentary patterns in the late Quaternary Southern Ocean. Seep-Sea Research II, 54, 2350-2366, doi:10.1016/j.dsr2.2007.07.025.

Divine, D.V., Koç, N., Isaksson, E., Nielsen, S., Crosta, X., Godtliebsen, F., 2010. Holocene Antarctic climate variability from ice and marine sediment cores: Insights on ocean–atmosphere interaction. Quaternary Science Reviews, 29(1), 303-312, doi:10.1016/j.quascirev.2009.11.012.

Dong, S., Sprintall, J., Gille, S.T., 2006. Location of the Antarctic polar front from AMSR-E satellite sea surface temperature measurements. Journal of Physical Oceanography, 36(11), 2075-2089, doi:10.1175/JPO2973.1.

Drysdale, R.N., Hellstrom, J.C., Zanchetta, G., Fallick, A.E., Sánchez Goñi, M.F., Couchoud, I., McDonald, J., Maas, R., Lohmann, G., Isola, I., 2009. Evidence for Obliquity Forcing of Glacial Termination II, Science, 325(5947), 1527-1531, doi:10.1126/science.1170371.

Dubois, N., Kienast, M., Normandeau, C., Herbert, T.D., 2009. Eastern equatorial Pacific cold tongue during the Last Glacial Maximum as seen from alkenone paleothermometry, Paleoceanography, 24, PA4207, doi:10.1029/2009PA001781.

Ehlert, C., Grasse, P., Frank, M., 2013. Changes in silicate utilisation and upwelling intensity off Peru since the Last Glacial Maximum–insights from silicon and neodymium isotopes. Quaternary Science Reviews, *72*, 18-35, doi:10.1016/j.quascirev.2013.04.013.

EPICA Community Members, 2004. Eight glacial cycles from an Antarctic ice core, Nature, 429(6992), 623 – 628, doi:10.1038/ nature02599.

EPICA Community Members, 2006. One-to-one coupling of glacial climate variability in Greenland and Antarctica. Nature, 444, 195-198, doi:10.1038/nature05301.

Esper, O., Gersonde, R., Kadagies, N., 2010. Diatom distribution in southeastern Pacific surface sediments and their relationship to modern environmental variables. Palaeogeography, Palaeoclimatology, Palaeoecology, 287, 1–27, doi:10.1016/j.palaeo.2009.12.006.

Esper, O., Gersonde, R., 2014a. New tools for the reconstruction of Pleistocene Antarctic sea ice. Palaeogeography, Palaeoclimatology, Palaeoecology, 399, 260-283, doi:10.1016/j.palaeo.2014.01.019.

Esper, O., Gersonde, R., 2014b. Quaternary surface water temperature estimations: New diatom transfer functions for the Southern Ocean. Palaeogeography, Palaeoclimatology, Palaeoecology, 414, 1-19, doi:10.1016/j.palaeo.2014.08.008.

Etourneau, J., Collins, L.G., Willmott, V., Kim, J.-H., Barbara, L., Leventer, A., Schouten, S., Sinninghe Damsté, J.S., Bianchini, A., Klein, V., Crosta, X., Massé, G., 2013. Holocene climate variations in the western Antarctic Peninsula: evidence for sea ice extent predominantly controlled by changes in insolation and ENSO variability. Climate of the Past, 9, 1431-1446, doi:10.5197/cp-9-1431-2013.

Fairbanks, R.G., 1989. A 17,000-year glacio-eustatic sea level record: influence of glacial melting rates on the Younger Dryas event and deep-ocean circulation. Nature, 342, 637-642, doi:10.1038/342637a0.

Feldberg, M.J., Mix, A.C., 2002. Sea-surface temperature estimates in the Southeast Pacific based on planktonic foraminiferal species: modern calibration and Last Glacial Maximum. Marine Micropaleontology, 44, 1–29, doi:10.1016/S0377-8398(01)00035-4.

Felis, T., McGregor, H.V., Linsley, B., Tudhope, A.W., Gagan, M.K., Suzuki, A., Inoue, M., Thomas, A.L., Esat, T.M., Thompson, W.G., Tiwari, M., Potts, D.C., Mudelsee, M., Yokoyama, Y., Webster, J.M., 2014. Intensification of the meridional temperature gradient in the Great Barrier Reef following the Last Glacial Maximum. Nature Communications, 5, 4102, doi:10.1038/ncomms5102.

Ferrari, R., Jansen, M.F., Adkins, J.F., Burke, A., Stewart, A.L., Thompson, A.F., 2014. Antarctic sea ice control on ocean circulation in present and glacial climates. Proceedings of the National Academy of Sciences, 111(24), 8753-8758, doi:10.1073/pnas.1323922111.

Ferry, A.J., Prvan, T., Jersky, B., Crosta, X., Armand, L.K., 2015a. Statistical modeling of Southern Ocean marine diatom proxy and winter sea ice data: Model comparison and developments. Progress in Oceanography, 131, 100-112, doi:10.1016/j.pocean.2014.12.001.

Ferry, A.J., Crosta, X., Quilty, P.G., Fink, D., Howard, W., Armand, L.K., 2015b. First records of winter sea-ice concentration in the southwest Pacific sector of the Southern Ocean. Paleoceanography, 30, doi:10.1002/2014PA002764.

Fischer, G., Fütterer, D., Gersonde, R., Honjo, S., Ostermann, D., Wefer, G., 1988. Seasonal variability of particle flux in the Weddell Sea and its relation to ice cover. Nature, 335(6189), 426-428, doi:10.1038/335426a0.

Fischer, G., Gersonde, R., Wefer, G., 2002. Organic carbon, biogenic silica and diatom fluxes in the marginal winter sea-ice zone and in the Polar Front Region: interannual variations and differences in composition. Deep Sea Research Part II: Topical Studies in Oceanography, 49(9-10), 1721-1745, doi:10.1016/S0967-0645(02)0009-7.

Fischer, H., Fundel, F., Ruth, U., Twarloh, B., Wegner, A., Udisti, R., Becagli, S., Castellano, E., Morganti, A., Severi, M., Wolff, W., Littot, G., Röthlisberger, R., Mulvaney, R., Hutterli, Kaufmann, P., Federer, U., Lambert, F., Bigler, M., Hansson, M., Jonsell, U., de Angelis, M., Boutron, C., Siggaard-Andersen, M.-L., Steffensen, J.P., Barbante, C., Gaspari, V., Gabrielli, P., Wagenbach, D., 2007. Reconstruction of millennial changes in dust emission, transport and regional sea ice coverage using the deep EPICA ice cores from the Atlantic and Indian Ocean sector of Antarctica. Earth and Planetary Science Letters, 260, 340-354, doi:10.1016/j.epsl.2007.06.014.

Ford, H.L., Ravelo, A.C., Polissar, P.J., 2015. Reduced El Niño–Southern Oscillation during the Last Glacial Maximum. Science, 347(6219), 255-258, doi:10.1126/science.1258437.

Frank, M., Gersonde, R., Rutgers van der Loeff, M., Bohrmann, G., Nürnberg, C.C., Kubik, P.W., Suter, M., Mangini, A., 2000. Similar glacial and interglacial export bioproductivity in the Atlantic sector of the Southern Ocean: Multiproxy evidence and implications for glacial atmospheric CO_2. Paleoceanography 15, 642-658, doi:10.1029/2000PA000497.

Fryxell, G.A., Prasad, A.K.S.K, 1990. Eucampia antarctica var. recta (Mangin) stat. nov. (Biddulphiaceae, Bacillariophyceae): life stages at the Weddell Sea ice edge. Phycologia, 29, 27-38, doi:10.2216/i0031-8884-29-1-27.1.

Geibert, W., Rutgers van der Loeff, M.M., Usbeck, R., Gersonde, R., Kuhn, G., Seeberg-Elverfeldt, J., 2005. Quantifying the opal belt in the Atlantic and southeast Pacific sector of the Southern Ocean by means of 230Th normalization. Global Biogeochemical Cycles 1(4), GB4001, doi:10.1029/2005gb002465.

Gersonde, R., 2011. The expedition of the research vessel „Polarstern" to the polar South Pacific in 2009/2010 (ANT-XXVI/2 - BIPOMAC). Reports on Polar and Marine Research, Bremerhaven, Alfred Wegener Institute for Polar and Marine Research, 632, pp. 330, hdl:10013/epic.37910.d001.

Gersonde, R., Zielinski, U., 2000. The reconstruction of late Quaternary Antarctic sea-ice distribution–the use of diatoms as a proxy for sea-ice. Palaeogeography, Palaeoclimatology, Palaeoecology, 162(3-4), 263-286, doi:10.1016/S0031-0182(00)00131-0.

Gersonde, R., Abelmann, A., Brathauer, U., Becquey, S., Bianchi, C., Cortese, G., Grobe, H., Kuhn, G., Niebler, H.S., Segl, M., Sieger, R., Zielinski, U., Fütterer, D.K., 2003a. Last glacial sea surface temperatures and sea-ice extent in the Southern Ocean (Atlantic-Indian sector): A multiproxy approach. Paleoceanography, 18(3), 1061, doi:10.1029/2002PA000809.

Gersonde, R., Abelmann, A., Cortese, G., Becquey, S., Bianchi, C., Brathauer, U., Niebler, H.-S., Zielinski, U., Pätzold, J., 2003b. The late Pleistocene South Atlantic and Southern Ocean surface waters - A summary of time-slice and time series studies. In: Wefer, G., Mulitza, S., Ratmeyer, V. (Eds.), The South Atlantic in the Late Quaternary: reconstruction of Material Budget and Current Systems, Springer Berlin, 499-529.

Gersonde, R., Crosta, X., Abelmann, A., Armand, L., 2005. Sea-surface temperature and sea ice distribution of the Southern Ocean at the EPILOG Last Glacial Maximum - a circum-Antarctic view based on siliceous microfossil records. Quaternary Science Reviews, 24(7-9), 869-896, doi:10.1016/j.quascirev.2004.07.015.

Gloersen, P.C., W.J., Cavalieri, D.J., Comiso, J.C., Parkinson, C.L., Zwally, H.J., 1992. Arctic and antarctic sea ice, 1978-1987: Satellite passive-microwave observations and analysis, NASA: Washington D.C.

Golledge, N. R., Mackintosh, A. N., Anderson, B. M., Buckley, K. M., Doughty, A. M., Barrell, D. J., Denton, G.H., Vandergoes, M.J., Andersen, B.G. and Schaefer, J. M., 2012. Last Glacial Maximum climate in New Zealand inferred from a modelled Southern Alps icefield. Quaternary Science Reviews, 46, 30-45, doi:10.1016/j.quascirev.2012.05.004.

Gomez, B. Carter, L., Trustrum, N.A., Page, M.J., Orpin, A.R., 2013. Coherent rainfall response to middle- and late-Holocene climate variability across the mid-latitude South Pacific. The Holocene, 23 (7), 1002-1007, doi:10.1177/0959683613479679.

Gomez, N., Mitrovica, J.X., Huybers, P., Clark, P.U., 2010. Sea level as a stabilizing factor for marine ice-sheet grounding lines. Nature Geoscience, 3, 850-853, doi:10.1038/ngeo1012.

Goosse, H., Roche, D.M., Mairesse, A., Berger, M., 2013. Modelling past sea ice changes. Quaternary Science Reviews, 79, 191-206, doi:10.1016/j.quascirev.2013.03.011.

Govin, A., Michel, E., Labeyrie, L., Waelbroeck, C., Dewilde, F. Jansen, E., 2009. Evidence for northward expansion of Antarctic Bottom Water mass in the Southern Ocean during the last glacial inception, Paleoceanography, 24, PA1202, doi:10.1029/2008PA001603.

Gouretski V., 1999. The Large-Scale Thermohaline Structure of the Ross Gyre. In: Spezie, G., Manzella, D.M.R. (Eds.), Oceanography of the Ross Sea, Springer, pp. 77-100, doi.10.1007/978-88-470-2250-8_6.

Graham, R.M., De Boer, A.M., 2013. The Dynamical Subtropical Front, Journal of Geophysical Research: Oceans, 118, 5676–5685, doi:10.1002/jgrc.20408.

Harangozo, S.A., 2004. The impact of winter ice retreat on Antarctic winter sea-ice extent and links to the atmospheric meridional circulation. International Journal of Climatology, 24, 1023-1044, doi:10.1002/joc.1046.

Hargraves, P.E., 1968. Species composition and distribution of net plankton diatoms in the Pacific sector of the Antarctic Ocean (Thesis). School of Marine Science, College of Williams and Mary, Virginia, pp.171.

Hasle, G.R., Syvertsen, E.E., 1996. Marine diatoms, in: Tomas, C. R. (Ed.), Identifying Marine Diatoms and Dinoflagellates. Academic Press Limited, London, 5-385.

Hays, J.D., Lozano, J.A., Shackleton, N., Irving, G., 1976. Reconstruction of the Atlantic and western Indian Ocean sectors of the 18,000 B.P. Antarctic Ocean. Geological Society of American Memories, 145, 337-372.

He, F., Shakun, J.D., Clark, P.U., Carlson, A.E., Liu, Z., Otto-Bliesner, B.L., Kutzbach, J.E., 2013. Northern Hemisphere forcing of Southern Hemisphere climate during the last deglaciation. Nature, 494, 81-85, doi:10.1038/nature11822.

Hebbeln, D., Marchant, M., Wefer, G., 2002. Paleoproductivity in the southern Peru–Chile Current through the last 33 000 yr. Marine Geology, 186(3), 487-504, doi:10.1016/S0025-3227(02)00331-6.

Heusser, L., Heusser, C., Pisias, N., 2006. Vegetation and climate dynamics of southern Chile during the past 50,000 years: results of ODP Site 1233 pollen analysis. Quaternary Science Reviews 25, 474-485, doi:10.1016/j.quascirev.2005.04.009.

Hillenbrand, C.-D., Larter, R.D., Dowdeswell, J.A., Ehrmann, W.,Ó Cofaigh, C., Benetti, S., Graham, A.G.C., Grobe, H., 2010. The sedimentary legacy of a palaeo-ice stream on the shelf of the southern Bellingshausen Sea: Clues to West Antarctic glacial history during the Late Quaternary. Quaternary Science Reviews, 29(19), 2741-2763, doi:10.1016/j.quascirev.2010.06.028.

Ho, S.L., Mollenhauer, G., Lamy, F., Martínez-Garcia, A., Mohtadi, M., Gersonde, R., Hebbeln, D., Nunez-Ricardo, S., Rosell-Melé, A., Tiedemann, R., 2012. Sea surface temperature variability in the Pacific sector of the Southern Ocean over the past 700 kyr. Paleoceanography, 27(4), PA4202, doi:10.1029/2012PA002317.

Hodell, D.A., Kanfoush, S.L., 2001. Abrupt cooling of Antarctic Surface Waters and Sea Ice Expansion in the South Atlantic Sector of the Southern Ocean at 5000 cal yr B.P., Quaternary Research, 56, 191-198, doi:10.1006/qres.2001.2252.

Hutson, W.H., 1980. The Agulhas Current During the Late Pleistocene: Analysis of Modern Faunal Analogs. Science, 207 (4426), 64-66, doi:10.1126/science.207.4426.64.

Huybers, P., Denton, G., 2008. Antarctic temperature at orbital timescales controlled by local summer duration. Nature Geoscience, 1(11), 787-792, doi:10.1038/ngeo311.

Imbrie, J., Kipp, N.G., 1971. A new micropaleontological method for Quantitative Paleoclimatology: Application to a late Pleistocene Caribbean Core. In: Turekian, K.K. (Ed.), The late Cenozoic Glacial Ages. Yale University Press, New Haven, Connecticut, 71-181.

IPCC, 2014: Climate Change 2014: Synthesis Report. Contribution of Working Groups I, II and III to the Fifth Assessment Report of the Intergovernmental Panel on Climate Change (Core Writing Team, R.K. Pachauri and L.A. Meyer (eds.)). IPCC, Geneva, Switzerland, 151 pp.

Jacot Des Combes, H., Esper, O., De La Rocha, C.L., Abelmann, A., Gersonde, R., Yam, R., Shemesh, A., 2008. Diatom δ^{13}C, δ^{15}N and C/N since the Last Glacial Maximum in the Southern Ocean: Potential impact of Species Composition. Paleoceanography, 23(4), PA4209, doi:10.1029/2008PA001589.

Jansen, E., Veum, T., 1990. Evidence for two-step deglaciation and its impact on North Atlantic deep-water formation. Nature 243, 612-616, doi:10.1038/343612a0.

Joughin, I, Alley, R. B., 2011. Stability of the West Antarctic ice sheet in a warming world. Nature Geoscience 4, 506-513, doi:10.1038/NGEO1194.

Jouzel, J., Masson-Delmotte, V., Cattani, O., Dreyfus, G., Falourd, S., Hoffmann, G., Minster, B., Nouet, J., Barnola, J.M., Chappellaz, J., Fischer, H., Gallet, J.C., Johnsen, S., Leuenberger, M., Loulergue, L., Luethi, D., Oerter, H., Parrenin, F., Raisbeck, G., Raynaud, D., Schilt, A., Schwander, J., Selmo, E., Souchez, R., Spahni, R., Stauffer, B., Steffensen, J.P., Stenni, B., Stocker, T.F., Tison, J.L., Werner, M., Wolff, E.W., 2007. Orbital and Millennial Antarctic Climate Variability over the Past 800,000 Years. Science, 317 (5839), 793-796, doi:10.1126/science.1141038.

Kaiser, J., Lamy, F. 2010. Links between Patagonian Ice Sheet fluctuations and Antarctic dust variability during the last glacial period (MIS 4-2). Quaternary Science Reviews, 29(11), 1464-1471, doi:10.1016/j.quascirev.2010.03.005.

Kaiser, J., Schefuß, E., Lamy, F., Mohtadi, M. and Hebbeln, D., 2008. Glacial to Holocene changes in sea surface temperature and coastal vegetation in north central Chile: high versus low latitude forcing, Quaternary Science Reviews, 27, 2064-2075, doi:10.1016/j.quascirev.2008.08.025.

Kalansky, J., Rosenthal, Y., Herbert, T., Bova, S., Altabet, M., 2015. Southern Ocean contributions to the Eastern Equatorial Pacific heat content during the Holocene. Earth and Planetary Science Letters, 424, 158-167, doi:10.1016/j.epsl.2015.05.013.

Kaplan, M.R., Fogwill, C.J., Sugden, D.E., Hulton, N.R.J., Kubik, P.W., Freeman, S.P.H.T., 2008. Southern Patagonian glacial chronology for the Last Glacial period and implications for Southern Ocean climate. Quaternary Science Reviews, 27(3), 284-294, doi:10.1016/j.quascirev.2007.09.013.

Kilian, R., Lamy, F., 2012. A review of Glacial and Holocene paleoclimate records from southernmost Patagonia (49–55°S). Quaternary Science Reviews, 53, 1-23, doi:10.1016/j.quascirev.2012.07.017.

Kim, J.-H., Schneider, R.R., Hebbeln, D., Müller, P.J., Wefer, G., 2002. Last deglacial sea-surface temperature evolution in the Southeast Pacific compared to climate changes on the South

American continent. Quaternary Science Reviews, 21, 2085-2097, doi:10.1016/S0277-3791(02)00012-4.

Kim, S.-J., Lü, J.M., Kim, B.-M., 2014. The Southern Annular Mode (SAM) in PMIP2 simulations of the Last Glacial Maximum. Advances in Atmospheric Sciences, 31(4), 863–878, doi:10.1007/s00376-013-3179-8.

Klages, J.P., Kuhn, G., Hillenbrand, C.-D., Graham, A.G.C., Smith, J.A., Larter, R.D., Gohl, K., Wacker, L., 2014. Retreat of the West Antarctic Ice Sheet from the western Amundsen Sea shelf at a pre- or early LGM stage. Quaternary Science Reviews, 91, 1-15, doi:10.1016/j.quascirev.2014.02.017

Knorr, G., Lohmann, G., 2003. Southern Ocean origin for the resumption of Atlantic thermohaline circulation during deglaciation. Nature, 424(6948), 532-536, doi:10.1038/nature01855.

Kobashi, T., Severinghaus, J.P., Brook, E.J., Barnola, J.-M., Grachev, A.M., 2007. Precise timing and characterization of abrupt climate change 8200 years ago from air trapped in polar ice. Quaternary Science Reviews, 26, 1212-1222, doi:10.1016/j.quascirev.2007.01.009.

Kohfeld, K.E., Graham, R.M., de Boer, A.M., Sime, L.C., Wolff, E.W., Le Quéré, C., Bopp, L., 2013. Southern Hemisphere westerly wind changes during the Last Glacial Maximum: Paleo-data synthesis. Quaternary Science Reviews, 68, 76-95, doi:10.1016/j.quascirev.2013.01.017.

Koutavas, A., Lynch-Stieglitz, J., Marchitto, T.M., Sachs, J.P., 2002. El Nino-like pattern in ice age tropical Pacific sea surface temperature. Science, 297(5579), 226-230, doi:10.1126/science.1072376.

Kozlova, O.G., 1966. Diatoms of the Indian and Pacific sectors of the Antarctic. National Science Foundation, Israel Program for Scientific Translation, Washington, D.C., 185 pp.

Kucera, M., Rosell-Melé, A., Schneider, R., Waelbroeck, C., Weinelt, M., 2005a. Multiproxy approach for the reconstruction of the glacial ocean surface (MARGO). Quaternary Science Reviews, 24, 813-819, doi:10.1016/j.quascirev.2004.07.017

Kucera, M., Weinelt, M., Kiefer, T., Pflaumann, U., Hayes, A., Weinelt, M., Chen, M.-T., Mix, A.C., Barrows, T.T., Cortijo, E., Duprat, J., Juggins, S., Waelbroeck, C., 2005b. Reconstruction of sea-surface temperatures from assemblages of planktonic foraminifera: multi-technique approach based on geographically constrained calibration data sets and its application to glacial Atlantic and Pacific Oceans. Quaternary Science Reviews, 24(7-9), 951-998, doi:10.1016/j.quascirev.2004.07.014.

Lambeck, K., Rouby, H., Purcell, A., Sun, Y., Sambridge, M., 2014. Sea level and global ice volumes from the Last Glacial Maximum to the Holocene. Proceedings of the National Academy of Sciences, 111(43), 15296-15303, doi:10.1073/pnas.1411762111.

Lambert, F., Delmonte, B., Petit, J.R., Bigler, M., Kaufmann, P.R., Hutterli, M.A., Stocker, T.F., Ruth, U., Steffensen, J.P., Maggi, V., 2008. Dust-climate couplings over the past 800,000 years from the EPICA Dome C ice core. Nature, 452(7187), 616-619, doi:10.1038/nature06763.

Lamy, F., Kaiser, J., Ninnemann, U., Hebbeln, D., Arz, H.W., Stoner, J., 2004. Antarctic Timing of Surface Water Changes off Chile and Patagonian Ice Sheet Response. Science, 304, 1959-1962, doi:10.1126/science.1097863.

Lamy, F., Kaiser, J., Arz, H.W., Hebbeln, D., Ninnemann, U., Timm, O., Timmermann, A., Toggweiler, J. R., 2007. Modulation of the bipolar seesaw in the Southeast Pacific during Termination 1. Earth and Planetary Science Letters, 259 (3), 400-413, doi:10.1016/j.epsl.2007.04.040.

Lamy, F., Kilian, R., Arz, H.W., Francois, J.-P., Kaiser, J., Prange, M., Steinke, T., 2010. Holocene changes in the position and intensity of the southern westerly wind belt. Nature Geoscience 3, 695-699, doi:10.1038/NGEO959.

Lamy, F., Gersonde, R., Winckler, G., Esper, O., Jaeschke, A., Kuhn, G., Ullermann, J., Martínez-Garcia, A., Lambert, F., Kilian, R., 2014. Increased Dust Deposition in the Pacific Southern Ocean During Glacial Periods. Science, 343(6169), 403-407, doi:10.1126/science.1245424.

Lamy, F., Arz, H., Kilian, R., Lange, C.B., Lembke-Jene, L., Wengler, M., Kaiser, J., Baeza-Urrea, O., Hall, I. R., Harada, N., Tiedemann, R., 2015. Glacial reduction and millennial-scale variations in Drake Passage throughflow. Proceedings of the National Academy of Sciences, 112(44), 13496-13501, doi:10.1073/pnas.1509203112.

Larter, R.D., Anderson, J.B., Graham, A.G.G., Gohl, K., Hillenbrand, C.-D., Jakobsson, M., Johnson, J.S., Kuhn, G., Nitsche, F.O., Smith, J.A., Witus, A.E., Bentley, M.J., Dowdeswell, J.A., Ehrmann, W., Klages, J.P., Londow, J., Ó Cofaigh, C., Spiegel, C., 2014. Reconstruction of changes in the Amundsen Sea and Bellingshausen Sea sector of the West Antarctic Ice Sheet since the Last Glacial Maximum. Quaternary Science Reviews, 100, 55-86, doi:10.1016/j.quascirev.2013.10.016.

Laskar, J., Robutel, P., Joutel, F., Gastineau, M., Correia, A.C.M., Levrard, B., 2004. A long-term numerical solution for the insolation quantities of the Earth. Astronomy & Astrophysics 428: 261-285, doi:10.1051/0004-6361:20041335.

Leduc, G., Vidal, L., Cartapanis, O., Bard, E., 2009. Modes of eastern equatorial Pacific thermocline variability: Implications for ENSO dynamics over the last glacial period, Paleoceanography, 24, PA3202, doi:10.1029/2008PA001701.

Lefebvre, W., H. Goosse, R. Timmermann, Fichefet, T., 2004. Influence of the Southern Annular Mode on the sea ice–ocean system, Journal of Geophysical Research, 109, C09005, doi:10.1029/2004JC002403.

Lisiecki, L.E., Raymo, M.E., 2005. A Pliocene-Pleistocene stack of 57 globally distributed benthic $\delta^{18}O$ records. Paleoceanography, 20(1), PA1003, doi:10.1029/2004PA001071.

Lisitzin, A.P., 1985. The silica cycle during the last ice age. Palaeogeography, Palaeoclimatology, Palaeoecology, 50, 247-270, doi: 10.1016/0031-0182(85)90070-7.

Locarnini, R.A., Mishonov, A.V., Antonov, J.I., Boyer, T.P., Garcia, H.E., Baranova, O.K., Zweng, M.M., Johnson, D. R., 2010. World Ocean Atlas 2009, Volume 1: Temperature. In: Levitus, S., (Ed.) NOAA Atlas NESDIS 68, U.S. Government Printing Office, Washington, D.C., pp. 184.

Lovenduski, N.S., Gruber, N., 2005. Impact of the Southern Annular Mode on Southern Ocean circulation and biology. Geophysical Research Letters, 32, L11603, doi:10.1029/2005GL022727.

Lovenduski, N.S., Gruber, N., Doney, S.C., Lima, I.D., 2007. Enhanced CO_2 outgassing in the Southern Ocean from a positive phase of the Southern Annular Mode. Global Biochemical Cycles 21, GB2026, doi:10.1029/2006GB002900.

Lüer, V., Cortese, G., Neil, H.L., Hollis, C.J., Willems, H., 2009. Radiolarian-based sea surface temperatures and paleoceanographic changes during the Late Pleistocene–Holocene in the subantarctic southwest Pacific. Marine Micropaleontology, 70(3), 151-165, doi:10.1016/j.marmicro.2008.12.002.

Lüthi, D., Le Floch, M., Bereiter, B., Blunier, T., Barnola, J.-M., Siegenthaler, U., Raynaud, D., Jouzel, J., Fischer, H., Kawamura, K., Stocker, T.F., 2008. High-resolution carbon dioxide concentration record 650,000-800,000 years before present. Nature,, 453, 379-382, doi:10.1038/nature06949.

Lumpkin, R., Speer, K., 2007. Global Ocean Meridional Overturning. Journal of Physical Oceanography, 37, 2550-2562, doi:10.1175/JPO3130.1.

Luz, B., 1977. Late Pleistocene paleoclimates of the South Pacific based on statistical analysis of planktonic foraminifers. Palaeogeography, Palaeoclimatology, Palaeoecology, 22, 61-78, doi:10.1016/0031-0182(77)90033-5.

Mackintosh, A., Golledge, N., Domack, E., Dunbar, R., Leventer, A., White, D., Pollard, D., DeConto. R., Fink, D., Zwartz, D., Gore, D., Lavoie, C., 2011. Retreat of the East Antarctic ice sheet during the last glacial termination. Nature Geoscience, 4(3), 195-202, doi: 10.1038/NGEO1061.

Maksym, T., Stammerjohn, S.E., Ackley, S., Massom, R., 2012. Antarctic sea ice—A polar opposite? Oceanography, 25(3), 140–151, doi:10.5670/oceanog.2012.88.

Marcott, S.A., Bauska, T.K., Buizert, C., Steig, E.J., Rosen, J.L., Cuffey, K.M., Fudge, T.J., Severinghaus J.P., Ahn, J., Kalk, M.L., McConnell, J.R., Sowers, T., Taylor, K.C., White, J.W.C., Brook, E.J., 2014. Centennial-scale changes in the global carbon cycle during the last deglaciation. Nature, 514(7524), 616-619, doi:10.1038/nature13799.

MARGO Project Members, 2009. Constraints on the magnitude and patterns of ocean cooling at the Last Glacial Maximum. Nature Geoscience, 2(2), 127-132, doi:10.1038/ngeo411.

Marr, J.P., Carter, L., Bostock, H.C., Bolton, A., Smith, E., 2013. Southwest Pacific Ocean response to a warming world: Using Mg/Ca, Zn/Ca, and Mn/Ca in foraminifera to track surface ocean

water masses during the last deglaciation. Paleoceanography, 28, 347-362, doi:10.1002/palo.20032.

Marshall, J., Speer, K., 2012. Closure of the meridional overturning circulation through Southern Ocean upwelling. Nature Geoscience, 5, 171-180, doi:10.1038/NGEO1391.

Martin, J.H., 1990. Glacial-interglacial CO_2 change: the iron hypothesis. Paleoceanography, 5, 1-13, doi:10.1029/PA005i001p00001.

Martínez-Garcia, A., Rosell-Melé, A., Geibert, W., Gersonde, R., Masqué, P., Gaspari, V., Barbante, C., 2009. Links between iron supply, marine productivity, sea surface temperature, and CO_2 over the last 1.1 Ma, Paleoceanography, 24, PA1207, doi:10.1029/2008PA001657.

Mashiotta, T.A., Lea, D.W., Spero, H.J., 1999. Glacial/interglacial changes in Subantarctic sea surface temperature and δ^{18}O-water using foraminiferal Mg. Earth and Planetary Science Letters, 170(4), 417-432, doi:10.1016/S0012-821X(99)00116-8.

Masson, V., Vimeux, F., Jouzel, J., Morgan, V., Delmotte, M., Ciais, P., Hammer, C., Johnson, S., Lipenkov, V.Y., Mosley-Thompson, E., Petit., J.-R., Steig, E.J., Stievenard, M., Vaikmae, R., 2000. Holocene climate variability in Antarctica based on 11 ice-core isotopic records. Quaternary Research, 54(3), 348-358, doi:10.1006/qres.2000.2172.

Mathiot, P., Goosse, H., Crosta, X., Stenni, B., Braida, M., Renssen, H., Van Meerbeeck, C.J., Masson-Delmotte, V., Mairesse, A., Dubinkina, S., 2013. Using data assimilation to investigate the causes of Southern Hemisphere high latitude cooling from 10 to 8 ka BP. Climate of the Past, 9, 887-901, doi:10.5194/cp-9-887-2013.

Mayewski, P.A., Rohling, E.J., Stager, J.C., Karlén, W., Maasch, K.A., Meeker, L.D., Meyerson, E.A., Gasse, F., van Kreveld, S. Holmgren, K., Lee-Thorp, J., Rosqvist, G., Rack, F., Staubwasser, M., Schneider, R.R., Steig, E.J., 2004. Holocene climate variability. Quaternary Research, 62, 243-255, doi:10.1016/j.yqres.2004.07.001.

Mayr, C., Lücke, A., Wagner, S., Wissel, H., Ohlendorf, C., Haberzettl, T., Oehlerich, M., Schäbitz, F., Wille, M., Zhu, J., Zolitschka, B., 2013. Intensified Southern Hemisphere Westerlies regulated atmospheric CO_2 during the last deglaciation. Geology, 41, 831-834, doi:10.1130/G34335.1.

McCartney, M.S., 1977. Subantarctic Mode Water. In: Angel, M.V. (Ed.), A Voyage of Discovery, Deep-Sea Research, pp. 103-119.

McCave, I.N., Crowhurst, S.J., Kuhn, G., Hillenbrand, C.-D., Meredith, M.P., 2014. Minimal change in Antarctic Circumpolar Current flow speed between the last glacial and Holocene. Nature geoscience, 7, 113-116, doi:10.1038/NGEO2037.

McManus, J.F., Francois, R., Gherardi, J.M., Keigwin, L.D., Brown-Leger, S., 2004. Collapse and rapid resumption of Atlantic meridional circulation linked to deglacial climate changes. Nature, 428 (6985), 834-837, doi:10.1038/nature02494.

Mikolajewicz, U., 1998. Effect of meltwater input from the Antarctic ice sheet on the thermohaline circulation. Annals of Glaciology, 27, 311-315.

Mix, A.C., Bard, E., Schneider, R., 2001. Environmental processes of the ice age: land, oceans, glaciers (EPILOG). Quaternary Science Reviews, 20(4), 627-657, doi:10.1016/S0277-3791(00)00145-1.

Moore Jr., T.C., Burckle, L.H., Geitzenauer, K., Luz, B., Molina-Cruz, A., Robertson, J.H., Sachs, H., Sancetta, C., Thiede, J., Thompson, P., Wenkam, C., 1980. The reconstruction of sea surface temperatures in the Pacific Ocean of 18,000 B.P. Marine Micropaleontology, 5, 215-247.

Moore, J.K., Abbott, M.R., Richman, G., 1999. Location and dynamics of the Antarctic Polar Front from satellite and surface temperature data. Journal Geophysical res. 104, C2, 3059-3075, doi:10.1029/1998JC900032.

Moreno, P.I., Kaplan, M.R., François, J.P., Villa-Martínez, R., Moy, C.M., Stern, C.R., Kubik, P.W., 2009. Renewed glacial activity during the Antarctic cold reversal and persistence of cold conditions until 11.5 ka in southwestern Patagonia. Geology, 37(4), 375-378, doi:10.1130/G25399A.1.

Morey, A.E., Mix, A.C., Pisias, N.G., 2005. Planktonic foraminiferal assemblages preserved in surface sediments correspond to multiple environmental variables. Quaternary Science Reviews, 24, 925-950, doi:10.1016/j.quascirev.2003.09.011.

Mosola, A.B., Anderson, J.B., 2006. Expansion and rapid retreat of the West Antarctic Ice Sheet in eastern Ross Sea: possible consequence of over-extended ice streams?. Quaternary Science Reviews, 25(17-18), 2177-2196, doi:10.1016/j.quascirev.2005.12.013.

Moy, C.M., Seltzer, G.O., Rodbell, D.T., Anderson, D.M., 2002. Variability of El Niño/Southern Oscillation activity at millennial timescales during the Holocene epoch. Nature, 420, 162-165, doi:10.1038/nature01194.

Neil, H.L., Carter, L., Morris, M.Y., 2004. Thermal isolation of Campbell Plateau, New Zealand, by the Antarctic Circumpolar Current over the past 130 kyr, Paleoceanography, 19, PA4008, doi:10.1029/2003PA000975.

Nelson, D.M., Tréguer, P., Brzezinski, M.A., Leynaert, A., Quéguiner, B., 1995. Production and dissolution of biogenic silica in the ocean: Revised global estimates, comparison with regional data and relationship to biogenic sedimentation. Global Biogeochemical cycle, 9(3), 359-372, doi:10.1029/95GB01070.

Nelson, D.M., Anderson, R.F., Barber, R.T., Brzezinski, M.A., Buesseler, K.O., Chase, Z., Collier, R.W., Dickson, M.-L., François, R., Hiscock, M.R., Honjo, S., Marra, J., Martin, W.R., Sambrotto, R.N., Sayles, F.L., Sigmon, D.E., 2002. Vertical budgets for organic carbon and biogenic silica in the Pacific sector of the Southern Ocean, 1996–1998. Deep Sea Research Part II: Topical Studies in Oceanography, 49(9-10), 1645-1674, doi: 10.1016/S0967-0645(02)00005-X.

Newnham, R.M., Vandergoes, M.J., Sikes, E., Carter, L., Wilmshurst, J.M., Lowe, D.J., McGlone, M.S., Sandiford, A., 2012. Does the bipolar seesaw extend to the terrestrial southern mid-latitudes? Quaternary Science Reviews, 36, 214-222, doi:10.1016/j.quascirev.2011.04.013.

NGRIP Members, 2004. High-resolution record of Northern Hemisphere climate extending into the last interglacial period. Nature, 431(7005), 147-151, doi:10.1038/nature02805.

Ó Cofaigh, C., Larter, R.D., Dowdeswell, J.A., Hillenbrand, C.-D., Pudsey, C.J., Evans, J., Morris, P., 2005. Flow of the West Antarctic Ice Sheet on the continental margin of the Bellingshausen Sea at the Last Glacial Maximum. Journal of Geophysical Research: Solid Earth, 110 , B11103, doi:10.1029/2005JB003619.

Olbers, D., Gouretski, V., Seiß, G., Schröter, J., 1992. Hydrographic Atlas of the Southern Ocean. Alfred-Wegener-Institut, Bremerhaven, 82 plates.

Olbers, D., Borowski, D., Völker, C., Wölff, J.-O., 2004. The dynamical balance, transport and circulation of the Antarctic Circumpolar Current. Antarctic Science, 16(4), 439-470, doi:10.1017/S0954102004005521.

Oksanen, J., Blanchet, F.G., Kindt, R., Legendre, P., Minchin, P.R., O'Hara, R.B., Simpson, G.L., Solymos, P., Stevens, M.H.H., Wagner, H., 2012. Vegan: community ecology package. R package version 2.0-3 (http://CRAN.R-project.org/package=vegan).

Orsi, A.H., Whitworth III, T., Nowlin Jr, W.D., 1995. On the meridional extent and fronts of the Antarctic Circumpolar Current. Deep Sea Research Part I: Oceanographic Research, 42(5), 641-673, doi:10.1016/0967-0637(95)00021-W.

Orsi, A.H., Johnson, G.C., Bullister, J.L., 1999. Circulation, mixing, and production of Antarctic Bottom Water. Progress in Oceanography, 43, 55-109, doi:10.1016/S0079-6611(99)00004-X.

Orsi, A. H., Whitworth III, T., 2005. Hydrographic Atlas of the World Ocean Circulation Experiment (WOCE). Volume 1: Southern Ocean (Eds. Sparrow, M., Chapman, P., Gould, J-), International WOCE Project Office, Southampton, U.K., ISBN 0-904175-49-9.

Otto-Bliesner, B. L., Brady, E. C., Shin, S.-I., Liu, Z., Shields, C., 2003. Modeling El Niño and its tropical teleconnections during the last glacial-interglacial cycle, Geophysical Research Letters, 30(23), 2198, doi:10.1029/2003GL018553, 2003.

Pahnke, K., Sachs, J. P., 2006. Sea surface temperatures of southern midlatitudes 0–160 kyr B.P. Paleoceanography, 21, PA2003, doi:10.1029/2005PA001191.

Pahnke, K., Zahn, R., Elderfield, H., Schulz, M., 2003. 340,000-Year Centennial-Scale Marine Record of Southern Hemisphere Climatic Oscillation. Science, 301(5635), 948-952, doi:10.1126/science.1084451.

Paillard, D., Labeyrie, L., Yiou, P., 1996. Macintosh Program performs time-series analysis. Eos, Transactions American Geophysical Union, 77, 379-379, doi:10.1029/96EO00259.

Parrenin, F., Barnola, J. M., Beer, J., Blunier, T., Castellano, E., Chappellaz, J., Dreyfus, G., Fischer, H., Fujita, S., Jouzel, J., Kawamura, K., Lemieux-Dudon, B., Loulergue, L., Masson-Delmotte, V., Narcisi, B., Petit, J.-R., Raisbeck, G., Raynaud, D., Ruth, U., Schwander, J., Severi, M., Spahni, R., Steffensen, J.P., Svensson, A., Udisti, R., Waelbroeck, C., Wolff, E., 2007. The EDC3 chronology for the EPICA Dome C ice core. Climate of the Past, 3(3), 485-497, doi:10.5194/cp-3-485-2007.

Paul, A., Schäfer-Neth, C., 2005. How to combine sparse proxy data and coupled climate models, Quaternary science reviews, 24, 1095-1107, doi:10.1016/j.quascirev.2004.05.010.

Peck, V.L., Allen, C.S., Kender, S., McClymont, E.L., Hodgson, D.A., 2015. Oceanographic variability in the West Antarctic Peninsula during the Holocene and the influence of upper circumpolar deep water. Quaternary Science Reviews, 119, 54-65, doi:10.1016/j.quascirev.2015.04.002.

Petrich, C., Eicken, H., 2010. Growth, Structure and Properties of Sea Ice. In: Thomas, D.N, Dieckmann, G.S. (Eds.), Sea ice (second edition). Wiley-Blackwell, 23-77.

Putnam, A.E., Denton, G.H., Schaefer, J.M., Barrell, D J., Andersen, B.G., Finkel, R.C., Schwartz, R., Doughty, A.M., Kaplan, M.R., Schlüchter, C., 2010. Glacier advance in southern middle-latitudes during the Antarctic Cold Reversal. Nature Geoscience, 3(10), 700-704, doi:10.1038/NGEO962.

R Core Team, 2012. R: A Language and Environment for Statistical Computing. R Foundation for Statistical Computing, Vienna, Austria. ISBN 3-900051-07-0, URL http://www.R-project.org/.

Rees, A.B.H., Cwynar, L.C., Fletcher, M.-S., 2015. Southern Westerly Winds submit to the ENSO regime: A multiproxy paleohydrology record from Lake Dobson, Tasmania. Quaternary Science Reviews, 126, 254-263, doi:10.1016/j.quascirev.2015.08.022.

Reimer, P.J., Bard, E., Bayliss, A., Beck, J.W., Blackwell, P.G., Bronk Ramsey, C., Buck, C.E., Cheng, H., Edwards, R.L., Friedrich, M., Grootes, P.M., Guilderson, T.P., Haflidason, H., Hajdas, I., Hatté, C., Heaton, T.J., Hoffmann, D.L., Hogg, A.G., Hughen, K.A., Kaiser, K.F., Kromer, B., Manning, S.W., Niu, M., Reimer, R.W., Richards, D.A., Scott, E.M., Southon, J.R., Staff, R.A., Turney, C.S.M., van der Plicht, J., 2013. IntCal13 and Marine13 Radiocarbon Age Calibration Curves 0-50,000 Years Cal BP. Radiocarbon 55, 1869-1887.

Rein, B., Lückge, A., Reinhardt, L., Sirocko, F., Wolf, A., Dullo, W.-C., El Niño variability off Peru during the last 20,000 years. Paleoceanography, 20, PA4003, doi:10.1029/2004PA001099.

Reynolds, R.W., Rayner, N.A., Smith, T.M., Stokes, D.C., Wang, W., 2002. An Improved In Situ and Satellite SST Analysis for Climate. Journal of Climate, 15(13), 1609-1625, doi:10.1175/1520-0442(2002)015<1609:AIISAS>2.0.CO;2.

Reynolds, R.W., Smith, T.M., Liu, C., Chelton, D.B., Casey, K., Schlax, M.G., 2007. Daily high-resolution-blended analyses for sea surface temperatures. Journal of Climate 20, 5473-5496, doi:10.1175/2007JCLI1824.1.

Rincón-Martínez, D., Lamy, F., Contreras, S., Leduc, G., Bard, E., Saukel, C., Blanz, T., Mackensen, A., Tiedemann, R., 2010. More humid interglacials in Ecuador during the past 500 kyr linked to latitudinal shifts of the equatorial front and the Intertropical Convergence Zone in the eastern tropical Pacific. Paleoceanography, 25, PA2210, doi:10.1029/2009PA001868.

Rintoul, S.R., 1991 South Atlantic interbasin exchange. Journal of Geophysical Research, 96, 2675–2692, doi:10.1029/90JC02422.

Rintoul, S. R., Hughes, C.W., Olbers, D., 2001. The antarctic circumpolar current system, In: Siedler, G., Church, J., Gould, J. (Eds.), Ocean circulation and climate: Observing and modelling the global ocean, Elsevier, New York, 271– 302.

Roche, D.M., Crosta, X., Renssen, H., 2012. Evaluating Southern Ocean sea-ice for the Last Glacial Maximum and pre-industrial climates: PMIP-2 models and data evidence. Quaternary Science Reviews, 56, 99-106, doi:10.1016/j.quascirev.2012.09.020.

Rohling, E.J., Pälike, H., 2005. Centennial-scale climate cooling with a sudden cold event around 8,200 years ago. Nature, 434, doi:10.1038/nature03421.

Rojas, M., Moreno, P., Kageyama, M., Crucifix, M., Hewitt, C., Abe-Ouchi, A., Ohgaito, R., Brady, E.C., Hope, P., 2009. The Southern Westerlies during the last glacial maximum in PMIP2 simulations. Climate Dynamics, 32(4), 525-548, doi: 10.1007/s00382-008-0421-7.

Romero, O.E., Armand, L. K., Crosta, X., Pichon, J.-J., (2005). The biogeography of major diatom taxa in Southern Ocean surface sediments: 3. Tropical/Subtropical species. Palaeogeography, Palaeoclimatology, Palaeoecology, 223(1), 49-65, doi:10.1016/j.palaeo.2005.03.027.

Romero, O.E., Kim, J.H. Hebbeln, D., 2006. Paleoproductivity evolution off central Chile from the Last Glacial Maximum to the Early Holocene. Quaternary Research, 65, 519-525, doi:10.1016/j.yqres.2005.07.003.

Ronge, T.A., 2014. Glacial and Interglacial Changes in Southwest Pacific Water Mass Ventilation and Circulation. Dissertation, Universität Bremen, pp. 166.

Round, F.E., Crawford, R.M., Mann, D.G., 1990. The Diatoms: biology and morphology of the genera. Cambridge University Press, Cambridge, pp. 747.

Sallée, J. B., Speer, K, Morrow, R., 2008. Response of the Antarctic Circumpolar Current to atmospheric variability. Journal of Climate 21(12), 3020-3059, doi:10.1175/2007JCLI1702.1.

Sarnthein, M., Balmer, S., Grootes, P.M., Mudelsee, M., 2015. Planktic and benthic ^{14}C reservoir ages for three ocean basins, calibrated by a suite of ^{14}C plateaus in the glacial-to-deglacial Suigetsu atmospheric ^{14}C record. Radiocarbon, 57(1), doi:10.2458/azu_rc.57.17916.

Saavedra-Pellitero, M., Flores, J.A., Lamy, F., Sierro, F.J., Cortina, A., 2011. Coccolitophore estimates of paleotemperature and paleoproductivity changes in the southeast Pacific over the past ~~27 kyr. Paleoceanography, 26, PA1201, doi:10.1029/2009PA001824.

Schaefer, J. M., Denton, G. H., Barrell, D. J., Ivy-Ochs, S., Kubik, P. W., Andersen, B. G., Phillips, F.M., Lowell, T.V., Schlüchter, C., 2006. Near-synchronous interhemispheric termination of the last glacial maximum in mid-latitudes. Science, 312(5779), 1510-1513 doi:10.1126/science.1122872.

Schlitzer, R., 2014. Ocean Data View. http://odv.awi.de.

Schmittner, A., 2003. Southern Ocean sea ice and radiocarbon ages of glacial bottom water. Earth and Planetary Science Letters 213, 53-62, doi:10.1016/S0012-821X(03)00291-7.

Schrader, H., Gersonde, R., 1978. Diatoms and silicoflagellates, In: Zachariasse, W.J., Riedel, W.R., Sanfilippo, A., Schmidt, R.R., Brolsma, M.J., Schrader, H.J., Gersonde, R., Drooger, M.M., Broekman, J.A. (Eds.), Micropaleontological Methods and Techniques — an Exercise on an Eight Metres Section of the Lower Pliocene of Capo Rossello, Sicily: Utrecht Micropaleontological Bulletin, 17, 129–176.

Schulz, K. G., Zeebe, R. E., 2006. Pleistocene glacial terminations triggered by synchronous changes in Southern and Northern Hemisphere insolation: The insolation canon hypothesis. Earth and Planetary Science Letters, 249(3), 326-336, doi:10.1016/j.epsl.2006.07.004.

Shakun, J.D., Clark, P.U., He, F., Marcott, S.A., Mix, A.C., Liu, Z., Otto-Bliesner, B., Schmittner, A., Bard, E., 2012. Global warming preceded by increasing carbon dioxide concentrations during the last deglaciation. Nature, 484(7392), 49-54, doi:10.1038/nature10915.

Shemesh, A., Burckle, L.H., Froelich, P.N., 1989. Dissolution and Preservation of Antarctic Diatoms and the Effect on Sediment Thanatocoenoses. Quaternary Research, 31, 288-308, doi:10.1016/0033-5894(89)90010-0.

Shemesh, A., Hodell, D., Crosta, X., Kanfoush, S., Charles, C., Guilderson, T., 2002. Sequence of events during the last deglaciation in Southern Ocean sediments and Antarctic ice cores. Paleoceanography, 17(4), 1056, doi:10.1029/2000PA000599.

Shevenell, A.E., Ingalls, A.E., Domack, E.W., Kelly, C., 2011. Holocene Southern Ocean surface temperature variability west of the Antarctic Peninsula. Nature, 470, 250-254, doi:10.1038/nature09751.

Shin, S.-I., Liu, Z., Otto-Bliesner, B.L., Kutzbach, J.E., Vavrus, S.J., 2003. Southern Ocean sea-ice control of the glacial North Atlantic thermohaline circulation, Geophysical Research Letters, 30(2), 1096, doi:10.1029/2002GL015513, 2003.

Siani, G., Michel, E., De Pol-Holz, R., DeVries, T., Lamy, F., Carel, M., Isguder, G., Dewilde, F., Lourantou, A., 2013. Carbon isotope records reveal precise timing of enhanced Southern Ocean upwelling during the last deglaciation. Nature Communications, 4, doi:10.1038/ncomms3758.

Sieger, R., Gersonde, R., Zielinski, U., 1999. A new extended software package for quantitative paleoenvironmental reconstructions. EOS, 80, 223.

Sigman, D.M., Hain, M.P., Haug, G.H., 2010. The polar ocean and glacial cycles in atmospheric CO2 concentration. Nature, 466(7302), 47-55, doi:10.1038/nature09149.

Sikes, E.J., Samson, C.R., Guilderson, T.P., Howard, W.R., 2000. Old radiocarbon ages in the southwest Pacific Ocean during the last glacial period and deglaciation. Nature, 405, 555-559, doi:10.1038/35014581.

Sikes, E.L., Howard, W.R., Neil, H.L., Volkman, J.K., 2002. Glacial-interglacial sea surface temperature changes across the subtropical front east of New Zealand based on alkenone unsaturation ratios and foraminiferal assemblages. Paleoceanography, 17(2), 2-1, doi:10.1029/2001PA000640.

Simpson, G.L., Oksanen, J., 2012. Analogue: analogue matching and modern analogue technique transfer function models. R Package Version 0.8–2 (http://cran.r-project. org/package=analogue).

Skinner, L.C., Fallon, S., Waelbroeck, C., Michel, E., Barker, S., 2010. Ventilation of the deep Southern Ocean and deglacial CO2 rise. Science, 328, 1147–1151, doi:10.1126/science.1183627.

Skinner, L., McCave, I.N., Carter, L., Fallon, S. Scrivner, A.E., Primeau, F., 2015. Reduced ventilation and enhanced magnitude of the deep Pacific carbon pool during the last glacial period. Earth and Planetary Science Letters, 411, 45-52, doi:10.1013/j.epsl.2014.11.024.

Smetacek, V., Assmy, P., Henjes, J., 2004. The role of grazing in structuring Southern Ocean pelagic ecosystems and biogeochemical cycles. Antarctic Science, 16(4), 541-558, doi:10.1017/S0954102004002317.

Smith, W.O., Nelson, D.M., 1986: The importance of ice edge phytoplankton production in the Southern Ocean. BioScience, 36, 251-257, doi:10.2307/1310215.

Smith, J.A., Hillenbrand, C.-D., Kuhn, G., Larter, R.D., Graham, A.G.C., Ehrmann, W., Moreton, S.G., Forwick, M., 2011. Deglacial history of the West Antarctic Ice Sheet in the western Amundsen Sea Embayment. Quaternary Science Reviews, 30(5-6), 488-505, doi:10.1016/j.quascirev.2010.11.020.

Sokolov, S., Rintoul, S.R., 2009. Circumpolar structure and distribution of the Antarctic Circumpolar Current fronts: 1. Mean circumpolar paths. Journal of Geophysical Research: Oceans, 114, C11018, doi:10.1029/2008JC005108.

Speer, K., Rintoul, S. R., Sloyan, B., 2000. The diabatic Deacon cell. Journal of Physical Oceanography 30, 3212-3222, doi:10.1175/1520-0485(2000)030<3212:TDDC>2.0.CO;2.

Spero, H.J., Lea, D.W., 2002. The cause of carbon isotope minimum events on glacial terminations. Science, 296(5567), 522-525, doi:10.1126/science.1069401.

Spindler, M., Dieckmann, G.S., 1986. Distribution and abundance of the planktic foraminiferNeogloboquadrina pachyderma in sea ice of the Weddell Sea (Antarctica). Polar Biology 5, 185-191.

Spolaor, A., Vallelonga, P., Plane, J.M.C., Kehrwald, N., Gabrieli, J., Varin, C., Turetta, C., Cozzi, G., Kumar, R., Boutron, C., Barbante, C., 2013. Halogen species record Antarctic sea ice extent over glacial–interglacial periods. Atmospheric Chemistry and Physics, 13(13), 6623-6635, doi:10.5194/acp-13-6623-2013.

Staines-Urías, F., González-Yajimovich, O., Beaufort, L., 2015. Reconstruction of past climate variability and ENSO-like fluctuations in the southern Gulf of California (Alfonso Basin) since the last glacial maximum. Quaternary Research, doi: 10.1016/j.yqres.2015.03.007.

Stammerjohn, S.E., Martinson, D.G., Smith, R.C., Yuan, X., Rind, D., 2008. Trends in Antarctic annual sea ice retreat and advance and their relation to El Niño-Southern Oscillation and Southern Annular Mode variability. Journal of Geophysical Research, 113, C03S90, doi:10.1029/2007JC004269.

Stammerjohn, S.E., Massom, R., Rind, D., Martinson, DG., 2012. Regions of rapid sea ice change: An inter-hemispheric seasonal comparison. Geophysical Research Letters, 39, L06501, doi:10.1029/2012GL050874, 2012.

Stenni, B., Sachs, J.P., Selmo, E., Souchez, R., Steffensen, J.P., Udisti, R., Jouzel, J., Masson-Delmotte, V., Röthlisberger, R., Castellano, E., Cattani, O., Falourd, S., Johnsen, S.J., Longinelli, A., 2006. EPICA Dome C Stable Isotope Data to 44.8 kyr BP. IGBP PAGES/World Data Center for Paleoclimatology. Data Contribution Series # 2006-112. NOAA/NCDC Paleoclimatology Program, Boulder CO, USA.

Stenni, B., Burion, D., Frezzotti, M., Albani, S., Barbante, C., Bard, E., Barnola, J.M., Baroni, M., Baumgartner, M., Bonazza, M., Capron, E., Castellano, E., Chappellaz, J., Delmonte, B., Falourd, S., Genoni, L., Iacumin, P., Jouzel, J., Kipfstuhl, S., Landais, A., Lemieux-Dudon, B.,

Maggi, V., Masson-Delmonte, V., Mazzola, C., Minster, B., Montagnat, M., Mulvaney, R., Narcisci, B., Oerter, H., Parrenin, F., Petit, J.R., Ritz, C., Scarchilli, C., Schilt, A., Schüpbach, S., Schwander, J., Selmo, E., Severi, M., Stocker, T.F., Udisti, R., 2011. Expression of the bipolar see-saw in Antarctic climate records during the last deglaciation. Nature Geo-sience 4, 46-50, doi:10.1038/NGEO1026.

Stephens, B.B., Keeling, R.F., 2000. The influence of Antarctic sea ice on glacial-interglacial CO_2 variations. Nature, 404 (6774), 171-174, doi:10.1038/35004556.

Stocker, T.F, 2003. South dials north. Nature 424, 496-499, doi:10.1038/424496a.

Stocker, T.F., Johnson, S.J., 2003. A minimum thermodynamic model for the bipolar seesaw. Paleoceanography, 18(4), 1087, doi:10.1029/2003PA000920.

Strother, S.L., Salzmann, U., Roberts, S.J., Hodgson, D.A., Woodward, J., Van Nieuwenhuyze, W., Verleyen, E., Vyverman, W., Moreton, S.G., 2015. Changes in Holocene climate and the intensity of Southern Hemisphere Westerly Winds based on a high-resolution palynological record from sub-Antarctic South Georgia., The Holocene, 25 (2), 263-279, doi:10.1177/0959683614557576.

Stuiver, M., Reimer, R.J., 1993. Extended database and revised CALIB radiocarbon dating program. Radiocarbon, 35, 215-230.

Stuiver, M., Reimer, P.J., Reimer, R.W., 2005. Calib, 7.0 ed, calib.qub.ac.uk.

Stuut, J.-B.W., Lamy, F., 2004. Climate variability at the southern boundaries of the Namib (southwestern Africa) and Atacama (northern Chile) coastal deserts during the last 120,000 yr. Quaternary Research, 62(3), 301-309, doi:10.1016/j.yqres.2004.08.001.

Sugden, D.E., Bentley, M.J., Fogwill, C.J., Hulton, N.R., McCulloch, R.D., Purves, R.S., 2005. Late-glacial glacier events in southernmost South America: A blend of 'Northern' and 'Southern' Hemispheric climatic signals?. Geografiska Annaler: Series A, Physical Geography, 87(2), 273-288, doi:10.1111/j.0435-3676.2005.00259.x.

Sullivan, C.W., Arrigo, K.R., McClain, C.R., Comiso, J.C., Firestone, J., 1993. Distributions of Phytoplankton Blooms in the Southern Ocean. Science, 17, 262, 1832-1837, doi:10.1126/science.262.5141.1832.

Tapia, R., Nürnberg, D., Ronge, T., Tiedemann, R., 2015. Disparities in glacial advection of Southern Ocean Intermediate Water to the South Pacific Gyre. Earth and Planetary Science Letters, 410, 152-164, doi: 10.1016/j.epsl.2014.11.031.

Talley, L.D, 2013. Closure of the global overturning circulation through the Indian, Pacific and Southern Oceans: schematics and transports. Oceanography, 26, 80-97.

ter Braak, C.J.F., Juggins, S., 1993. Weighted averaging partial least squares regression (WA-PLS): an improved method for reconstructing environmental variables from species assemblages. Hydrobiologia ,269(270), 485–502.

Thomas, D.N., Dieckmann, G.S., 2010. Sea Ice (second edition). Wiley-Blackwell, pp. 621

Thompson, D.W.J., Wallace, J.M., 2000. Annular modes in the extratropical circulation. Part I: month-to-month variability. Journal of Climate, 13(5), 1000-1016, doi.10.1175/1520-0442(2000)013<1000:AMITEC>2.0.CO;2.

Thompson, D.W.J., Solomon, S., Kushner, P.J., England, M.H., Grise, K.M., Karoly, D.J., 2011. Signatures of the Antarctic ozone hole in Southern Hemisphere surface climates change. Nature Geoscience, 4, 741–749, doi:10.1038/NGEO1296.

Thornalley, D.J.R., Barker, S., Broecker. W.S, Elderfield, H., McCave, N., 2011. The Deglacial Evolution of North Atlantic Deep Convection. Science, 331, 202-205, doi:10.1123/science.1196812.

Toggweiler, J.R., Russell, J. L., Carson, S. R., 2006. Midlatitude westerlies, atmospheric CO_2, and climate change during the ice ages, Paleoceanography, 21, PA2005, doi:10.1029/2005PA001154.

Tréguer, P.J., De La Rocha, C.L., 2013. The World Ocean Silica Cycle. Annual Review of Marine Science, 5, 477-501, doi:10.1146/annurev-marine-121211-172346.

Treguer, P., Nelson, D.M., Van Bennekom, J., DeMaster, D.J., Leynaert, A., Quéguiner, B., The Silica Balance in the World Ocean: A reestimate. Science, 268, 375-379, doi:10.1126/science.268.5209.375.

Trenberth, K.E., Branstator, G.W., Karoly, D., Kumar, A., Lau, N.-C., Ropelewski, C., 1998. Progress during TOGA in understanding and modeling global teleconnections associated with

tropical sea surface temperatures, Journal of Geophysical Research, 103, C7, 14,291-14,324, doi:10.1029/97JC01444.

Turner, J., Comiso, J.C., Marshall, G.J., Lachlan-Cope, T.A., Bracegirdle, T., Maksym, T., Meredith, M.P., Wang, Z., Orr, A., 2009. Non-annular atmospheric circulation change induced by stratospheric ozone depletion and its role in the recent increase of Antarctic sea ice extent, Geophysical Research Letters, 36, L08502, doi:10.1029/2009GL037524.

Udintsev G.B. (ed.), 2003. International geological-geophysical atlas of the Pacific. Scale 1:10,000,000. Size 70 x 100 cm, full colour, 192p. Published by Intergovernmental Oceanographic Commission (IOC), UNESCO. Moscow-St. Petersburg, Russia.

Varma, V., Prange, M., Lamy, F., Merkel, U., Schulz, M., 2011. Solar-forced shifts of the Southern Hemisphere Westerlies during the Holocene. Climate of the Past, 7, 339-347, doi:10.5194/cp-7-339-2011.

Veres, D., Bazin, L., Landais, A., Toyé Mahamadou Kele, H., Lemieux-Dudon, B., Parrenin, F., Martinerie, P., Blayo, E., Blunier, T., Capron, E., Chappellaz, J., Rasmussen, S.O., Severi, M., Svensson, A., Vinther, B., Wolff, E.W., 2013. The Antarctic ice core chronology (AICC2012): an optimized multi-parameter and multi-site dating approach for the last 120 thousand years. Climate of the Past, 9, 1733-1748, doi:10.5194/cp-9-1733-2013.

Verleye, T.J., Louwye, S., 2010. Recent geographical distribution of organic-walled dinoflagellate cysts in the southeast Pacific (25 – 53°S) and their relation to the prevailing hydrographical conditions. Palaeogeography, Palaeoclimatology, Palaeoecology, 298, 319-340, doi:10.1016/j.palaeo.2010.10.006.

Verleye, T.J., Martinez, P., Robinson, R.S., Louwye, S., 2013. Changes in the source of nutrients associated with oceanographic dynamics offshore southern Chile (41° S) over the last 25,000 years. Quaternary Research, 80(3), 495-501, doi:10.1016/j.yqres.2013.07.002.

WAIS Divide Project Members, 2013. Onset of deglacial warming in West Antarctica driven by local orbital forcing. Nature, 500, 440-444, doi: 10.1038/nature12376.

Walker, M.J.C., Bryant, C., Coope, G.R., Harkness, D.D., Lowe, J.J., Scott, E.M., 2001. Towards a radiocarbon chronology of the Late-Glacial: sample selection strategies. Radiocarbon, 43(2B), 1007-1019.

Weaver, A.J., Saenko, O.A., Clark, P.U., Mitrovica, J.X., 2003. Meltwater pulse 1A from Antarctica as a trigger of the Bølling-Allerød warm interval. Science, 299(5613), 1709-1713 doi: 10.1126/science.1081002.

Whitworth III, T., Nowlin Jr., W.D., Worley, S.J., 1982 The net transport of the Antarctic Circumpolar Current through Drake Passage, Journal of Physical Oceanograpy, 12 , 960–971, doi:10.1175/1520-0485(1982)012<0960:TNTOTA>2.0.CO;2.

Worby, A.P., Comiso, J.C., 2004. Studies of the Antarctic sea ice edge and ice extent from satellite and ship observations. Remote Sensing of Environment 92, 98-111, doi:10.1016/j.rse.2004.05.007.

Yokoyama, Y., Lambeck, K., De Deckker, P.P.J., Fifield, L.K., 2000. Timing of the last glacial maximum from observed sea-level minima. Nature, 406, 713-716, doi:10.1038/35021035.

Yuan, X., 2004. ENSO-related impacts on Antarctic sea ice: a synthesis of phenomenon and mechanisms. Antarctic Science, 16(04), 415-425, doi:10.1017/S0954102004002238.

Zielinski, U., 1993. Quantitative estimation of palaeoenvironmental parameters of the Antarctic Surface Water in the Late Quaternary using transfer functions with diatoms. Reports on Polar Research, vol. 126. Alfred Wegener Institute for Polar and Marine Research, Bremerhaven, pp. 148.

Zielinski, U., Gersonde, R., 1997. Diatom distribution in Southern Ocean surface sediments (Atlantic sector): Implications for paleoenvironmental reconstructions. Palaeogeography, Palaeoclimatology, Palaeoecology, 129(3-4), 213-250, doi:10.1016/S0031-0182(96)00130-7.

Zielinski, U., Gersonde, R., 2002. Plio-Pleistocene diazom biostratigraphy from ODP leg 177, Atlantic sector of the Southern Ocean. Marine Micropaleontology, 45, 225-268, doi:10.1016/S0377-8398(02)00031-2.

Zielinski, U., Gersonde, R., Sieger, R., Fütterer D., 1998. Quaternary surface water temperature estimations: Calibration of a diatom transfer function for the Southern Ocean, Paleoceanography, 13(4), 365–383, doi:10.1029/98PA01320.

Zhang, X., Lohmann, G., Knorr, G., Xu, X., 2013. Different ocean states and transient characteristics in Last Glacial Maximum simulations and implications for deglaciation. Climate of the Past, *9*, 2319-2333, doi:10.5194/cp-9-2319-2013.

Zwally, H.J., Comiso, J.C., Parkinson, C.L., Cavalieri, D.J., Gloersen, P., 2002. Variability of Antarctic sea ice 1979–1998. Journal of Geophysical Research: Oceans, 107(C5), 9-1-9-19, doi:10.1029/2000JC000733.

A1 − Antarctic Zone nutrient conditions during the last two glacial cycles

Anja S. Studer[1,2], Daniel M. Sigman[1], Alfredo Martínez-García[2], **Verena Benz[3]**, Gisela Winckler[4,5], Gerhard Kuhn[3], Oliver Esper[3], Frank Lamy[3], Samuel L. Jaccard[6], Lukas Wacker[7], Sergey Oleynik[1], Rainer Gersonde[3], and Gerald H. Haug[2]

[1]Department of Geosciences, Princeton University, Princeton, New Jersey, USA, [2]Geological Institute, ETH Zürich, Zürich, Switzerland, [3]Alfred-Wegener-Institut, Helmholtz-Zentrum für Polar- und Meeresforschung, Bremerhaven, Germany, [4]Lamont-Doherty Earth Observatory, Columbia University, Palisades, New York, USA, [5]Department of Earth and Environmental Sciences, Columbia University, Palisades, New York, USA, [6]Institute of Geological Sciences and Oeschger Centre for Climate Change Research, University of Bern, Bern, Switzerland, [7]Laboratory of Ion Beam Physics, ETH Zurich, Zurich, Switzerland

Abstract

In a sediment core from the Pacific sector of the Antarctic Zone (AZ) of the Southern Ocean, we report diatom-bound N isotope ($\delta^{15}N_{db}$) records for total recoverable diatoms and two distinct diatom assemblages (pennate and centric rich). These data indicate tight coupling between the degree of nitrate consumption and Antarctic climate across the last two glacial cycles, with $\delta^{15}N_{db}$ (and thus the degree of nitrate consumption) increasing at each major Antarctic cooling event. Coupled with evidence from opal- and barium-based proxies for reduced export production during ice ages, the $\delta^{15}N_{db}$ increases point to ice age reductions in the supply of deep ocean-sourced nitrate to the AZ surface. The two diatom assemblages and species abundance data indicate that the $\delta^{15}N_{db}$ changes are not the result of changing species composition. The pennate and centric assemblage $\delta^{15}N_{db}$ records indicate similar changes but with a significant decline in their difference during peak ice ages. A tentative seasonality-based interpretation of the centric-to-pennate $\delta^{15}N_{db}$ difference suggests that late summer surface waters became nitrate free during the peak glacials.

Authors contribution: I provided a first age model established with diatom abundance stratigraphy and participated in the selection of the depth for radiocarbon analysis. Furthermore I helped with the interpretation of the age model as well as the calibration of the AMS^{14}C ages.

A2 – List of Abbreviations

Water masses, climatic intervals, and (pale-) oceanographic/ climatic terms

AAIW	Antarctic Intermediate Water
AABW	Antarctic Bottom Water
ACC	Antarctic Circumpolar Current
ACR	Antarctic Cold Reversal
AHO	Antarctic Holocene Maximum
AICC12	Antarctic Ice Core Chronology 2012
AMOC	Atlantic Meridional Overturning Circulation
APF	Polar Front
AZ	Antarctic Zone
B/A	Bølling/Allerød
BP	Before Present (<1950)
CDW	Circumpolar Deep Water
EAC	East Australian Current
ENSO	El Niño Southern Oscillation
EDC	EPICA Dome C ice core
(E-) LGM	(EPILOG-) Last Glacial Maximum
E-T-F	Eltanin-Tharp Fracture Zone
GICC05	Greenland Ice Core Chronology 2005
GAPF	Glacial APF
GSACCF	Glacial SACCF
GSSTF	Glacial Southern Subtropical Front
HASO	Hydrographic Atlas of the Southern Ocean
HCS	Humboldt Current System
HNLC	High Nutrient-Low Chlorophyll
HS1	Heinrich Stadial 1
MIS	Marine Isotope Stage
MWP	Meltwater Pulse
NADW	North Atlantic Deep Water
NH	Northern Hemisphere
PAR	Pacific Antarctic Ridge

PIB	Pine Island Bay
PFZ	Polar Front Zone
POOZ	Permanent Open Ocean Zone
SAF	Subantarctic Front
SACCF	Southern Antarctic Circumpolar Current Fronts
SAM	Southern Annular Mode
SAZ	Subantarctic Zone
SAMW	Subantarctic Mode Water
SH	Southern Hemisphere
SO	Southern Ocean
(s) SIZ	(seasonal) Sea Ice Zone
SPC	South Pacific Current
(S/W) SST	(Summer/Winter) Sea surface temperature
SI	Sea Ice
SSI	Summer Sea Ice
STF	Subtropical Front
STZ	Subtropical Zone
SWW	Southern Westerly Winds
THC	Thermohaline Circulation
U-F	Udintsev Fracture Zone
WAIS	West Antarctic Ice Sheet
WDC	WAIS Divide ice core
WOA	World Ocean Atlas
YD	Younger Dryas

Proxy and analytical definitions

AMS	Accelerator Mass Spectrometry
AQL	Average Quality level
CQL	Chronostratigraphic Quality Level
EQL	Estimate Quality Level
GAM	Generalized Additive Model
GC	Gravity corer
IKM	Imbrie and Kipp Method

KC	Kasten Corer
MAT	Modern Analogue Technique
MICADAS	Mini radioCarbon Dating System
MSCL	Multi-Sensor Core Logger
NIST-19	carbonate standard from the National Institute of Standards and Technology
PC	Piston Corer
RMSEP	Root Mean Square Error of Prediction
TC	Trigger Corer
TF	Transfer Function
VPDB	Vienna Pee Dee Belemnite
WA	Weighted Average
WAPSL	Weighted Averaging Partial Least Squares
XRF	X-Ray Fluorescence

Project names, facilities, and institutes

AWI	Alfred Wegener Institute
BMBF	Bundesministerium für Bildung und Forschung
BIPOMAC	Bipolar Climate Machinery
CLIMAP	Climate, Long-Rage Investigations, Mapping and Prediction
DFG	Deutsche Forschungsgemeinschaft
ETH	Eidgenössische Technische Hochschule
EPICA	European Project for Ice Coring in Antarctica
EPILOG	Environmental processes of the ice age: land, oceans, glaciers
EU-FP7	European Union – Seventh Framework Programme for Research and Technological Development
IPCC	Intergovernmental Panel on Climate Change
MARGO	Multiproxy approach for the reconstruction of the glacial ocean surface
MARUM	Zentrum für Marine Umweltwissenschaften
NGRIP	North Greenland Ice Core Project
NOSAMS	National Ocean Science AMS
NOAA	National Oceanic and Atmospheric Administration
ODP	Ocean Drilling Program

PACES	Polar Regions and Coasts in a Changing Earth System
POLMAR	AWI graduate School
WHOI	Woods Hole Oceanographic Institut

Other

SW	South-West
N-S	North-South
S-N	South-North
E-W	East-West
W-E	West-East